Unsteady Aerodynamics in an Axial Flow Compressor

by

Jeremy David

J. D. Hughes, B.E. (Hons.)

School of Engineering

Submitted in fulfilment of the requirements
for the degree of
Doctor of Philosophy

University of Tasmania

February 2001

Statement of Originality

This thesis contains no material which has been accepted for the award of any other degree or diploma in any tertiary institution. To the best of my knowledge and belief, this thesis contains no material previously published or written by another person, except when due reference is made in the text.

Jeremy Hughes

Authority of Access

This thesis may be made available for loan and limited copying in accordance with the *Copyright Act 1968*.

Jeremy Hughes

Abstract

Current methods for designing compressor blades in axial turbomachines assume that the flow through each blade row is steady. However, interactions associated with the relative motion of neighbouring blade rows are known to produce a disturbance field with both random and periodic components. Despite a growing amount of research into the influence of these disturbances on the downstream row in a rotor-stator or stator-rotor blade row pair, these effects are still not generally accounted for at the design stage. Recent advances in Low Pressure Turbine blade design have shown that incorporating unsteady effects can lead to increases in blade loading beyond the loading limits inferred from steady flow calculations.

The current experimental work investigates the unsteady flow behaviour in the neighbourhood of the outlet stator in a 1.5 stage axial flow compressor using thermal anemometry. The aim is to provide a base for more accurate unsteady modelling, and facilitate the development of compressor blade designs which gain maximum benefit from unsteady effects. High-speed data acquisition with synchronised sampling was used to acquire data ensembles for a specific set of rotor wakes, and estimate the periodic and random components of the stator inflow disturbance field. The stator inflow disturbance flow field was altered by clocking of the inlet guide vane row relative to the stator row, and by changing the rotor-stator axial blade row spacing.

The interaction of inlet guide vane and rotor wakes was examined using hot-wire measurements downstream of the rotor row. The interaction process was shown to restrict the relative motion of rotor wake fluid and produce local accumulations of low energy fluid on the suction side of the inlet guide vane wakes. Significant circumferential variations in both time-mean velocity and the periodic disturbance component were observed. Clocking of the downstream stator row relative to the inlet guide vanes altered the mid-span stator blade boundary layer behaviour. Hot-wire measurements performed downstream of the stator were used to evaluate the influence of blade row clocking on the stator mid-span viscous losses. The magnitude of periodic fluctuations in ensemble-average stator wake thickness was significantly influenced by IGV wake-rotor wake interaction effects. The changes in time-mean stator losses were marginal.

The periodically unsteady laminar to turbulent transition of the stator blade boundary layer was examined using a hot-film surface array mounted on both the suction and pressure surfaces. Observations were made for stator blade loading or incidence cases near stall, design and maximum flow, and for a range of relative axial and circumferential blade row positions. Ensemble average plots of turbulent intermittency and relaxation factor (extent of calmed flow following the passage of a turbulent spot) are presented for a range of inflow disturbance cases. These show the strength of periodic wake-induced transition phenomena to be significantly influenced by incidence,

clocking and blade row spacing effects. The periodic, wake-induced, transition in separation bubbles was also altered by changes in blade row spacing. Significant differences between suction and pressure surface transition behaviour were observed, particularly with regard to the strength and extent of calming.

Subsequent collaborative work (not reported within) evaluated the quasi-steady application of conventional transition correlation to predict unsteady transition onset on the blading of an embedded axial compressor stage. The viscous/inviscid interaction code MISES was used to calculate the blade surface pressure distributions and boundary layer development. Predictions of the temporal variation in transition onset based on the measured temporal variation of inflow turbulence were compared with the transition onset observations from the compressor stator. Computations for both natural and bypass transition modes indicated that the natural transition mode predicted by a modified e^n method tended to dominate on the compressor blades. The success of the MISES transition onset predictions provided strong circumstantial evidence for the importance of natural transition mechanisms in strongly decelerating flow and provided the impetus further experimental investigation.

Transitional flow data from the surface film gauges were also analysed using wavelet techniques. The primary use of the wavelet analysis was to facilitate identification of transient instability phenomena in the complex periodic transitional flows present in the stator blade boundary layer. Wavelet analysis and high-pass filtering techniques revealed significant wave packet activity in the unstable laminar flow regions. An algorithm was developed to identify instability waves within the Tollmien-Schlichting (T-S) frequency range. This was combined with a turbulent intermittency detection routine to produce space~time diagrams showing the probability of instability wave occurrence prior to regions of turbulent flow. The implications for transition prediction in decelerating flow regions on axial turbomachine blades are discussed.

Acknowledgements

All projects which extend over a significant period of time are only possible with the support of many people. The author wishes to take this opportunity to express his gratitude to Dr. Greg Walker for his excellent supervision, guidance and continued support and friendship. Some of the initial experimental observations were obtained with the help of Miss Isabel Köhler and her help is gratefully acknowledged. Discussions with post graduate students, past and present, and in particular Dr Jason Roberts and Dr Bill Solomon, were particularly useful and are also acknowledged. The experimental work would not have been possible without the assistance of the School of Engineering technical staff. Thanks are extended to Prof. J. Paul Gostelow for his thought provoking discussions and use of computing facilities at the University of Leicester.

Regular interaction with Rolls-Royce plc, Derby, United Kingdom was an extremely enjoyable component of the work. The support and interest from Dr Peter Stow and Mr John Coupland of the Aerothermal Methods Group, and Dr Simon Gallimore of the Compressor Design Office was greatly appreciated.

Last, but certainly not least, I wish to acknowledge the encouragement and continual support of my wife, Catherine, and my parents, Ann and Ian.

Contents

List Of Figures

List Of Tables

Nomenclature

a	Circumferential offset of stator blade leading edge from centre of IGV wake avenue
c	Blade chord
c_1, c_2, c_3	3-Hole probe calibration coefficients
d	Diameter
f_1, f_2, f_3	3-Hole probe correlation functions
i	Blade incidence
l	Length
n	Turbulent spot generation rate
$n = ln(A/A_0)_{max}$	Amplification Ratio
p	Static pressure
s	Surface distance
$s^* = s/s_{max}$	Dimensionless surface distance from leading edge
t	Time
$t^* = t/T$	Dimensionless time
u	Streamwise velocity
w	Relative velocity
w	Circumferential distance relative to IGV trailing edge
x	Distance along chord line
y	Distance normal to wall
A	Amplitude
Cp	Coefficient of pressure
E	Anemometer output voltage
E_0	Anemometer voltage at zero flow
$H = \delta^*/\theta$	Boundary layer shape factor
Nu	Nusselt number
P	Stagnation pressure Eqn. (4.1)
Q	Heat transfer
$Re_{ref} = U_{mb}c/\nu$	Reference Reynolds number
$Re_w = Ud/\nu$	Wire Reynolds number
$Re_1 = w_1 c/\nu$	Chord Reynolds number
$Re_{NS} = \frac{U}{\nu}\frac{\Delta U}{\omega}$	Non-steady Reynolds number
$Re_{\delta^*} = U\delta^*/\nu$	Displacement Thickness Reynolds number
$Re_\theta = U\theta/\nu$	Momentum thickness Reynolds number
S	Blade pitch
T	Rotor blade passing period *or* Temperature
Tu	Random disturbance level (turbulence)

$\tilde{Tu}$	Periodic disturbance level (unsteadiness)
Tu_D	Total disturbance level
U_{mb}	Rotor mid-span velocity
U	Local free-stream velocity
V_a	Mean axial velocity
W_n	Wavelet transform
α	Flow angle
β	Blade angle
γ	Turbulent intermittency
δ^*	Displacement thickness
θ	Momentum thickness *or* Blade camber angle
$\lambda_\theta = \frac{\theta^2}{\nu}\frac{dU}{dx}$	Pohlhausen pressure gradient parameter
κ	Probability of non-turbulent relaxing flow
ν	Kinematic viscosity
ξ	Blade stagger angle
ρ	Density
σ	Spot propagation parameter
τ	Autocorrelation time lag Eqn. (5.1)
τ	Quasi-wall shear stress
τ_w	Wall shear stress
$\phi = V_a/U_{mb}$	Flow coefficient
ω	Circular frequency

Superscripts, Subscripts, etc.

crit	critical
dyn	Dynamic
max	Maximum
s	Pitchwise average
t	Transition
tot	Total
IGV	Inlet Guide Vane
LAG	Large Axial Gap
PP or P	Pressure surface
RAG	Reduced Axial Gap
RMS	Root mean square
SS or S	Suction surface
SLE	Stator Leading Edge
STE	Stator Trailing Edge
$0, 1, 2$	Initial, Inlet, Outlet
$\underline{< >}$	Ensemble (phase-lock) average value
	Time-mean
$'$	Instantaneous fluctuation from time-mean
$''$	Instantaneous fluctuation from ensemble mean

Chapter 1

Introduction

One of the earliest practical proposals to use a gas turbine engine as a power unit for aircraft propulsion is documented in the Royal Aeronautical Establishment's report *An Aerodynamic Theory of Turbine Design* issued by Dr. A. A. Griffith in 1926. From their first introduction in the late 1930's, which is accredited to the insight and perseverance of Van Ohain in Germany and Whittle in the United Kingdom, gas turbines have dramatically advanced. Modern gas turbine engines operate at extreme pressures and temperatures whilst obtaining high levels of overall efficiency. Axial compressors are key components of gas turbine engines which find application in power plants for ships and aircraft, to drive oil and gas pumping stations and to generate electricity. Since its introduction, the spread of the gas turbine power plant has been so prolific that although considered technically mature by many, small advancements provided by further research and development are still capable of providing large economic benefits.

The continuing improvements in computing power, combined with economic pressures to reduce time and cost of developing turbomachinery components, has seen a steady infusion of three dimensional (3D) computational fluid dynamics (CFD) modelling into the aerodynamic design process of multistage axial flow machines. As reported by Adamczyk [3], this has allowed the designers to place less emphasis on the empirically based results of simple mean-line and axisymmetic models for all but the early phases of the design. For axial compressors this increase in the use of 3D CFD has produced radically different blade designs to account for the spatially varying time-mean flow field in the regions dominated by end wall effects. As these 3D blade design techniques mature, attention focuses on the possibility of advancing turbomachinery performance by considering the inherently unsteady nature of the flow. Work documented by Valkov and Tan [133, 134] and Van Zante et al. [136] has indicated that accounting for the unsteady interaction of the rotor tip clearance and wake flows with a downstream stator row can lead to a loss value which is significantly different from that determined by assuming the viscous flow to be mixed out prior to the interaction.

The emphasis of CFD development has to date been placed on modelling three-dimensional flows. This is a demanding problem and the associated numerical and gridding issues have received considerable attention. Unfortunately, the resolution afforded to the region near blade surfaces is constrained by computing power and modelling techniques and is almost always inadequate. Turbulence modelling has rarely taken account of the laminar boundary layer, its stability and separation limitations

and the attendant transition phenomena. It is quite common for models of multistage turbomachines to assume that the boundary layer is turbulent from the leading edge of all blade rows.

This thesis is concerned with the unsteady transition behaviour on the blading of an axial flow compressor. Although the problem of transition in flows over turbine blades has been studied in detail for some time, the problem of unsteady transition on axial compressor blades has received comparatively little attention. The work performed at General Electric and the University of Tasmania has shown that significant unsteady wake-induced transition effects also exist on compressor blades. It has been established that the wake-induced transition phenomena can delay separation on both compressor and turbine blades. The effects of calming in increasing transition length and resisting laminar separation appear to be as least as strong as for turbine blades.

The current literature on both steady and unsteady boundary layer transition in turbomachines is reviewed in Chapter 2. Due to the complex nature of this problem much of the previous attention has been concentrated on experimental observations; only recently have direct numerical simulations contributed to an increased level of understanding . The review starts with an overview of the basic mechanisms which lead to the breakdown of a laminar boundary layer into a turbulent state. The relevant merits of current numerical schemes for predicting the onset and length of the transition zone in steady flow are discussed. Some important observations obtained from experimental facilities which simulate the embedded stage environment are reviewed. Particular attention is drawn to the recent improvement in Low Pressure Turbine design methodology which benefits from the effects of unsteady boundary layer transition.

The general details of the 1.5 stage axial research compressor used in the present investigation are provided in Chapter 3. Instrumentation and calibration methods, along with data acquisition and control of the machine are discussed. The experimental programme is summarised in Chapter 4. The outlet stator blade surface velocity distributions, obtained from blade pressure tappings, for the different rotor-stator axial spacing configurations are also presented.

The interaction between wakes of adjacent blade rows in an axial turbomachine are known to produce regular spatial variations in both the time-mean and unsteady flow fields in a frame relative to the upstream row. Chapter 5 investigates this phenomenon with the aid of time-resolved hot-wire measurements downstream of the rotor blade row. This work extends the observations of Lockhart and Walker [88] by providing quantitative information on the development of the disturbance field downstream of the rotor blade row, and has in part been previously reported by Walker et al. [147]. These measurements of the periodic variation of stator inlet turbulence provided the initial conditions for the quasi-steady approach for determining the periodic variation in transition onset as reported by Solomon et al. [127]. Time-mean turbulent length scale data in the neighbourhood of the stator row are presented, and comparisons are drawn with similar measurements from other low-speed research compressors.

Chapter 6 examines how the changes in free-stream disturbance field, reported in Chapter 5, influence the viscous losses of the outlet stator. Hot-wire measurements carried out downstream of the stator blade row are used to evaluate both the fluctuating and time-mean stator blade wake properties. The influence of IGV wake street clocking and rotor-stator axial spacing are both examined. The majority of the results from large axial spacing configuration appear in the work reported by Walker et al. [145].

The unsteady flow field seen by an embedded blade row in a multistage axial turbomachine is dominated by the effects of the adjacent upstream stage. The major source of periodic disturbance is usually provided by relative motion of blade wakes from the row immediately upstream. The second upstream row provides the greatest contribution to the random disturbance field through dispersion of its chopped wake segments. Chapter 7 reports a detailed study of unsteady transition on both surfaces of the mid-span element of the outlet stator blade row in the 1.5 stage research compressor. The periodically unsteady stator inlet flow field is varied by changing the blade incidence, clocking of the IGV row and altering the axial row spacing. The hot-film observations obtained with relatively large axial distance between blade rows has been previously reported by Walker et al. [146]. Some details of the separated flow transition cases are also reported by Hughes et al. [74]. The relative importance of periodic and random freestream disturbances for transition on the stator blade element at mid-span are discussed.

Following the relative success of Solomon et al. [127] in predicting the transition onset in the current machine with a modified natural transition criterion, the surface hot-film data presented in Chapter 7 are re-analysed for evidence of natural transition phenomena in Chapter 8. A wavelet based algorithm is developed to aid in the identification of instability waves within the T-S frequency range: the initial development work is reported by Hughes et al. [74]. The algorithm is combined with a turbulent intermittency detection routine to produce space~time diagrams showing the probability of instability wave occurrence prior to regions of turbulent flow. These diagrams are also presented by Hughes and Walker [73] and Walker and Hughes [144]. Extensive regions of amplifying instability waves are identified. This work indicates that linear stability theory remains important for transition in an adverse pressure gradient, even under elevated free-stream turbulence levels. The related implications for transition prediction in decelerating flow regions on axial turbomachine blades are discussed.

The conclusions are presented in Chapter 9. There is a review of the important findings of the previous chapters, along with some speculation about the potential to improve compressor blade performance by modifying the blade surface pressure distribution to gain maximum benefit from unsteady blade boundary layer transition phenomena.

Chapter 2

Literature Review

2.1 Introduction

The region of flow where the boundary layer changes state from laminar to turbulent and its importance to turbomachinery blade design has been well established by many workers, with recent reviews provided by Mayle [93] and Hourmouziadis [69]. A thorough description of transitional flow requires both the location where turbulent spots are first produced and their subsequent behaviour until the formation of a fully turbulent boundary layer. Numerical predictions for the design of turbomachinery blading therefore need robust methods for determining the onset location and the streamwise distribution of intermittency for the range of adverse conditions under which a machine is required to operate.

This chapter intends to survey previous publications that are relevant to the present study. Some basic aspects of boundary layer transition in steady flow are reviewed, including a thorough treatment of natural transition in support of the findings of Chapter 8. Also included is a discussion of the important mechanisms of bypass and separated flow transition. Attention is given to methods which are employed to predict both transition onset and length in blade-to-blade design type calculations. The review concludes with a historical overview of experimental observations which have provided significant insight into the behaviour of periodically disturbed boundary layers common in turbomachinery.

2.2 Modes of Transition

2.2.1 Natural Transition

The transition process whereby a laminar boundary layer evolves into a turbulent state is a complicated process. The multiplicity of factors which directly influence this process has effectively prohibited the development of a unified theory to predict the onset of turbulence. When artificial forcing of disturbances in the flow does not exist, the route to turbulence is classified as *Natural transition.* This path to turbulent flow is usually observed in boundary layers subjected to low levels of freestream disturbances. Disturbances in the freestream, such as sound and vorticity, enter the boundary layer as steady and/or unsteady fluctuations of the basic state. This initial step is called *recep-*

tivity (see Morkovin [99]), and it provides the initial conditions of amplitude, frequency and phase for the breakdown of laminar flow. Initially these disturbances are too small to measure and they are observed only after the onset of an instability (Saric [113]). The type of instability that occurs depends on Reynolds number, surface roughness, surface curvature, cross flow and initial conditions. The following paragraphs discuss the stages of linear and non-linear growth of the instability waves and their subsequent breakdown into turbulent spots. It is the linear growth region of instabilities that characterises the mode of transition as *natural*.

The initial understanding of laminar-turbulent transition was developed from the experimental and theoretical studies in the well know pipe flow experiments performed by Reynolds, combined with the theoretical work of Rayleigh (see Schlichting [114]). Rayleigh used the method of small disturbances and, by neglecting the effects of viscosity, derived the inviscid stability equation from the Navier-Stokes equations. An important result from this equation is that velocity profiles with a point of inflection are unstable. This implies that at infinite Re_x all boundary layers subjected to an adverse pressure gradient are unstable to disturbances, because the existence of an inflection point is directly related to an increasing pressure, whereas favourable pressure gradients exert a stabilising effect. The Rayleigh equation was later extended to include the effects of viscosity, leading to the *Orr-Sommerfield* or viscous stability equation (see Schlichting [114])

$$\phi^{iv} - 2\tilde{\alpha}^2\phi'' + \tilde{\alpha}^4\phi = i\tilde{\alpha}Re(\tilde{U} - \tilde{c})(\phi'' - \tilde{\alpha}^2\phi) - iRe\tilde{\alpha}\tilde{U}''\phi \tag{2.1}$$

Eqn. (2.1) results from substitution of small two-dimensional harmonic disturbances into the incompressible Navier-Stokes equations, and is given above in dimensionless form with the length scale as the displacement thickness δ^* and velocity scale as the boundary layer edge velocity U_e. The stream function of a single two-dimensional harmonic disturbance is given by

$$\Psi(x, y, t) = \phi(y)e^{i(\alpha x - \omega t)} \tag{2.2}$$

with x the streamwise and y the wall normal coordinates and t time. For spatial amplification theory, the circular frequency ω is real and the wavenumber α is complex ($\alpha = \alpha_r + i\alpha_i$): the amplitude varies with streamwise distance x as $e^{-\alpha_i x}$. For temporal amplification theory, the circular frequency ω is assumed to be complex ($\omega = \omega_r + i\omega_i$), and the amplitude of disturbances varies with time as $e^{\omega_i t}$. For the latter case, the wavelength of the disturbance is $2\pi/\alpha$ and the circular frequency is the real part of ω. The complex part of ω is the amplification factor of the disturbance.

For a given flow with a specified mean velocity profile, Reynolds number and appropriate boundary conditions, Eqn. (2.1) can be solved for a complex eigenvalue, the real part of which is the phase velocity of the disturbance and the imaginary part is the amplification factor. Fig. 2.1 presents the eigenvalues in the form of a stability diagram, where the amplification rate is plotted as a function of wavenumber and Reynolds number. This diagram describes the three possible states of a disturbance at a given Reynolds number: damped, neutral or amplified. The locus of neutral amplification defines the boundary between stable and unstable flow, or the neutral stability

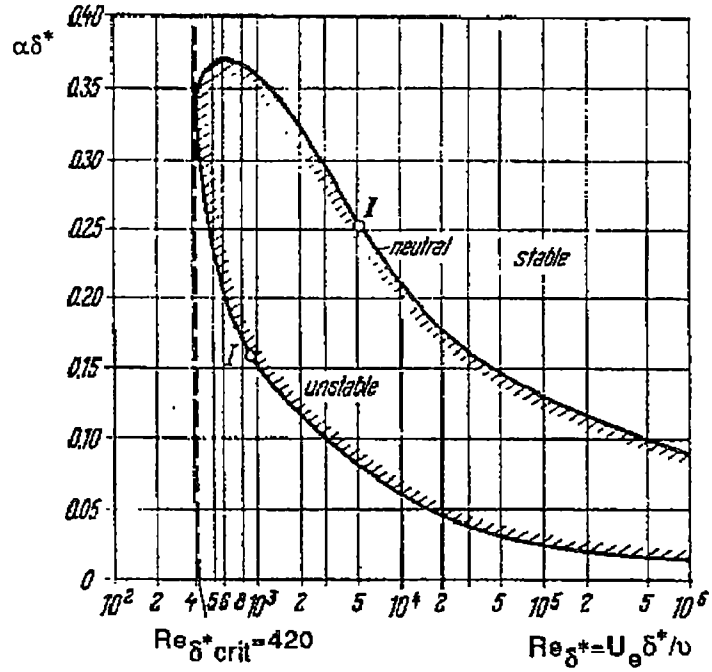

Figure 2.1: Curve of neutral stability for the wavelength $\alpha\delta^*$ of the disturbances in terms of the boundary layer displacement thickness Reynolds number Re_{δ^*} for a flat plate laminar boundary layer (from Schlichting [114]).

curve. The neutral curve consists of two branches, a lower branch (Branch I) where disturbances of a fixed frequency first become unstable for increasing Reynolds number and an upper branch (Branch II) which marks the position where disturbances become stable again. The Reynolds number below which all disturbances are damped is called the critical Reynolds number Re_{crit}.

The Orr-Sommerfield equation was first solved by Tollmien and Schlichting around the 1930's, but their results were not initially accepted because of the lack of any convincing experimental evidence in support. The necessary confirmation was eventually supplied by the classic experiments of Schubauer and Skramstad [117] which were carried out in the early 1940's, but not published until 1948 due to war time restrictions. The measurement of modulated sinusoidal wave trains with almost no random character in the flat plate laminar boundary layer confirmed that instability waves (Tollmien-Schlichting waves - from now referred to as T-S waves) were indeed a precursor for transitional flow. The success of these experiments was in part due to the development of a wind tunnel which exhibited extremely low levels of turbulence in the working section. Turbulence levels varied from 0.035% to 0.014% of which a large component was due to noise from the fan. Schubauer and Skramstad [117] also used a vibrating ribbon to introduce disturbances of a fixed frequency with a controlled initial amplitude and quantitatively verified the wave length, phase velocity and amplitude as a function of Reynolds number, against the predictions of instability theory. Although exact correspondence with the theory did not exist in every case, all the essential features were in agreement. These measurements consolidated the relevance of linear

a) Time history sketch of vortex truss

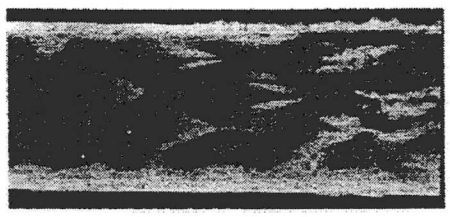

b) Smoke tunnel photograph

Figure 2.2: Fig. 6 reproduced from Knapp and Roache [82]. Regions of vortex trusses under zero pressure gradient.

stability theory for boundary layer flow under low freestream turbulence conditions.

At a certain stage in the development, the originally two-dimensional T-S waves develop a variation in wave amplitude in the spanwise direction under the influence of nonlinear interactions between the primary (T-S waves) and three-dimensional secondary disturbances. This non-linear interaction process is called secondary instability. Evidence of this process was observed in the investigation of boundary layer transition on ogive nose cylinders aligned parallel with the flow reported by Knapp and Roache [82]. The appearance of a three-dimensional disturbance and formation of λ-vortices under both zero and adverse pressure gradients was clearly illustrated by smoke visualisation photographs and their zero pressure gradient result is reproduced here in Fig. 2.2. Two basic types of secondary instability exist. When three-dimensional waves are of the same fundamental frequency as the T-S wave (fundamental resonance), an aligned pattern of maxima in the wave amplitude is observed. λ-vortices are formed at the position of the maxima in the wave amplitude, and this pattern of vortices is known as K-type breakdown after the work of Klebanoff et al. [81]. When the three dimensional waves have a sub-harmonic frequency (sub-harmonic resonance), a staggered pattern of λ-vortices is formed, and this is known as N-type breakdown (in reference to the work performed at Novosibirsk). N-type breakdown can be sub-divided into C-type (from Craick) and H-type (from Herbert) depending on the wavelength in the spanwise direction in relation to the T-S wave length, where C-type is larger and H-type is smaller.

When T-S waves are artificially excited with a vibrating ribbon they appear as two-dimensional periodic wave trains. If external excitation is not present and the instability waves appear as the result of *natural* conditions, then the T-S waves are neither two-dimensional nor are they continuous in space/time; they appear instead as wave packets modulated in the streamwise and spanwise directions. Gaster and Grant [46] investigated the development of an instability which was excited with a small-amplitude short-duration pulse which generated a band of wave frequencies, and the resulting wave packet developed through the selective amplification of the unstable modes according to linear stability theory. These workers observed that near the source

of the disturbance, the wave packet appeared elliptical in shape and later developed into a bow shape: this seemed to be due to the development of oblique waves with sub-harmonic frequencies. The close agreement for the first two thirds of the measured wave packet development with the theoretical model of Gaster [45] confirmed that the wave packet was indeed a superposition of T-S waves. It is important to note that two-dimensional waves never completely represent the breakdown process that follows the growth of linear disturbances, as the transition is *always* three-dimensional in bounded shear flows.

More recent experiments on artificially generated turbulent spots such as those of Tso et al. [132], Breuer and Haritonidis [15], Breuer and Landahl [16] and Cohen et al. [21] show that transitional flows generated by external disturbances can still exhibit regions were linear growth mechanisms are dominate. Perturbations of the boundary layer by a pulsed jet or surface membrane produce a combination of transient and three-dimensional wave packet disturbances. For weak initial disturbance amplitudes the transient component decays and turbulent breakdown occurs well downstream of the initial disturbance location after the wave packet has been sufficiently amplified. The initial wave packet growth is well described by linear stability theory. For strong initial disturbance amplitudes the transient component grows rapidly and turbulent breakdown occurs almost immediately (see Section 2.2.2).

The final stages of the instability process and the start of transition are marked by the initiation of turbulent spots (or "breakdowns") through the appearance of high frequency fluctuations in the regions of high shear near the heads of the vortex loops. Knapp and Roache [82] noted that the waves appeared to breakdown in sets, and that a short calming period of laminar flow after the passage of a turbulent spot was observed similar to Schubauer and Klebanoff [116]. This laminar region was terminated by either the appearance of instability waves or further turbulent spots.

2.2.2 Bypass Transition

Boundary layer transition does not always follow the path described in Section 2.2.1. It is possible that the initial instability can be so strong that the growth of linear disturbances is *by-passed* (Morkovin [99]) in such a way that turbulent spots appear or secondary instabilities occur almost immediately and the flow quickly becomes turbulent. This phenomena is not well understood and a theory for the reliable predicted onset of turbulent spots via this mode does not exist. *Bypass* transition has been documented in cases of strong disturbance environments, e.g. roughness or high levels of freestream turbulence (see for example Abu-Ghannam and Shaw [1], Blair [10] or Gostelow et al. [50]). The influence of freestream turbulence in promoting bypass transition makes it particularly relevant to turbomachinery flows.

2.2.3 Separated Flow Transition

When a laminar boundary layer separates from the surface, as is possible for regions of flow subjected to strong adverse pressure gradients typical on turbomachinery blading, transition may occur in the free-shear layer and re-attach as a transitional or turbulent boundary layer forming a laminar separation bubble. On the suction side of modern controlled diffusion aerofoils transition via a separation bubble is likely to occur either

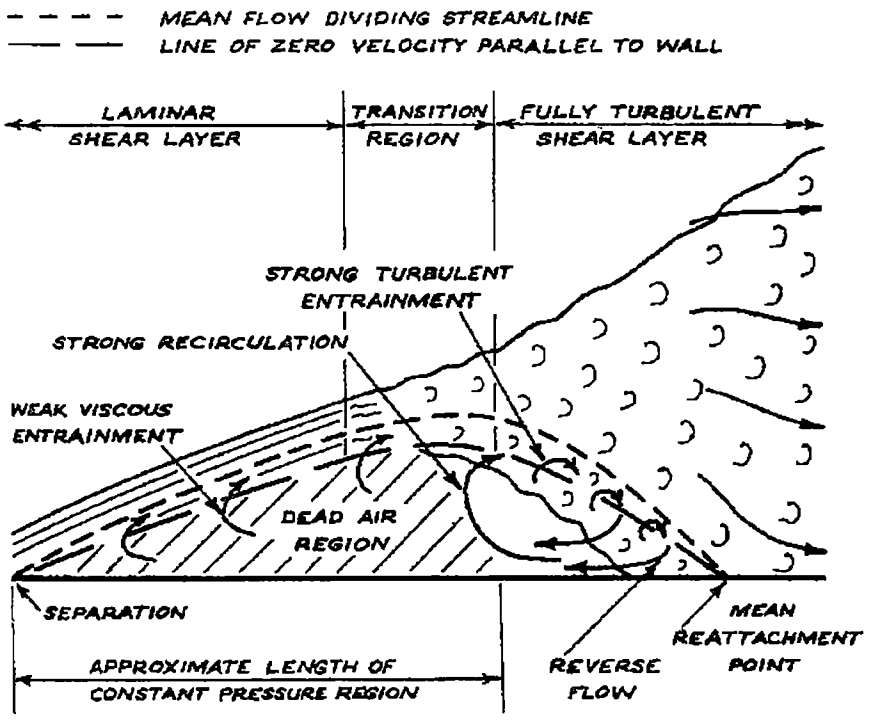

Figure 2.3: Flow mechanisms in a two-dimensional separation bubble (from Walker [138]).

in the region of steep deceleration that follows the overspeed in velocity caused by high curvature around the leading edge (see for example Walreavens and Cumpsty [149] and Tain [129]) or in the region of deceleration that starts post peak suction and continues to the trailing edge (i.e leading edge or mid-chord bubbles). Fig. 2.3 illustrates a typical two-dimensional laminar separation bubble and a discussion, similar to that provided by Walker [138], of the important flow mechanisms follows.

In the forward part of the bubble where the flow is laminar, there is little entrainment of fluid by the separated laminar shear layer and consequently the velocity of the reversed flow near the surface is small. This low velocity gives rise to a region of *dead air* in which the surface pressure remains nearly constant and approximately equal to the value at separation. The model proposed by Horton [68], which was later extended by Roberts [109, 110] to include the effects turbulence level on transition location, assumes an instantaneous transition in the laminar shear layer. Detailed measurements (see for example Malkiel and Mayle [91]) have shown it is more realistic to assume that transition to turbulent flow occurs over a finite distance. When transition commences, the rate of entrainment by the shear layer rapidly increases, and the mean flow streamlines curve back towards the surface. The dividing streamline returns to the surface at the re-attachment point and closes the bubble. Continuity requires a much higher reverse flow velocity under the separated turbulent shear layer because of the faster rate at which fluid is entrained by the turbulent flow. In the rearward part of the bubble the flow is very unsteady due to eddies reaching out from the growing turbulent shear layer: there is a zone which exhibits strong recirculation and limits the downstream

extent of the dead air region. A dramatic increase in surface pressure is required to balance the inertia forces generated by the curvature of the streamline in the reversing flow immediately upstream of the re-attachment point. The pressure continues to rise rapidly for a short distance after re-attachment due to the boundary layer displacement thickness initially tending to decrease.

Mayle [93], in his review of important modes of transition for turbomachines, makes a separate classification for this type of transition. Walker [142], in his discussion of Mayle's work, questioned the use of a single mode to describe transition in a separated laminar shear layer as both natural and bypass type transition processes should be expected in this case. Walker [142] does acknowledge the fact that there are physical phenomena peculiar to separated flow, such as an increased receptivity to freestream turbulence, but suggests a unified approach for transition modelling in attached and separated layers for both natural and bypass mechanisms would be preferable. Numerical codes with both attached flow bypass transition and separated flow transition criteria are able to predict laminar separation bubbles, but in a much less satisfactory manner: inconsistencies between the two different criteria mean that continuous movement of the predicted transition onset through the incipient separation point is impossible; this often leads to numerical instabilities in iterative calculations, such as viscous-inviscid interaction procedures.

2.3 Predicting Transition Onset

The most popular method for predicting the onset of transitional flow in external aerodynamics (low freestream disturbance type) situations is the e^n method of Smith and Van Ingen (see Mack [90, 89]). This method is based on linear stability theory and involves the calculation of amplification ratios of disturbances and therefore accounts for flow history effects. It was noted by comparison with a large body of experimental data that the transition Reynolds number Re_t could be correlated with a fixed value of $n = ln(A/A_0)_{max}$: Smith suggested n =9, while Van Ingen suggested $n = 7$ or 8. The e^n method, while well adapted to design studies in a constant disturbance environment, is not well suited to the effects of different disturbance sources such as freestream turbulence, sound and vibration on transition (Mack [90]). One major problem is that there is little guidance for the choice of the parameter n for disturbance environments which differ significantly from the original correlation environment. Mack [90] attempted to account for the effects of freestream turbulence by relating the parameter n directly to the freestream disturbance level and proposed the relation

$$n = -8.43 - 2.4ln(Tu) \tag{2.3}$$

This correlation has been further modified for turbulence levels significantly higher than originally intended and has been implemented, in parallel with a correlation for bypass transition, in the two-dimensional viscous/inviscid coupled flow solver of Youngren and Drela [152] and is discussed in further detail in Section 8.2. One feature that is ignored in the modified e^n method is influence of distribution of the disturbance energy over the frequency range, or more simply, the initial amplitude is assume to be independent of disturbance frequency.

The prediction of bypass transition is heavily reliant on empirical correlations. The correlations for the onset of transition derived from the experimental work of Dunham [35] or Abu-Ghannam and Shaw [1] are typical of the current methods used to account for transition in the design of turbomachinery blading. In the Abu-Ghannam and Shaw experiments, the effects of freestream turbulence and pressure gradient on transition behaviour of a flat plate boundary layer were measured. The turbulence level was varied between 0.5% and 5% by the installation of various turbulence generating grids upstream of the plate leading edge; the pressure gradient on the plate was imposed via an adjustable plywood tunnel ceiling. The Abu-Ghannam and Shaw correlation for transition onset was developed from their own experimental results combined with the earlier correlation of Hall and Gibbings [57] and is given below,

$$Re_{\theta S} = 163 + exp\left\{F(\lambda_\theta) - \frac{F(\lambda_\theta)}{6.91}\tau\right\} \tag{2.4}$$

where τ is freestream turbulence level in percent and,

$$F(\lambda_\theta) = \begin{cases} 6.91 + 12.75\lambda_\theta + 63.64\lambda_\theta^2 & (\lambda_\theta < 0) \\ 6.91 + 2.48\lambda_\theta - 12.27\lambda_\theta^2 & (\lambda_\theta > 0) \end{cases} \tag{2.5}$$

Although the Abu-Ghannam and Shaw correlation has been used to predict bypass transition on turbomachinery blading with reasonable success, it is not without criticism.

The use of a lower limit of $Re_\theta = 163$, which corresponds to the minimum Reynolds number for which linear stability theory predicts amplification of small disturbances in zero pressure gradient flow, has been questioned. This assumption is not valid in adverse pressure gradients where lower critical Re_θ values are predicted by linear stability theory. Abu-Ghannam and Shaw [1] used the rapid rise in surface velocity from a surface pitot tube or hot-wire to infer the transition onset point. Narasimha [101] points out that this does not necessarily correspond to the location where spots first form, as a small number of spots must be present to change the velocity distribution. Furthermore, Abu-Ghannam and Shaw [1] followed the recommendation of Dunham [35], in an attempt to account for flow history, by correlating the freestream turbulence effect with the average values taken midway between the leading edge and the point under consideration. This value is difficult to define in an arbitrary pressure gradient flow.

Hourmouziadis [69] presents the experimental transition onset data with correlation predictions for the work of McDonald and Fish [98], Dunham [35], Abu-Ghannam and Shaw [1] and Blair [9] and notes generally good agreement. However the scatter attributed to pressure gradient effects is of the same order of magnitude as the scatter of the test results. Hourmouziadis [69] states that there is no specific trend among the results of different investigators, and therefore advocates use of a straight line correlation which ignores pressure gradient effects, of the form,

$$\frac{Re_2^*}{1000} = \left(\frac{Tu\,[\%]}{0.3}\right)^{-0.65} \tag{2.6}$$

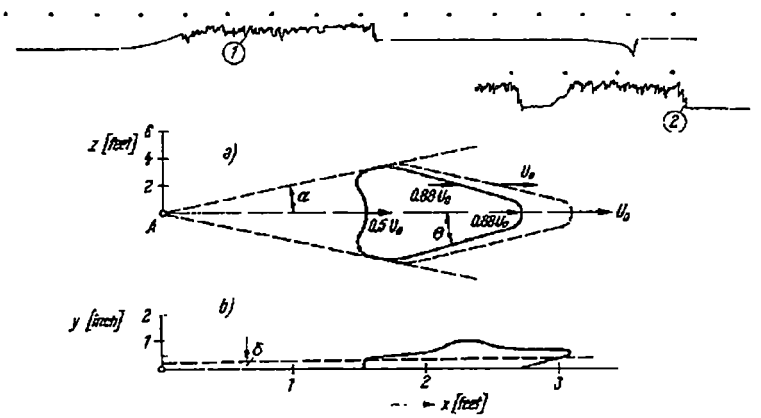

Figure 2.4: Growth of an artificial turbulent spot in a laminar boundary layer on a flat plate at zero incidence as measured by Schubauer and Klebanoff [116] (from Schlichting [114]).

to predict the onset of transition for the design of low pressure turbines. Mayle [93] also suggests that transition onset, for turbulence levels common of gas turbines (> 3%), is practically independent of the pressure gradient and proposes a correlation of the form

$$Re_{\theta t} = 400 Tu^{-\frac{5}{8}} \tag{2.7}$$

A result similar to that of Hourmouziadis [69], i.e. $Re_{\theta t} = 460 Tu^{-0.65}$.

Johnson and Ercan [76, 77] and Mayle and co-workers [97, 96] have proposed models which aim to remove much of the empiricism currently necessary to predict the transition onset under conditions favourable to bypass transition. Johnson and Ercan present a model for the growth of near wall disturbances under the influence of high freestream turbulence and employ the breakdown criteria originally proposed by Johnson [75] to predict the onset of transition. In their model, the rate of growth of the disturbances is correlated with the wall skin friction coefficient. Mayle and co-workers have proposed an alternative model whereby the laminar fluctuations preceding transition are primarily caused by the work of the imposed fluctuating freestream pressure forces on the boundary layer flow. The development of these disturbances is calculated using a laminar kinetic energy equation, and transition onset is predicted when the disturbance fluctuations exceed a certain value of the wall friction velocity. These models fundamentally disagree as to the most important frequencies for promoting the initial disturbances, and further investigation will be required to resolve this. Both models are relatively untested, however, encouraging comparisons with measurements have been presented and the development of models which replicate the relevant physics should be pursued.

2.4 Turbulent Spots and the Calmed Region

Emmons [36] observed the growth of *islands of turbulence* surrounded by laminar flow

in a horizontal water channel boundary layer undergoing transition. These *turbulent spots* were visible in the disturbed surface of the water and appeared at random times and locations. Prior to the work of Emmons [36] it was generally accepted that the transition zone (i.e. the region of flow that begins with the appearance of turbulent spots and ends through an asymptotic approach to fully turbulent flow) was laminar and turbulent flow separated by a jagged fluctuating 'front' (Narasimha [101]). The identification of turbulent spots in a flat plate laminar boundary was experimentally verified by Schubauer and Klebanoff [116]. The spot was initiated repetitively by an electric spark, which made it possible to delineate the spot boundaries. Under a zero pressure gradient the spot was found to exhibit a wedge shaped footprint, with the nose of the spot slightly overhanging (see Fig. 2.4). The leading edge travelled downstream at 0.88 of the freestream velocity, whilst the trailing edge travelled at 0.5. Schubauer and Klebanoff [116] also noted a region of calmed flow following the passage of a turbulent spot.

Since the work of Schubauer and Klebanoff [116], the propagation of turbulent spots in laminar boundary layers has been extensively studied and a review is provided by Riley and Gad-el-Hak [108]. Most of the studies have been performed in the absence of a pressure gradient and therefore its influence on the rate at which laminar flow is contaminated by turbulent fluid is not well understood. Drastically different turbulent spot spreading behaviour under the influence of an adverse pressure gradient has been observed by Gostelow et al. [51], Seifert and Wygnanski [120] and van Hest [135]. Gostelow et al. [51] reported spots which spread at an included angle $60°$, almost three times that of zero pressure gradient results. The spots no longer exhibited the characteristic arrow-head shape and were found to interact significantly with the surrounding flow. It has been speculated that the mechanism which enhances this spreading is related to the destabilising role of the adverse pressure gradient in the neighbourhood of the spot. Both Gostelow et al. [51] and Seifert and Wygnanski [120] observed an increase in the strength and duration of the calmed region, and the latter speculates that the calmed region scales with the span of the spot rather than its length. Gostelow et al. [53] showed that there was strong similarity between the turbulent spots (and the calmed region) artificially generated in a flat plate boundary layer and the wake-induced turbulent strips observed on the compressor blade used in the current investigation. Detailed measurements on the flat plate showed that the calmed region exhibited a significantly more stable velocity profile and was thinner than the surrounding natural boundary layer.

2.5 Predicting Transition Length

The main variable describing the transition zone is *intermittency* (γ), which can be defined as the fraction of time that the flow is turbulent at any point. Emmons [36] developed a statistically based theory to calculate the streamwise distribution of intermittency at any point $P(x, y, t)$ in the flow, i.e.

$$\gamma(P) = 1 - exp\left[-\int_{R(P)} g(x', y', t')dV\right] \tag{2.8}$$

where $R(P)$ is the dependence cone for point P and g is the function describing the probability that a turbulent spot will be formed at (x', y', t'). Emmons [36] assumed the function g to be equal everywhere in the boundary layer and therefore constant.

Narasimha [101] notes that the intermittency measurements of Schubauer and Klebanoff [116] did not agree with Emmons' theory, and their intermittency data was fitted to an error function which had no obvious connection to Eqn. (2.8). This paradox was resolved by Narasimha's [100] hypothesis of concentrated breakdown, whereby the formation of turbulent spots occurs at a preferred streamwise location randomly in time and in a cross-stream position. Narasimha [100] combined Emmons' intermittency expression with the concentrated breakdown hypothesis, and assuming that the vertices of the propagation cone follow straight line trajectories, arrived at a universal expression for the distribution of intermittency,

$$\gamma = \begin{cases} 1 - exp\left[-(x - x_t)^2 n\sigma/U\right] & (x \geq x_t) \\ 0 & (x \leq x_t) \end{cases} \tag{2.9}$$

When $n\sigma$, U and x_t are specified, Eqn. (2.9) describes a characteristic shape for the intermittency distribution, and hence the length of transitional flow. Eqn. (2.9) generally provides a good description of constant pressure gradient flows. Narasimha [101] notes that deviations from the universal intermittency distribution are observed for flows with changing pressure gradients and used the term *sub-transitions* to describe this behaviour.

The early length correlation of Dhawan and Narasimha [29] sought to find a relationship between the length of transitional flow and the conditions at transition onset. Examination of the data available at the time showed considerable scatter due to differences in definition of the start/end of transition and the Mach numbers and disturbance levels under which the experiments were performed. The correlation of Dhawan and Narasimha [29] essentially represents transition behaviour in constant pressure flow.

Chen and Thyson [20] extended the transitional flow model of Narasimha [100] and developed a model which purported to account for the influence of pressure gradient on the intermittency distribution and transition length. This was achieved by allowing the spot propagation velocities to vary in proportion to the external velocity. Walker et al. [148] reported a complete breakdown in low Reynolds number airfoil computations due to the Chen-Thyson model predicting excessive lengths for flows with laminar separation. This was supported by the theoretical model of Walker [141] which suggested for flows subjected to strong adverse pressure gradients that the transition zone length should be almost an order of magnitude shorter than that predicted by Chen and Thyson [20]. It was pointed out by Walker and Gostelow [143] that the Chen-Thyson model predicted a transition length little different from that in zero pressure gradient flow. The shortcomings of the Narashima and Chen-Thyson models in arbitrary pressure gradient flows was addressed by the work of Solomon et al. [126]. The transitional flow length computations presented by Solomon et al. [126], used the experimental results of Gostelow et al. [52] to account for the large influence of local pressure gradient on the turbulent spot spreading rates. This model successfully provided an explanation for the deviation from the universal intermittency distribution or sub-transitions caused by a rapidly changing pressure gradient.

2.6 Unsteadiness in Turbomachinery

For the design of a multistage axial turbomachine the methods which attempt to model the complex flow field are a necessary simplification. One common assumption is that the blade rows are considered to be located far enough apart that the flow field can be approximated as steady in both the rotating and stationary reference frames. In a real turbomachine this is obviously not the case: the flow field environment of an embedded stage is inherently unsteady. The major source of disturbances is provided by the relative motion of the blade wakes from the row immediately upstream. Hodson [64] divides the disturbance field into *potential* and *wake* interactions.

The potential flow field of a blade row extends both upstream and downstream and decays exponentially with a length scale (dependent on the Mach number) which is typically of the order of the blade chord. When a downstream row moves through the potential field of the row immediately upstream it experiences changes in apparent flow angle and velocity. The viscous wakes from the upstream row also cause an unsteady perturbation of the flow experienced by the downstream row at a correspondingly smaller disturbance scale. This wake disturbance comprises variations in turbulence length scale and intensity combined with changes in mean velocity associated with the wake deficit. As the wake deficit passes the leading edge of the downstream row it causes local fluctuations in incidence. Evans [38] measured the variation in stator incidence in a single stage compressor and found a minimum fluctuation of 12°, with variations as high as 15° depending on flow coefficient. Although wakes are a viscous flow phenomena, it is possible to interpret the interactions associated with a passing wake by using potential flow theory to consider only the influence of the velocity deficit inside the wake. This idea is similar to the early models proposed for secondary flow theory (see Squire and Winter [128]) and is also commonly used for numerical simplification of unsteady flow (see Giles and Haimes [47]). This will be referred to as potential interaction associated with rotor wake chopping. Vortex shedding phenomena can also contribute to the unsteady disturbance field. Giles [48] suggests that the interaction associated with the passing pressure field at the trailing edge of an upstream blade row may cause additional unsteadiness which affects the vortex shedding mechanisms. This would introduce a periodic disturbance, not necessarily phase-locked to the rotor passing frequency, that exhibits a disturbance scale larger than that associated with the random turbulent fluctuations inside the wake.

If the velocity deficit that exists inside the wake region is observed from a system that moves with the freestream, it appears as a *negative-jet* of fluid. The relative direction of the wake flow as it passes over the suction and pressure surfaces differs for turbine and compressor blades. For a compressor blade the effect of the negative-jet is to entrain fluid from the suction surface boundary layer, whereas on the pressure surface the jet effect directly impresses turbulent fluid onto the boundary layer. The opposite holds for the case of a turbine blade. Kerrebrock and Mikolajczak [79] used the negative-jet concept to explain the pitchwise variation in total temperature observed downstream of a stator row in a high Mach number compressor stage. The transport of fluid inside the rotor wake was intercepted by the pressure surface as it convected through the stator passage, causing a local accumulation of high entropy fluid. Hodson [64] observed a similar phenomenon in a turbine rotor passage where the relative loss was higher on the suction side of the blade due to a similar effect. Numerical analyses of

the wake interaction in a two-dimensional turbine rotor by Hodson [64], Giles [48] and Hodson and Dawes [66] confirm the transport of wake fluid by the negative-jet effect, and their illustrations of the perturbation velocity vectors (obtained by differencing the unsteady and steady flow solutions) clearly depict a pair of convected vortices with the wake flow. This arises from the fact that continuity requires that the flow caused by the negative-jet effect is replaced from elsewhere, and thus sets up a system of vortices on either side of the wake. The role of the negative-jet in the unsteady transition process is not well understood. Mayle [93] concluded that this effect was insignificant, whereas Walker [142] takes a contrary view.

2.7 Some Experimental Observations

There are many reasons why the adverse nature of the conditions inside an actual turbomachine effectively prohibit detailed time-resolved measurements. Observations of the behaviour of an embedded stage can lead to increased understanding, and consequentially improved modelling, of the complex nature of unsteady flow. Therefore several levels of simplification are employed by researchers in order to obtain high quality data at representative conditions. The simplest experimental approach is to use a mechanism to generate wakes which can pass over a wind tunnel flat plate. This allows models of larger physical dimensions to be used and increases the flexibility of testing when compared to a real machine. The Reynolds number of the flow and the wake passing period can be changed independently. The levels of wake turbulence (and defect) can also be altered without changing the pressure distribution. Early flat plate work ignored the effects of pressure gradient, although more recent attempts use tunnel wall contouring to impose a realistic pressure gradient. At this level of simplification there exist problems with generating wakes which represent a lifting airfoil, and the flat plates are usually designed to avoid flow interactions in the neighbourhood of the leading edge. The effects of real blade pressure gradient and curvature can be introduced if the flat plate is replaced by a cascade of blades. Bars are still used to generate wakes representing the presence of an upstream blade row. This type of apparatus can not account for the interactions associated with the passing potential fields of neighbouring blade rows common in modern closely spaced machines, and the flow is only represented on a two dimensional basis. Measurements in large-scale low-speed turbomachines ensure a realistic disturbance environment. This introduces the difficulties of three dimensionality, operating range and increased expense. Even with low-speed machines, and therefore larger blade dimensions, detailed measurements are difficult. Mach number similarity is not preserved for any of the above-mentioned cases and therefore the effect of compressibility/sonic behaviour, which is prevalent in the early stages of most components in an actual turbomachine, is ignored. The following section reviews some of the important findings obtained with the type of apparatus discussed above.

The transition behaviour of a flat plate boundary layer under the influence of sinusoidal freestream oscillations was examined by Obremski and Fejer [102]. The onset of transitional flow was found to depend on the value of the non-steady Reynolds number

$$Re_{NS} = \frac{U}{\nu}.\frac{\Delta U}{\omega} \tag{2.10}$$

where the characteristic length ($L = U/\omega$) is the distance travelled by a fluid particle in the freestream during one sinusoidal oscillation and the characteristic velocity (ΔU) is the amplitude of the oscillation. For Re_{NS} greater than 27000, turbulent spots were periodically produced at the frequency of the outer flow. The transition onset Reynolds number depended primarily on the amplitude of the external flow and not the frequency. For Re_{NS} less than the critical value ($Re_{NS} \approx 25000$) the transition onset occurred at a relatively constant Reynolds number, which was independent of the external amplitude or frequency. Obremski and Fejer identified *creative* and *convective* modes for the initiation of turbulent spots. In the creative mode a rapid spreading of the spot boundaries in both the upstream and downstream directions was observed, possibly related to the breakdown process sequentially moving along an instability wave train associated with the initial spot development. For the convective mode the instability waves were not present and the spot behaviour agreed well with the observations of turbulent spots in zero pressure gradient steady flow as measured by Schubauer and Klebanoff [116].

Walker [138] provided the first evidence of the periodic nature of the wake-induced transition process on the compressor stator blade used in the current research machine. Contrary to the accepted view at the time, Walker's work showed an extensive region of laminar boundary layer flow existed prior to the onset of turbulence despite the high disturbance levels created by the upstream stage. Walker was encouraged by the similarity of the observed transition onset fluctuations with the experimental work of Obremski and Fejer [102], and proposed a tentative model for the stator blade boundary layer behaviour under the influence of rotor wake passing. The model assumed that the disturbances that promoted transition travelled at 35% of the average freestream velocity and the effect of the wake unsteadiness was to periodically alter the streamwise position of the neutral stability point and subsequent amplification rates. Instabilities therefore experienced regions of increased or reduced amplification depending on their location in space~time orientation relative to the passage of the rotor wake. Walker's model did not account for the effect of elevated turbulence levels associated with the passing wake on the transition onset point.

The understanding of the influence of wake turbulence on unsteady transition was enhanced by the work of Pfeil et al. [106]. Their work investigated boundary layer transition process on a flat plate under the influence of periodic wake passing. The unsteady flow was produced by means of a rotating cylinder cascade mounted upstream of the plate and transverse to the flow direction. Each cylinder generated two types of wake per revolution, one near and one far from the plate leading edge. The negative-jet direction of the two wakes differed in sign. There was also a decrease in turbulent intensity from the wake generated in the far position. Pfeil et al. proposed a transition model where the high levels of turbulence associated with the passing wakes caused transition at a forced position some distance upstream of the natural transition point. The turbulent spots produced at this forced location spread and formed an intermittent laminar-turbulent boundary layer. The turbulent spots were followed in time by a region of becalmed boundary layer flow. The calmed region was attributed to the

fact that the propagation speed of the T-S waves was inhibited by the faster moving turbulent patch, and therefore natural transition could not occur behind a turbulent patch creating a calmed zone. Pfeil et al. were not able to ascertain the relative importance of increased turbulence and periodic fluctuations inside the wake on the transition onset location.

Doorly and Oldfield [32] used Schlieren photographs and thin-film heat transfer gauges to measure the fluctuations in the aerodynamic and heat transfer performance of a linear turbine cascade under Reynolds and Mach number conditions representative of a modern gas turbine engine. The unsteady flow at the inlet to the cascade was produced by wake generating bars mounted on the rim of a rotatable disk. The rotational speed of the rods was controlled to achieve the correct velocity vector diagram and also allowed operation at subsonic and near sonic speeds. At the near sonic condition the combined effect of wake and shock wave passing were evaluated. The measurements revealed that both the shock wave and passing wake generated separate turbulent patches. The leading edge of the turbulent patch remained beneath the path of the wake and there appeared to be no significant lag between the wake arrival and the development of a self sustaining turbulent spot.

Addison and Hodson [4] analysed time resolved hot-wire and hot-film data from a low-speed single-stage axial flow turbine. Their observations showed that the incident wake turbulence did not result in immediate transition of the blade boundary layer. Instead, there existed perturbed laminar boundary layer flow (inferred from the similarity of the measured and calculated boundary layer integral properties) under the wake path and the onset of transition did not commence until the boundary layer momentum thickness Reynolds number had reached some critical value. Addison and Hodson [5] proposed a model to account for the effects of wake passing on the blade boundary layers. It was identified through the use of the reduced frequency parameter that diffusion across the boundary layer was far more rapid than the periodic time of the unsteady flow and this suggested the interactions could be treated as quasi-steady. They found that the periodic unsteadiness due to the wake velocity defect was of secondary importance in triggering wake-induced transition compared with the elevated freestream turbulence in the passing wakes. Their model did require assumptions for the decay of turbulent intensity, both in the freestream and inside the boundary layer, and the distortion of the wake through the rotor passage to obtain reasonable agreement with the measurements of transition onset. A similar quasi-steady model for the prediction of transition onset for compressor blades was reported by Solomon et al. [127]. This model also achieved reasonable agreement without accounting for the effects as proposed by Addison and Hodson [5]. This is probably due to the differing natures of the blade potential flow fields and wake-jet directions for compressors and turbines.

In a similar apparatus, Dong and Cumpsty [30, 31] measured the unsteady boundary layer on a supercritical type compressor blade with and without incident wakes. It was later reported by Cumpsty et al. [24], that the appearance of a mid-chord separation bubble (under conditions of no wakes and low background freestream turbulence) was not a design intent, although not entirely unexpected. Under the influence of passing wakes, strong wake-induced turbulent spots were observed on the suction surface with relaxing flow following the spot for a considerable portion of the blade passing period. In the region between wake-induced turbulent patches, the breakdown was associated with T-S waves and the reappearance of the mid-chord separation bubble. The spots

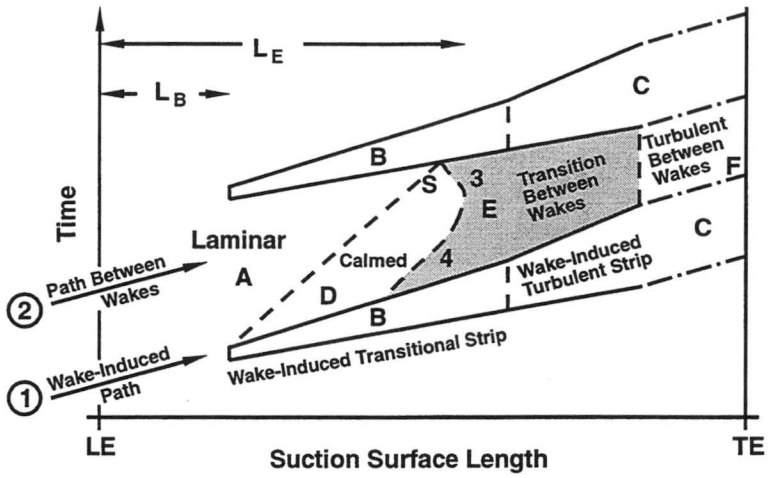

Figure 2.5: Boundary layer development for the baseline compressor operating test point 2B from Halstead et al. [58].

on the pressure surface were found to be similar to those on the suction surface, and this was used to argue the irrelevance of the wake-jet effect for this particular case. For cases with high levels of background freestream turbulence, Dong and Cumpsty observed little difference in the time-mean trailing edge momentum thickness for cases with and without wake passing. This parallels the measurements of heat transfer from a turbine blade under the influence of wake passing in the presence of high levels of background freestream turbulence reported by Doorly and Oldfield [32].

Orth [105] conducted further observations of wake-induced transition in the same facility used by Pfeil. The phase-lock averaged results revealed some important details of the flow behaviour not previously reported. Orth quotes a non-steady Reynolds number of 600 for his observations, a value significantly lower than the critical value identified by Obremski and Fejer [102]. Similar to Addison and Hodson [4, 5] it was observed that the disturbance caused by the wake was introduced into a thin boundary layer at an early position, but this did not lead to an immediate transition. Instead, the disturbances convected along inside the boundary layer until they had developed sufficiently. The onset location was heavily dependent on the intensity. Orth did not support the idea of Pfeil et al. [106] or Addison and Hodson [4] that there existed a connection between the outer wake and the turbulent patch within the boundary layer. After initially disturbing the boundary layer the wake apparently had no further effect on the transition process. Orth showed that the developing spot lagged behind the wake which promoted it. It appeared that the spot generated by the far wake lagged further behind than the near wake spot. Similar observations were made of the work reported by Funazaki [42, 43]. Orth's observations for wake-induced transition agreed with the steady flow work of Abu-Ghannam and Shaw [1] that with increasing turbulence intensity the onset of transition shifts to lower Reynolds numbers and the effect of pressure gradient becomes less significant.

The work of Halstead et al. [58, 59, 60, 61] is one of the most comprehensive experimental and computational investigations of wake-induced blade boundary layer transition in a turbomachine. This work includes measurements in both a 4-stage com-

pressor and 2-stage turbine. Halstead et al.'s measurements clearly show large extents of laminar and transitional boundary layer for both machines despite the adverse disturbance environment created by the upstream stages. The boundary layers were shown to develop along two separate paths (wake-induced and inter wake-induced) which are closely coupled by the calmed region that follows the wake-induced region. The wake-induced strips were found to be transitional, and the variation in the strength of the calmed region that follows was attributed to the level of wake-induced intermittency. The high levels of shear stress in the calmed region were effective in suppressing flow separation and delaying transition onset in the region between wakes. Decreasing the Reynolds number reduced the strength of the wake-induced strips, and for the compressor case laminar separation eventually spread across the entire wake passing cycle. A summary of the compressor boundary layer development at the baseline operating point is reproduced in Fig. 2.5. The effects of blade loading, wake passing frequency and turbine nozzle clocking were also assessed by Halstead et al. [58, 59, 60, 61].

Halstead's experimental observations of wake-induced transition in a multistage compressor were paralleled by a similar study in a 1.5 stage compressor reported by Solomon and Walker [124, 125]. Observations of wake-induced transition with a significantly different blade surface pressure distribution and lower Reynolds number range were in general agreement with Halstead's work. The presentation of time-resolved boundary layer intermittency removed much of the ambiguity associated with interpreting boundary behaviour from other statistical quantities as reported by Halstead. Detailed pressure surface measurements revealed significant differences in the wake-induced phenomena. On both surfaces the amplitude of periodic effects associated with wake-induced transition was shown to vary with incidence. This prompted Solomon and Walker [125] to suggest there is potential for optimising the design of turbomachine blade profiles through the choice of surface pressure distributions which maximise the beneficial aspects of periodic transition phenomena. Comparison of these two studies indicate a full upstream stage combined with sufficiently high Reynolds numbers provide all the essential features necessary to give a reasonable indication of the flow behaviour on blading in the multi-stage environment typical of modern gas turbine engines.

The investigations of Schulte and Hodson [119] for a Low-Pressure Turbine cascade showed that the wake-induced transitional strip and its associated calmed region can be used to suppress the separation that occurs in the absence of wake passing. Schulte and Hodson found that at an optimum wake passing frequency the additional loss incurred by the wake-induced strip was less than the reduction of loss obtained through the suppression of the separated flow area. It was concluded that the loss of an attached boundary layer cannot be significantly reduced due to unsteady wake passing, as the benefit of the low loss calmed region is negated by the increased turbulent flow which proceeds it in time. Schulte and Hodson [118] have developed an unsteady model which accounts for the effect of the calmed region on the transition process using a probability based intermittency approach similar to Emmons [36]. The results of this model closely match experimental measurements of unsteady boundary layer parameters through the transition zone, and indicate that the behaviour of the calmed region is well predicted by the laminar unsteady boundary layer equations. This model gives important insights into the wake-induced transition process and the nature of the becalmed flow following a turbulent spot. Their work has facilitated the design of turbine blade profiles (as

reported by Curtis et al. [25]) with significant increases in loading which do not exhibit the associated increases in loss predicted by steady flow calculations.

2.8 Summary

The previous sections have outlined the physical phenomena important in determining the boundary layer transition process in a multistage environment typical of an axial turbomachine. Numerical models, with particular attention to those currently employed for design purposes, have been discussed and their strengths and weaknesses highlighted. To accurately account these influences, an unsteady model of the transitional flow region needs to be able to determine the time varying location of transition onset (in either attached or separated flow), combined with the subsequent intermittency distribution (or transitional length) and the extent of the calmed region and its effectiveness in delaying separation and/or transition development during the wake passing cycle. Successful prediction methods not only need to consider these important influences, but need to remain relatively simple and robust in order to be considered for routine design calculations.

The unsteady disturbance environment in a multistage machine is predominately responsible for the periodic transition process on the blade surfaces. It is important to understand how the properties of the surrounding flow field influence this process, and how this varies during a wake passing cycle. Variations in turbulence intensity and length scale, combined with passing blade potential fields and wake chopping phenomena are all influencing factors. Recent numerical predictions have demonstrated that the calmed flow following a wake-induced turbulent strip can be predicted by a conventional unsteady boundary layer calculation if a suitable time varying intermittency distribution is prescribed. The onset of transitional flow, particularly under the influence of wake passing, remains difficult to predict a priori and is still largely determined from empirical correlations based on flat plate experiments. The physical mechanisms leading to breakdown into turbulent spots is not well understood and remains an active area of research.

Chapter 3

Experimental facilities

3.1 Introduction

In the late 1940's a joint project on compressor aerodynamics was commenced by the University of Tasmania and the Australian Aeronautical Research Laboratories (ARL). The long term aim was to produce more efficient blade profile shapes for axial compressors. Inviscid potential flow theory was to be used to calculate blade shapes which utilised prescribed velocity distributions to achieve this goal. Three sections designed by the method of Lighthill [87] were tested in a two-dimensional low-speed cascade tunnel and compared with a standard blade of circular arc camber line distribution: the British C4 section. It was planned that the most satisfactory would then undergo further testing and comparison with the standard blade in a high-speed cascade and finally in the vortex wind tunnel. Initial testing revealed regions of laminar separation on the suction surface of all blades. Blight and Howard [11] compared the four sections, and showed an inferior performance of the "Lighthill" sections which they attributed to the steep pressure gradients on the suction surface at the rear of the blade causing boundary layer separation. The most promising of the "Lighthill" sections was then tested in a high-speed cascade tunnel and compared with the C4 blade under high Mach number conditions. The final stage of the project was the design and manufacture of the single stage compressor or "Vortex Wind Tunnel": this was performed at the ARL in Melbourne. By 1954 the compressor had been shipped to Tasmania and set up in a temporary building at the University and initial testing commenced. At that time only cast aluminium blades were available for testing. In 1959 the compressor was moved to its current location in the Aerodynamics Laboratory, and an extensive programme of testing on the newly available machined C4 blades commenced.

This chapter describes the general details of the research compressor. Blade profile data, instrumentation and data acquisition techniques are discussed. Detailed information on the original research facility and the testing alluded to above is well documented by Oliver [104] and Walker [138]. More recent modifications associated with updating the facility to digital control are presented by Solomon [123].

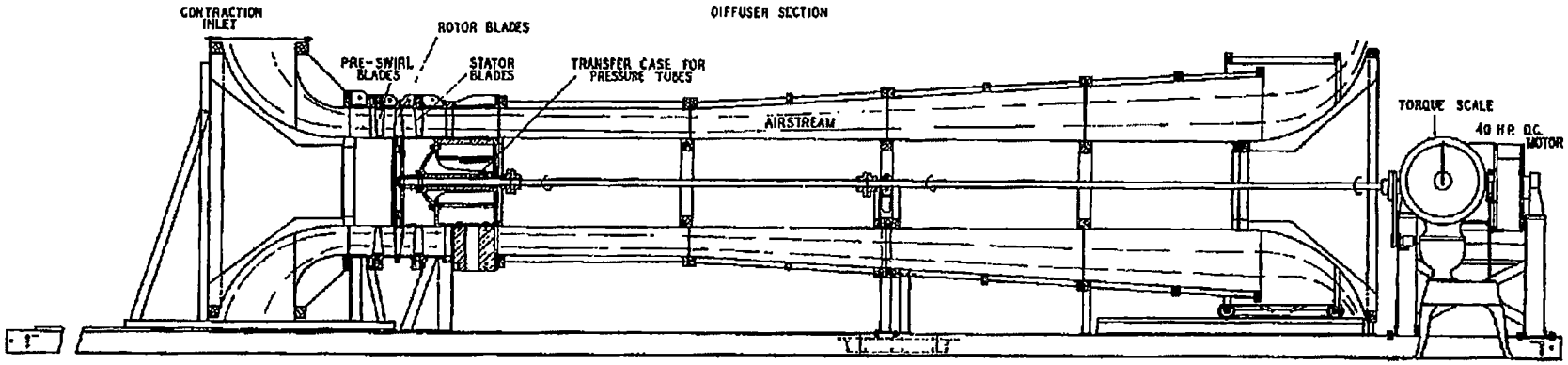

Figure 3.1: Longitudinal cross-section of research compressor.

3.2 Tunnel Description

The compressor is a 1.5 stage axial flow machine, comprising Inlet Guide Vane (IGV), rotor and stator rows. The machine working section has been fabricated from cast and machined aluminium sections: the inlet and diffuser are primarily made from framed plywood sections. Fig. 3.1 shows the general machine layout. Surrounding air from the laboratory enters the compressor radially through a cylindrical screened inlet 2134 mm in diameter by 610 mm wide and is turned through 90° by the inlet contraction to the axial direction. The inlet is covered with wire gauze to promote inlet uniformity and as a means of filtering incoming air to protect sensitive instrumentation. The working section annulus has hub and casing diameters of 685.8 mm and 1143 mm respectively: the contraction ratio based on area is 6.25:1. The parallel walled working section, which contains the compressor blade rows, has a nominal length of 1135 mm or approximately one diameter. The working section is followed by a further parallel walled section of approximately 1.25 diameters in length, which contains three large struts supporting the main rotor bearings. Fig. 3.2 shows the compressor with inlet and rotor and stator blade rows removed, revealing the rotor bearing and strut assembly. Oliver [104] reported that the three struts are at an appreciable angle to the outlet flow (approximately 22° at mid-blade height), but this did not appear to influence any of the readings except those of the tunnel wall static pressure downstream of the struts. The following diffuser section is approximately four diameters (4572 mm) in length. The diffuser has a conical outer wall with included whole angle of 7° and a cylindrical centre through which the rotor drive shaft passes. At exit a sliding throttle arrangement controls the flow rate through the machine and turns the air back to the radial direction. The air then re-circulates through the laboratory back to the machine inlet.

Fig. 3.3 shows the rotor disc and blade assembly removed from the compressor. When assembled the rotor disc is connected via a long drive shaft to a 30kW D.C. motor located at the rear of the tunnel. A Natronics Stardrive thyristor controller varies speed between 150 rpm and 750 rpm, with a safety cut-off limit above 800 rpm. The speed is measured with a Baldwin Precision shaft encoder which emits 6000 pulses per revolution. External hardware converts the encoder signal and supplies the thyristor controller with an analogue feedback voltage signal. Solomon [123] states that the speed is controlled to an accuracy better than ± 0.1 rpm at 500 rpm.

A combination of seven cast and machined Aluminium shell pieces bolted together form the outer casing of the working section. Accurate alignment of the shell pieces is achieved with a series of flanged joints. With adjacent pieces unbolted the entire inlet section can be moved along rails to provide access to the blade rows at various axial stations. Three of the shell pieces also contain 100 mm square perspex windows, which permit a limited amount of visual inspection while the machine is running.

Instrument slots in the outer casing of the compressor allow radial and axial traversing of measuring probes at a fixed circumferential position. The IGV and stator rows are each mounted on rotatable supporting rings to permit circumferential traversing of these blades relative to a stationary probe or clocking of one stationary row relative to the other. The circumferential position of the stationary rows is adjusted with a threaded screw acting against a bracket attached to the external casing. The handle and bracket of the IGV traversing system are visible in the top left of Fig. 3.2. Stepper motors connected to both IGV and stator systems provide the facility for automated

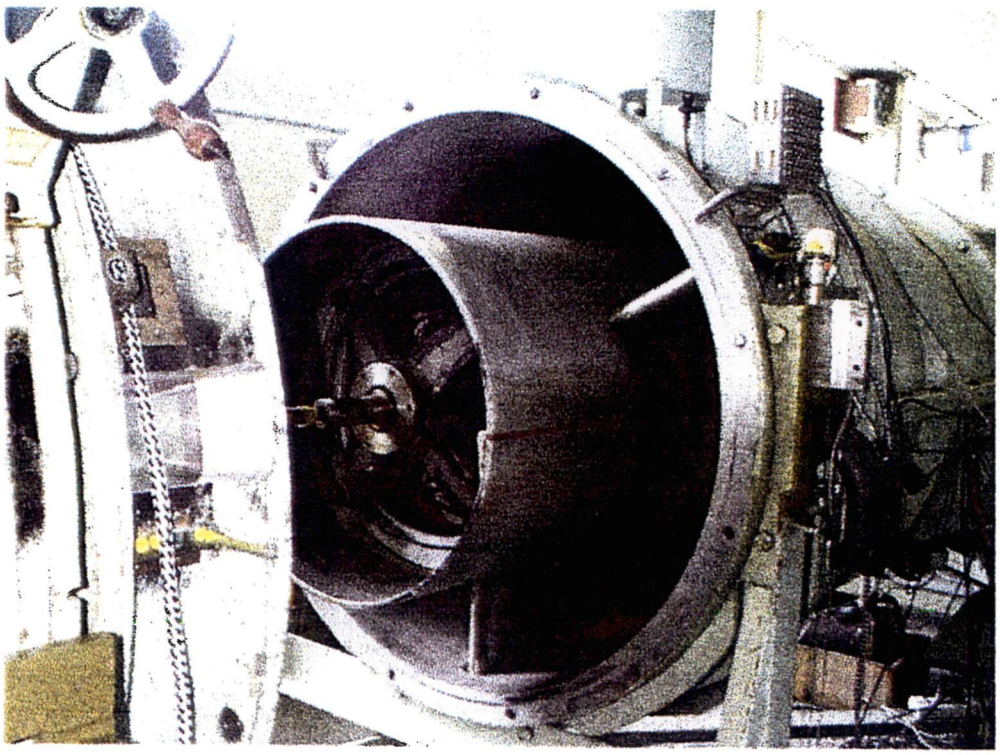

Figure 3.2: Compressor with inlet section removed: rotor and stator blade rows also removed, revealing the rotor bearing and support struts.

circumferential traversing. A linear potentiometer on each traversing unit allows positioning of the blades to within ±0.2 mm at mid-blade height. The blade rows also have external mounted vernier scales which can be read to 0.0254 mm (0.001″) when referenced to mid-span. A combination of the vernier scales and linear potentiometer allowed the blade rows to be positioned with an accuracy of ± 0.08mm or ± 0.1% of mid-span stator pitch for circumferential flow traverse measurements.

3.3 Compressor Details

The compressor has 38 blades in both the stationary rows (IGV and stator) and 37 blades in the rotor row, with space/chord ratios of 0.99 and 1.02 respectively at mid-blade height. The blades have a constant chord of 76.2 mm at all radii and are machined from aluminium to a tolerance of 0.08 mm (Oliver [104]). For a sample of eight blades in each row, measured mid-span chords of 76.18±0.04 mm, 76.12±0.12 mm and 76.20±0.04 mm were recorded for the IGV, rotor and stator rows respectively. The hub and casing diameters through the working section are constant giving all blades a hub/tip ratio of 0.6 and an aspect ratio of 3.0. The blades sections were designed for free vortex flow with 50% reaction at mid-blade height at a flow coefficient of $\phi = 0.76$. However, for the work of Solomon [123] the rotor was re-staggered by 2.0° and has not been adjusted for the current investigation. The re-stagger has effectively increased the rotor incidence by 2.0° and the rotor would be expected to stall at a higher flow

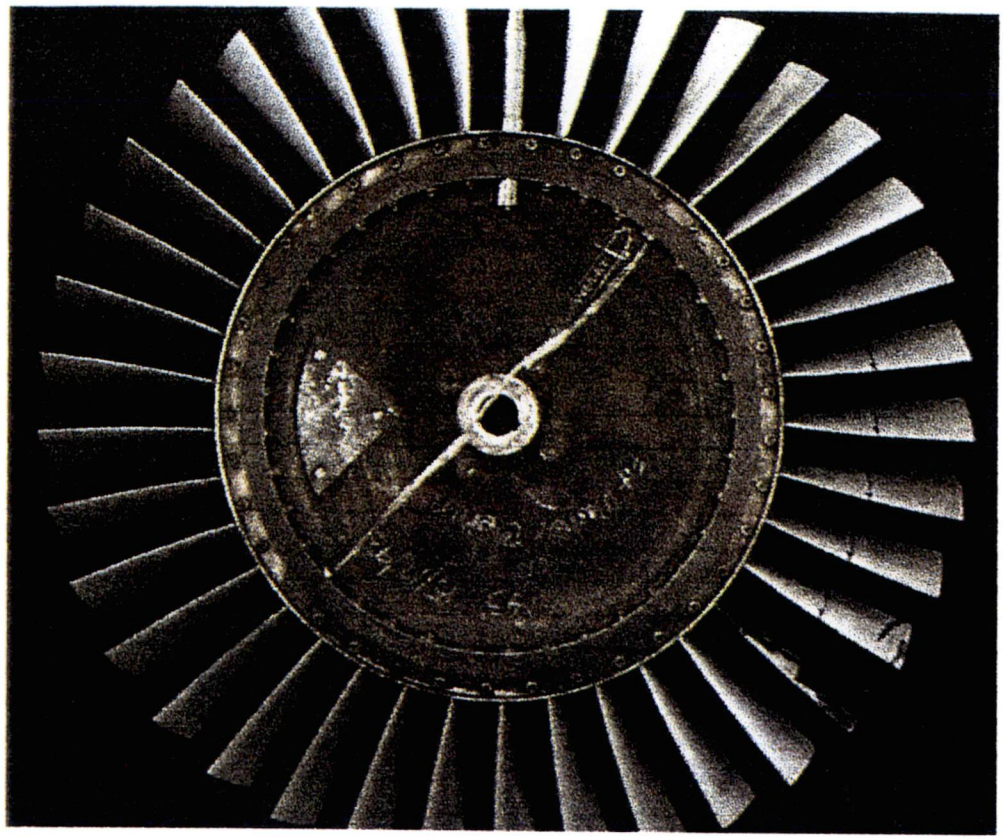

Figure 3.3: Rotor disc and blade assembly: photograph obtained when the rotor was removed from the machine during the rebuild necessary to alter rotor-stator axial spacing. Blade at top dead centre replaced by pin for support during disc removal process.

coefficient than observed by previous workers. The blade angles are presented in Table 3.1.

The blades are all British C4 section with maximum thickness/chord ratio of 10% wrapped around circular arc camber lines and stacked along a radial line through the middle of the camber lines. The polynomials defining the C4 thickness profile were obtained from Howell [71],

$$\pm y = \begin{cases} 1.5492\sqrt{x} - 0.06563x - 0.002528x^2 + 0.00002811x^3 & : x \leq 30 \\ 3.866 + 0.07871x - 0.001467x^2 + 0.000003448x^3 & : x > 30 \end{cases} \tag{3.1}$$

where x and y are in % chord. The maximum thickness is at $x = 30\%$ chord with radius of curvature at the leading edge of 1.2% chord. A circle of radius of 0.5753% chord which is tangent to the polynomials is fixed at the trailing edge and intersects the upper polynomial at 99.488% chord.

In the current machine the axial distance between blade rows may be varied by removing sections of the outer casing of the compressor and replacing them with sections of different length. This alters the position of the stationary blade rows relative to the rotor, whilst maintaining the overall length of the outer casing. In the present investigation, data were obtained for two rotor-stator blade row spacing configurations.

Table 3.1: Blade Angles.

		Hub	Mid	Casing
I.G.V.	θ	34.4°	27.8°	24.3°
	β_1	0.0°	0.0°	0.0°
	β_2	34.4°	27.8°	24.3°
	ξ	17.2°	13.9°	12.6°
Rotor*	θ	52.5°	31.1°	19.1°
	β_1	28.5°	43.0°	49.7°
	β_2	-24.0°	11.9°	30.6°
	ξ	2.2°	27.5°	40.2°
Stator	θ	32.9°	31.1°	29.4°
	β_1	53.7°	45.0°	39.8°
	β_2	20.8°	13.9°	10.4°
	ξ	37.2°	29.5°	25.1°

* Re-staggered rotor angles as per Solomon [123].

Unfortunately both time constraints and the expense associated with manufacturing casing segments prohibited testing of additional rotor-stator spacing configurations. The use of two test configurations is not in support of a predicted linear variation. The upper portion of Fig. 3.4 shows the first configuration with axial spacings, at mid-blade height, of 119% chord and 106% chord between IGV-rotor and rotor-stator blade rows, respectively. The lower portion of Fig. 3.4 shows the change in the outer casing configuration necessary to reduce the rotor-stator axial spacing to 41.6% chord, while essentially retaining the same IGV-rotor spacing. The rebuild of the compressor involves the insertion of a jacking rig to aid the removal of the rotor disc from the main drive shaft, and removal of the stator blade row from the machine to allow different shell pieces to be inserted behind it. The reduced rotor-stator axial spacing in the second configuration is the minimum obtainable with the existing casing sections. Although the reduced axial spacing configuration is approximately 10% chord larger than quoted for embedded stage modelling (see Section 4.3), the reduction from the large axial spacing configuration will increase the potential flow interactions. The dimensions for Fig. 3.4 were derived from the original drawings of the casing pieces and blade stacking diagrams: the measured rotor-stator gap at mid-span of 80.9±0.95 mm and 31.7±0.63 mm for the two spacing cases compare favourably with these values.

3.4 Instrumentation

This section describes the instrumentation used in the current investigation. Where appropriate the accuracy of the instrument and calibration techniques are also discussed.

3.4.1 Pitot-Static tube

The inlet axial velocity was measured with an Airflow Developments 4 mm O.D. pitot-static tube with ellipsoidal nose inserted with its stem 115 mm upstream of the centre

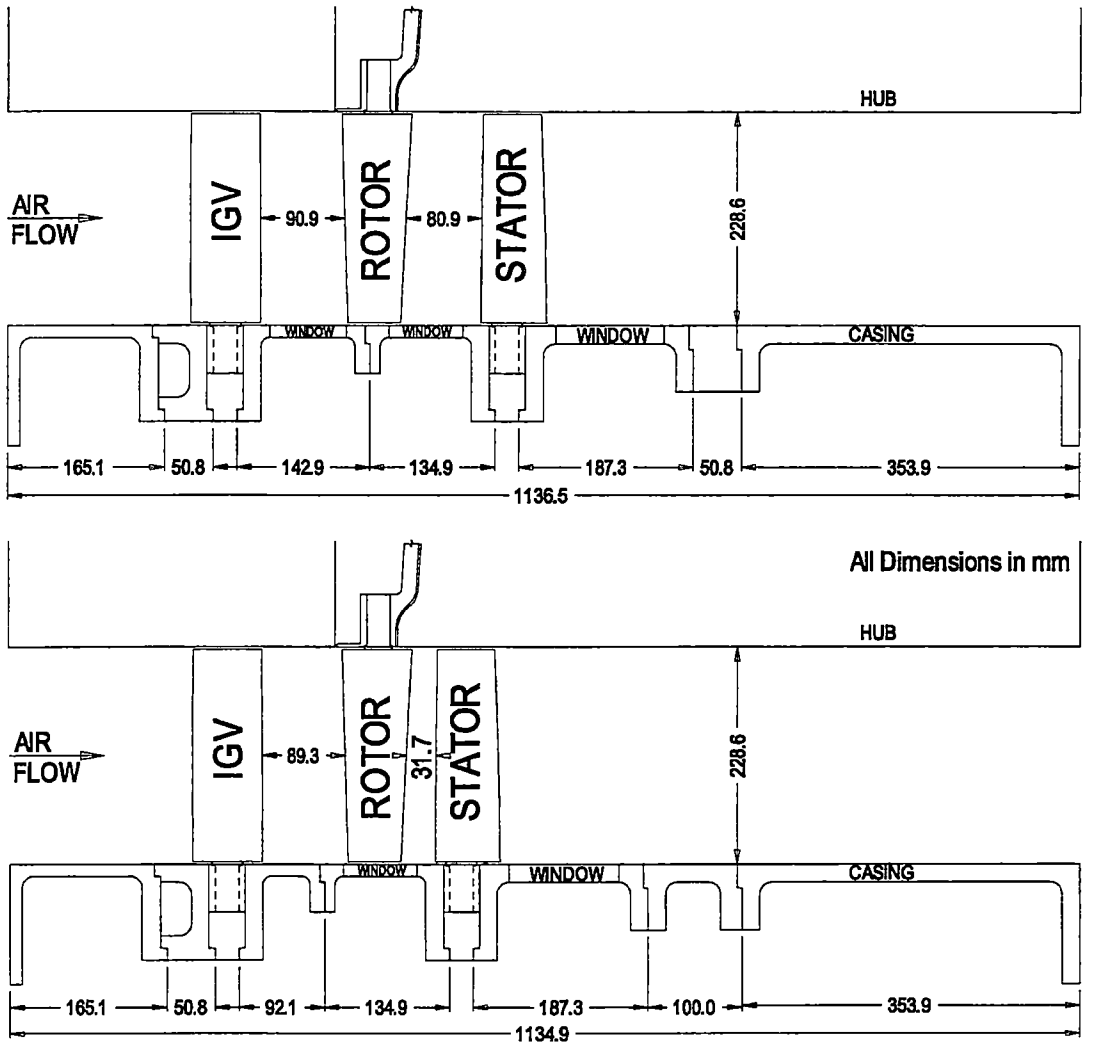

Figure 3.4: Axial blade row spacing for the current investigation. Upper Part: Outer casing configuration for 106% chord rotor-stator axial spacing at mid-blade height. Lower Part: Outer casing configuration for 41.6% chord rotor-stator axial spacing at mid-blade height.

of the IGV row. The probe was positioned at a radial distance of 127 mm from the hub which closely corresponds to the mean flow height of the blades (Oliver [104]). Although the probe is in the same axial plane as the downstream measuring station, the whirl velocity imparted by the rotor means the wake from this instrument does not interfere with the stator passages where data were obtained. The pressure measured by the static tapping is used as a reference for the pressure measuring system (see Section 3.4.5). The axial velocity measured by the pitot-static tube is used to calculate the flow coefficient of the machine.

3.4.2 Thermometer

Tunnel air temperature was measured by a Stow Laboratories platinum resistance thermometer inserted in the top of the tunnel upstream of the IGV row. Solomon [123] compared this thermometer against a mercury in glass thermometer and found it to be accurate to ±0.2% of reading. Readings from this instrument are used to evaluate the properties of the working fluid.

3.4.3 Relative humidity probe

A Vaisala HUMICAP humidity sensor measured the ambient relative humidity. The manufacturer specifies an accuracy of ±2% relative humidity depending on the calibration reference. The probe is mounted externally to the tunnel, on the side of the nearby instrument rack close to the compressor inlet.

3.4.4 Multimeter

An Analogic DP100 $5\frac{1}{2}$ digit digital multimeter was used to record the AC voltage output from the anemometer bridge. The multimeter was controlled via an RS-232 connection and the filtering was set such that all values were averaged over 5 seconds. Although the manufacture specifies an accuracy of 0.25% of reading for AC values in the range 100Hz-10kHz, it was considered that at best 3 significant figures were useful when evaluating the fluctuating component derived from the thermal anemometry measurements.

3.4.5 Pressure transducing system

Two Datametrics pressure transducers were used to measure atmospheric and differential pressures. A 0-1000 torr (0-133.3 kPa) Barocell 572 capacitive type transducer was used to measure atmospheric pressure: A ±100 torr (± 13.3 kPa) Barocell 572 capacitive type transducer was used to measure differential pressures. The transducers were connected to a thermal base to reduce temperature drift effects. Both transducers used the static pressure from the inlet pitot-static tube as a reference. The differential pressure transducer was connected to a Scanivalve rotary pressure switch. This allowed the use of a single high quality differential transducer for multiple pressure measurements, in particular blade static pressure surveys and 3-hole probe measurements. Both transducers were connected to individual Datametrics 1015 signal conditioners that scale the output to −5 to +5 volts suitable for input to the data acquisition system. The signal conditioners have seven selectable gain values ranging from ×1 to ×0.001; these correspond to maximum fullscale values of 13.3 kPa and 13.3 Pa respectively. The system is set to auto-range with the downrange point at 28% fullscale and uprange point at 105% of fullscale. The manufacturer specifies an accuracy of ±0.03% and hysteresis of ±0.003% of fullscale. Solomon [123, see Appendix D] discusses the accuracy of the pressure measuring system as a whole, including transducer and data acquisition system. For pressures above 4 Pa and provided that the number of samples is large enough to ensure that the standard error is small compared with the instrument uncertainty, Solomon [123] states that the resulting 95% confidence value of the mean is ±0.11%.

3.4.6 3-Hole probe

A United Sensor CA120 cobra type 3-hole probe with 3 mm diameter sensing head was used for all flow angle measurements. The probe was also used to provide velocity data for in-situ hot-wire calibrations: this is discussed in more detail in Section 3.4.8. The sensing head consists of three 0.75 mm O.D. tubes connected side by side with the outer tubes ground to 45° . Fig. 3.5 shows the overall size of the sensing head and connecting tubes. The reference bar (not shown in Fig. 3.5) is at 90±0.2° to the probe axis and has a reference number for each tube stamped into it. The tubes are labelled 1 through 3 with the centre tube labelled 1.

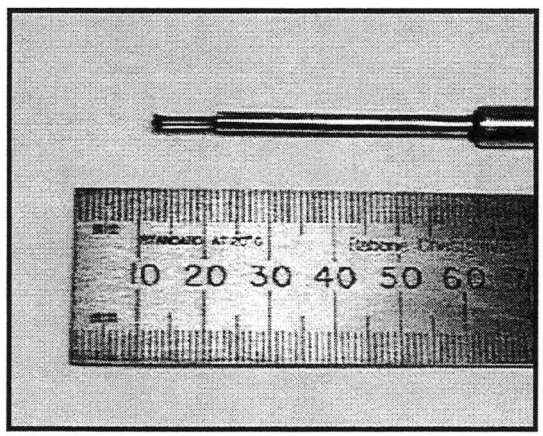

Figure 3.5: United Sensor CA120 3-hole probe.

Solomon [123] calibrated the probe in a closed circuit wind tunnel. By considering the potential flow around a cylinder, the following functions can be shown to depend on the flow angle α relative to the probe head, the geometry of the probe and, in a real fluid, Reynolds number.

$$f_1(\alpha, \text{geometry}, Re) = \frac{p_2 - p_3}{p_1 - p_3} \tag{3.2}$$

$$f_2(\alpha, \text{geometry}, Re) = \frac{p_1 - p_3}{\frac{1}{2}\rho U^2} \tag{3.3}$$

$$f_3(\alpha, \text{geometry}, Re) = \frac{P - p_1}{\frac{1}{2}\rho U^2} \tag{3.4}$$

where P is the total pressure and U is the velocity at the probe. Over a range of velocities (10 to 28 m/s) no significant Reynolds number effects were observed for the current probe. This was attributed to sharp edges controlling the separation behaviour. For a single probe the geometry unknown is eliminated and for this particular calibration the Reynolds Number effects can be ignored, reducing the functional dependency to α only. The curves fitted to the measured data for f_1, f_2, and f_3 are given in Fig. 3.6. Solomon [123] states that the scatter in the f_3 data suggested an uncertainty of the order of 0.5% which is close to the uncertainty expected from consideration of the pressure instrumentation accuracy and measured standard deviations of individual pressure signals.

For measurements in the compressor, all probe pressures were measured relative to the inlet static pressure p_{in}. With the probe in an unknown flow $p_2 - p_3$, $p_1 - p_3$ and $p_1 - p_{in}$ were determined. The flow angle α was found from the f_1 calibration function. A dynamic pressure co-efficient, Cp_{dyn} was found from the f_2 probe calibration function.

$$Cp_{dyn} = \frac{(p_1 - p_3)}{f_2(\alpha)(P_{in} - p_{in})} \tag{3.5}$$

$$= \left(\frac{U}{U_{in}}\right)^2 \tag{3.6}$$

A total head co-efficient was also found using the f_3 curve.

$$Cp_{tot} = \frac{f_3(\alpha)\frac{1}{2}\rho U^2 + (p_1 - p_{in})}{P_{in} - p_{in}} \tag{3.7}$$

$$= \frac{P - p_{in}}{\frac{1}{2}\rho U_{in}^2} \tag{3.8}$$

3.4.7 Anemometers

The hot-wire and hot-film anemometry work was performed using two TSI IFA-100 systems containing TSI Model 150 anemometer bridges and TSI Model 157 signal conditioners. Five channels were available for simultaneous data acquisition. Anemometer settings allowed AC or DC coupling of signals and the specification of a low-pass filter cut-off frequency. Each anemometer was controlled via an RS-232 connection allowing for signal conditioner parameters to be set individually for each channel. The manufacturer states that the signal conditioner has an offset accuracy of 0.15% and a gain accuracy of 0.15%. The resistance measurement repeatability is 0.002Ω and the bridge setting accuracy is ±0.002Ω.

3.4.8 Hot-wires

Fig. 3.7 shows the hot-wire probes used in the current investigation. All are DISA type single sensor type probes with 5μm diameter and 1.25 mm sensing length. The sensing wire is platinum-plated tungsten with gold-plated ends to reduce the interference effects from the supports and give more uniform temperature distribution along the sensing element. The overall distance between wire supports including the gold plating is 3 mm. Typical sensing element resistance at 20° C was 3.5Ω with the wire temperature coefficient of resistance $\alpha_{20} = 0.36\%$ per ° C. An overheat ratio (R_{op}/R_{20}) of 1.6 was used for all hot-wire measurements, giving a mean wire temperature around 185° C.

3.4.8.1 Probe calibration

Collis and Williams [22] indicated that the heat loss from cylindrical wires of infinite length could be correlated in terms of Nusselt number and Reynolds number by a relation of the form,

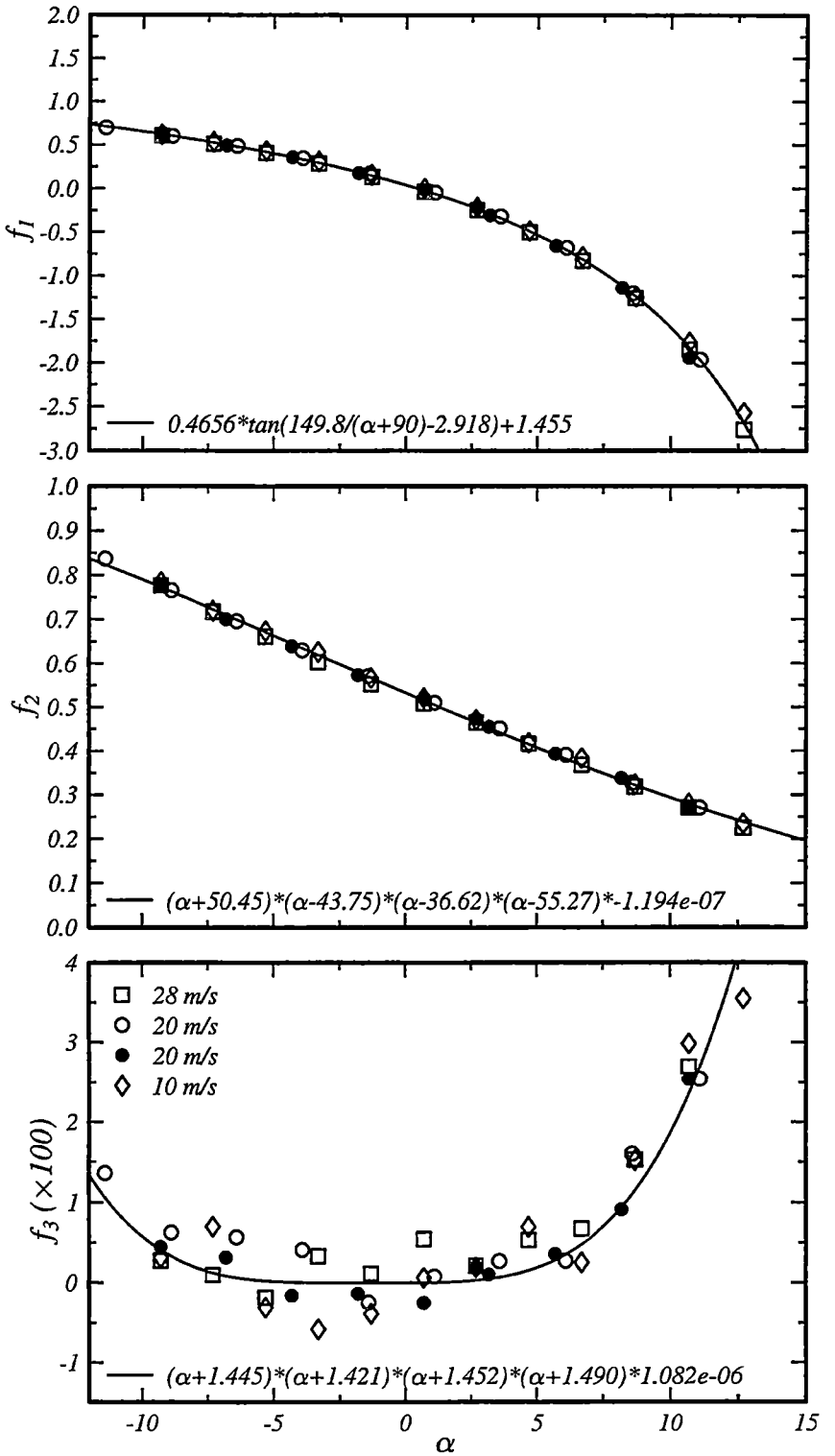

Figure 3.6: Three Hole probe calibration functions from Solomon [123].

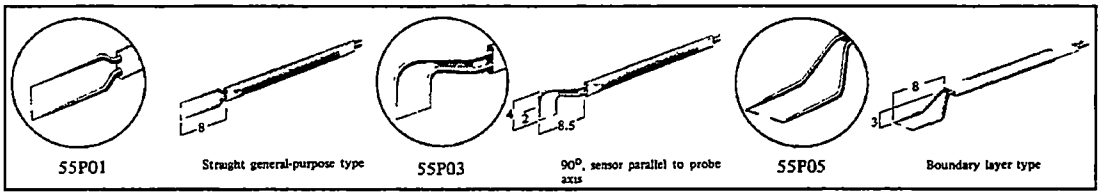

Figure 3.7: Hot-wire probes used in the current investigation. Left to right: Disa (Dantec) probe types 55P01, 55P03 and 55P05.

$$Nu\left(\frac{T_m}{T_a}\right)^{-0.17} = 0.24 + 0.56Re_w^{0.45} \tag{3.9}$$

Following the practice of Walker [138], a quadratic term has been added to improve the calibration at low velocities.

$$Nu\left(\frac{T_m}{T_a}\right)^{-0.17} = A + BRe_w^{0.45} + C(Re_w^{0.45})^2 \tag{3.10}$$

where

$$Nu = \frac{Q_w}{\pi l \Delta T k_f} \tag{3.11}$$

$$= \frac{E^2 R_p}{\pi l \Delta T k_f R_t^2} \tag{3.12}$$

$$\Delta T = T_m - T_a \tag{3.13}$$

$$Re = \frac{\rho U d}{\mu} \tag{3.14}$$

and A, B and C are the calibration coefficients which must be determined for each individual wire.

All calibrations were performed in-situ in the compressor. With the IGV and stator in reference positions, calibration velocities were measured with the 3-hole probe at various stations between the blade rows. Care was taken to ensure the 3-hole probe was placed outside the wake streets of the stationary blade rows, in order to minimise the fluctuations in velocity at the measurement point. Periodic re-calibration was performed by axially traversing the hot-wire probe to the nearest calibration station. Errors inherent with measuring fluctuating signals with pneumatic probes in turbomachines are well documented (see Samoilovich and Yablokov [112]), however the error introduced by essentially calibrating the hot-wire against the pneumatic probe data was believed to outweigh errors and difficulties introduced with routinely reassembling the probe for calibration outside the tunnel. Solomon [123] reports errors of up to 10% between the 3-hole probe data and hot-wire measurements in the compressor, for wires calibrated in a recirculating wind tunnel. This large discrepancy was attributed to a change in lead resistance which occurred when reassembling the hot-wire probe inside

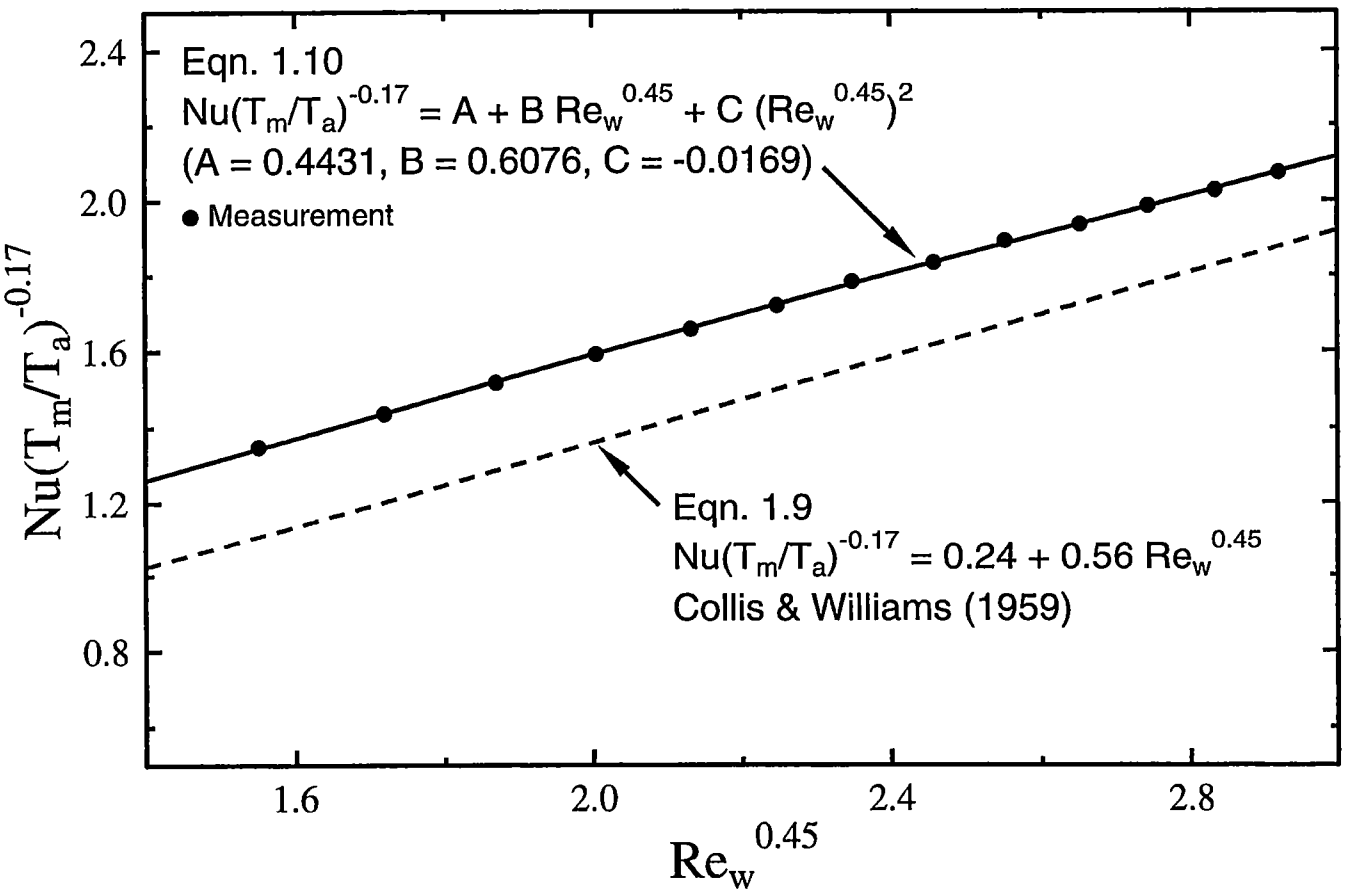

Figure 3.8: In-situ calibration of a DISA 55P03 hot-wire probe. Probe located 20%c upstream of the stator leading edge.

the compressor. To overcome this discrepancy Solomon [123] adjusted the lead resistance to match the velocity measurements obtained from the 3-hole probe, essentially performing the same procedure as used in the current investigation. The fact that the hot-wire measurements were primarily intended for gathering turbulence information supports the use of this in-situ calibration method. A typical resulting calibration is shown in Fig. 3.8 and is compared with Eqn. (3.9). Collis and Williams [22] calibrated wires with l/d ratio in the range 10^3 to 10^4: wires used in the current investigation were of $l/d = 250$. The l/d ratio difference accounts for the relative vertical shift between the two calibration curves. The inaccuracies involved with this type of in-situ calibration procedure would make the method questionable for more sensitive work such as boundary layer surveys.

3.4.8.2 Drift correction

The major causes of calibration drift during operation were dust or dirt particles accumulating on, or impacting, the sensing wire. Generally the accumulation of deposits resulted in a gradual vertical shift of the calibration curve over time; whereas impacts large enough to strain the wire resulted in a sudden jump of the calibration curve. An effort was made to minimise and correct for drift effects on the measured data. The effects of dust accumulation were minimised by spraying the sensing wire with cleaning fluid at regular intervals. For traverse measurements, the acquisition routine logged the time of each measurement point and at the completion of the traverse data were re-measured at a number of points. The difference in velocity was attributed to a drift in the calibration curve and a least squares method was used to fit a linear relationship to drift with time. The relationship was constrained to give zero drift at the start of the traverse. It was assumed that calibration drift effect resulted in a shift of the curve without altering the slope. For each measurement point, using the elapsed time since the start of the traverse, a correction was applied to the constant (A) in Eqn. (3.10) to account for these effects.

3.4.8.3 Turbulence measurements

All hot-wire measurements were performed with a single sensing element probe, with the sensing wire axis aligned in the radial direction. The wire was not rotated and therefore the radial fluctuations were effectively ignored. Decomposition of the streamwise velocity components into axial and tangential contributions was not performed. Ravindranath and Lakshminarayana [107] present measurements obtained downstream of the rotor, in the rotating reference frame, in a machine similar to the one described above. All three components of the velocity field were measured with a triple element sub-miniature probe. The measurements show large levels of turbulence component inside the rotor wake: in particular the radial component. The pitchwise distributions of axial and tangential turbulence are qualitatively similar to the results presented in Chapter 5. It is therefore likely that the total level of turbulence derived from the current procedure underestimates the true level of turbulence in the machine. Since only the streamwise velocity fluctuations have been measured correctly (the normal fluctuation will be predominately registered as a rotation of the velocity vector around the sensing element rather than a true fluctuation), and assuming that the turbulence is

isotropic (although not a valid assumption for wake flow) it may be necessary to multiply the indicated turbulence level by $\sqrt{3}$ in order to obtain agreement with correlations for transition onset based on flat plate measurements where all three components of the freestream turbulence have been measured. Nevertheless the measured RMS bridge voltage was used to evaluate the total disturbance level Tu_D by assuming,

$$U' = \frac{dU}{dE}E' \tag{3.15}$$

where E is the bridge voltage and for the above form of the calibration curve,

$$\frac{dU}{dE} = 2\frac{U}{E}\frac{Nu}{Re}\frac{\frac{T_m}{T_a}^{-0.17}}{(0.45BRe^{-0.55} + 0.9CRe^{-0.1})} \tag{3.16}$$

The term total disturbance has been used to distinguish the above from the periodic unsteadiness $\widetilde{Tu}$ and freestream turbulence Tu. The evaluation of the turbulence and unsteadiness data from the hot-wire measurements is given in detail in Appendix A.

3.4.8.4 Frequency response

The frequency response of hot-wires was determined using the square wave test of Freymuth and Fingerson [41]. Fig. 3.9 shows the result of the square wave test for the same wire as calibrated in Fig. 3.8. The frequency response is given by,

$$f_c = \frac{1}{1.3\tau} \tag{3.17}$$

and for Fig. 3.9, the time constant $\tau = 8.55\mu s$ giving a cut-off frequency of the order of 90kHz. Cut-off frequencies varied depending on individual wires and values above 70kHz were readily obtainable. All signals were filtered at 20kHz to avoid aliasing during digitisation.

3.4.9 Hot-film array

The Senflex brand surface hot-film array consisted of a 0.05 mm thick polymide sheet with electron beam deposited nickel sensors. The sensor elements were manufactured with a pitch of 2.54 mm and there were 61 sensors in total. All sensors were in-line and the film was wrapped around the blade with sensors at mid-blade height (see Fig. 3.10). Solomon [123] performed inviscid flow calculations to determine the changes in the blade surface velocity distribution caused by wrapping the surface array around the blade. Minimal changes were predicted and they were not expected to significantly alter the boundary layer development. The greatest change occurred at the trailing edge, where the wrapped case gave a change in outlet angle of 0.3° . The blade profile was altered where the connecting wires were attached to the sensor tracks, but this region is located within the wall boundary layer and should not significantly alter the flow at mid-blade height. The sensor locations are given in Appendix B.

Boundary layer investigations with surface-mounted hot-films rely upon the similarity between the velocity profile adjacent to the wall and the temperature profile of

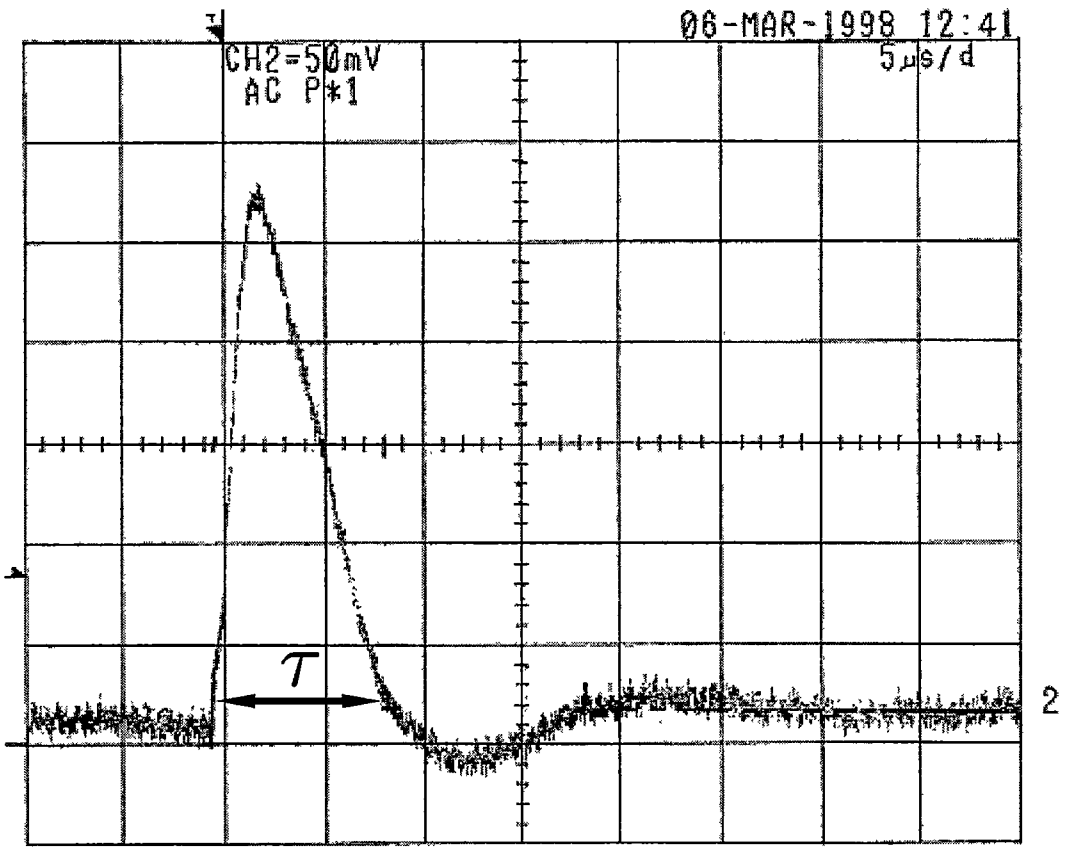

Figure 3.9: Digital oscilloscope output showing the results of a square wave test to determine the frequency response of a DISA 55P03 hot-wire probe.

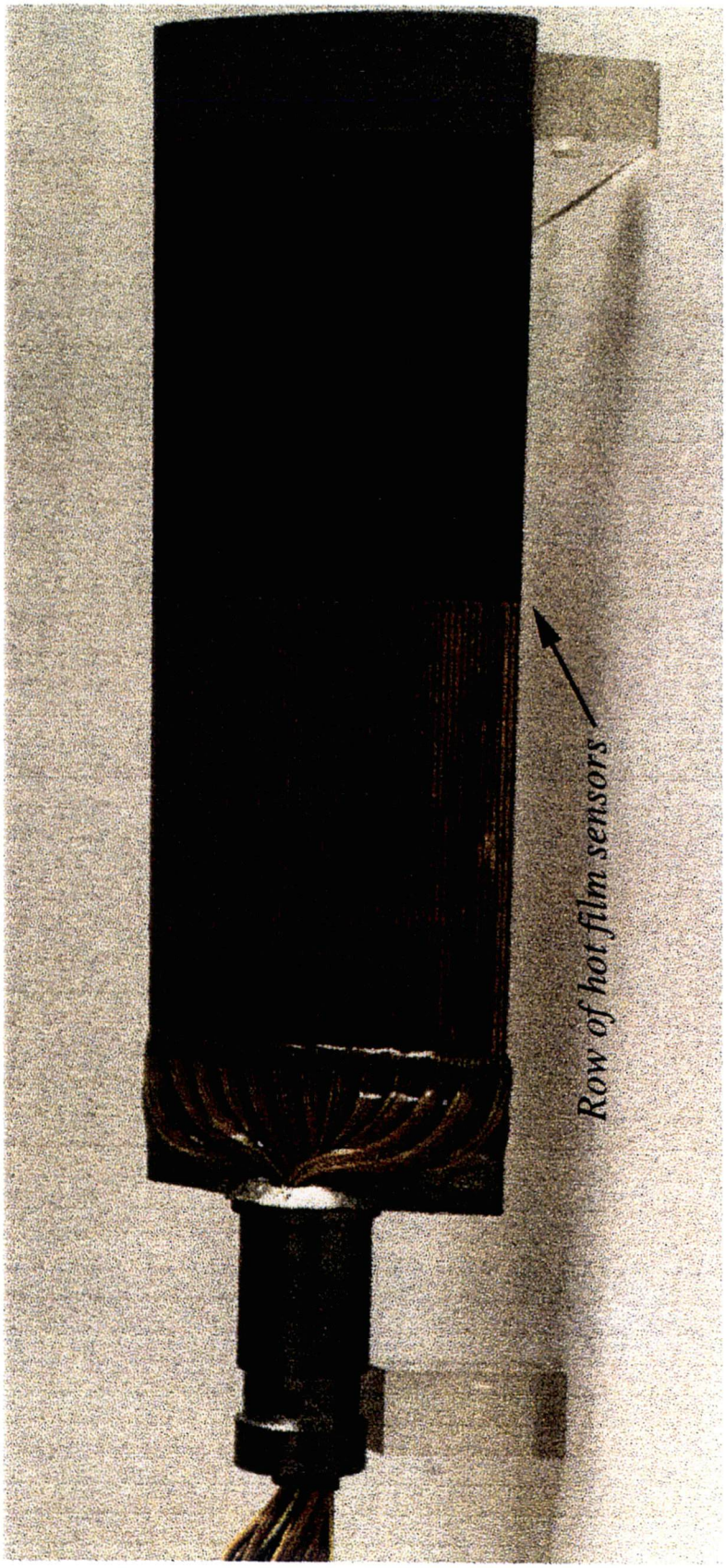

Figure 3.10: Stator blade instrumented with hot-film array from Solomon [123].

the thermal boundary layer that is generated by the heated element. Bellhouse and Schultz [7] show that provided the thermal boundary layer produced by the heated element has a thickness less than the linear part of the velocity layer (for turbulent boundary layers this means the thickness must be smaller than the laminar sub-layer) then

$$\tau_w = k\left(\frac{E^2 - A^2}{\Delta T}\right)^3 \tag{3.18}$$

Here E is the instantaneous output voltage from the anemometer, ΔT is the temperature difference between the air and the heated sensor, and A represents the heat loss to the substrate. The constants A and k are determined by calibration.

Various methods (see Brown [18], Hodson [64] and Davies et al. [26]) have been proposed to calibrate hot-film sensors for skin friction measurements in steady laminar and turbulent boundary layers. In unsteady flows the relatively large heat flux to the substrate and time lags inherent in this process make accurate calibration difficult and the ensuing results questionable. Problems involved with applying a suitable calibrating flow to the hot-film array glued to the stator surface precluded any attempts at calibrating the sensors. In addition, as outlined below, qualitative data are sufficient to determine the state of development of a boundary layer which further reduces the need for accurate calibration information.

For the present investigation the semi-quantitative approach described by Hodson et al. [67] was employed. Hodson [65] established that the rate of heat loss to the substrate can be approximated by the square of the zero-flow voltage, E_0, measured under zero flow conditions. This approximation ignores the heat transfer, due to natural convection and radiation, to the air and from the plated leads which form part of the electrical circuit on the substrate. Also, if the bulk temperature of the blade is equal to the air temperature, the temperature difference ΔT is proportional to E_0^2. Provided the above assumptions hold then,

$$\tau \propto \left(\frac{E^2 - E_0^2}{E_0^2}\right)^3 \tag{3.19}$$

The wall shear stress τ_w is proportional to τ, which is referred to as quasi-wall-shear stress to reflect its semiquantitative nature. The units associated with τ are arbitrary. This method also minimises the effects of small differences in sensor geometry and electrical properties on measurements acquired from different sensors. As a result, relative magnitudes of quasi-wall-shear stress obtained from sensors in an array can be directly compared to each other.

3.4.9.1 Frequency response

The frequency response of the hot-films, determined using the square wave test, was around 30kHz. This is much lower than the hot-wire because of the large component of heat transfer to the substrate. All hot-film measurements were performed with the sensor overheat ratio equal to 1.5.

3.5 Compressor Control

The compressor and measurement systems were controlled by two IBM-compatible 486 personal computers: the compressor control PC and the data acquisition PC. The main function of the compressor control PC is to control the machine operating point and acquire data from slow response instrumentation. The PC uses a Metrabyte DAS-20 data acquisition board and TurboPASCAL based software to measure differential pressure, atmospheric pressure, temperature and relative humidity at regular intervals. The signal from the optical shaft encoder is hardware processed to provide compressor speed in a BCD format, at a selectable rate of either 1 Hz or 10 Hz, for the data acquisition system.

The main control of the tunnel speed is by an analogue control loop built into the motor drive unit. Continuous adjustment of the hardware speed set-point signal through the PC 12-bit D/A converter is used to maintain speed at the set-point value. The software varies the set-point, typically at 5 second intervals, to maintain constant speed, Reynolds number or Mach number. This control loop corrects for long term changes in compressor operating point which are primarily caused by changes in atmospheric conditions. Running averages of air density, kinematic viscosity and inlet axial velocity are calculated. From this information the flow coefficient ϕ and reference Reynolds Re_{ref} are displayed in real time.

Suspected low frequency variations in the flow coefficient were investigated by Solomon [123]. Evidence of periodic behaviour, with period approximately equal to 30 seconds, was found from measurements of the inlet dynamic pressure. Although the source of the variations were unclear, it was attributed to either large scale eddies in the return flow or a Helmholtz style resonance in the room or diffuser. At an operating point of $Re_{ref} = 120\ 000$ and $\phi = 0.7$, the variation in inlet velocity was $\pm 0.8\%$ or the equivalent of a flow coefficient of $\phi = 0.7 \pm 0.006$.

3.6 Data Acquisition

The second IBM-486 PC was used to perform the high-speed data acquisition operations. The data acquisition PC uses a UEI Win-30DS/4 data acquisition board and LabView software to acquire data from the hot-wire and hot-film anemometers (see Section 7.2 for details). The data acquisition board has an accuracy of $\pm 0.06\%$ for channels 0–3 and $\pm 0.16\%$ for channels 4–15. An RS232C link allows the data acquisition PC to set test-points and read the current operating conditions from the compressor control PC. This setup allows the software on the compressor control PC to remain unchanged while software on the data acquisition PC can be customised for each new testing schedule.

Ensemble-average values of measured quantities were obtained from repeated records with the sampling for each record triggered at the same point on each rotor revolution by an optical encoder mounted on the motor end of the drive shaft. This ensures that the wakes of the same rotor blades were observed in each record. The records covered about 6 rotor blade passing periods for a set of wakes previously found by Solomon [123] to exhibit good periodicity. These blades were marked at mid-span and can easily be identified on the right hand side of Fig. 3.3. An optical sensor, which was triggered

directly from one of the rotor blade tips, was added to the machine in order to investigate the effects of unsteady shaft and or coupling twist on the ensemble averaged data. Testing revealed that the relative timing of the two signals at a given operating point had a standard deviation equivalent to less than 0.8% of a blade passing period. There was a small change in the relative timing of the signals across the speed range attributed to shaft and coupling twist. No consistent trend was observed as the aerodynamic loading was changed at constant speed. Problems were encountered when using the new sensor to trigger the data acquisition processes and are attributed to the shape of the pulse produced. It was therefore decided to use the shaft encoder to trigger all data acquisition processes. This also means that the ensemble average results are directly comparable to measurements previously obtained in this machine.

Chapter 4

Experimental Overview

4.1 Introduction

In 1985 Wisler [150], and again more recently Wisler et al. [151], outlined the advantages of low-speed testing in order to improve compressor and LP turbine performance: greater accuracy, at reduced cost, and at lower risk. The principal aerodynamic advantage of low-speed testing is that it provides an opportunity for detailed, accurate measurements of the complex flow over and through the blade rows. The main disadvantage of low-speed testing is that Mach number similarity is not preserved and therefore the effects of compressibility cannot be evaluated. For this reason low-speed testing of transonic fans, early stages of HP compressors and most HP turbine nozzles is not possible. However low-speed testing is ideal for the middle and rear stages of HP compressors and LP turbines.

The current low-speed testing programme investigates the stator mid-span unsteady boundary layer behaviour with the aid of thermal anemometry. The upstream IGV and rotor rows provide the important characteristics for modelling an embedded stage in a multi-stage axial machine. Both the periodically passing rotor wakes and the relative position of the upstream IGV wake are shown to influence the stator blade boundary layer behaviour. Single component hot-wire measurements detail the unsteady flow upstream, in the passage, and downstream of the stator blade row. Hot-film observations show the response of the stator blade boundary layer to changes in the inflow disturbance field brought about by blade row clocking and reduction in rotor-stator axial row spacing. Hot-wire measurements close to the stator trailing edge are used to quantify changes in performance of the blade element at mid span.

4.2 Blade Row Clocking

Recent numerical and experimental studies have speculated that a performance improvement is possible for turbines with identical blade counts in the stator rows by correctly aligning the wakes from the first stator row with the subsequent stator rows downstream. This type of blade row clocking was investigated numerically by Eulitz et al. [37] for a multistage turbine. They predicted an efficiency improvement of 0.4% when the dispersed wake street of an upstream stator was incident on the downstream vane, but the model assumed a fully turbulent flow and ignored unsteady wake-induced

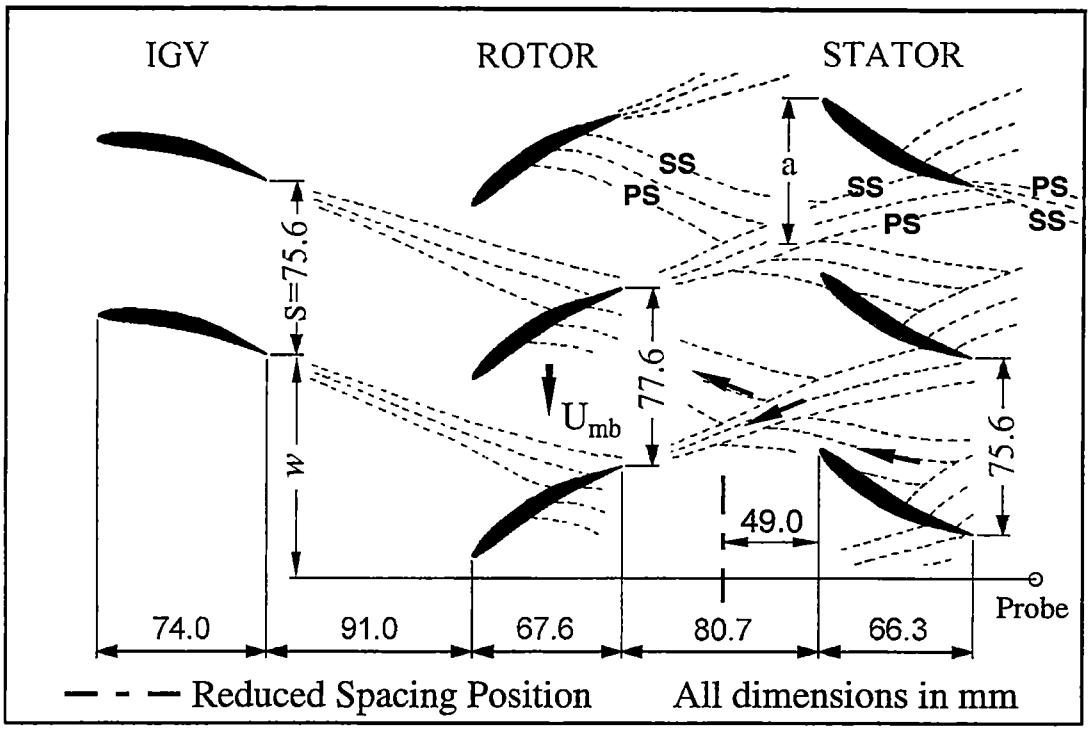

Figure 4.1: Cross-section of compressor blading at mid-blade height, showing typical instantaneous wake dispersion. SS = Suction Side. PS = Pressure Side. Arrows indicate relative flow in wakes. a = circumferential offset of stator leading edge from the centre of the IGV wake street. w = circumferential offset of measurement probe from IGV trailing edge.

transition effects on the downstream vane. Both experimental and analytical studies (see Huber et al. [72] and Griffin et al. [56]) were conducted to investigate the impact of stator clocking on the performance of the Space Shuttle Main Engine Alternate Fuel Turbopump Turbine test article. These studies concluded that there was a measurable difference in efficiency ($\simeq$ 0.3%) for both high and low Reynolds number flows due to stator clocking effects. Maximum efficiency occurred when the calculated time average first vane wake impinged upon the second vane leading edge. The minimum efficiency occurred when the first vane wake passed down the middle of the second vane passage.

Clocking in multistage compressors has also recently received attention. Barankiewicz and Hathaway [6] investigated the effects of stator clocking in the NASA Lewis Research Center's Four-Stage Axial Compressor Facility. The impact of stator row clocking on both the overall machine and the third stator blade row performance were presented. Changes in overall performance due to stator clocking of 0.2% were observed. Although this study quantified the overall performance changes, the mechanisms responsible for the changes were not elucidated.

Typical dispersion of the IGV and rotor wakes as they are convected through the downstream blade rows of the Tasmanian research compressor is illustrated in Fig. 4.1. The coordinate a is used to define the circumferential offset of stator leading edge from the centre of the avenue of dispersed IGV wake segments. The dimensionless quantity

a/S is used to define the blade row clocking positions. Initially, the mid-span stator element performance was investigated at four relative clocking positions: a/S= 0.00, 0.25, 0.50 and 0.75 (see Chapter 6). The value a/S= 0.00 corresponds to the IGV wake street passing over the stator blade at mid-span. For a/S= 0.25 and 0.75, the IGV wake street is located close to the stator suction and pressure surfaces, respectively. At a/S= 0.50 the IGV wake street passes down the middle of the stator passage. Subsequent experiments concentrate on the a/S= 0.00 and 0.50 cases: these correspond approximately to the cases of minimum and maximum rotor wake periodicity experienced by the stator blade element at mid-blade height (as indicated by measurements of the temporal variation of ensemble average stator wake momentum thickness reported in Chapter 6).

As illustrated in Fig. 4.1, the IGV wake street is segmented and rotated relative to the local flow direction as it passes through the rotor row: the degree of rotation is dependent on the rotor loading. Accurate identification of the IGV wake street by the time it reaches the stator leading edge is not trivial. IGV-rotor wake interactions occurring downstream of the rotor trailing edge produce areas of low energy fluid on the suction side of the IGV wakes (see Chapter 5). This causes a local minimum in pitchwise velocity traverses which can be easily misidentified as the IGV wake street. The degree of accumulation of low energy fluid will vary with the strength of the respective wakes and the axial row spacing. The most accurate method of identifying the wake street is by its random turbulence component.

For the initial observations, with the large axial spacing between the rotor and stator rows, the location of the IGV wake street with flow coefficient was estimated from the random turbulence levels obtained from hot-wire observations downstream of the stator trailing edge and from inviscid flow calculations of Solomon [123]. Identifying the IGV wake street downstream of the stator trailing edge proved difficult if the random turbulence components from both the IGV and stator wake streets were not well separated in the pitchwise direction. Generally, this meant that accurate identification was only possible if the IGV wake street passed down the middle of the stator passage. Solomon's observations were recorded with the positions of the IGV and stator blade rows unchanged with flow coefficient variation. For the medium loading case the relative clocking position was easily identified, but with the changes in blade loading the wake streets were placed closer together and this clouded the exact location of the IGV wake street. The subsequent detailed measurements (see Chapter 6) indicate an accuracy of about $\pm 0.1w/S$.

For the observations with the reduced axial spacing between the rotor and stator rows, the location of the IGV wake street was determined from detailed hot-wire measurements at the stator trailing edge. A combination of increased familiarity with the measurement techniques and prior knowledge of the wake behaviour allowed the clocking accuracy to be increased, although it is still limited to around $\pm 0.05w/S$at best. For all data sets both stationary rows were simultaneously clocked relative to the measuring probe. For measurements in the rotor-stator axial gap, upstream and outside the influence of the stator potential field, it may be argued that clocking of both rows is unnecessary. Nevertheless, as a precautionary measure both rows were simultaneously clocked. By not clocking both rows together the disturbance inflow and behaviour of the hub boundary layer may be altered and possibly induce changes in the machine behaviour and the flow at mid-span, particularly at the higher loading conditions.

4.3 Axial Row Spacing

Analytical and numerical studies of the influence of rotor-stator axial gap on axial compressor performance have recently been reported by Deregel and Tan [28] and Adamczyk [2]. They examine the potential for performance improvement by passing a wake through a blade row prior to being mixed out by viscous diffusion, and indicate potential increases in efficiency and pressure rise coefficient of 1 or 2 percent. This idea was originally proposed by Smith [121] to account for the behaviour of the General Electric (GE) 4-stage Low-Speed Research Compressor (LSRC). However, these analyses do not account for a possible accompanying variation in blade losses. The data obtained in the current investigation, gathered primarily for the study of wake-induced transition phenomena, is also used to estimate whether or not potential efficiency gains from reduced mixing losses in an upstream blade wake is enhanced or diminished by associated changes in the downstream blade row losses as the axial gap is altered.

For modern aeroengines the minimum axial row spacing is dictated by surge deflection and aeroelastic criteria rather than an optimum aerodynamic configuration. Current literature indicates that the typical axial row spacing of an embedded compressor stage is of the order of $\frac{1}{3}$ of the blade chord. The ninth stage of the Pratt & Whitney 11 stage compressor modelled by Graf et al. [54], and the mid-stage of the GE Energy Efficient Engine (E^3) 10-stage compressor modelled by Halstead et al. [59] and Manwaring and Wisler [92], have rotor-stator axial gaps of 32% chord. Gorrell et al. [49] investigated the effects of upstream wakes on the performance of a transonic compressor stage by varying the axial spacing of an upstream wake generator. The wake generator was placed at three axial positions, giving 'close', 'mid' and 'far' spacings of 12%, 26% and 56% chord. The authors state that the mid and far spacings are representative of axial gaps found in compressors and modern fans.

As mentioned in Chapter 3, data were obtained for two configurations of rotor-stator axial blade row spacings. The first configuration, with 106% chord axial spacing between rotor and stator rows, will be referred to as the Large Axial Gap (LAG) case. This blade row spacing is significantly larger than is found in modern gas turbine aeroengines, where as already indicated the overall length is minimised for weight and vibration reasons. The large axial spacing means that the rotor wakes are more diffuse when they reach the stator leading edge, and that the interactions of the rotor potential field with the neighbouring blade rows are significantly reduced. The second configuration for the current investigation has an axial spacing of 41.6% chord between rotor and stator rows. This is still larger than current modern axial spacings and will be referred to as the Reduced Axial Gap (RAG) case.

4.4 Experimental Summary

4.4.1 Reynolds number

All measurements were conducted at mid-span with the machine operating at a constant reference Reynolds number (based on rotor mid-blade height peripheral speed and stator blade chord) of $Re_{ref} = 120\ 000$. The constant Re_{ref} means that the stator inlet Reynolds number, Re_1, varies with flow coefficient. Table 4.1 shows the variation in Re_1 with flow coefficient for the various test cases considered. The values of inlet

Table 4.1: Circumferentially averaged stator incidence $i°$ and Reynolds number Re_1 at mid-blade.

Loading	High	Medium	Low
ϕ	0.600	0.675	0.840
	Large Axial Gap		
$i°$	4.1	1.2	-6.2
Re_1	112000	117000	130000
	Reduced Axial Gap		
$i°$	2.9	-0.4	-6.9
Re_1	114000	120000	132000

Reynolds number are low compared with those typical of aircraft gas turbine engine operation, as reported by Hourmouziadis [69] and Mayle [93]. For a medium sized by-pass engine at cruise altitude, Hourmouziadis [69] reports that the Reynolds number varies from 700 000 to 1 000 000 in the low pressure (LP) compressor, rising above 1 000 000 in the high pressure (HP) compressor. The LP turbine exhibits a minimum Reynolds number around 100 000. The high temperatures (which give low viscosity values) and low pressure values in the rear part of the engine combine to give the lower Reynolds numbers. The values for the current testing are also generally lower than those in the experimental studies of Halstead et al. [59], where the inlet Reynolds number for the baseline case is 245 000. Reynolds numbers decrease with increasing cruise altitude and decreasing engine size.

The test compressor was nevertheless operating above the critical Reynolds number range where laminar separation starts to cause a significant increase in blade losses. As discussed by Solomon [123] the critical Reynolds number for the test machine is lower than that for modern compressors because of the generally milder pressure gradients on the suction surface of C4 blading. Walker [140] discusses the influence of freestream turbulence on critical Reynolds number, and points out that an increase in turbulence level will generally cause a fall in the critical Reynolds number through promoting earlier transition in the separated shear layer. Roudebush and Lieblein [111] present experimental results showing the dramatic fall in critical Reynolds number through the influence of increased freestream turbulence for blades tested in a cascade configuration. Both the observations of Solomon [123] and the detailed experiments of Walker [140] indicate that the critical Reynolds number for the current blading, under machine conditions, is around 60 000. It should also be noted that the surface hot-film observations on the stator blading reported by Solomon and Walker [124, 125] show essentially similar behaviour to that in the higher Reynolds number multistage compressor experiments of Halstead et al. [59].

4.4.2 Flow coefficient

Data were obtained for flow coefficients ($\phi = V_a/U_{mb}$) of 0.600, 0.675 and 0.840, and will be referred to as high, medium and low loading cases respectively. The loading cases range from near stall (high loading) to maximum flow (low loading), with the medium loading case close to the Howell [70] nominal incidence value of 0.6°. The incidence values and inlet Reynolds numbers shown in Table 4.1 were determined from

flow angle measurements obtained from 3-hole probe traverses near the centre of the axial gap between the rotor and stator rows. For these results the axial and radial velocity components were mass averaged. Errors in flow angle measurements are of the order of 0.4% (uncertainty in f_1) or 0.05° (uncertainty in α) with a constant reference angle uncertainty of ±0.2° and setting angle uncertainty of ±0.1°. The reduction in axial spacing appears to have brought about a decrease in incidence (approximately 1°) and slight increase in inlet Reynolds number for all loading cases. The change is significantly higher than could be justified by experimental error, and is also supported by the observed differences in the stator suction surface velocity distributions (see Section 4.5).

4.4.3 Deviations from 2-D Boundary Layer Flow

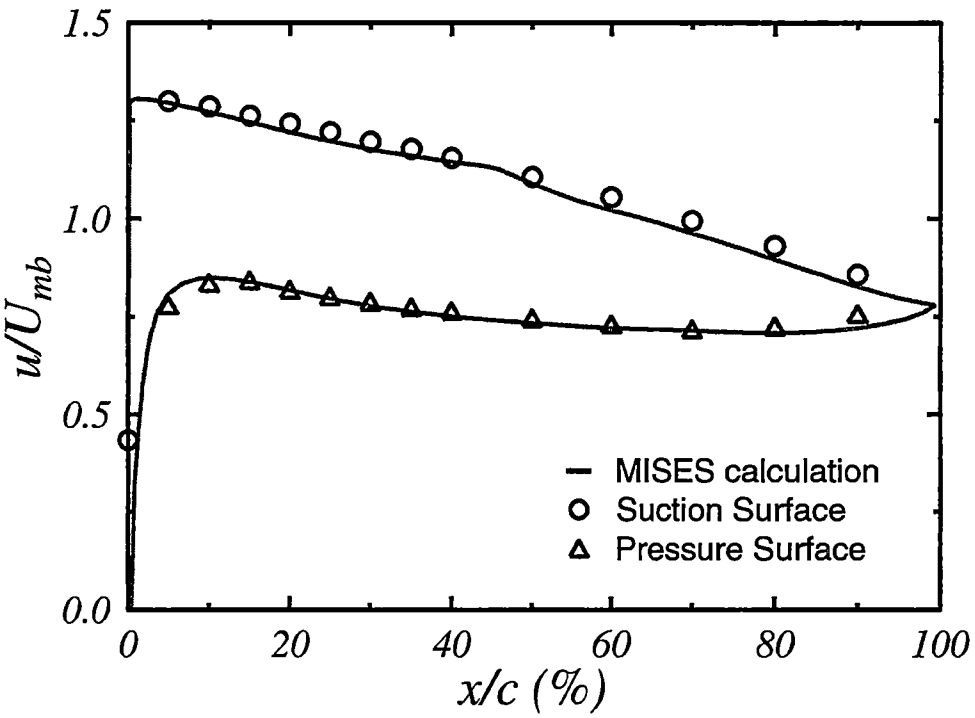

Figure 4.2: Comparison of the measured and calculated stator surface velocity distributions. $Re_{ref} = 120\ 000$, $\phi = 0.675$.

Walker [138] investigated the two-dimensionality of the flow at mid-blade height on the stator by comparing the measured boundary layer momentum thickness values with values calculated with the two-dimensional momentum integral equation using the measured surface velocity distributions. The largest discrepancy occurred at the highest incidence value ($i = 4.7°$), where the hub boundary layer separates and the difference in measured and calculated momentum thickness, at 90% surface distance, was as high as 15%. For lower incidence values, closer to the design and highest efficiency points, the comparison was in good agreement with the deviation below 5% for much of the suction surface. Flow visualisation and measurements of the axial velocity ratio both indicated a slight convergence of the bulk flow, and in absence of boundary layer

separation this was expected to resemble the departures from 2-D flow present in the blade boundary layers. Comparisons of the measured surface velocity distribution and results from the 2-D viscous/inviscid interaction code MISES (see Youngren and Drela [152]) are presented in Fig. 4.2. This further supports the near two-dimensionality of the mid-span stator flow. Both the MISES code and the surface velocity distributions are addressed in detail in later chapters

4.4.4 Experimental chapters

Table 4.2 summarises the experimental work undertaken in the current investigation. The test points are defined in terms of the reference Reynolds number Re_{ref}, flow coefficient ϕ and relative clocking position a/S. As previously discussed, the rotor speed was continuously adjusted during the acquisition of data to maintain the set point of $Re_{ref} = 120\ 000$. The throttle position was adjusted at the start of each set of measurements, such that a sixty second average of ϕ fell within a tolerance of ± 0.005 of the set point. The throttle position was not subsequently adjusted during testing.

Chapters 4–7 contain the experimental observations, with individual chapters concentrating on the following topics,

- The remainder of this Chapter details the stator blade surface velocity distributions obtained from surface pressure tappings.
- Chapter 5 details the hot-wire observations of the IGV-rotor wake interactions downstream of the rotor row. Selected results are also presented to show the wake transport through the stator blade row.
- Chapter 6 details the hot-wire observations downstream of the stator trailing edge and evaluates the blade element performance.
- Chapter 7 details the boundary layer behaviour as recorded by the stator surface-mounted hot-films.

Each chapter presents the large axial spacing observations first. Where reduced axial gap results have been recorded for similar conditions these are subsequently presented, and comparisons of the large and reduced axial spacing results are discussed.

4.5 Stator Blade Surface Velocity Distributions

The stator mid-blade height surface velocity distributions are presented for the operating conditions outlined in Table 4.1. The measurements of Solomon [123] are presented for the LAG cases: the change in incidence indicated in Table 4.1 brought about by reduction in axial spacing prompted measurements of the suction surface distribution for the RAG case. The total pressure on the stagnation streamline was estimated from 3-hole probe measurements at the mid-spacing position of both axial spacing cases.

4.5.1 Pressure tapping locations

Two separate stator blades were instrumented with surface pressure tappings: one with an array of tappings on the suction surface, the other with an array on the pressure

Table 4.2: Summary of experimental testing.

	Flow coefficient ϕ					
	0.600		0.675		0.840	
a/S	RAG	LAG	RAG	LAG	RAG	LAG
0.00	BPSS, HF HWMG, HWDS 3HPDR	HF HWRSG, HWSP HWMG, HWDS 3HPDS	BPSS, HF HWMG, HWDS 3HPDR	HF HWRSG, HWSP HWMG, HWDS 3HPDS	BPSS, HF HWMG, HWDS 3HPDR	HF HWRSG, HWSP HWMG, HWDS
0.25		HWDS 3HPDS		HWDS		HWDS
0.50	BPSS, HF HWMG, HWDS 3HPDR	HF HWDS 3HPDS	BPSS, HF HWMG, HWDS 3HPDR	HF HWRSG, HWSP HWDS	BPSS, HF HWMG, HWDS 3HPDR	HF HWDS
0.75		HWDS 3HPDS		HWDS		HWDS

BPSS Stator blade suction surface pressure tappings (Chapter 4)
HF Stator blade surface hot-film survey (Chapter 7)
HWRSG Hot-wire measurements through rotor-stator axial gap (Chapter 5)
HWSP Hot-wire measurements through stator passage (Chapter 5)
HWMG Hot-wire measurements at mid rotor-stator axial gap (Chapter 5)
HWDS Hot-wire measurements close downstream of stator trailing edge (Chapter 6)
3HPDR 3-Hole probe measurements downstream of rotor
3HPDS 3-Hole probe measurements close downstream of stator trailing edge

RAG 41.6% chord rotor-stator axial gap
LAG 106% chord rotor-stator axial gap

surface. These blades were arranged so that the measurement surfaces faced into the same flow passage. The tappings have a diameter of approximately 0.5mm, and each blade surface has an array of tappings in a matrix of 5 radial stations by 14 chordwise stations. At each chordwise station, the five radial tappings all open into the same connecting tube. Therefore, in order to perform measurements at one particular radial station the other four must be sealed with cellotape. Only the tappings at the mid-blade height radial station were used for the results presented. In the streamwise direction the tappings are spaced at 5% chord intervals for the first 40% of chord and then at 10% chord intervals, with the last tapping located at 90% chord. Appendix B provides the locations of the mid-blade height tappings in both graphical and tabular form.

4.5.2 Experimental detail

The experimental methodology for obtaining the surface pressure distributions is outlined below. The time constant for the pressure measuring apparatus (including transducing system, Scanivalve and connecting tubes) was determined by observing the 99.9% settling time as the system was stepped between adjacent ports with the largest pressure differential. Once determined, a minimum time delay equivalent to twice the settling period was employed between measurements at each Scanivalve port. For the LAG cases (reported by Solomon [123]), the pressure at each port was read 30 times at a rate of 6 Hz and the average and RMS values recorded. Minimisation of the low frequency fluctuation effects (see Section 3.5) was achieved by repeating the measuring process 12 times. For the RAG cases, the pressure at each port was read 180 times at a rate of 6 Hz and again the average and RMS values recorded. In this case the measurement process was repeated 4 times. The experimental uncertainty was determined by combining the instrumentation uncertainty and the standard deviation of the readings. For the LAG medium loading case the uncertainty in C_p was in the range 0.1%–0.2% over the pressure surface and 0.1%–0.4% on the suction surface. For the equivalent RAG case, the uncertainty was 0.1%–0.2% over the suction surface. The 40% chord station was an exception in both cases, where the uncertainty was 1.7% and 0.6% for the respective cases. This location shows a large relative uncertainty because the mean pressure differential is close to zero.

4.5.3 Calculation of surface velocity distributions

To calculate the surface velocities the total pressure on the stagnation streamline is required. The 3-hole probe measurements midway between the rotor and stator rows were used to determine the flow direction and thus the location of the stagnation streamline. Solomon [123] compared the total pressure coefficient as determined from measurements with a United Sensor KBC Kiel probe with the results obtained for the 3-Hole probe. The 3-hole probe exhibited twice the uncertainty (0.5%) of the Kiel probe, but for measurements at the mid-station between blade rows the results were in good agreement. Calculations were also performed with the MISES two-dimensional flow solver of Youngren and Drela [152], to estimate the amount of curvature of the stagnation streamline between the measuring station and the stator stagnation point. It was determined that the error in locating the stagnation streamline direction from the inlet air angles was below 1.5° for the cases of interest. This converted to a max-

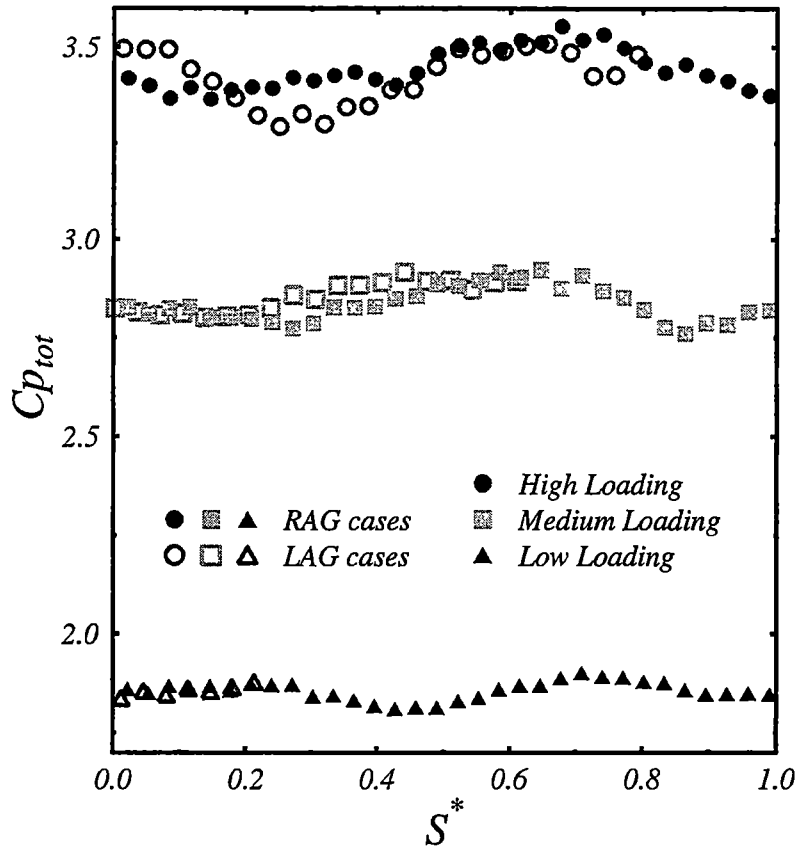

Figure 4.3: Pitchwise variation of total pressure coefficient Cp_{tot} with loading for both axial row spacing configurations. Open symbols represent LAG cases. Closed symbols represent RAG cases. 3-hole probe measurements 15.8 mm and 41.0 mm upstream of stator leading edge for the two respective cases.

imum likely error in determining Cp_{tot} of 0.3%. The total pressure coefficient values obtained from the 3-hole probe measurements are presented in Fig. 4.3. The open symbols represent the LAG cases; the closed symbols represent the RAG cases. Although the two spacing configurations are compared in Fig. 4.3 on a common datum relative to the IGV wake street, the results were obtained near the centre of the axial gap and therefore at different distances relative to the rotor trailing edge. As the loading increases there is a noticeable difference between the two spacing cases. Wake-wake interaction (see Chapter 5) and rotor wake decay phenomena, which are both loading dependent, contribute to the increasing difference in total pressure coefficient curves with increased loading.

The surface pressures were measured relative to the inlet static pressure p_{in} and can be expressed as pressure coefficients relative to the machine inlet dynamic pressure,

$$Cp_i = \frac{p_i - p_{in}}{P_{in} - p_{in}} \tag{4.1}$$

With the value of Cp_{tot} determined, the surface velocity distributions were calculated

from,

$$\frac{u}{U_{mb}} = \phi\sqrt{Cp_{tot} - Cp_i} \tag{4.2}$$

4.5.4 Surface velocity distributions

The corresponding surface velocity distributions obtained for the large axial spacing configuration are shown in Fig. 4.4. This figure highlights the effects of incidence on the blade surface velocity at constant Re_{ref}. In general the C4 blade exhibits a peak velocity closer to the leading edge than more modern blade profile shapes. For the high and medium loading cases presented, the peak suction surface velocity occurs within the first 5% of chord. This is followed by a roughly linear deceleration to the trailing edge. For the medium loading case, viscous/inviscid coupled blade-to-blade calculations (reported Solomon et al. [127]) indicate the presence of a short laminar separation bubble with separation and reattachment at s^* =0.54 and s^* = 0.57 respectively. This is experimentally supported by the low-speed cascade results of Blight and Howard [12] and the measured time-mean boundary layer profiles reported by Solomon [123]. In the low loading case the suction surface distribution exhibits a plateau which peaks much further rearward near 30% chord; a discontinuity in velocity gradient around 70% chord indicates the development of a mid-chord laminar separation bubble. China clay visualisations and steady flow laminar boundary layer calculations performed by Walker [138], for similar operating conditions, confirm the presence of the mid-chord laminar separation bubble for the low loading case.

The stator pressure surface velocity distributions all show a deceleration over the forward part of the blade, followed by an acceleration towards the trailing edge. The deceleration is very mild for the high loading case, but progressively strengthens as incidence is decreased. For the low loading case, the velocity gradient becomes severe enough to cause a leading edge laminar separation bubble.

The velocity distributions in Fig. 4.4 were measured with the IGV trailing edge and stator leading edge at the same circumferential location. There is a variation in the clocking position (a/S) relative to the upstream wake street if the relative blade positions are not altered with loading. Solomon [123] measured changes in the velocity distribution of $\pm 1.5\%$ u/U_{mb} at $s^* = 0.6$ (the approximate location of the separation bubble) as the IGV row was clocked over one blade pitch at medium loading. Tests of the same blade section by Blight and Howard [11] in a two-dimensional cascade under steady flow conditions with an inlet turbulence level of 0.2% showed a greater development of separation on the suction surface at incidences close to the medium and low loading cases.

The blade containing the pressure side tappings was replaced by a blade with the hot-film array attached. The RAG suction surface pressure distributions were obtained at the end of the experimental programme, and time considerations prohibited a complete rebuild of the machine necessary to remove the hot-film instrumented blade and reinstall the pressure-side tapped blade. Relevant information obtained from changes in the suction surface distribution supported testing without the pressure side blade installed. The suction surface velocity distributions for the RAG case are presented in Fig. 4.5, and compared with the LAG results from Fig. 4.4. Initial leak testing of

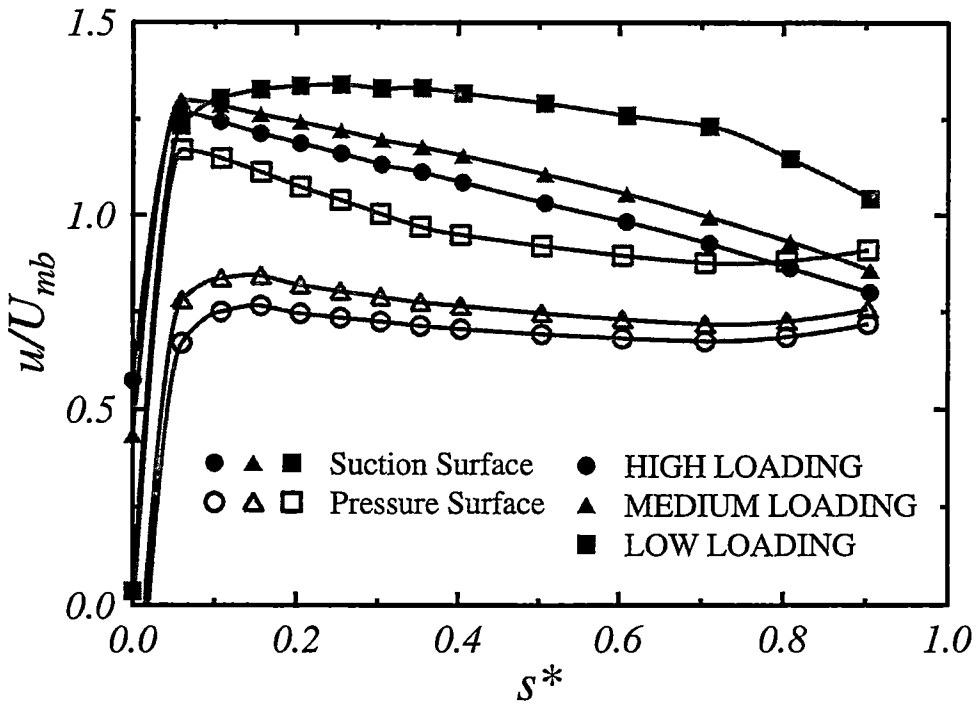

Figure 4.4: Variation of stator blade surface velocity distribution with loading at mid-blade height. Large axial spacing configuration. $Re_{ref} = 120000$.

the pressure measuring system revealed sealing difficulties associated with the tappings located along the 30%c station. The results from this location show variation much greater than can be attributed to experimental uncertainty and have consequently been omitted. Solomon [123] reported a similar, but much less significant, discontinuity in surface velocity at the same location and attributed this to either a change in blade surface curvature associated with the C4 defining polynomials or an irregularity with this particular tapping.

Results are presented for both the a/S= 0.00 and 0.50 clocking cases. Changes in surface velocity distribution with reduction in axial row spacing over the forward part of the blade are small. The greatest difference (6.8% u/U_{mb}) occurs at the 90% chord tapping position for the high loading case. There is minimal difference in the results for the two clocking cases, which is consistent with the clocking results of Solomon [123] for the LAG test cases. Hot-film surveys (see Chapter 7) indicate that there is a general trend for transition to move forward with reduction in axial row spacing and consequently the turbulent boundary layers are thicker towards the trailing edge. For the high and medium loading cases the displacement effects of the thicker boundary layers accelerate the bulk flow, and contribute to the increasing difference in the velocity distributions as the trailing edge is approached. For the low loading both clocking cases for the RAG results lie under the LAG results, indicating a reduction in blade lift consistent with the measured reduction in blade incidence. Detailed examination of the low loading results also show a general trend for the severity of the mid-chord separation bubble to decrease with both axial row spacing and blade clocking. This is discussed in further detail in Chapter 7.

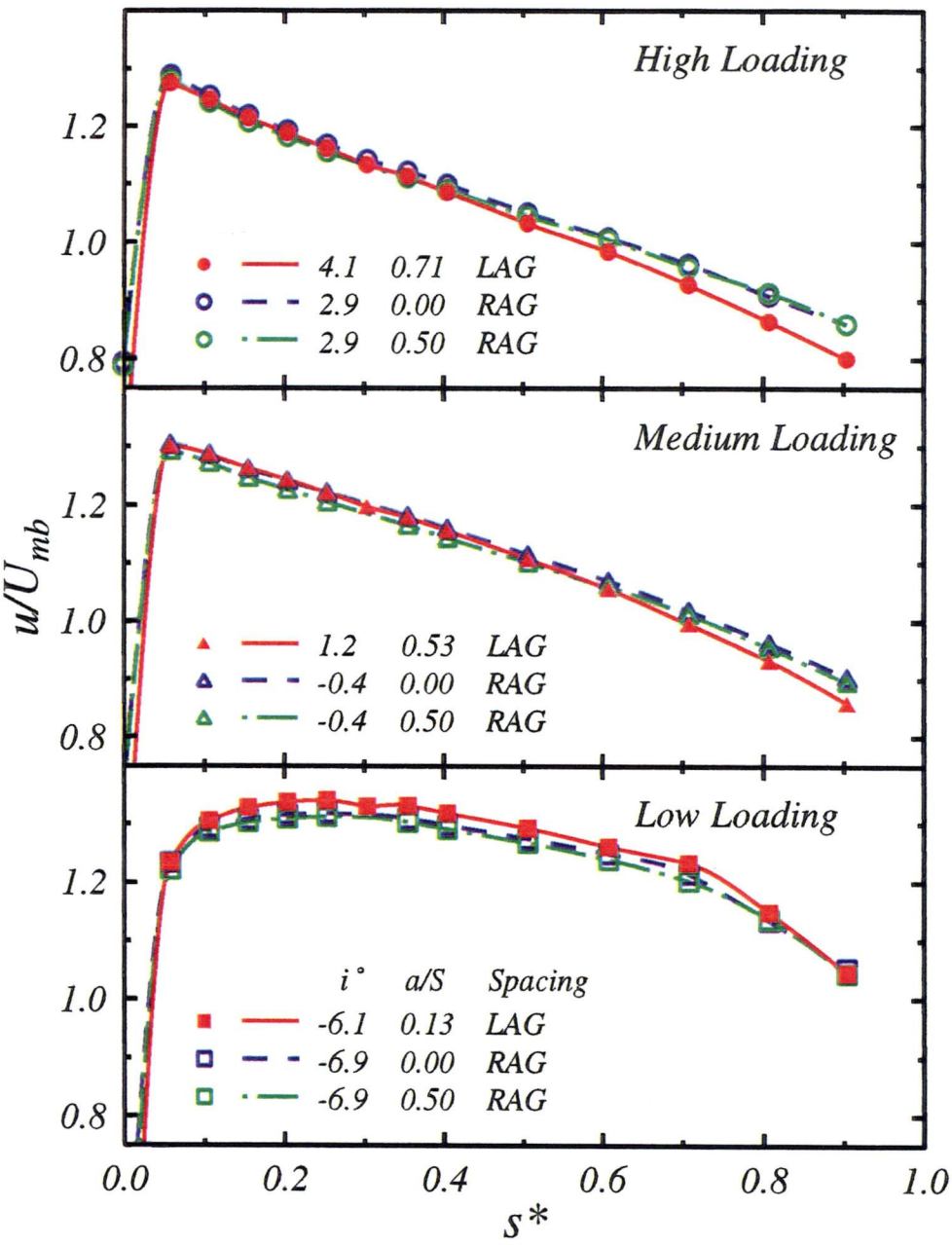

Figure 4.5: Variation of suction surface velocity distribution with blade loading and axial row spacing. LAG = 106% c rotor-stator axial gap. RAG = 41.6% c rotor-stator axial gap.

The range of pressure distributions presented encompass the design conditions for modern high-pressure compressor airfoils, which typically exhibit a well-rounded suction peak around 20% chord. (See the baseline compressor case 2B reported by Halstead et al. [58].) The suction surface velocity distribution for the high loading case of the present investigation is quite similar to that for the near stall case of Halstead et al. [58]. Hence the results should still give useful indications of the importance of unsteady flow effects for modern compressor blade sections, despite the blade section tested being of an older generation,

Chapter 5

Rotor Wake Measurements

5.1 Introduction

During the design of a multistage axial compressor, blade boundary layer calculations are generally performed using a boundary layer code (integral or differential) coupled to an inviscid flow solver. It is not uncommon for a single turbulence intensity, constant in time, to be used to describe inflow turbulence characteristics. This stems from the fact that measurements of the turbulence levels experienced by gas turbine engine blading are difficult to make and are not widely available. It is generally accepted that turbulence levels are high enough that the dominant mode of transition for attached boundary layers is bypass transition (see Mayle [93]). Boundary layer codes generally employ correlations such as those of Abu-Ghannam and Shaw [1] or Mayle [93] to predict the onset of bypass transition. The unsteadiness associated with the relative motion of the neighbouring blade rows is generally ignored, or at best accounted for by artificially raising this single turbulence level. In order to calculate the periodically unsteady blade boundary layers, the variation of freestream turbulence level over a blade passing cycle is needed. This information combined with the mean in-flow angle and velocity are the minimum requirements to perform an unsteady boundary layer calculation, at least on a quasi-steady basis. For a full unsteady calculation a complete description of the time variance in inflow conditions would be required. This would include the periodic variation in turbulence level (and possibly length scale), flow angle and velocity.

This chapter investigates the flow downstream of the rotor blade row in order to quantify the stator inlet flow field. In particular, the interaction processes between the wakes of the IGV and rotor blade rows are studied in detail. The data obtained extends the work of Lockhart and Walker [88] by providing quantitative information on the development of the periodic and random disturbance fields downstream of the compressor stage. As mentioned, these data are an essential prerequisite for the prediction of periodic transition phenomena in a following blade row, as the work of Halstead et al. [58, 59, 60, 61] indicates. The development of circumferential variations in the time-mean flow associated with these wake interaction processes and their importance relative to the mean flow variations resulting from intra-stator transport of rotor wake fluid as described by Kerrebrock and Mikolajczak [79] is also addressed.

Table 5.1: Axial locations of pitchwise hot-wire traverses, for the medium-loading. Large Axial Gap case. LE = Leading Edge, TE = Trailing Edge.

	Rotor-Stator Gap							
Station	1	2	3	4	5	6	7	8
%chord Axially Down-Stream of Rotor TE	4.6	7.5	16.6	26.8	40.2	53.7	70.1	88.6
	Stator Passage							
Station	9	10	11	12	13	14	15	
%chord Axially Down-Stream of Stator LE	0.2 SLE	10.3	25.7	50.3	75.6	87.0 STE	101.4	

5.2 Range of Investigation

The unsteady rotor outlet flow field was investigated through hot-wire pitchwise measurements acquired at fifteen axial stations varying from 4.6% chord axial distance downstream of the rotor trailing edge, through to 14.4% chord downstream of the stator trailing edge. Table 5.1 gives the location of each pitchwise traverse station measured axially relative to the rotor trailing edge or stator leading edge (normalised by true chord) for the LAG configuration. Detailed measurements for the medium loading condition are presented. Measurements were also obtained for the RAG configuration, but only at a station located at approximately the mid-point of the rotor-stator axial gap.

For the measurements in the rotor-stator gap, a Disa 55P03 type hot-wire probe (see Fig. 3.7) was positioned with the sensing axis aligned with the stator trailing edge, and was supported by a mounting tube aligned in the radial direction. For measurements inside the stator passage a 55P01 type probe was supported downstream of the stator row by a mounting tube aligned in approximately the local flow direction. The only exceptions were data acquired at the stator leading edge, where a 55P01 type probe was orientated with the mounting tube approximately normal to the local flow direction. In all cases the probes were calibrated and operated with the sensing wire in the same orientation. The probe was traversed across one blade pitch at mid-blade height. A total of 32 evenly spaced measurement positions was used across a single stator passage.

5.3 IGV Wake Dispersion by Rotor

The variation of IGV wake dispersion with flow coefficient, obtained from a circumferential hot-wire traverse immediately downstream of the rotor, is shown in Figs. 5.1 and 5.2. These data were acquired by moving the IGV and stator rows together at a fixed circumferential offset ($a/S = 0.0$). This was done as a precaution even though previous measurements had shown no measurable influence of the stator circumferential position on the unsteady flow field at this station. Data were obtained over one IGV pitch only, but have been plotted over two blade pitches by assuming pitch-wise pe-

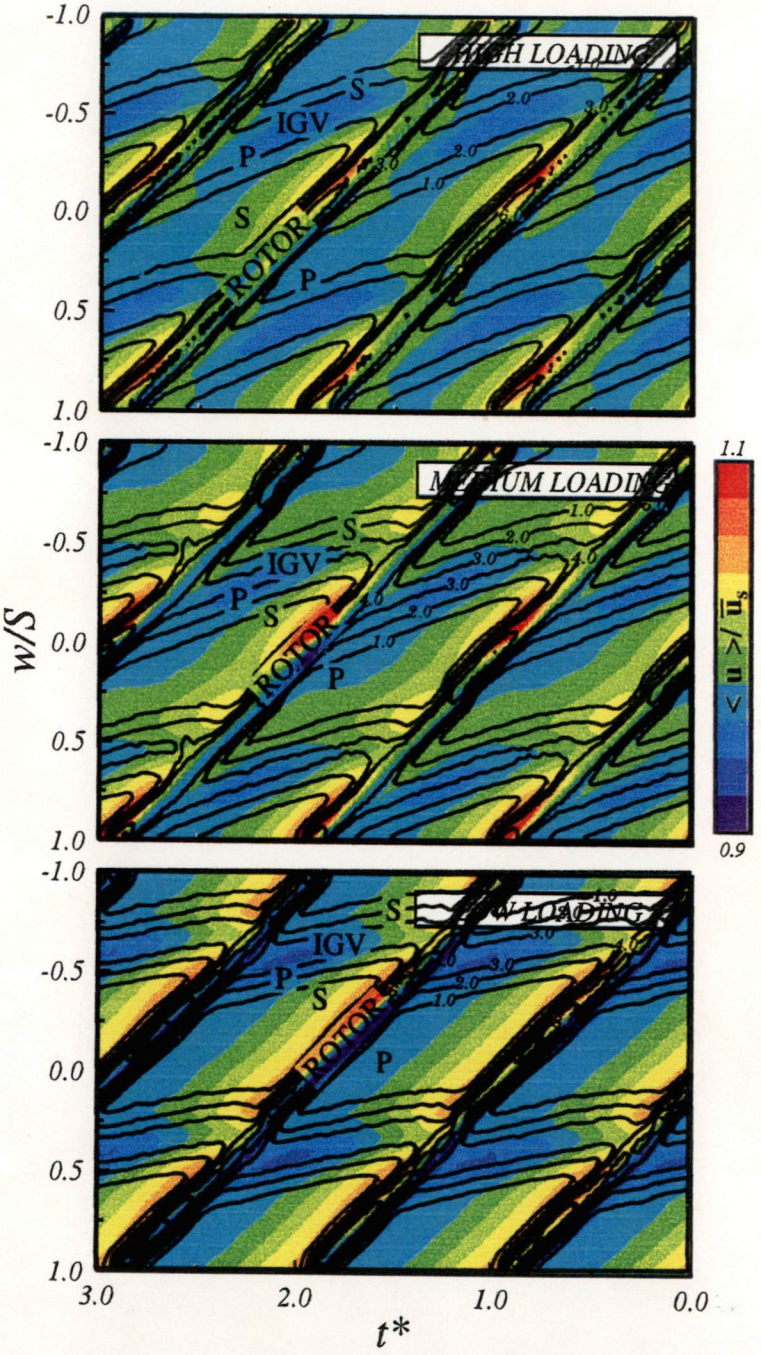

Figure 5.1: Contours indicate ensemble average turbulence level, $<Tu>$ (%). This figure may be used as an overlay for Fig. 5.2. S = suction side; P = pressure side.

Figure 5.2: Variation of IGV wake dispersion with flow coefficient. Hot-wire measurements 4.6% chord axially downstream of rotor trailing edge at mid-passage. Colour contours indicate non-dimensional ensemble average velocity $<u>/\overline{u}_s$. LAG case, ϕ = 0.675, Re_{ref} = 120 000.

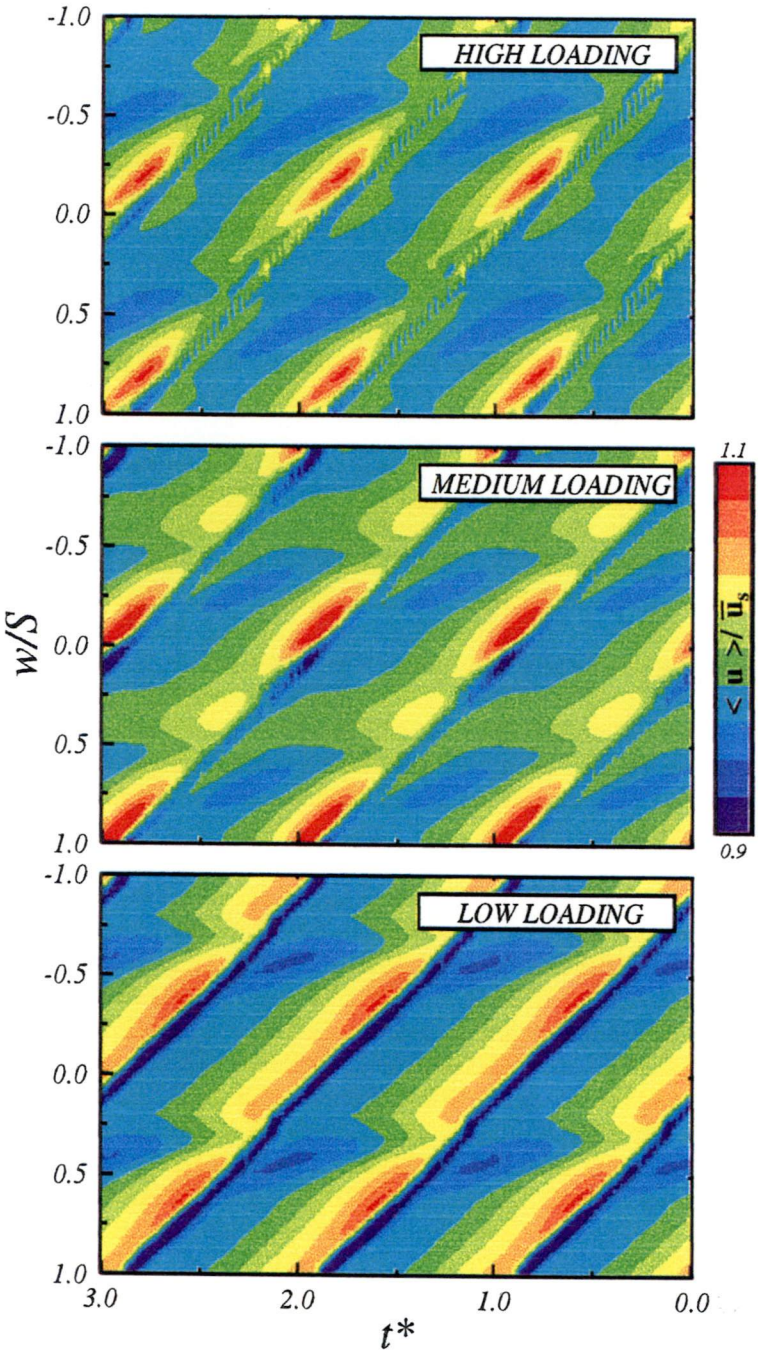

Figure 5.2: Variation of IGV wake dispersion with flow coefficient. Hot-wire measurements 4.6% chord axially downstream of rotor trailing edge at mid-passage. Colour contours indicate non-dimensional ensemble average velocity $<u>/\overline{u}_s$. LAG case, $\phi = 0.675$, $Re_{ref} = 120\ 000$.

riodicity. Ensemble average velocity $<u>$ (non-dimensionalised by pitch-wise average time-mean velocity $\overline{u}_s$) is indicated by the colour shading. These figures represent the instantaneous spatial distribution which would be observed on a cylindrical surface if the flow disturbances were convected unaltered downstream of the measuring station with zero whirl. The variable w/S on the axis represents dimensionless circumferential position relative to the inlet guide vanes: w is measured relative to the IGV trailing edge in the pitchwise direction (see Fig. 4.1). The non-dimensional time t^*(relative to the rotor blade passing period) on the abscissa has been plotted in the reverse direction so that the earliest observed points appear at the right, corresponding to the furthest downstream axial position. The data have been time-shifted to make the rotor-IGV relative circumferential position constant at a particular values of t^* for each probe relative position w/S. This is necessary because the IGV was clocked relative to the trigger point which was fixed relative to the machine and the probe.

The line contours in Fig. 5.1, which may be used to overlay the velocity field measurements of Fig. 5.2, indicate ensemble average values of random velocity fluctuations about the ensemble mean (or "turbulence") $<Tu>$. The rotor wakes can be identified as the parallel bands of high turbulence running diagonally from bottom left to top right as in Fig. 4.1. The avenue of dispersed IGV wake segments runs horizontally from left to right. This differs from the picture in Fig. 4.1 because whirl velocity has been ignored. The suction and pressure surface sides of both IGV and rotor wakes (indicated by symbols S and P) are at the top and bottom of the wake regions, respectively. Selected contours of 1, 2, 3, 4, 6, and 8% $<Tu>$ have been labelled to aid the interpretation of the results.

The rotation of the IGV wake segments relative to the local flow direction increases with rotor blade loading as the flow coefficient is decreased from 0.840 to 0.600. The curvature of the IGV wake segments near the suction side of the rotor wake indicates a retardation of flow by the rotor suction surface boundary layer, which can be seen to thicken as loading is increased. This feature is very similar to the numerical predictions of Deregel and Tan [28]. The peak turbulence level in the IGV wakes is about 3%, whilst the minimum turbulence level in the free-stream (corresponding to inflow regions uncontaminated by wakes) is about 0.5%.

The rotor wakes exhibit periodic variations in thickness indicative of blade loss fluctuations, and gradually thicken as loading is increased (as indicated by separation of the turbulence contours). There is a strong gradient in ensemble average velocity across the rotor blade passage at $\phi = 0.840$. This decreases as loading is increased, and is evidently a potential flow effect. A common feature observed at all loadings is a region of higher velocity in the corner between the suction side of the rotor wake and the pressure side of the IGV wake segment. This may be partly due to the negative jet effect of the relative flow in the IGV wake. The higher rotor wake turbulence level at low loading (which may appear anomalous) is thought to result from the proximity of the suction surface transition zone to the rotor blade trailing edge.

5.4 IGV-Wake Rotor-Wake Interactions

The dispersion of IGV wakes by the rotor row and their subsequent interaction with the rotor blade wakes, as observed from circumferential hot-wire traverses at four ax-

ial stations between 4.6% and 26.8% chord downstream of the rotor, are shown in Figs. C.1–C.8 (See Appendix C). Fig. C.3 shows a consistent gradient in ensemble average velocity across the rotor blade passage at 4.6% chord downstream of the trailing edge which is evidently a potential flow effect. The gradient weakens with increasing axial distance downstream of the rotor until it is no longer apparent in Fig. C.8. As previously mentioned, the region of higher velocity in the corner between the suction side of the rotor wake and the pressure side of the IGV wake segment may be partly due to the viscous negative jet effect of the relative flow in the IGV wake. However, the fact that this feature extends outside the viscous wake regions (identified by values of random disturbance $<Tu>$ significantly higher than background levels) suggests that it is largely a potential flow effect associated with fluctuating lift on the rotor. The persistence of this phenomenon with increasing distance downstream shown in Figs. C.3–C.8 is indicative of shed vorticity. The dominant viscous flow effect downstream of the rotor is the accumulation of low energy fluid within the rotor wakes on the suction side of the IGV wake street. This feature is little evident in Fig. C.3, but develops rapidly with increasing distance downstream where it is visible as a patch of low ensemble average velocity in Figs. C.7 and C.8.

Adjacent to the contour plots of ensemble average velocity and turbulence in Figs. C.3–C.8 are the circumferential distributions of dimensionless time-mean velocity $\overline{u}/\overline{u}_s$ and the random, periodic and total disturbance levels Tu, $\widetilde{Tu}$ and Tu_D. To show more clearly the flow development downstream of the rotor, the respective plots for different axial positions have been superimposed in Fig. 5.3, with the origin for circumferential position shifted to the local centre of the IGV wake street. The mean velocity shows a significant reduction around $w/S_{IGV} = 0.6$ where low energy rotor wake fluid is accumulating on the suction side of the IGV wake street. This accumulation appears largely due to turbulent mixing from adjacent IGV wake segments reducing the rotor wake velocity defect around $w/S_{IGV} = 0.0$ and restricting the relative flow towards the rotor trailing edge within the rotor wakes. The restriction also causes a slight increase in mean velocity on the pressure side around $w/S_{IGV} = 0.3$. By the station 26.8% chord downstream of the rotor, a circumferential variation in time-mean velocity of around 4% has developed due to the IGV wake-rotor wake interaction. The circumferential distribution of random disturbance level Tu varies between a minimum of about 1% between the IGV wakes and a maximum of about 3% in the centre of the IGV wake street. There is a general slight increase in Tu with axial distance downstream of the rotor. This is more noticeable around $w/S_{IGV} = 0.7$ where the rotor wake fluid accumulates and some inflow of IGV wake fluid may also be occurring.

The total disturbance level Tu_D is dominated by the periodic disturbance component $\widetilde{Tu}$, and the circumferential distributions of these two quantities are closely similar at all axial stations shown in Fig. 5.3. Note that the local peak values of Tu_D and $\widetilde{Tu}$ correspond to circumferential positions where there is a lower time-mean velocity due to local accumulation of low energy fluid within the rotor wakes. A marked circumferential variation in $\widetilde{Tu}$ is already evident at the station closest to the rotor trailing edge. The peak value of $\widetilde{Tu}$ occurs around $w/S_{IGV} = 0.3$, and cannot be explained simply in terms of fluctuating rotor wake thickness (which reaches a maximum around $w/S_{IGV} = 0.5$). Other factors such as potential flow effects of rotor circulation and thickness, and unsteady energy transfer (vortex shedding) must be involved. The viscous effect

of low energy fluid redistribution within the rotor wakes causes a rapid increase in $\widetilde{Tu}$ around $w/S_{IGV} = 0.6$ and probably contributes to the equally rapid decline in $\widetilde{Tu}$ around $w/S_{IGV} = 0.3$ with increasing distance downstream.

Fig. 5.4 shows snapshots of the instantaneous ensemble average velocity and turbulence fields over a rotor blade passing cycle, similar to Fig. 4.1. There are five sub-figures evenly spaced at intervals of $t^* = 0.2$, with the correct sequence indicated by the large inter-connecting arrows. Each of these sub-figures was generated by interpolating the velocity and turbulence measurements between the 15 pitchwise traverse stations outlined in Table 5.1. The axial station positions relative to the rotor and stator blade rows are indicated by the small arrows along the top of the first sub-figure. The colour shading again indicates non-dimensional ensemble average velocity ($<u>/\overline{u}_s$), with overlaid line contours indicating the random turbulence level ($<Tu>$). This information is similar to that presented in Figs. 5.1 and 5.2, except the time based abscissa has now been replaced with the machine axial position. The rotor blade trailing edge and stator blade leading and trailing edge positions are clearly indicated. The relative pitchwise position of the blade rows at each instant of time is also indicated. The direction of the rotor blade row motion is down the page.

The boundaries of the IGV and rotor wake regions are easily identified from the $<Tu>$ contours. By starting at the rotor trailing edge and simultaneously increasing both downstream axial distance and circumferential distance in phase with rotor passing, the development of a low velocity region associated with low energy fluid accumulation can be traced. This accumulation is easily identified by the dark blue colour shading (indicating low ensemble average velocity) and high turbulence levels inside the rotor wake. At $t^* = 0.0$ a well developed accumulation is located at approximately 65% of the rotor-stator gap. There is a region of higher velocity near the rotor wake suction side and IGV wake pressure side intersection. It is most evident in sub-figures $t^* = 0.2$ and $t^* = 0.4$ at approximately the 30% rotor-stator gap position and is indicated by a small patch of yellow colour shading. This feature is thought to be associated with vortex shedding. As previously noted in conjunction with Figs. C.1–C.8 it clearly extends outside the viscous wake region. A paired vortex of opposite sign would also be expected but this cannot readily be identified. It could be that this occurs in conjunction with the low energy fluid accumulation caused by convective effects.

The segmentation and rotation of the rotor wake by the stator blade row is clearly evident in Fig. 5.4. This mechanism is identical to that discussed in Section 5.3 with respect to the IGV-wake rotor-blade interaction. At stator outlet there is a tendency for high turbulence fluid to accumulate on the stator pressure surface, although the mechanism for this appears to take place inside the rotor-stator axial gap, rather than inside the stator passage. Chapter 6 shows that the location of this low energy fluid at stator outlet is highly dependent on relative IGV wake street position, and therefore the mechanism of intra-stator transport of rotor wake fluid described by Kerrebrock and Mikolajczak [79] appears to be relatively weak in this case.

5.5 Length Scale Measurements

As the understanding of wake/blade boundary layer interaction (and subsequent boundary layer development) increases, more advance CFD modelling techniques will require

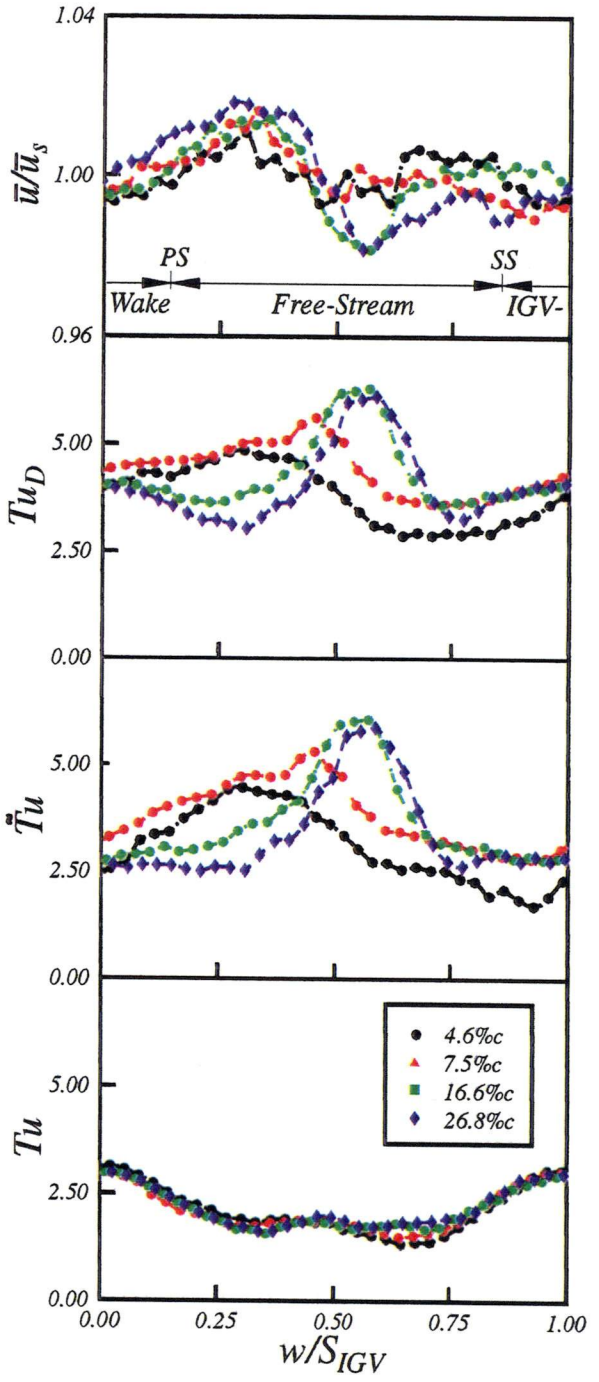

Figure 5.3: Time-mean and unsteady flow development downstream of rotor. Superposition of Figs. C.3–C.8 results with origin for circumferential position at local centre of IGV wake street. SS = Suction Side, PS = Pressure Side.

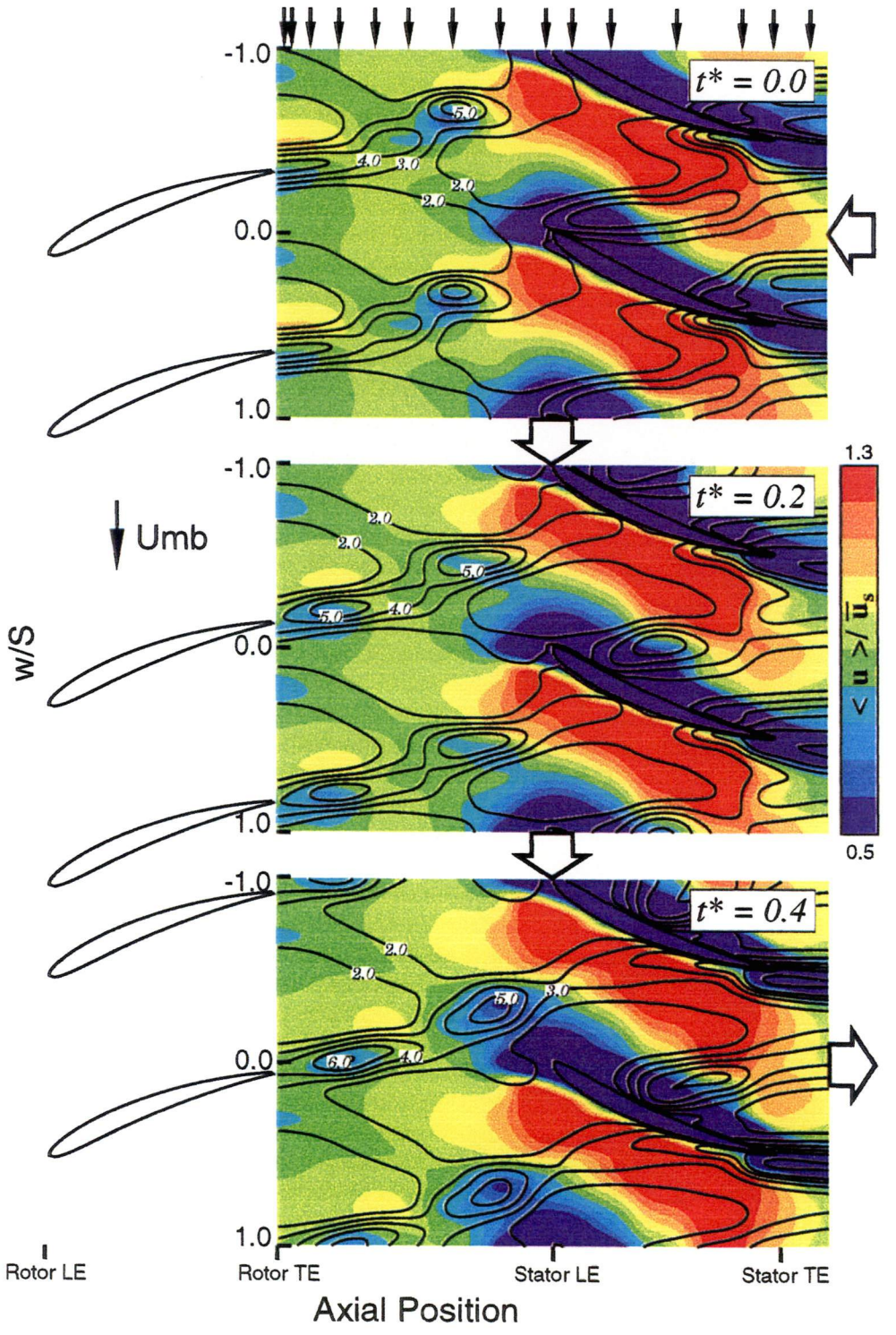
t* = 0.0
t* = 0.2
t* = 0.4
-1.0
0.0
1.0
Umb
w/S
1.3
0.5
$\overline{u}_s / < u >$
Rotor LE
Rotor TE
Stator LE
Stator TE
Axial Position

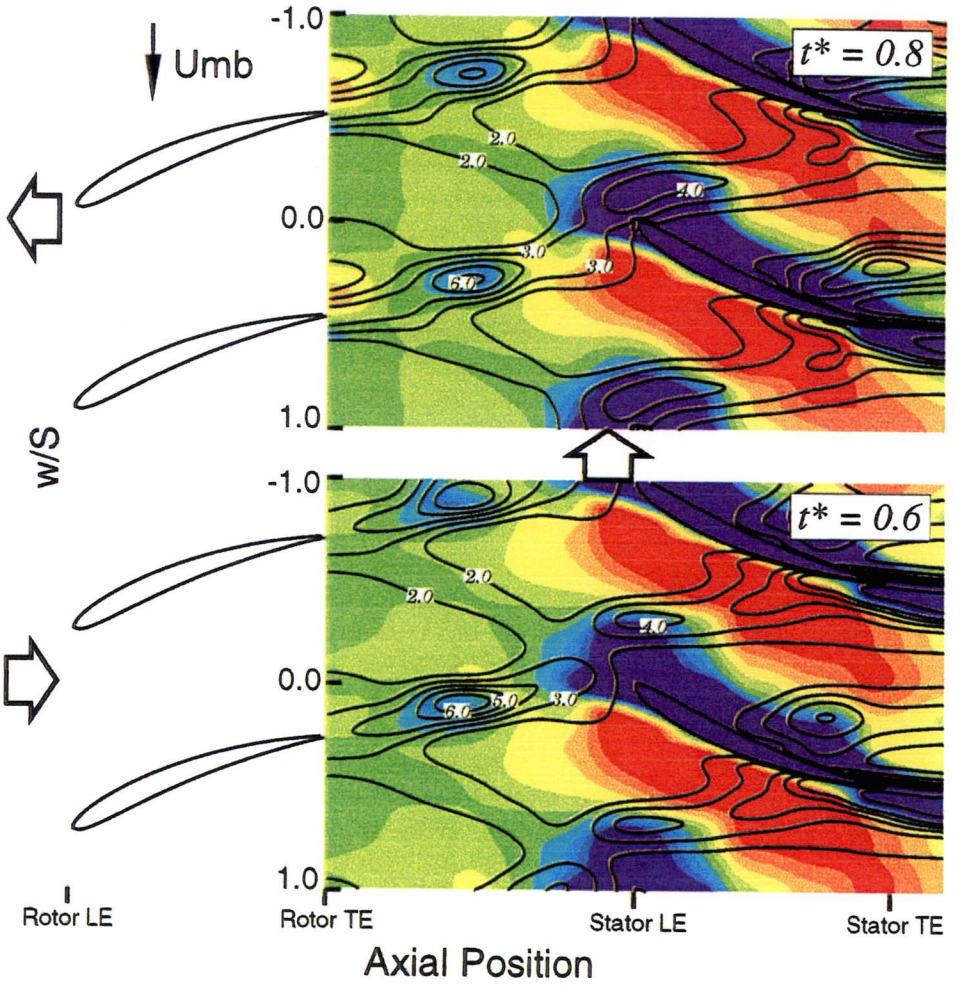

Figure 5.4: Cycle of instantaneous ensemble average velocity ($<u>/\overline{u}_s$: colour shading) and turbulence ($<Tu>$: line contours) fields over a rotor blade passing period. Snapshots at 20% of rotor passing period ($t^* = 0.2$). Sequence direction indicated by the large arrows. Small arrows at top of first sub-figure indicate measurement planes. LAG case, $\phi = 0.675$, $Re_{ref} = 120\ 000$.

more detailed specification of the inflow turbulence field. Mayle [95] speculates that both the freestream turbulence level and length scale directly influence the turbulent spot production rate and therefore the transition process. Camp and Shin [19] present a method for separating the blade passing components from the turbulent fluctuations, thus allowing the calculation of turbulent intensities and length scales in multistage compressors.

The length scales both upstream and downstream of the stator blade row have been calculated using a method similar to Camp and Shin [19], and an overview of the procedure follows. The integral length scale can be calculated assuming Taylor's hypothesis and using the autocorrelation function (ACF) of a single velocity signal to determine the integral time scale. The autocorrelation is given by,

$$ACF(\tau) = \frac{\frac{1}{\Delta T}\int_0^{\Delta T} u(t)U(t+\tau)dt}{\frac{1}{\Delta T}\int_0^{\Delta T} u^2(t)dt} \tag{5.1}$$

where ΔT is large compared to the period of the lowest frequency component of the signal. The integral length scale is then calculated by integrating the autocorrelation function with respect to the time lag (τ), which is multiplied by the mean velocity to give the length scale.

$$Integral\ Length\ Scale = \overline{u}\int_0^{\infty} ACF(\tau)d\tau \tag{5.2}$$

Since the autocorrelation of a periodic signal is itself periodic, the components of the velocity signal at the rotor blade passing (and its harmonics) must be removed by digital filtering prior to the calculation of the autocorrelation function. In practice the upper limit for the integration of Eqn. (5.2) was modified to be the first zero crossing.

Camp and Shin [19] used 'long' continuous dataset which covered a minimum of 50 rotor blade passing periods to evaluate the turbulent length scales. For the current work a continuous dataset was constructed from the 'short' sets of ensemble data previously acquired, which typically covered just over 6 rotor blade passing periods and were repeated 512 times. Only an integer number of rotor passing periods from each ensemble dataset was added to form a 'long' semi-continuous dataset. Datasets which covered more than 1500 rotor passing periods were easily constructed using this method. A limited number of 'long' datasets were also acquired by continuous sampling over the same number of blade passing periods. These were used to confirm that the uncertainty introduced by piecing together the semi-continuous datasets was less than the measurement variability seen in the results from the continuous datasets.

The turbulent intensity and length scale measurements for the current machine have been superimposed on Camp and Shin's original figures in Figs. 5.5 and 5.6. The University of Tasmania compressor is indicated by the open symbols, whereas the previously measured machines are indicated by the closed symbols. The turbulent intensity is generally lower than has been calculated for the third stator row in the other machines; but it must be remembered that the measurements were obtained in the neighbourhood of first stator row. As indicated in Fig. 5.4, there still exist regions of freestream fluid which are uncontaminated by upstream wakes at the stator inlet.

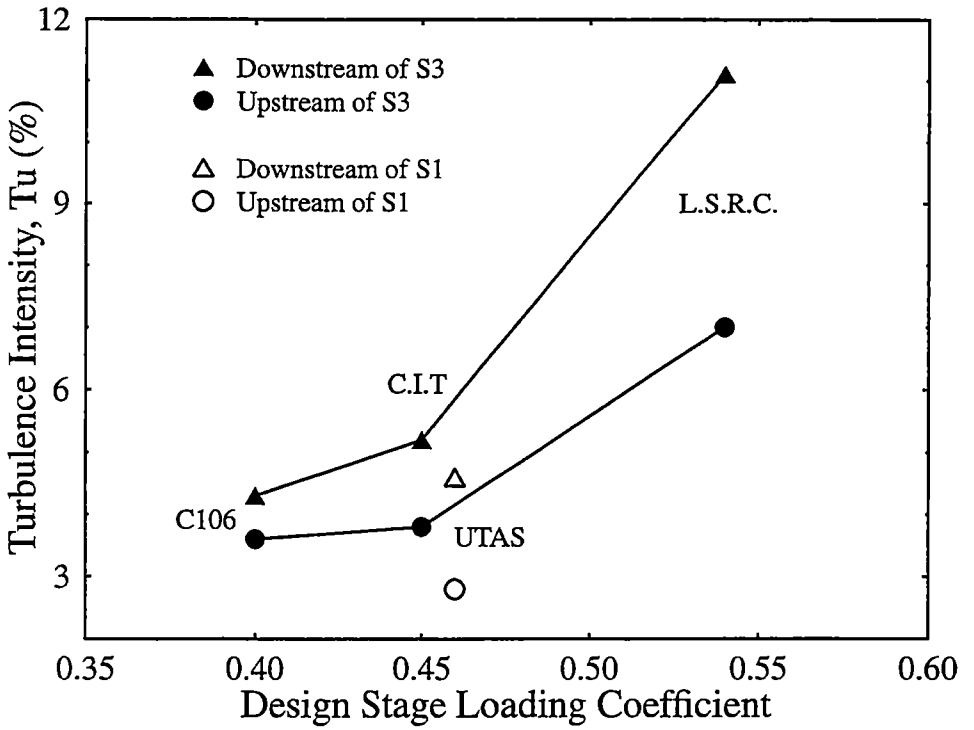

Figure 5.5: Turbulence intensity as a function of design stage loading coefficient. Fig. 6 from Camp and Shin [19] with the results for the current machine superimposed. UTAS = University of Tasmania Compressor - Hobart, C106 compressor = Whittle Laboratory - Cambridge University, CIT = Cranfield Institute of Technology compressor - Cranfield, LSRC = Low-Speed Research Compressor - General Electric

At locations further rearward in the machine the general turbulence level would rise due to the mixing of wakes from upstream blade rows. Fig. 5.6 shows the comparison of the length scale measurements. The data plotted for the current machine differs slightly from the Camp and Shin results as it is the pitchwise average length scale, rather than the results from one pitchwise location only. The pitchwise averaging will tend to reduce the length scale, particularly in the region downstream of the stator trailing edge where the average eddy size in the stator wake (which is around 2% of chord) is much lower than the freestream. Even accounting for a slight reduction in the length scale due to the averaging process, the comparison is nevertheless encouraging.

5.6 Conclusions

The dispersion of inlet guide vane wakes by the rotor, and subsequent interactions between the IGV and rotor blade wakes, produced regular circumferential variations in both the time-mean and unsteady flow downstream of the rotor blade row. Accumulation of low energy rotor wake fluid near the suction side of the IGV wake street developed rapidly downstream of the rotor trailing edge. For a multistage axial machine this mechanism of circumferential flow redistribution should dominate over the

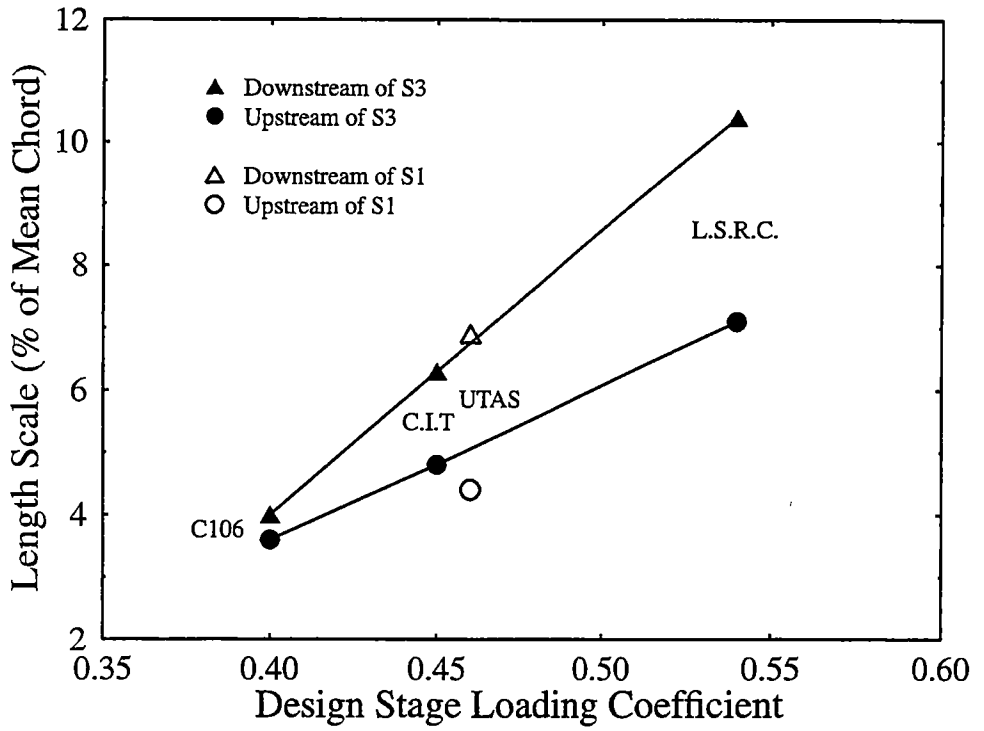

Figure 5.6: Length scale as a function of design stage loading coefficient. Fig. 7 from Camp and Shin [19] with the results for the current machine superimposed.

interception of wake fluid by the surfaces of downstream blade rows as described by Kerrebrock and Micolajczak[79].

The (time-averaged) total disturbance level Tu_D downstream of the rotor reached values of 6% in regions outside the IGV wake street. However, the unsteady flow field was largely dominated by the periodic disturbance component $\widetilde{Tu}$ and the random disturbance level Tu was much lower, peaking at 3% within the IGV wake street. The ensemble average turbulence level $<Tu>$ reached peak values of 9% within the regions of low energy rotor wake fluid at circumferential locations where the time-average turbulence level Tu was a minimum; but these values may have been increased by phase jitter in different realisations and may overestimate the peak value of turbulence averaged over a short interval.

As is further discussed in Chapter 7, the boundary layers on a downstream blade respond in different ways to the various disturbance components. The random disturbance component influences laminar-turbulent transition directly. However, the periodic component will operate more indirectly by modifying the blade surface pressure distribution and/or boundary layer velocity profiles. The use of total disturbance level as a predictor of transition therefore appears questionable.

Chapter 6

Stator Wake Measurements

6.1 Introduction

The early investigations of Walker [139] showed that the periodic disturbances associated with passing wakes may produce periodic unsteady transition phenomena on the surfaces of axial turbomachine blades. It has also long been appreciated that wake dispersion and mixing effects in an axial turbomachine with multiple blade rows may cause uneven energy addition and redistributions of losses, with resultant periodic circumferential variations in both the time-mean and unsteady flow fields (see Smith [121], Kerrebrock and Mikolajczak [79], Lockhart and Walker [88] and Zierke and Okiishi [153]). Subsequent improvements in computing power and high-speed data acquisition capability have led to greater understanding of unsteady flow processes and brought about a renewed interest in this field. Recent analytical and numerical studies of the influence of rotor-stator axial gap on axial compressor performance (see Deregel and Tan [28] and Adamczyk [2]), indicate potential increases in efficiency and pressure rise of one or two percent. These analyses do not, however, account for variations in blade losses which may accompany a change in the free-stream disturbance field.

This chapter investigates the influence of free-stream disturbance field variations, associated with wake dispersion and interaction effects (described in Chapter 5) on the stator blade losses. This is achieved by clocking the inlet guide vane (IGV) relative to the stator blade row and changing the axial rotor-stator blade row spacing. This information is used to assess how variations in free-stream unsteadiness may affect the performance characteristics of an axial turbomachine blade row. The optimisation of axial gap is not the focus of the present work. The problem of optimising the axial gap requires a proper appreciation of these issues.

6.2 Range of Investigation

The variation of unsteady stator losses was investigated through hot-wire measurements acquired at an axial distance of 14.4% chord downstream of the stator trailing edge. Initially the investigation focused on the influence of IGV clocking, and observations were made at the large rotor-stator axial spacing (LAG case) for values of $a/S =$ 0.00, 0.25, 0.50 and 0.75. As indicated in Fig. 4.1, coordinate a is the circumferential distance of the stator leading edge from the centre of the avenue of dispersed IGV

wake segments. Measurements were performed for the high, medium and low loading conditions outlined in Section 4.4.2. Later measurements were performed at the reduced rotor-stator spacing (RAG case), but only for the clocking cases $a/S = 0.00$ and 0.50.

For all cases, the hot-wire probe was positioned with the sensor axis aligned with the stator trailing edge, and was supported from downstream by a mounting tube aligned approximately in the local flow direction. The probe was traversed across one blade pitch at mid-blade height. A total of 32 measurement stations was used across the stator passage, with the circumferential spacing varying from 6.7% of stator pitch (S) in the region outside the influence of the stator wake street, down to 0.67% of S inside the stator wake. Fine spatial resolution inside the stator wake was necessary to allow accurate determination of the unsteady variation in stator blade loss.

6.3 Stator Outlet Flow Field

The variation of the periodically unsteady outlet stator flow field with IGV clocking is shown in Figs. D.5, D.6, D.11 and D.12, for the LAG configuration at the medium loading incidence. Data were obtained from circumferential hot-wire traverses downstream of a single stator passage, but have been plotted over two blade pitches by assuming pitchwise periodicity. The interpretation is similar to the results presented in Chapter 5, except for the additional feature of the stator wake which appears as a horizontal band of low velocity and high turbulence level. These figures have been complemented by the distributions of dimensionless time-mean velocity $\overline{u}/\overline{u}_s$ and time-mean disturbance plotted at far left. The total disturbance Tu_D has been separated into its periodic $\widetilde{Tu}$ and random Tu components (see Appendix A for details) by evaluating the Tuover an integral number of rotor passing periods and subtracting it from the measured Tu_D.

Separate figures are shown for values of $a/S = 0.00$, 0.25, 0.50 and 0.75 to indicate the effect of clocking the stator relative to the IGV wake street. The case $a/S = 0.00$ nominally corresponds to the stator leading edge lying in the centre of the IGV wake street. The IGV wake regions are identified from the bands of higher turbulence level reaching values of over 2%. The IGV wake is more diffuse than at the rotor exit (see Chapter 5), and the minimum background turbulence level has risen to 1%. The minimum total disturbance level Tu_D is much higher at about 3%, indicating the effect of unsteadiness from passing rotor wakes. The clocking effect is clearly evident from the movement of the higher turbulence bands and associated concentrations of low energy rotor wake fluid which appear as regions of low ensemble average velocity. The peak turbulence level outside the stator wakes, which occurs near these low velocity regions, reaches values of over 6%. The stator wakes exhibit periodic variations in thickness indicative of blade loss fluctuations. This is most easily identified from Figs. D.1, D.2, D.7 and D.8, which can be used to overlay the respective unsteady velocity and turbulence fields and show the periodic variation of stator wake edge location. The algorithm for identifying the location of the stator wake edge is described in Section 6.3.1. There is a noticeably greater fluctuation in stator wake thickness for $a/S = 0.25$ and 0.50, which is most clearly evident on the suction side.

As discussed in Chapter 5, marked regions of low energy fluid accumulation still occur within the rotor wakes on the suction side of the IGV wake street. These have

not diffused to any great extent over a distance of two chord lengths downstream of the rotor trailing edge. Comparison of Figs. D.11 and D.12 show how the IGV wakes and low energy rotor fluid regions move relative to the stator as the IGV row is clocked through one quarter of a blade space from a/S= 0.50 to a/S= 0.75. It can be seen that the rapid accumulation of rotor wake fluid against the suction side of the IGV wake street has intercepted most of the relative flow within the rotor wakes in these cases; interception of rotor wake fluid by the pressure side of the stator blade (as described by Kerrebrock and Mikolajczak [79]) is comparatively weak.

The circumferential variations of time-mean velocity and total disturbance level for different a/S values at the medium loading case have been superimposed in Fig. 6.1 to indicate more clearly the effects of IGV clocking. Variations of up to 5% in $\overline{u}/\overline{u}_s$ and 3% in Tu_D outside the stator wake region can be seen to move in phase with the IGV wake street. The amplitude of these periodic circumferential variations in the mean flow is strongly loading dependent, and evidently associated with the strength of the rotor wakes. The variation in $\overline{u}/\overline{u}_s$ increases to about 10% for the high loading case and decreases to around 2% for low loading case. The minimum values of Tu_D are again much higher than those of Tu, indicating a significant level of periodic fluctuation $\widetilde{Tu}$ in the free-stream region. Note that the local peak values of Tu_D outside the stator wakes correspond to circumferential positions where there is a lower time-mean velocity due to local accumulation of low energy fluid within the rotor wakes.

Similar plots of the time mean and periodically unsteady stator outlet flow field are shown in Figs. D.17 and D.18, for the RAG configuration. Both the a/S= 0.00 and 0.50 IGV clocking cases are presented. These figures complement the results obtained at the larger rotor-stator blade row spacing. Again, the unsteady turbulence field (see Figs. D.15 and D.16) and the periodic variation in stator wake location (see Figs. D.13 and D.13) can be used to overlay the unsteady velocity field measurements. There is a general improvement in the alignment of the IGV wake street with the stator blade element, with the IGV wake shifted approximately 0.1 S towards the stator suction surface when compared to the LAG results. Comparison of the results obtained at the two row spacing configurations show qualitatively similar behaviour, although the time-mean turbulence levels in the stator wake appear to have increased from 7% to approximately 10% as the axial gap is reduced. The RAG data was primarily gathered to distinguish the influence of axial row spacing from IGV clocking on the stator blade element performance.

6.3.1 Evaluation of Stator Wake Properties

It is of interest to evaluate the stator wake properties to provide some quantitative indication of the stator losses. This is not a trivial problem, however, because of the non-uniform free-stream outside the stator wake region. Fig. 6.2 shows typical circumferential distributions of ensemble average velocity and turbulence obtained downstream of the stator at several different values of dimensionless time t^*. The free-stream flow is not uniform at any stage, and there is a differential in free-stream velocity across the stator wake which changes sign with the phase of the rotor wake passage. These variations may result from non-uniform energy addition, vortex shedding phenomena, redistribution of low energy fluid associated with intra-wake relative flows, or a combination of all three effects.

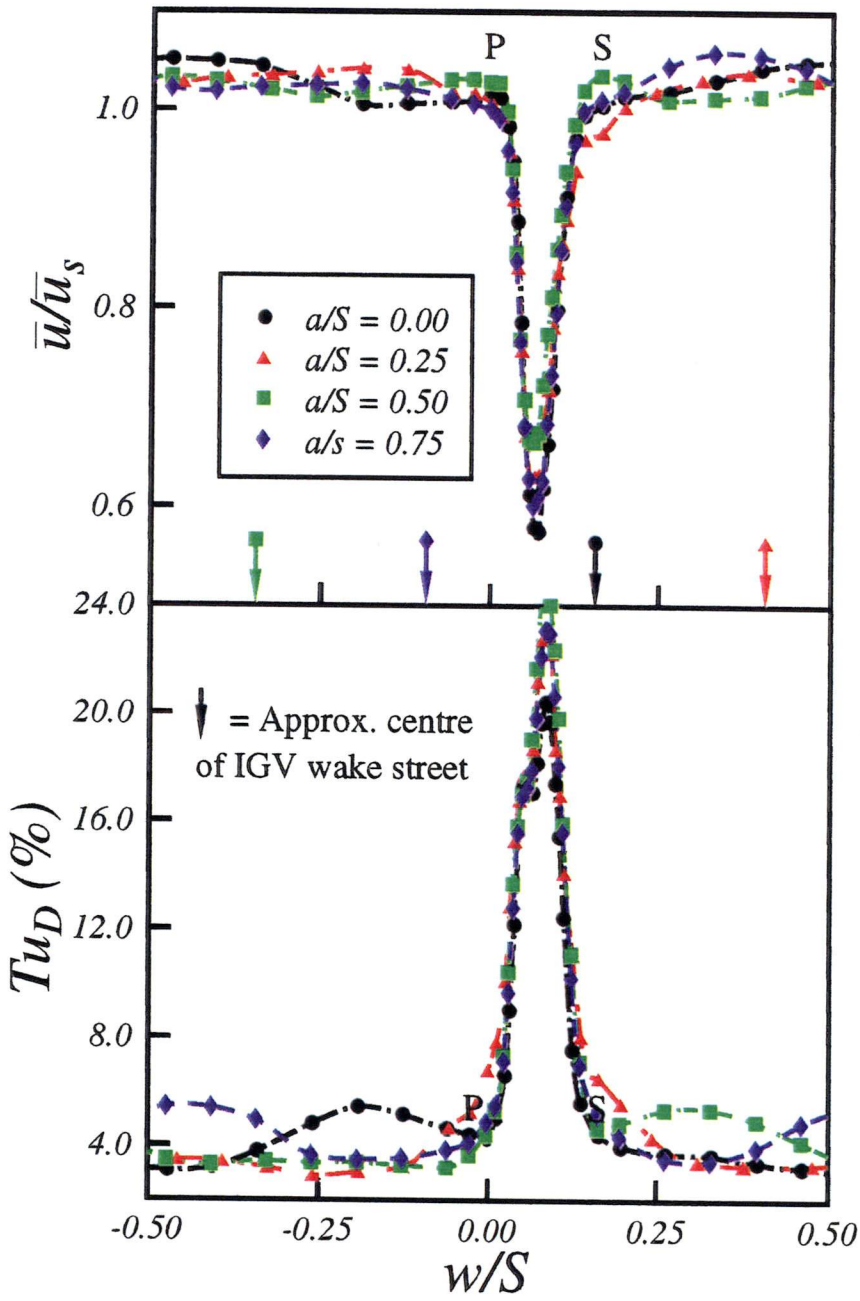

Figure 6.1: Influence of IGV clocking on circumferential variation of time mean velocity and total disturbance level. Hot-wire measurements 14.4% chord axially downstream of stator trailing edge at mid-passage. LAG case, $\phi = 0.675$, $Re_{ref} = 120{,}000$. S = suction side; P = pressure side.

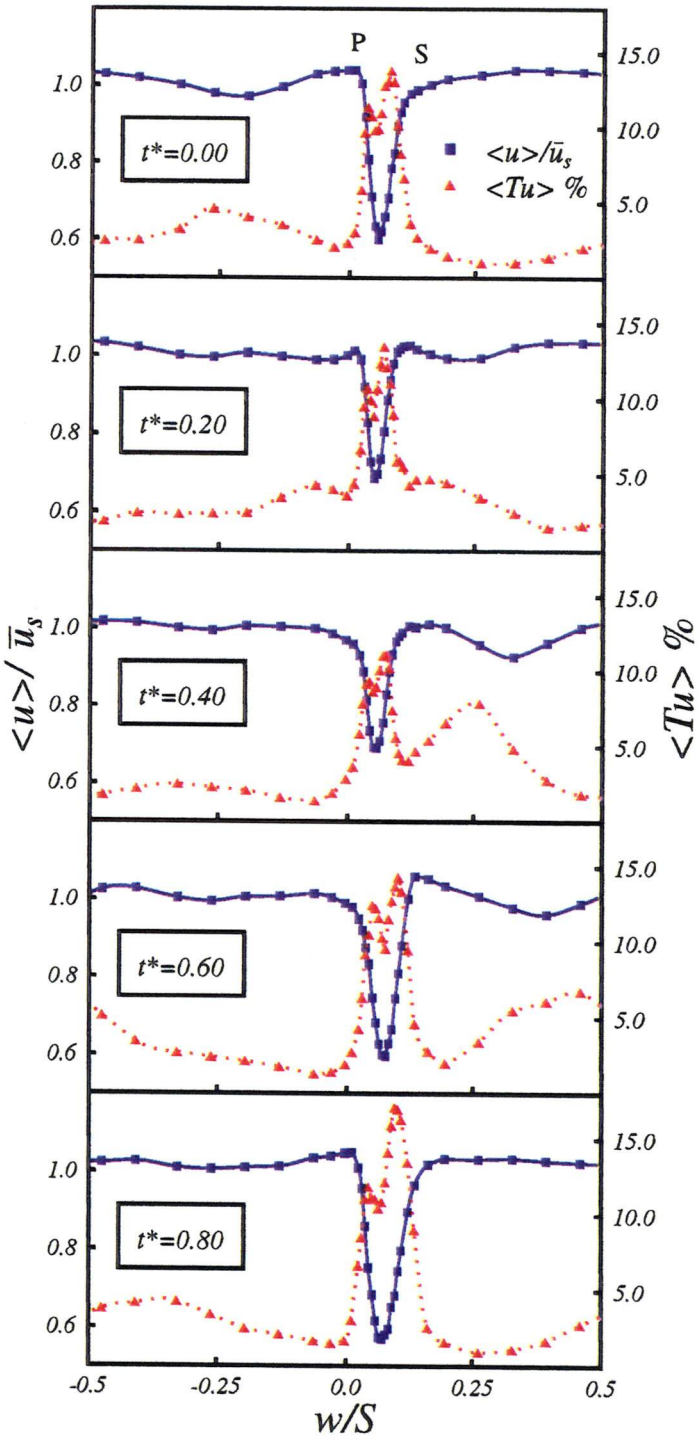

Figure 6.2: Typical variation in circumferential distributions of ensemble mean velocity and turbulence with phase of rotor wake passage. Hot-wire measurements 14.4% chord axially downstream of stator trailing edge at mid-passage. LAG Case, ϕ =0.675, Re_{ref} = 120,000. S = suction side; P = pressure side.

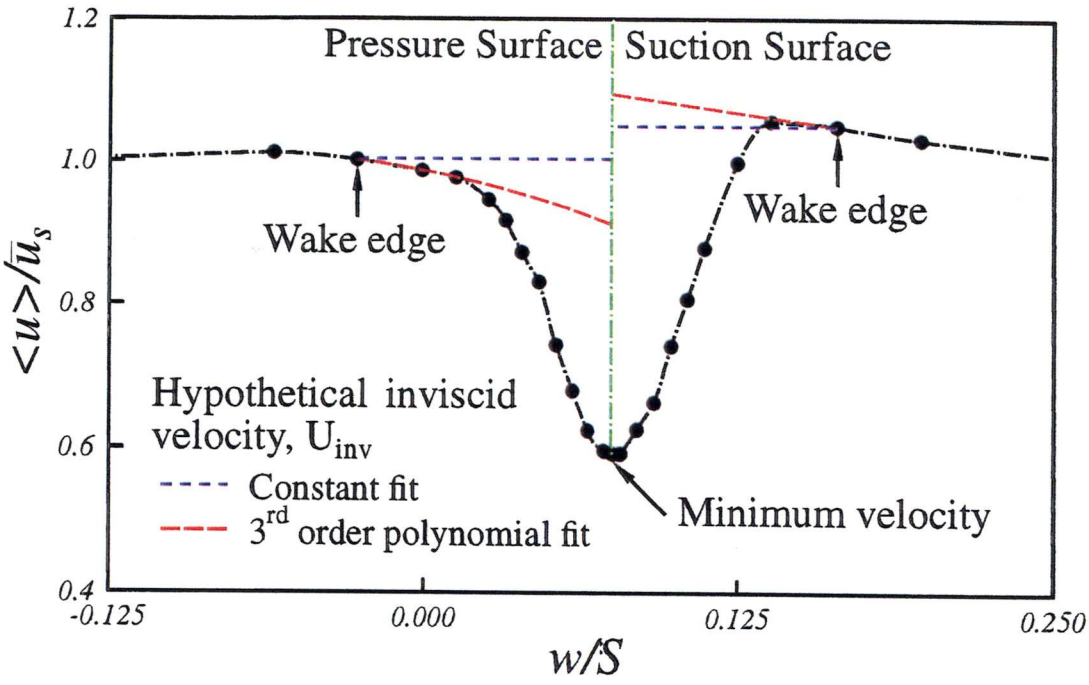

Figure 6.3: Alternative models for inviscid velocity distribution used for computing stator wake properties.

An algorithm for identifying the stator wake region was developed by examining changes in curvature of the ensemble average velocity profile. It was expected that a local peak in curvature would generally occur just inside the wake boundary. This provided an adequate means of identification in the majority of cases, but there were still some situations where no distinct peak in curvature occurred. Such ambiguities were resolved by further considering changes in slope of the turbulence distributions, thus making possible a completely automatic processing of the wake data. A typical example of an ensemble average velocity profile with the identified wake edge points is shown in Fig. 6.3. The periodic variations in identified wake edge location have been overlaid on the turbulence and velocity flow fields for both the LAG and RAG cases (see Appendix D).

Having decided on the wake boundaries, it is next necessary to prescribe an appropriate inviscid velocity distribution $U_{inv}(S)$ so that the wake properties can be evaluated. Two alternative models were considered:

(a) a constant value equal to the local velocity at the wake edge point; and

(b) a 3rd power polynomial of best fit to several points outside the wake edge.

The polynomial fit would be the more appropriate model if the free-stream region were a steady inviscid flow. However, that is not true in the present case where free-stream velocity variations may result from variable energy addition and loss redistribution phenomena.

For each of the above models, the hypothetical inviscid distribution was extrapolated to the circumferential position corresponding to the minimum velocity within the

wake. A discontinuity in the inviscid distribution was allowed to occur at this location, and momentum thickness values for the pressure and suction side shear layers were calculated separately from

$$<\theta>/c = \frac{s}{c}. \int_0^\infty \frac{\overline{u}/\overline{u}_s}{U_{inv}/\overline{u}_s}\left[1 - \frac{\overline{u}/\overline{u}_s}{U_{inv}/\overline{u}_s}\right] \cos\alpha \, d\left(\frac{w}{s}\right)\Big|_{t^*=const} \tag{6.1}$$

where α is the mean flow angle from axial. Although the dimensional momentum flux would suggest that the separate wake values could be weighted in proportion to the square of the appropriate freestream velocity before combining, it was considered the simple addition would give representative values for the whole wake momentum thickness as the loss coefficient suggests this would scale in proportion to θ/c. Purely inviscid flow modelling requires a velocity discontinuity within the wake region to represent the pressure differential which exists across a curved shear layer. It should be noted that ensemble average values were used to evaluate Eqn. (6.1) and not all unsteady terms are correctly accounted in the present evaluation of loss, however, it is assumed that this error is negligible.

6.3.2 Influence of IGV Clocking and Axial Row Spacing on Stator Losses

A detailed discussion of compressor blade losses and their evaluation has been given by Cumpsty [23]. For steady two-dimensional cascade flow the wake momentum thickness at the normal outlet measuring station (around one chord length downstream of the blades) can be related to the total pressure loss coefficient for the cascade using the expression developed by Lieblein and Roudebush [86]. It is assumed here that the values of wake momentum thickness evaluated by the above procedure from the measurements 14.4% chord axial distance downstream of the stator trailing edge will be reasonably representative of the stator blade viscous losses. A significant proportion of the wake mixing losses will have occurred by this stage (see Denton [27]), where the maximum observed value of wake velocity profile shape factor H was around 1.5. There are no detectable differences in behaviour between the momentum thickness values and the total pressure loss coefficient values calculated from Lieblein and Roudebush's [86] analysis.

Both the time-mean and ensemble average values of wake momentum thickness are of interest. The time-mean value is relevant to blade row efficiency, whilst temporal variations in ensemble average values provide information on periodic fluctuations in shear layer thickness associated with wake-induced transition on the stator blade surfaces. Studies by Cumpsty et al. [24], Halstead et al. [58, 59, 60, 61] and Solomon and Walker [125] all provide evidence of a greater susceptibility to turbulent separation of the thicker boundary layer regions within wake-induced turbulent strips.

Fig. 6.4 shows the influence of IGV clocking on the temporal variation of ensemble average stator wake momentum thickness for the medium loading case. Values of $<\theta>/c$ calculated using both the constant and polynomial fitted hypothetical inviscid flow models are presented. These values have been smoothed with a 4th power best fit polynomial which extends approximately 20% of a rotor blade passing period (or $\delta t^* = 0.2$) either side of the point under consideration. The smoothing process was employed

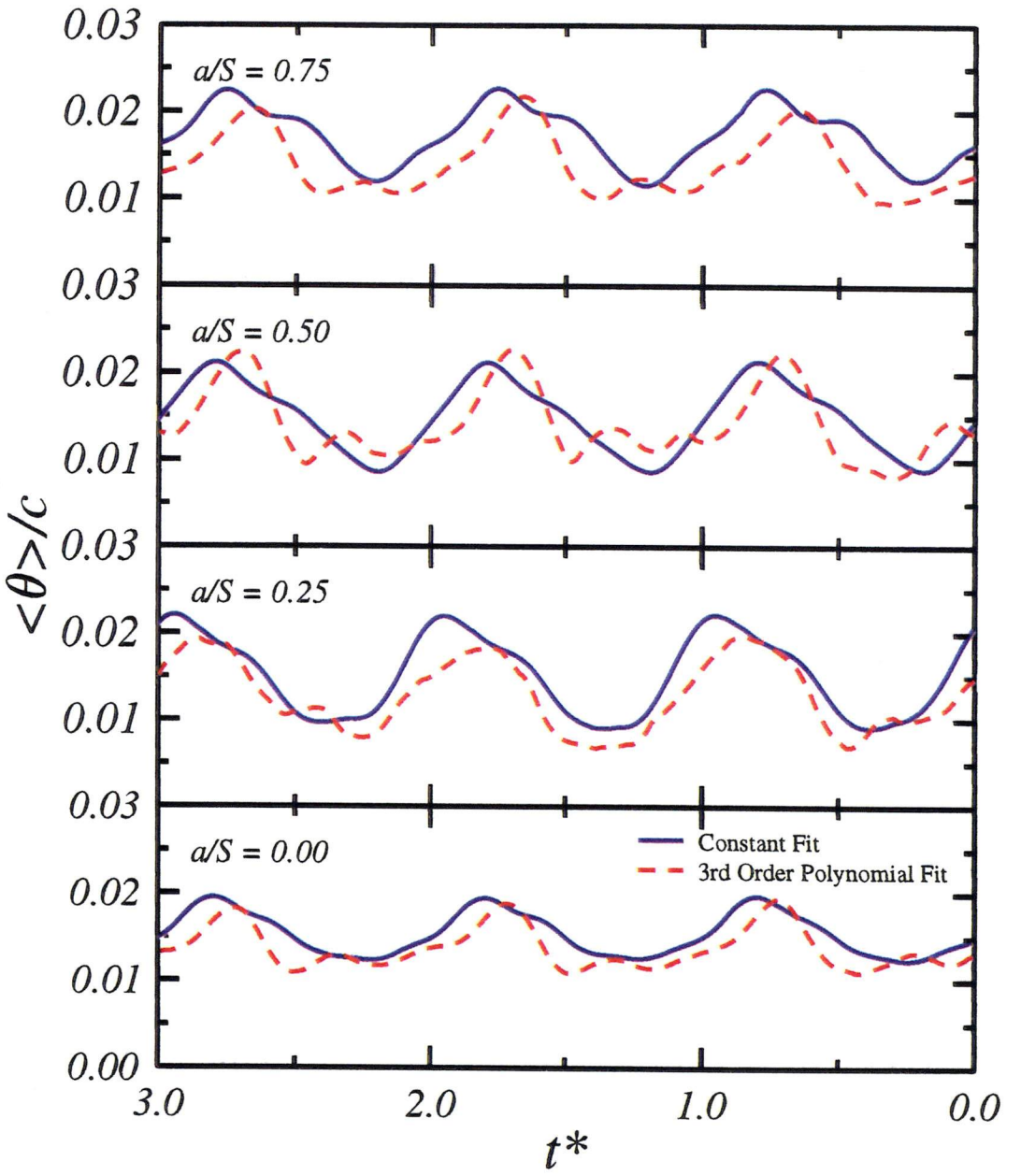

Figure 6.4: Influence of IGV clocking on temporal variation of ensemble average stator wake momentum thickness. Hot-wire measurements 14.4% chord axially downstream of stator trailing edge at mid-passage. LAG case, $\phi = 0.675$, $Re_{ref} = 120{,}000$.

Table 6.1: Influence of IGV clocking and flow coefficient on time-mean stator wake thickness and stator wake unsteadiness. LAG case.

ϕ	a/S	$\overline{\theta}/c$		S.D.%($\overline{\theta}$/c)	
		$U_{inv}(poly)$	$U_{inv}(const)$	$U_{inv}(poly)$	$U_{inv}(const)$
0.600	0.00	0.0139	0.0197	19	19
	0.25	0.0153	0.0167	34	24
	0.50	0.0176	0.0236	27	21
	0.75	0.0172	0.0213	18	13
0.675	0.00	0.0136	0.0153	17	16
	0.25	0.0128	0.0151	32	30
	0.50	0.0140	0.0147	28	27
	0.75	0.0139	0.0171	25	19
0.840	0.00	0.0098	0.0134	23	10
	0.25	0.0105	0.0131	25	21
	0.50	0.0110	0.0126	23	24
	0.75	0.0119	0.0138	18	10

to remove the occasional point were the processing routine failed, and does not significantly alter the original results. The momentum thickness values obtained from the constant inviscid velocity model are about 10% greater on average than the polynomial inviscid model, and this indicates the order of accuracy which can be expected in the absolute values of momentum thickness. The variation of $<\theta>$/c with t^* is broadly sinusoidal, with phase differences of $\pm$ 0.1 in t^* according to the dimensionless IGV wake street location a/S.

The periodic variation in $<\theta>$/c noted previously from Figs. D.5, D.6, D.11 and D.12 is more clearly evident in Fig. 6.4. Its amplitude is greatest for $a/S = 0.75$ and 0.50, when the IGV wake street passes through the centre of the stator blade passage and the stator blades are subjected to higher levels of periodic unsteadiness from the passing rotor wake disturbances. Here the maximum value of $<\theta>$/c is nearly 2.5 times the minimum. The lowest level of unsteadiness in the stator wake thickness occurs for $a/S = 0.00$, when the IGV wake street is incident on the stator blade leading edge. Here the ratio of maximum to minimum $<\theta>$/c has fallen to around 1.5. This reduction is mostly due to an increase in the minimum value of $<\theta>$/c, but the maximum value is nevertheless about 10% lower than for $a/S = 0.50$.

The results for both spacing configurations and all three loading cases have been summarised in Table 6.1 and Table 6.2. The time-mean values of dimensionless wake momentum thickness $\overline{\theta}/c$ have been evaluated from an average of the ensemble means over three rotor blade passing periods. The degree of unsteadiness in the stator wake is indicated by the standard deviation (SD) in values of $<\theta>$/c over the same interval. There is a consistent trend in the data for significantly higher values of wake unsteadiness, S.D. ($<\theta>$/c), to occur when the IGV wake passes down the middle of the stator passage (i.e. $a/S = 0.75$ and 0.50). The minimum value of S.D. ($<\theta>$/c) always occurs for $a/S = 0.00$, when the stator blades are immersed in the IGV wake street, although for the LAG cases the unsteadiness for $a/S = 0.75$ is closely comparable.

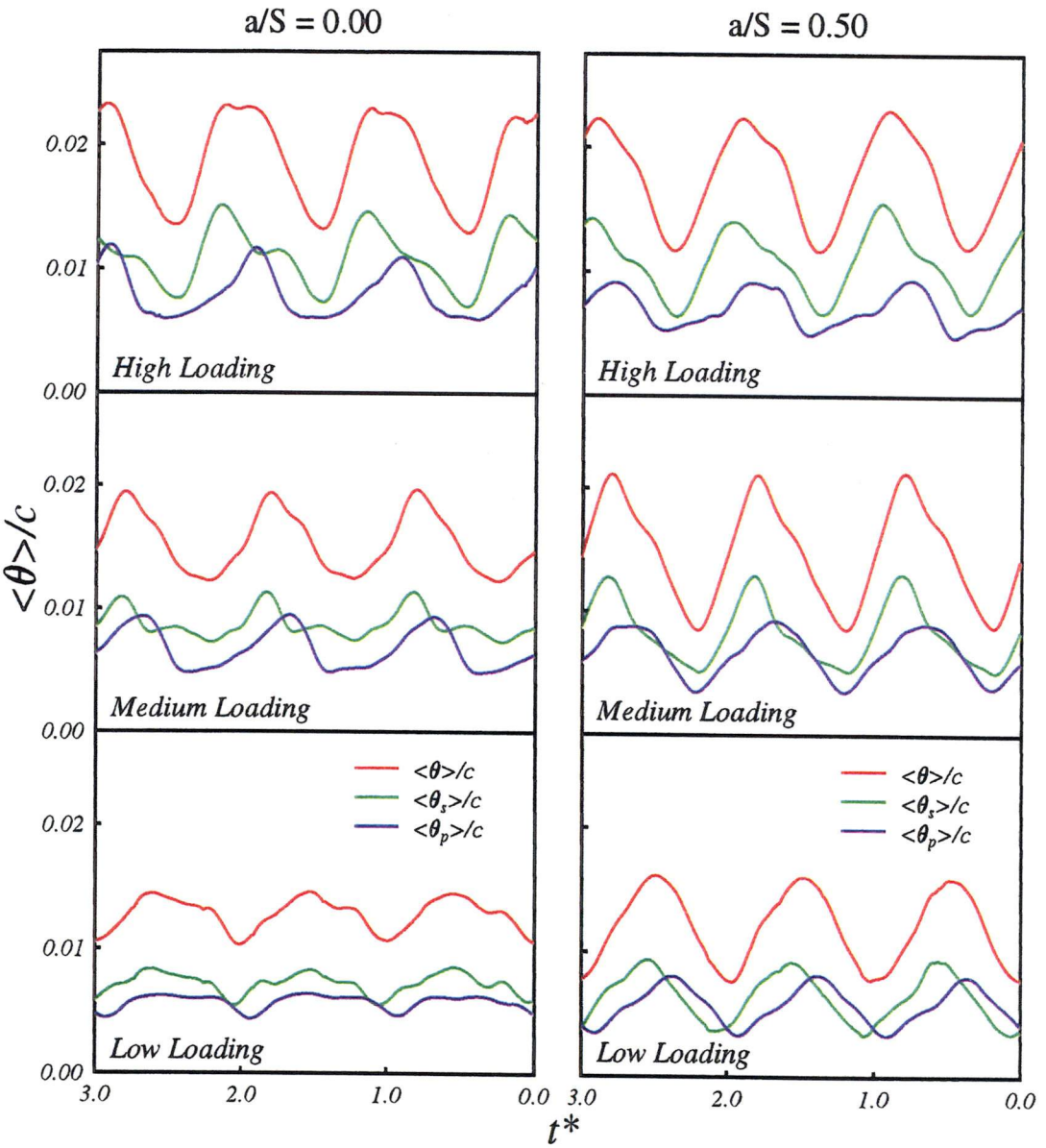

Figure 6.5: Temporal variation of stator wake momentum thickness 14.4% chord axially downstream of stator trailing edge at mid-passage, showing division into pressure and suction side components and influence of IGV clocking. LAG case, Re_{ref} = 120,000

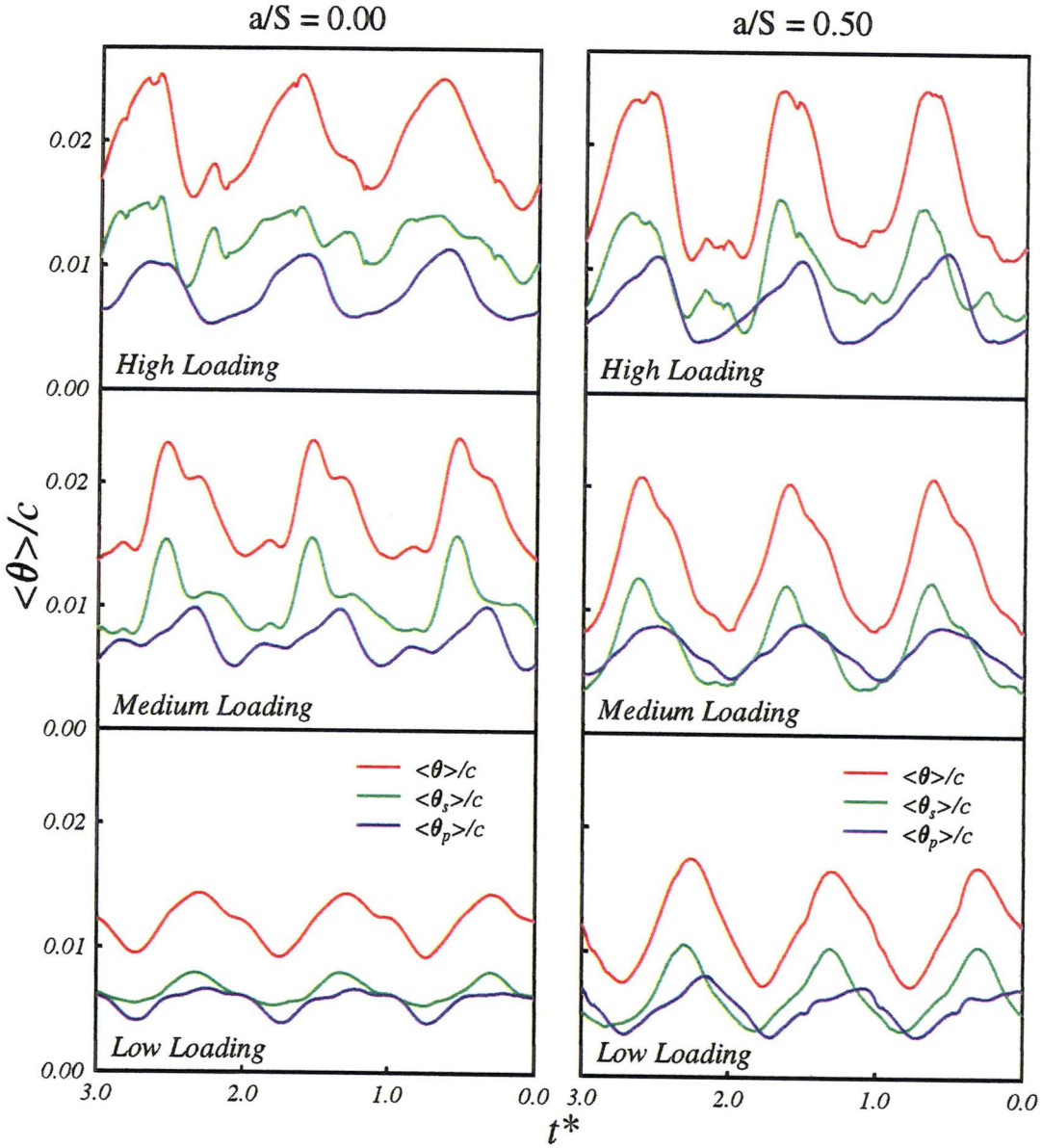

Figure 6.6: Temporal variation of stator wake momentum thickness 14.4% chord axially downstream of stator trailing edge at mid-passage, showing division into pressure and suction side components and influence of IGV clocking. RAG case, Re_{ref} = 120,000

Table 6.2: Influence of IGV clocking and flow coefficient on time-mean stator wake thickness and stator wake unsteadiness. RAG case.

ϕ	a/S	$\overline{\theta}/c$		%S.D.($\overline{\theta}$/c)	
		$U_{inv}(poly)$	$U_{inv}(const)$	$U_{inv}(poly)$	$U_{inv}(const)$
0.600	0.00	0.0126	0.0234	18	17
	0.50	0.0105	0.0195	27	29
0.675	0.00	0.0154	0.0177	21	18
	0.50	0.0124	0.0139	46	29
0.840	0.00	0.0120	0.0140	28	13
	0.50	0.0122	0.0139	38	27

6.4 Discussion

It is difficult to draw firm conclusions on the values of time-mean wake thickness $\overline{\theta}/c$, as these show no clear trend. The fluctuation in $\overline{\theta}/c$ with a/S is similar in magnitude to the uncertainty in evaluating $\overline{\theta}/c$ from different models for $U_{inv}(S)$ for all cases. For the LAG configuration the values of $\overline{\theta}/c$ for the minimum unsteadiness configuration of $a/S = 0.00$ are slightly less than the average for all a/S values with polynomial $U_{inv}(S)$ model; but with the constant $U_{inv}(S)$ model they tend to be about the average of $\overline{\theta}/c$ over all a/S values. For the reduced spacing configuration the evidence favours a reduction in loss for a/S= 0.50 at the high and medium loading conditions: evidence for this reduction is presented in detail in Chapter 7. General comparisons with clocking studies can be further complicated by the variation in blade element performance with radius, however, the observed fluctuations are similar to those presented by Eulitz et al. [37] in their numerical study of the influence of IGV clocking on axial turbine performance.

It is stressed that only a single blade element has been considered here. The blade elements at different radii will lie at different values of a/S due to skewing of the IGV wake street associated with the radial variation of whirl velocity in the compressor. The integrated effect on performance for the whole stator blade will therefore be less than that for an isolated element. No significant variation in flow coefficient could be detected with IGV clocking at constant throttle.

The fluctuations in ensemble average stator wake thickness $<\theta>$/c for the minimum and maximum unsteadiness configurations of $a/S = 0.00$ and 0.50 are shown in Fig. 6.5 and Fig. 6.6 for all three loading cases and both spacing configurations. The suction and pressure side contributions to the total wake thickness are shown separately. Whilst there may have been some decay in wake asymmetry in the 14.4% chord axial distance downstream of the trailing edge, these curves should give a useful indication of the loss fluctuations on the individual blade surfaces. Additional data obtained at 1.5% chord axial distance downstream of the stator for a more limited range of conditions are presented by Solomon [123].

For both axial spacing configurations there is a consistent trend of periodic momentum thickness variations with increasing loading. For $a/S = 0.00$ and $\phi = 0.840$ the pressure and suction side fluctuations are almost identical (see either Fig. 6.5 or Fig. 6.6). As the loading increases there is an increase in the suction side momentum

thickness relative to the pressure side contribution. This is also accompanied by a phase shift in the location of peak momentum thickness on the two sides due to the increasing difference in arrival time of disturbances at the trailing edge on the suction and pressure side as a result of blade circulation. The oscillations in individual shear layer thicknesses are clearly indicative of periodic wake-induced transition in the blade boundary layers. They closely resemble the measured boundary layer thickness fluctuations in the unsteady compressor cascade tests of Cumpsty et al. [24] and the multistage compressor tests of Halstead et al. [59]. The fluctuations in total wake momentum thickness have developed harmonic content due to the combination of these two out-of-phase components. The general behaviour is quite similar for the maximum stator wake unsteadiness configuration of $a/S = 0.50$. However, there is much greater periodicity and the ratio of maximum to minimum momentum thickness is significantly greater for both shear layer components in all cases.

The amplitude of the stator wake unsteadiness can be explained in terms of transition phenomena on the blade surface. The peak momentum thickness corresponds to the boundary layer thickening caused by wake-induced transition initiated by the rotor wakes. This is slightly lower for the case $a/S = 0.0$, where the IGV wake street is incident on the stator blade and the amplitude of rotor wake disturbances is somewhat lower because of IGV wake-rotor wake interactions. The minimum momentum thickness in the stator wake corresponds to later transition within the stator blade boundary layers in the region between the rotor wakes where the turbulence level is lower. It is likely for typical turbomachine blade profiles that the delay in transition onset due to lower turbulence levels will be partially offset due to increased adverse pressure gradients as the onset proceeds rearward on the blade surface.

As explained by Mayle [93], this is controlled by other flow transition modes. The particular transition mode will depend on pressure gradient and the level of free-stream turbulence: the inlet turbulence level varies from about 0.5% in the background to approximately 3% within the IGV wake street.

Whilst the peak turbulence in the IGV wakes varies little with loading, the average turbulence over the region between rotor wakes steadily increases with loading. This follows from the increased dispersion of IGV wakes associated with higher rotor circulation. It is interesting to note that the ratio of maximum to minimum stator wake thickness also decreases steadily as loading is increased. This is suggestive of earlier transition between the rotor wakes causing a more uniform stator wake. This result is also observed to occur with the reduction in rotor-stator axial gap.

6.5 Conclusions

As discussed in Chapter 5 the dispersion of inlet guide vane wakes by the rotor, and subsequent interactions between the IGV and rotor blade wakes, produce regular circumferential variations in both the time-mean and unsteady flow downstream of the rotor in the test compressor. The influence of these variations on stator losses was examined through ensemble average measurements of the stator wake properties.

Separate evaluation of the suction and pressure side momentum thickness components for the stator wake were attempted. The individual components showed a lower harmonic content than the composite wake thickness, which was influenced by phase

lags between periodic wake-induced phenomena on the stator blade suction and pressure surfaces. Significantly lower amplitudes of periodic fluctuations in the stator wake were observed when the stator blades were immersed in the avenue of dispersed IGV wake segments.

No firm conclusions could be drawn about the time-mean stator loss values, as the observed variation in losses was comparable in magnitude with the uncertainty in the data. However, there does appear to be a more consistent trend for the losses to be reduced when the avenue of dispersed IGV wake segments passes down the middle of the stator passage as the axial row spacing is reduced. The unsteady variations of flow behaviour on blade surfaces and in the wakes are strong and should be taken into account when determining blade clocking effects and rotor-stator axial gaps for axial turbomachines.

Chapter 7

Hot-film Surveys

7.1 Introduction

The unsteady flow field seen by an embedded blade row in a multistage axial turbomachine is dominated by the effects of the adjacent upstream stage. The major source of periodic disturbance is usually provided by relative motion of blade wakes from the row immediately upstream. The second upstream row provides the greatest contribution to the random disturbance field through dispersion of its chopped wake segments. Further upstream rows contribute lower level periodicity and a generally increased level of background random turbulence.

The blade boundary layer behaviour under these conditions is dominated by periodic wake-induced transition. Transition by other modes is observed in regions between the wake-induced transitional or turbulent strips. Mayle [93, 94] refers to this phenomenon as "multimode transition". The problem has been extensively studied since the late 1970's and a good summary of the relevant literature is provided by Mayle's [93, 94] reviews. Most workers investigating this problem have used large scale experiments on flat plates, with moving bar wakes and turbulence grids to simulate the periodic and random disturbance components of the actual disturbance field in a turbomachine. Little attention has been paid to leading edge effects (which were generally suppressed in these experiments) and only more recently has the direction of the wake-jet impinging on the plate surface been considered (see Orth [105], Funazaki et al. [44] and Kittichaikarn et al. [80]). This chapter reports a detailed study of unsteady transition on both surfaces of the mid-span element of the outlet stator blade row in the 1.5 stage research compressor. The stator inlet conditions are varied by changing the blade incidence, clocking of the IGV row and altering the axial row spacing. The relative importance of periodic and random freestream disturbances for transition on the stator blade element at mid-span are discussed.

7.2 Data acquisition

Five TSI-IFA 100 constant temperature anemometers were used to simultaneously acquire data from the hot-film sensor array located at mid-span. Using all five channels, a complete survey of the blade surface could be achieved with 12 separate sets of simultaneously acquired data. Sensor-sensor interference was minimised by using every

second gauge during data acquisition. The film array and the method of operation are outlined in Section 3.4.9. The output from each anemometer channel was AC coupled and high-pass filtered at 0.1Hz. The TSI signal conditioners were PC controlled via an RS-232C connection and used to automatically set the amplification for each spatial measurement point, in order to optimise the signal to noise ratio. The data was sampled at 50kHz using a 12 bit analog-to-digital converter and then digitally stored. The signal was also low-pass filtered at a cut-off frequency of 20kHz to avoid aliasing. During sampling, every second sensor was operated to minimise interference effects from neighbouring sensors. The frequency response of the hot-film measurements was determined to be better than 30kHz. The rotor blade passing frequency was around 300Hz for tests conducted at $Re_{ref} = 120\ 000$.

Ensemble-average values of measured quantities were obtained from 512 records, with sampling triggered at the same point on each rotor revolution so that the wakes of the same rotor blades were observed in each record. Each record consisted of 1024 samples covering about 6 rotor blade passing periods. Time-mean flow data were determined from separate sets of flow observations with continuous sampling at random phase relative to the rotor motion and an averaging time of about 30 seconds.

7.3 Intermittency Detection

Narasimha [101] defines intermittency γ "as the fraction of time that the flow is turbulent at any point". In order to determine intermittency, instruments with sufficient spatial and temporal resolution to detect perturbations associated with turbulence must be used. General features of most intermittency detection algorithms include the consecutive steps of sensitising, smoothing and thresholding to determine the turbulent portions of the signal. First, the signal is sensitised using a detector function, to accentuate the difference between the laminar and turbulent regions. The sensitised signal is then smoothed to remove spurious regions to produce a criterion function. This criterion function is then compared to a threshold level to identify regions of turbulent flow. Solomon [123, see Chapter 7] provides a thorough review of intermittency detection methods, and it is Solomon's algorithm which has been employed to produce the results presented in this chapter.

Initially, Solomon and Walker [125] developed an intermittency detection algorithm which was based on the Turbulent Energy Recognition Algorithm (TERA) of Falco and Gendrich [39]. It used a detector function of the form $|\delta\tau/\delta t|$, where τ is the quasi-shear-stress indicated by a surface hot-film sensor, and turbulent events were identified if the average of the detector function exceeded the threshold for a given time interval (or window period). Fully automatic processing of the data acquired from the hot-film array proved difficult with this method. Solomon [123] subsequently developed an improved method which amalgamated the peak-valley counting (PVC) ideas of Zohar [154] with the PDF-based threshold detection algorithm of Hazarika and Hirsch [62]. Solomon's [123] algorithm differs slightly from Zohar [154], in that the peak-valley counting is performed after the application of the detector function rather than before. The procedure uses an iterative approach to setting the threshold level. Initially the threshold is set to $0.7(\delta\tau/\delta t)_{RMS}$ to produce an intermittency result, from which the probability density functions for the turbulent and non-turbulent parts of the detector

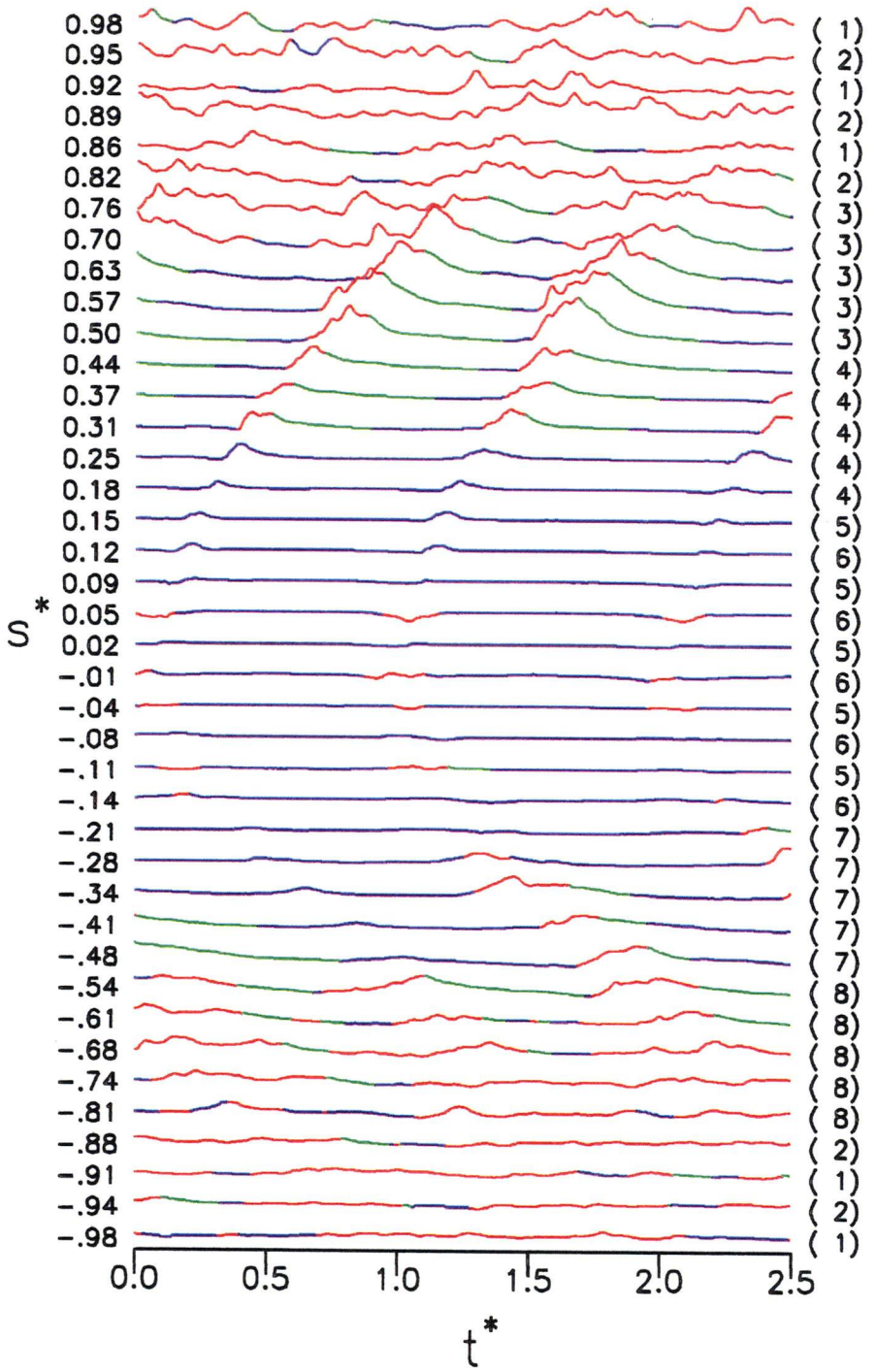

Figure 7.1: Variation of quasi-wall-shear stress with time. Instantaneous records plotted over both stator surfaces: negative s^* indicates pressure surface distance. Colour represents flow state as determined by intermittency detection algorithm. Red: Turbulent flow. Green: relaxing non-turbulent flow. Blue: Laminar Flow. Numbering at right indicates groups of time records that were acquired simultaneously.

function are fitted by Gaussian distributions. The intersection of the two Gaussian curves in then used as the threshold level for the next iteration. The region close to the blade leading edge caused problems with the automatic threshold setting and to avoid this a lower limit was imposed. This method allows for fully automatic processing of the hot-film data apart from the setting of a window period. A consistent value of 450μs (or 14% of rotor blade passing period) was used to define the window period for all data processing. The intermittency detection algorithm also has a relatively simple method for identify regions of relaxing non-turbulent flow κ. This type of flow was identified by $d\tau/dt$ remaining negative following the passage of a turbulent spot.

The results of the detection algorithm as applied to the surface mounted film array are illustrated in Fig. 7.1. Both surfaces have been plotted, with negative values of s^* indicating the pressure surface. The colour of individual time records indicates the flow state. Red is turbulent flow, green is relaxing non-turbulent flow and blue indicates laminar flow. The instantaneous data from each channel has been normalised by the long term mean value of quasi-shear stress for that channel. This normalisation procedure tends to reduce the apparent fluctuation level in the region of the leading edge, where the shear stress levels are high, and accentuates the fluctuations were the shear stress value is low and the flow is close to separation. The numbering on the right-hand side indicates sets of records that were acquired simultaneously. Fig. 7.1 shows strong evidence of wake-induced transition on both surfaces, with the first turbulent spots identified at $s^* = 0.31$ and -0.28 on the suction and pressure surfaces respectively. The suction surface transition is more regular than the pressure surface, and this is supported by the appearance of relaxing non-turbulent flow following nearly all wake-induced patches. There are regions on both sides of the leading edge where turbulence has been identified, but does not persist; this is discussed in more detail later. It is encouraging to note that there is also strong agreement between the identification of turbulence from wavelet analysis of individual records (see Chapter 8) and the intermittency detection algorithm outlined above.

7.4 Stator Surface Hot-Film Observations

7.4.1 Ensemble average RMS quasi-shear stress

Time-distance contour plots of ensemble average RMS quasi-shear stress observations for the large axial spacing (LAG) configuration are presented in Figs. 7.2 and 7.3. These figures show the response of the mid-span stator blade boundary layer transition processes to variations in blade loading and IGV clocking. Fig. 7.2 represents the effect of blade loading when the stator blade is immersed in the IGV wake street ($a/S = 0.00$), whereas Fig. 7.3 is the alternative clocking case ($a/S = 0.50$) with the IGV wake segments passing down the middle of the stator passage.

Following the recommendations of Solomon and Walker [124] the values of $<\tau_{RMS}>$ have been normalised by the local time-mean quasi-shear stress $\overline{\tau}$. The RMS quasi-shear stress tends to identify the centre of transition regions, as it reaches a maximum where the most frequent switching between laminar and turbulent flow (with correspondingly low and high wall shear stress) is occurring. The space-time ($t^* \sim s^*$) diagrams of $<\tau_{RMS}>/\overline{\tau}$ are overlaid with trajectories of particles travelling at $1.0U$, $0.88U$, $0.70U$, $0.50U$ and $0.35U$ to assist in interpretation of the wake-induced transition phenomena.

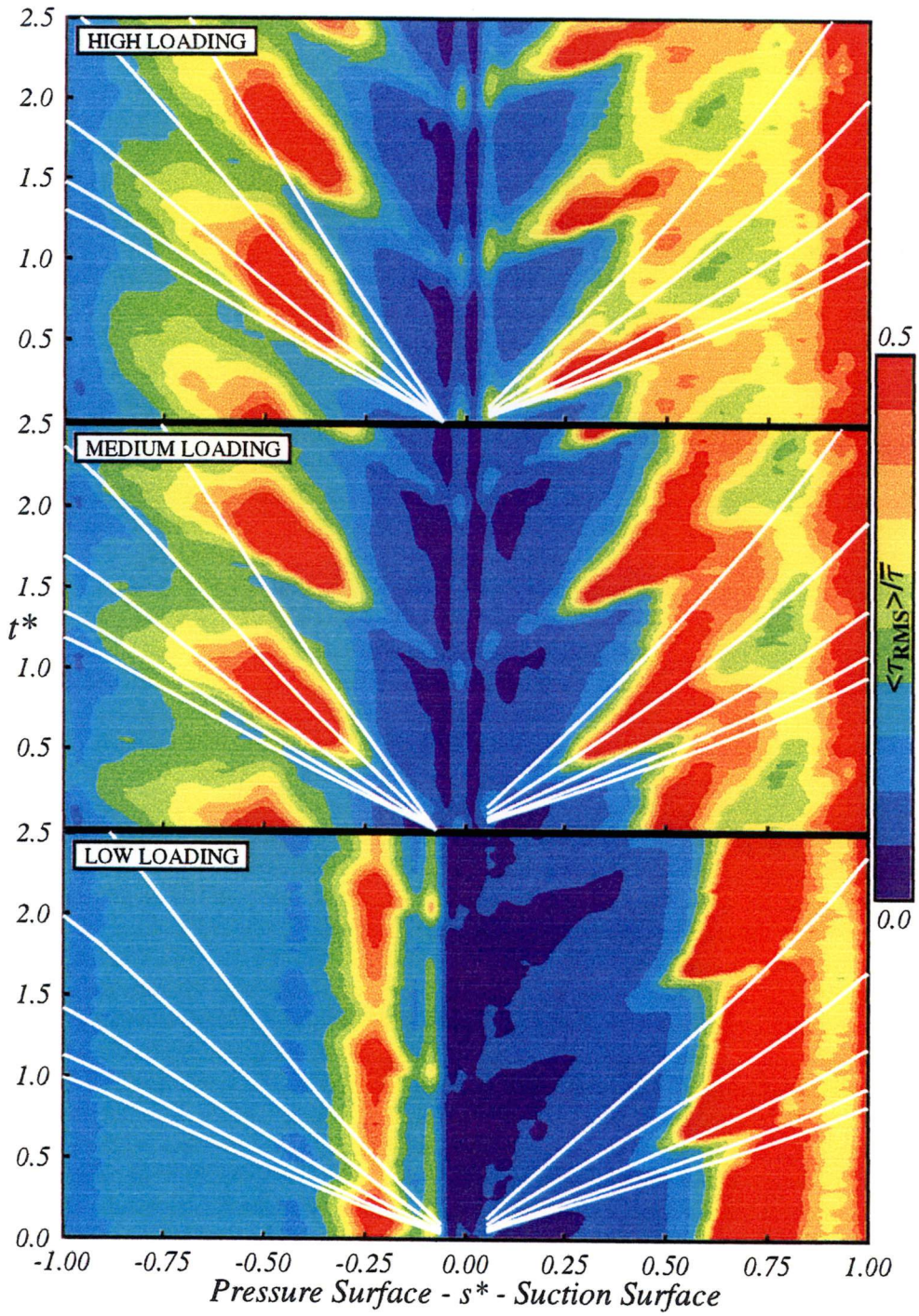

IGV wake street on stator ($a/S = 0.00$)

Figure 7.2: Variation of ensemble average RMS quasi-shear stress (normalised by $\overline{\tau}$) with blade loading. Surface hot-film observations on stator at mid-blade height. LAG case, $Re_{ref} = 120\ 000$, $a/S = 0.00$.

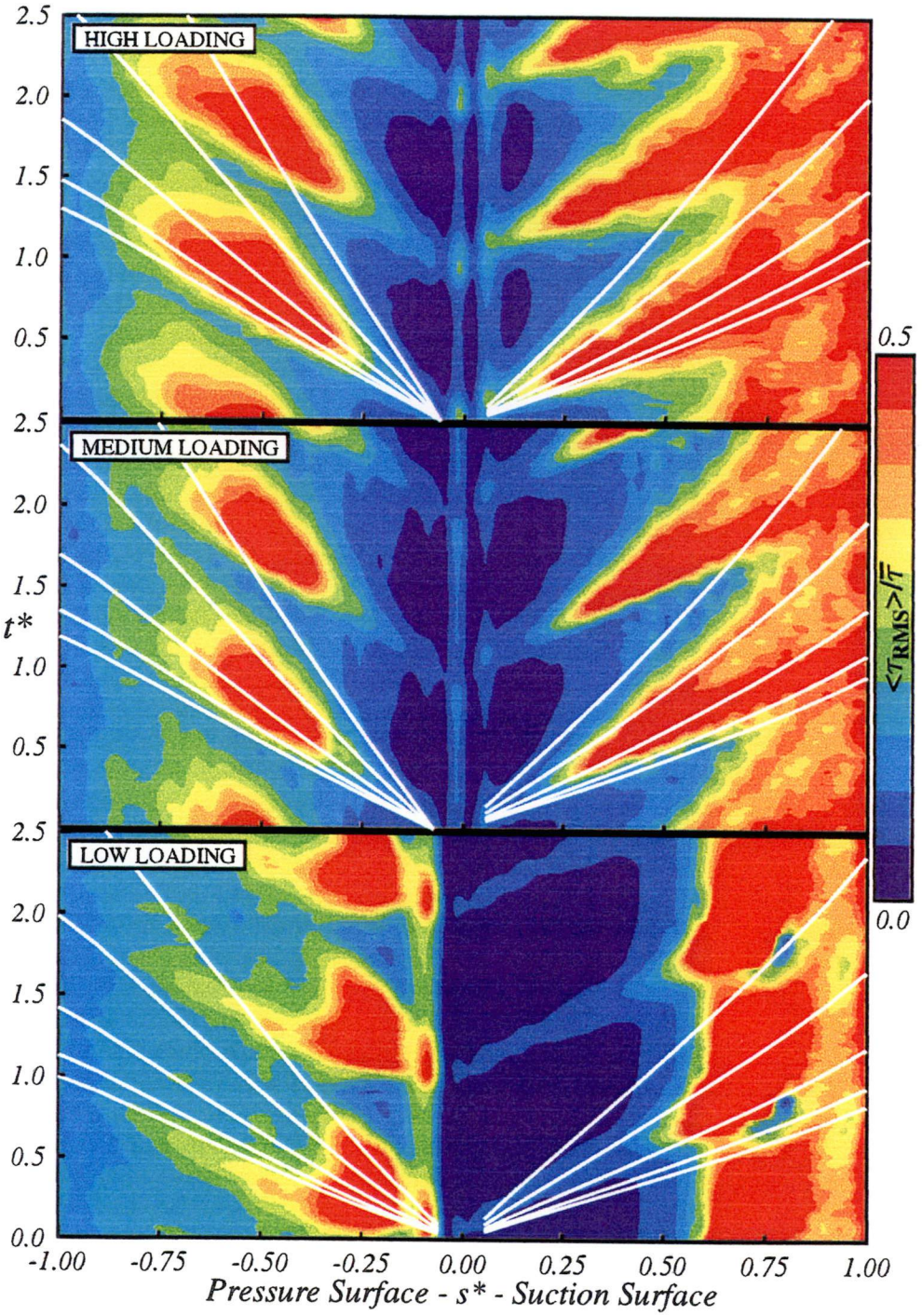

IGV wake street in passage ($a/S = 0.50$)

Figure 7.3: Continuation of Fig. 7.2. Particle trajectories for $1.0U$, $0.88U$, $0.7U$, $0.5U$, $0.35U$ overlaid. LAG case, $Re_{ref} = 120\ 000$, $a/S = 0.50$.

The $1.0U$ line represents the approximate speed at which a wake convects over the blade, and is the lowest contour line on each diagram. The values of $0.88U$ and $0.5U$ correspond to typical leading and trailing edge velocities of a turbulent spot in zero pressure gradient (see Schubauer and Skramstad [117]). $0.7U$ is an approximate mean velocity of propagation for a turbulent strip (see Mayle [94]) and $0.35U$ is a typical convection speed for T-S waves (see Obremski et al. [103]). These trajectories originate approximately at the stator leading edge ($s^* = 0$) at the instant t^* corresponding to the rotor wake passage. Due to difficulties associated with determining the velocity in the region of the stagnation point from discrete data, the trajectories have been adjusted to ensure that they coincide with the wake location at the first surface pressure measurement point ($s^* = \pm\ 0.05$) after the leading edge. The time offset required to place the rotor wake at the origin ($s^* = 0$) at $t^* = 0$ was determined by examining the ensemble mean and RMS traces for the hot-film gauge nearest to the stagnation point for each case. The colour legend at right quantifies the shaded regions, with the maximum and minimum values indicated at the top and bottom respectively.

Gauges adjacent to the stator leading edge show marked fluctuations on each surface, except on the suction surface in the low loading case where the incidence is large and negative. These fluctuations could arise partly from local turbulent breakdown, but are thought to be caused mainly by leading edge potential flow interactions. The leading edge peaks in $<\tau_{RMS}>$ are generally lower for the clocking case $a/S=$ 0.00, where the stator is immersed in the IGV wake street and therefore subjected to a lower level of periodic disturbance associated with the rotor wake passage.

The high and medium loading cases show strong rotor wake-induced periodicity, with wedge-shaped regions of high $<\tau_{RMS}>$ extending close to the leading edge on both suction and pressure surfaces. These are interspersed with regions of lower $<\tau_{RMS}>$ where transition is delayed. The latter effect is most marked for $a/S=$ 0.50, where the IGV wake street lies in the middle of the stator passage and the stator blades are subjected to a higher level of periodic disturbance from the rotor wakes. The level of dimensionless $<\tau_{RMS}>$ in the wake-induced transition path initially falls away from the leading edge, but subsequently rises as sustained transition commences.

The behaviour at low loading is noticeably different due to transition occurring through laminar separation bubbles on both surfaces. The periodicity and extent of suction surface transition is significantly reduced for both clocking cases. Here transition occurs through a mid-chord bubble, with re-attachment around $s^* = 0.75$ where the wall shear stress fluctuations peak. As previously noted the normalising process accentuates the values of dimensionless shear stress fluctuations in regions of low wall shear prior to turbulent re-attachment. Pressure surface transition occurs through a leading edge bubble with re-attachment around $s^* =$ -0.10. There is evidently a much greater susceptibility to changes in the freestream disturbance field when transition occurs close to the leading edge.

A region of high dimensionless $<\tau_{RMS}>$ is observed close to the trailing edge on the stator suction surface in all cases. This is due to incipient turbulent separation reducing the value of the normalising quantity $\overline{\tau}$, rather than a true increase in wall shear stress fluctuations.

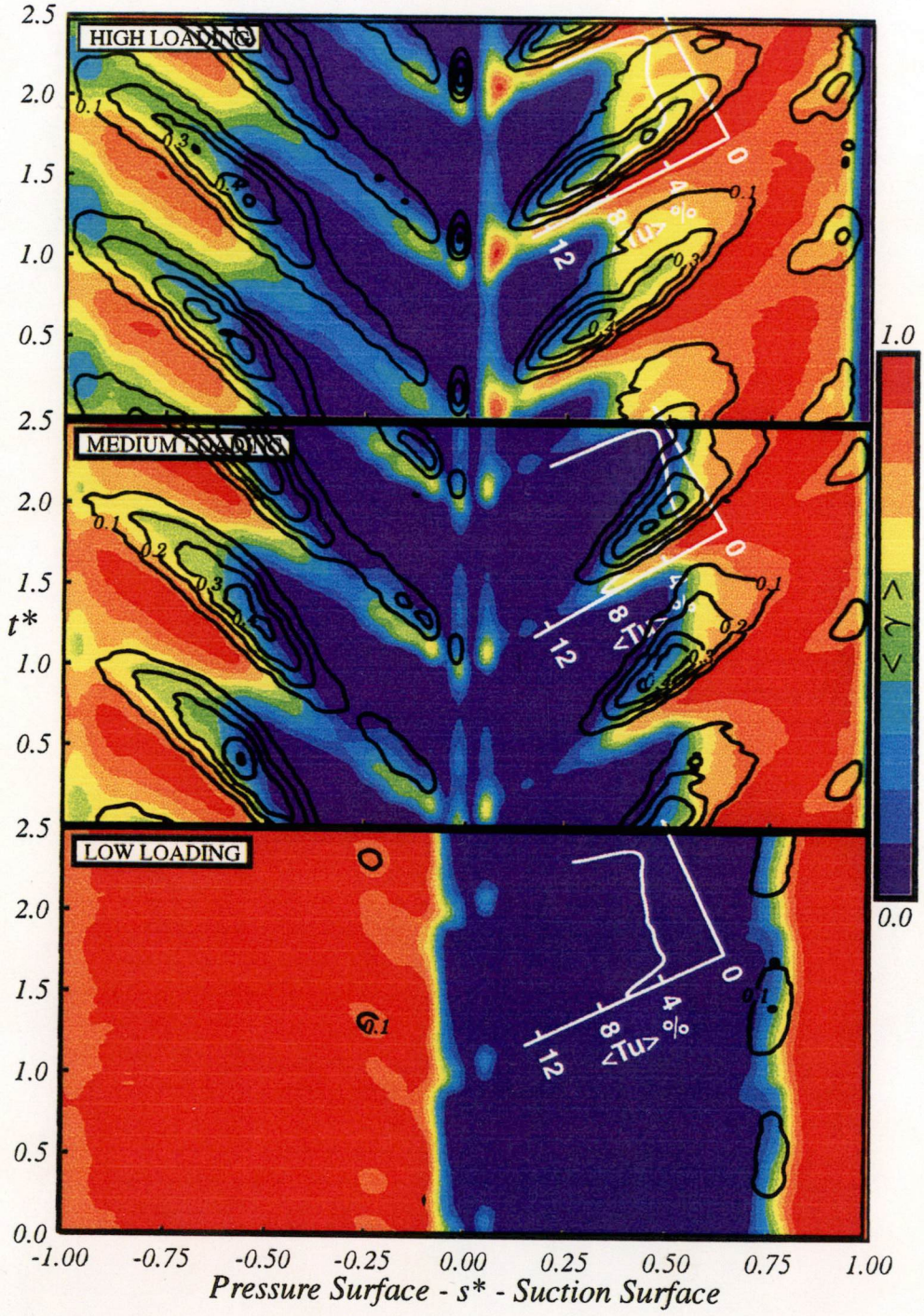

IGV wake street on stator ($a/S = 0.00$)

Figure 7.4: Ensemble average probability of relaxing flow $<\kappa>$. LAG case, Re_{ref} = 120 000, $a/S = 0.00$.

Figure 7.5: Ensemble average intermittency $<\gamma>$. LAG case, Re_{ref} = 120 000, a/S = 0.00.

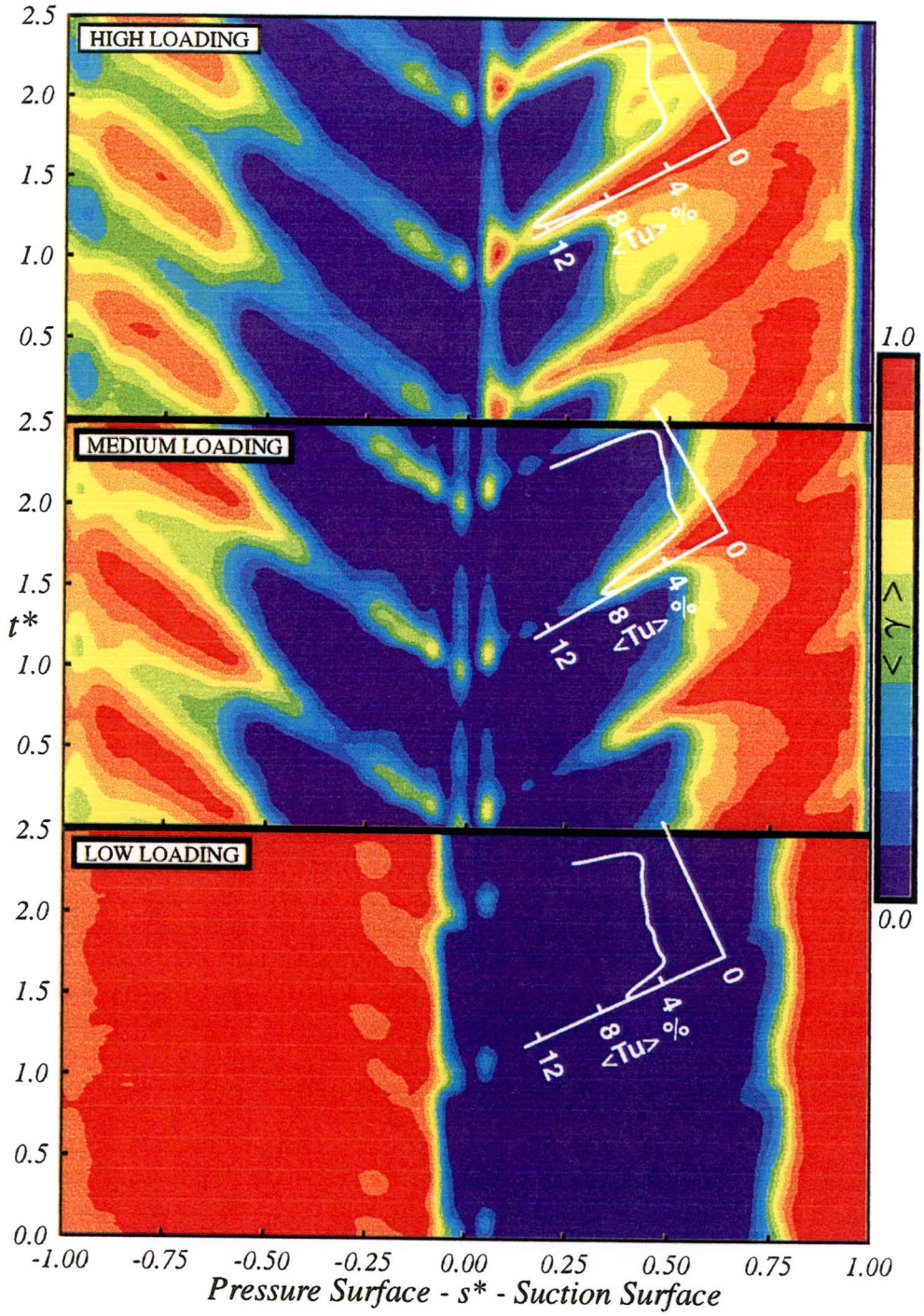

IGV wake street on stator ($a/S = 0.00$)

Figure 7.5: Ensemble average intermittency $<\gamma>$. LAG case, $Re_{ref} = 120\,000$, $a/S = 0.00$.

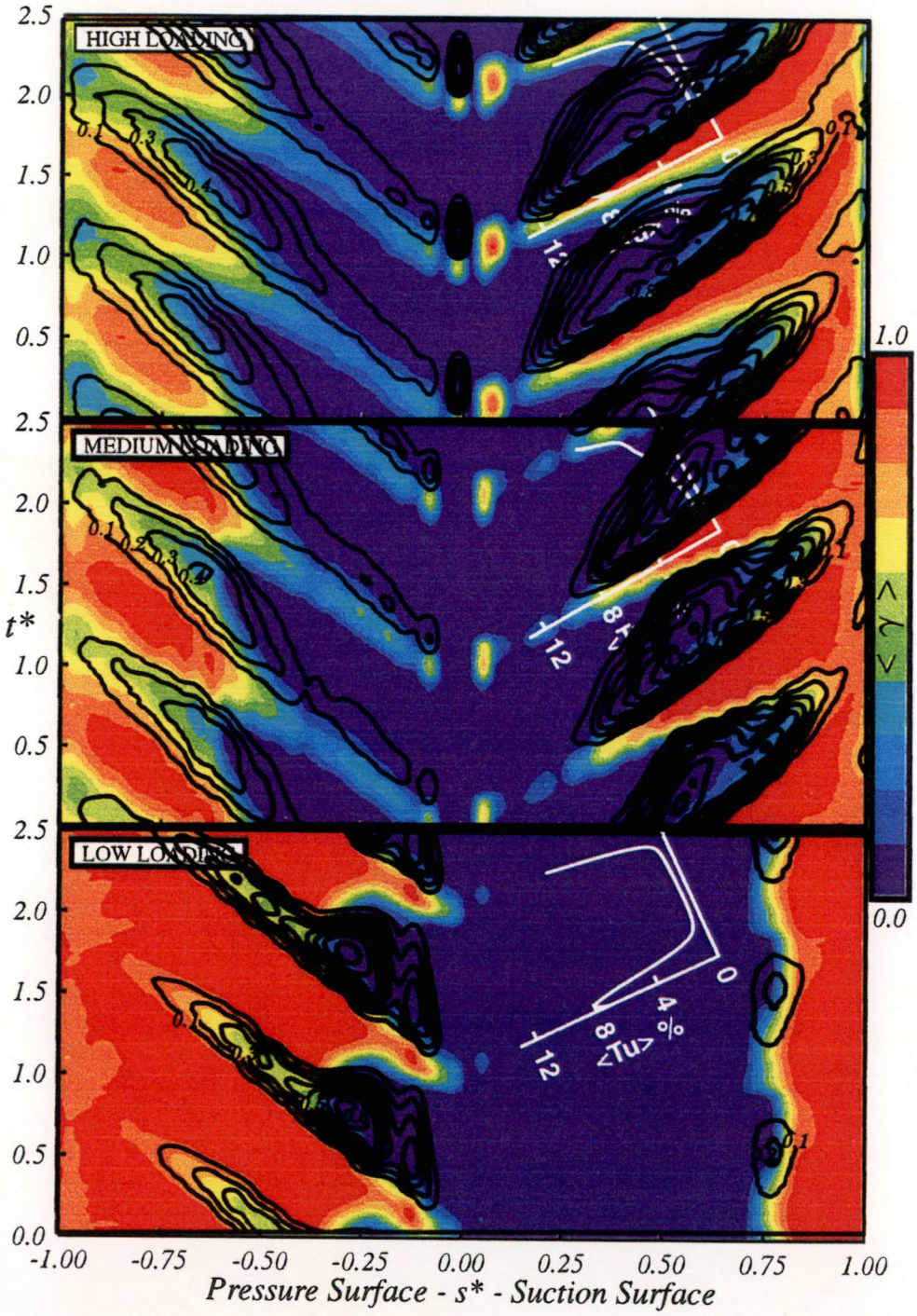

IGV wake street in passage ($a/S = 0.50$)

Figure 7.6: Ensemble average probability of relaxing flow <κ>. LAG case, Re_{ref} = 120 000, $a/S = 0.50$.

Figure 7.7: Ensemble average intermittency <γ>. LAG case, Re_{ref} = 120 000, a/S = 0.50.

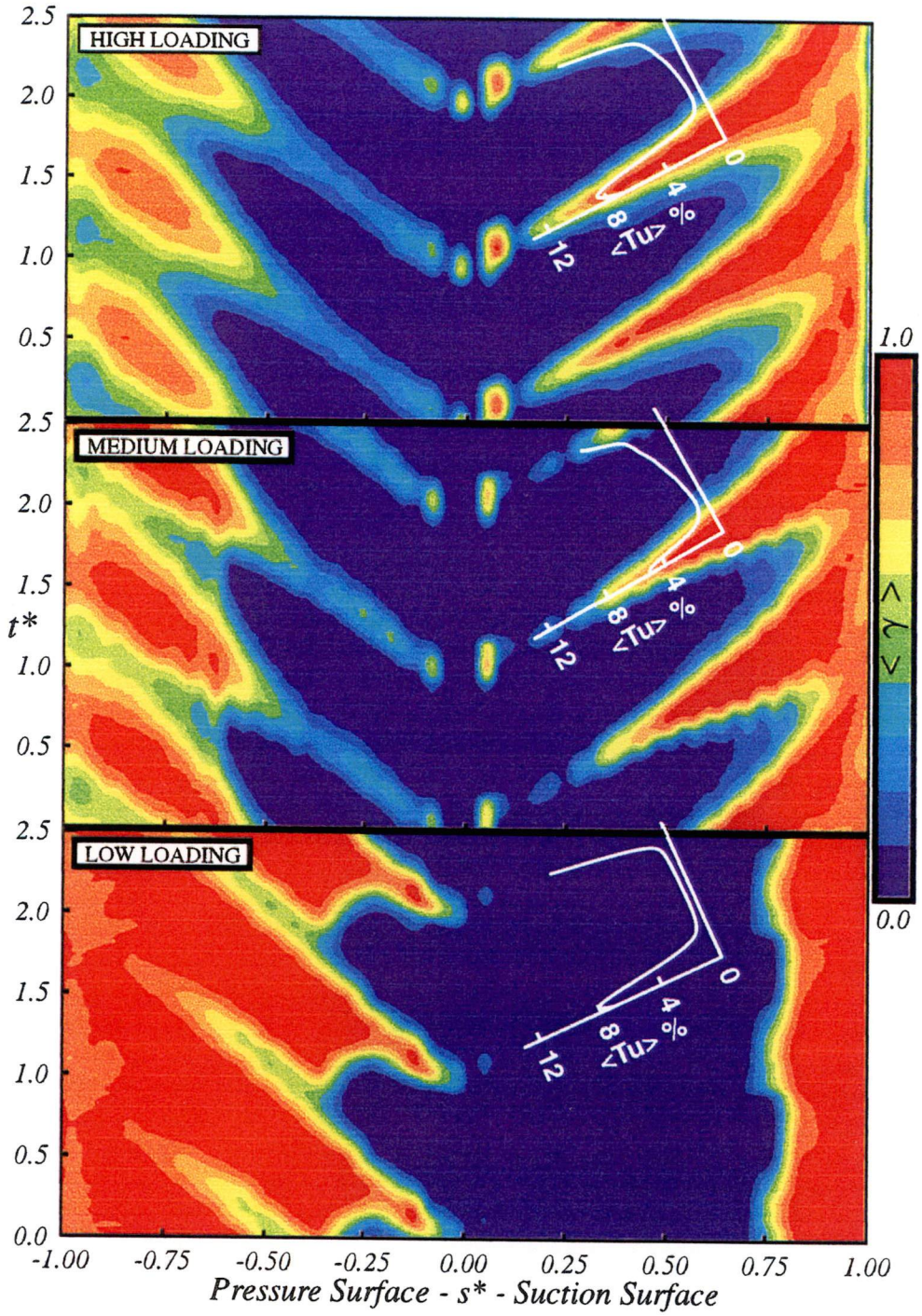

IGV wake street in passage ($a/S = 0.50$)

Figure 7.7: Ensemble average intermittency $<\gamma>$. LAG case, $Re_{ref} = 120\,000$, $a/S = 0.50$.

7.4.2 Ensemble average intermittency and relaxing flow probability

Ensemble average values of turbulent intermittency $<\gamma>$ corresponding to the RMS shear stress measurements presented in Section 7.4.1 are indicated by colour shading on the space-time diagrams of Figs. 7.5 and 7.7 for the large axial spacing (LAG) configuration. The grading is indicated by the colour legend at right, and is from blue for laminar flow ($<\gamma> = 0$) through to red for fully turbulent flow ($<\gamma> = 1$). Superimposed on Figs. 7.5 and 7.7 are curves showing the periodic variation in random freestream disturbance level $<Tu>$ obtained from the inflow measurements at approximately the mid-point of the rotor-stator axial gap. The overlaid graphs have been aligned such that the ordinate lies approximately along the $0.7U$ trajectory, with good phase agreement between the location of peak random turbulence and the forward most turbulent onset location. The peak value of $<Tu>$ is always observed within passing rotor wake regions. Direct comparisons of freestream turbulence variations for the two clocking cases are reported by Solomon et al. [127] and Hughes and Walker [73].

Figs. 7.4 and 7.6 can be used to overlay line contours of constant ensemble average relaxing non-turbulent flow probability $<\kappa>$ on the respective intermittency distributions shown in Figs. 7.5 and 7.7. The non-turbulent relaxing flow is characterised by a higher wall shear stress, with a resulting increase in stability and resistance to separation compared to a steady laminar boundary layer subjected to the same streamwise pressure gradient. Higher values of $<\kappa>$ indicate a greater degree of such "calming" effects, and a more regular appearance of the preceding turbulent spots which are a necessary pre-requisite for this type of flow.

There is some identification of turbulence close to the leading edge which mirrors the high levels of $<\tau_{RMS}>$ seen in Figs. 7.2 and 7.3. This may be partly due to genuine incipient turbulent spots which subsequently decay, or to spurious turbulence identification associated with leading edge potential flow fluctuations produced by passing freestream disturbances. It is also possible that the potential flow fluctuations associated with rotor wake chopping, which produce temporal fluctuations in stator incidence, give rise to a local amplification of turbulence in the neighbourhood of the leading edge similar to that reported by Hobson et al. [63]. In any case, this "turbulence" rapidly decays away from the leading edge. There is an associated region of calmed flow ($<\kappa> > 0$) near the leading edge on the pressure surface, possibly also spurious, which is anti-symmetric with the turbulent flow patch identified on the suction surface. The strength of these leading edge effects increases with loading.

It should be recognised that the values of intermittency obtained from surface hot-film observations will underestimate the peak value of intermittency obtained in a decelerating boundary layer. This explains the anomalous fall in $<\gamma>$ close to the trailing edge on the suction surface, where the turbulent or transitional boundary layer is approaching separation. The anomalous increase in $<\kappa>$ in this region is probably due to incipient separation events being mis-identified as relaxing flow. Apart from these local leading and trailing edge effects, Figs. 7.5 and 7.7 are considered to give a fairly reliable indication of the transitional flow behaviour on the stator blade surface. The contours of $<\gamma>$ certainly give a much clearer indication of transitional flow behaviour than those of $<\tau_{RMS}>$. The wake-induced turbulent strips appear as dark tongues followed by regions of strong calming with high values of relaxing flow

probability $<\kappa>$.

The contours of $<\kappa>$ give the best indication of transitional flow periodicity. This is significantly greater for the clocking case a/S= 0.50 shown in Fig. 7.6, which corresponds to the IGV wakes passing through the stator passage and relatively pure rotor wakes impinging on the stator leading edge. In this case, peak values of $<\kappa>$ exceeding 0.8 are observed on the pressure surface at low loading, and on the suction surface at high and medium loading. On the pressure surface at the low loading condition, transition is occurring through a leading edge bubble and the probability of relaxing flow is accentuated by an extended decay of the shear stress from the initially high levels in the turbulent spot to the very low levels associated with the separation bubble. As noted by Halstead et al. [59] the randomness of passing wake disturbances in the free stream means that a turbulent spot and associated calming region need not occur on each wake passage. In cases where a wake-induced turbulent spot and calmed region are absent, transition by other modes is free to occur; this indicates that a wake-induced turbulent strip is occurring in over 80% of rotor wake passing events. Peak values of $<\kappa>$ on the pressure surface only reach about 0.4 at medium and high loading, and there is little variation in the transition behaviour for these two cases. The lowest periodicity occurs on the suction surface for the low loading case, where the blade is operating at large negative incidence and transition occurs through a mid-chord separation bubble with turbulent re-attachment around s^* = 0.75. Negligible evidence of wake-induced transition is observed, and is emphasised by the lack of calming effects and the nearly vertical contours of $<\gamma>$.

The transitional flow periodicity is markedly reduced for the clocking case a/S= 0.00 shown in Fig. 7.5, which corresponds to the IGV wake street being incident on the stator. On the suction surface at high and medium loading the peak value of $<\kappa>$ is now only 0.4, and the chord-wise extent of transitional flow is much smaller. On the pressure surface at low loading, the flow periodicity has almost disappeared. Solomon et al. [127] show evidence that the change in pressure surface behaviour is largely due to changes in the inflow random turbulence caused by IGV clocking. For the cases showing weaker periodicity with a/S= 0.50 (namely the pressure surface at high and medium loading, and the suction surface at low loading) the transitional flow behaviour is quite similar to that for a/S= 0.00.

Transition in the wake-induced path apparently commences at the leading edge on both suction and pressure surfaces in the high and medium loading cases. However, the values of intermittency initially decay or remain at a low level until some critical situation is reached and sustained transition can occur. The values of $<\gamma>$ then increase monotonically until transition is complete (ignoring the spurious reductions near the trailing edge described above). As expected, there is a general trend for the transition onset to move forward on the suction surface and rearward on the pressure surface as loading is increased.

This behaviour is most clearly seen on the pressure surface at high and medium loading, where a streak of low level intermittency in the rotor wake path extends to the leading edge, but sustained transition does not commence until about s^* = -0.4. Another factor here could be the impingement of the rotor wake jet on the stator pressure surface, which will directly impress turbulent rotor wake fluctuations on the boundary layer fluid. This provides further potential for the inception of unsustainable turbulent spots, or the mis-identification of these freestream fluctuations as boundary

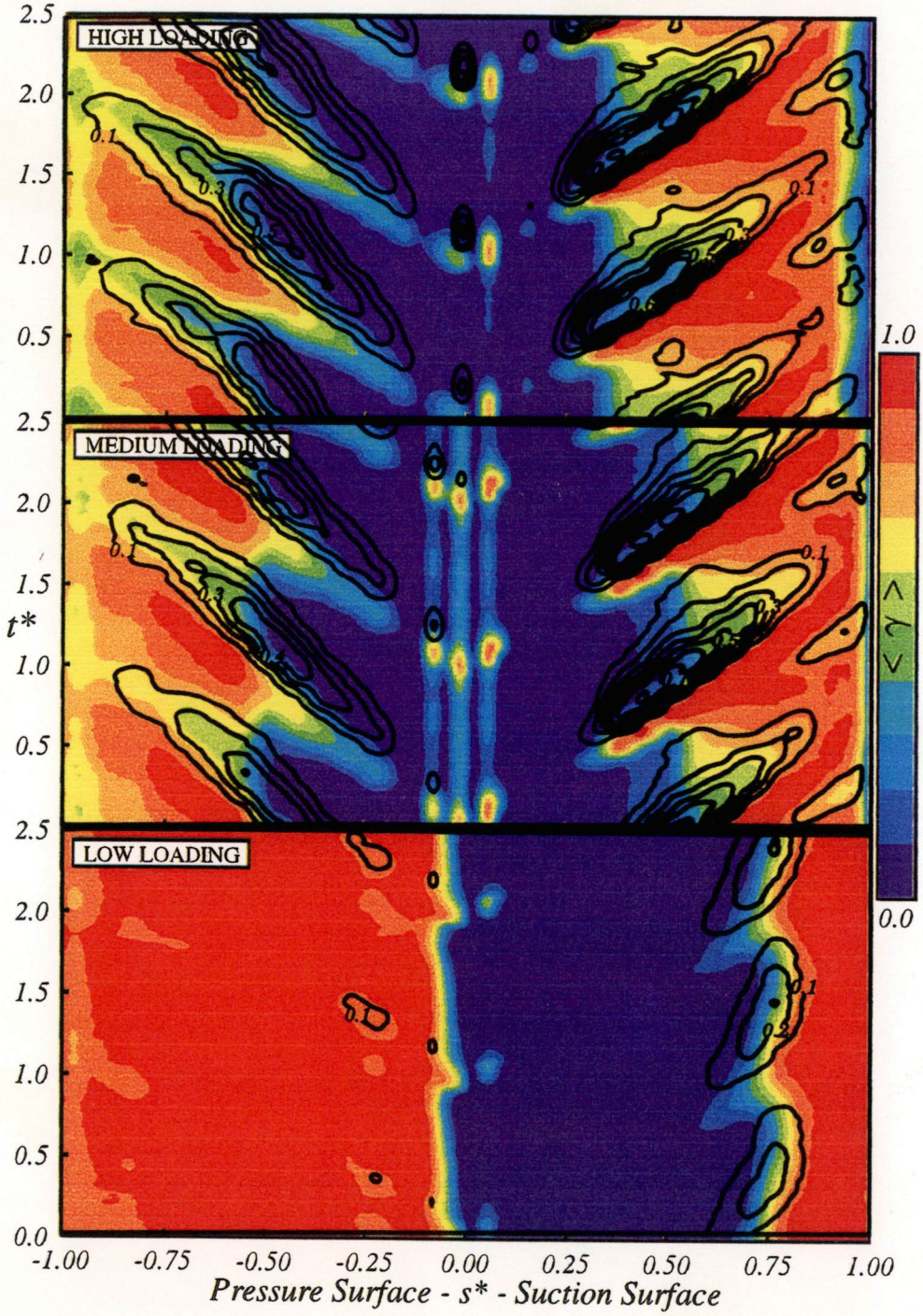

IGV wake street on stator ($a/S = 0.00$)

Figure 7.8: Ensemble average probability of relaxing flow <κ>. SAG case, Re_{ref} = 120 000, $a/S = 0.00$.

Figure 7.9: Ensemble average intermittency <γ>. SAG case, Re_{ref} = 120 000, a/S = 0.00.

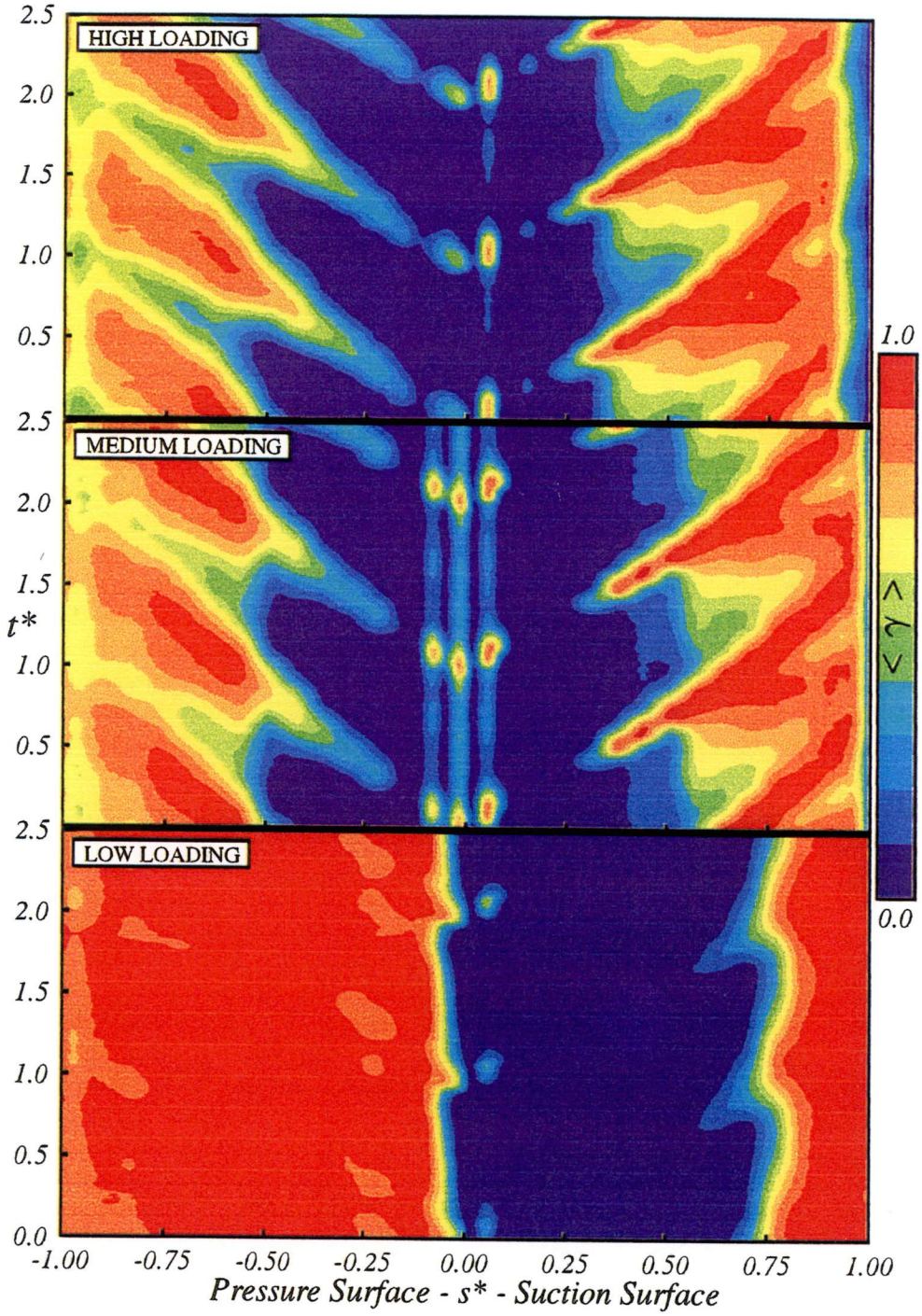

IGV wake street on stator ($a/S = 0.00$)

Figure 7.9: Ensemble average intermittency $<\gamma>$. SAG case, $Re_{ref} = 120\ 000$, $a/S = 0.00$.

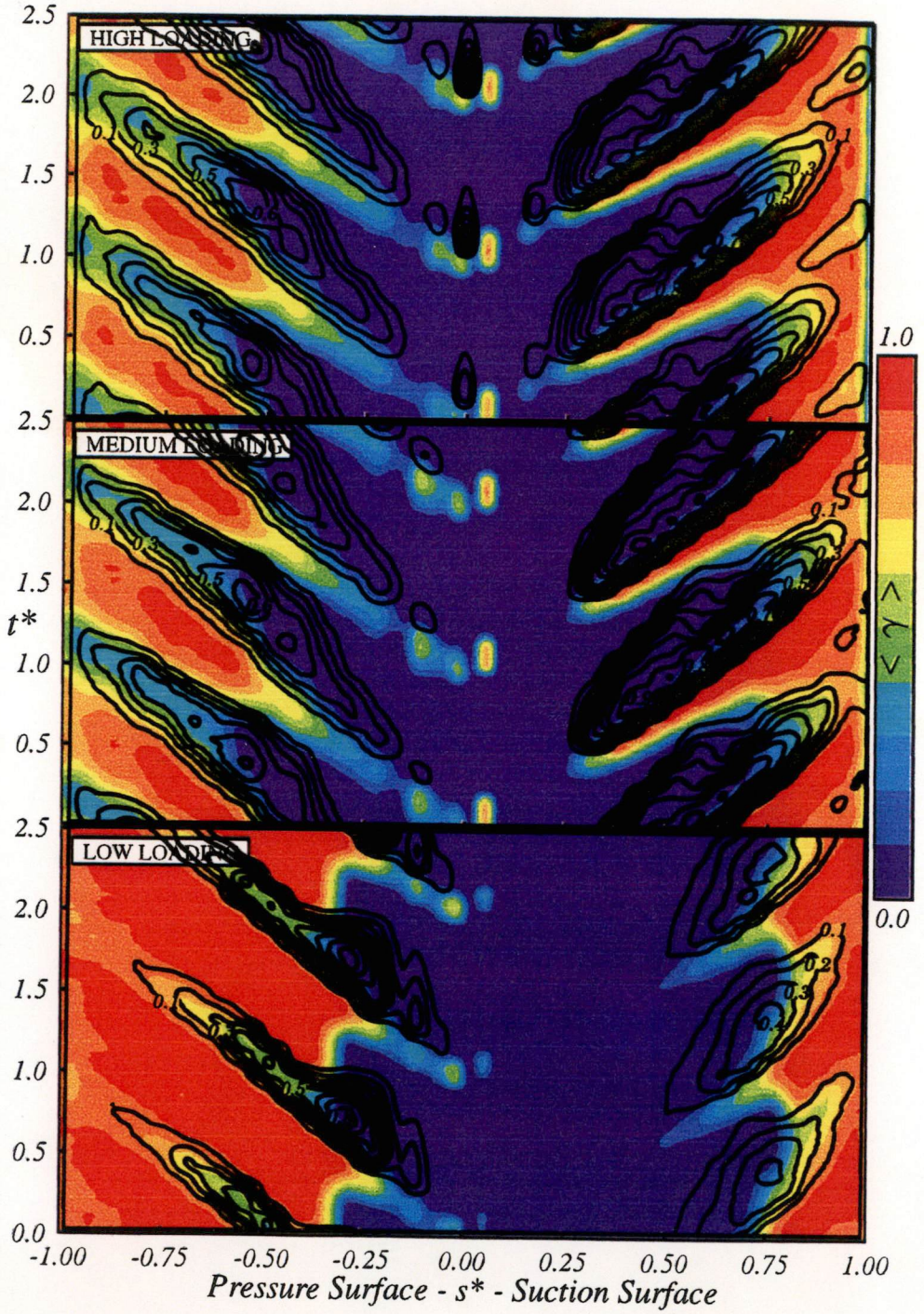

IGV wake street in passage ($a/S = 0.50$)

Figure 7.10: Ensemble average probability of relaxing flow <κ>. SAG case, Re_{ref} = 120 000, a/S = 0.50.

Figure 7.11: Ensemble average intermittency <γ>. SAG case, Re_{ref} = 120 000, a/S = 0.50.

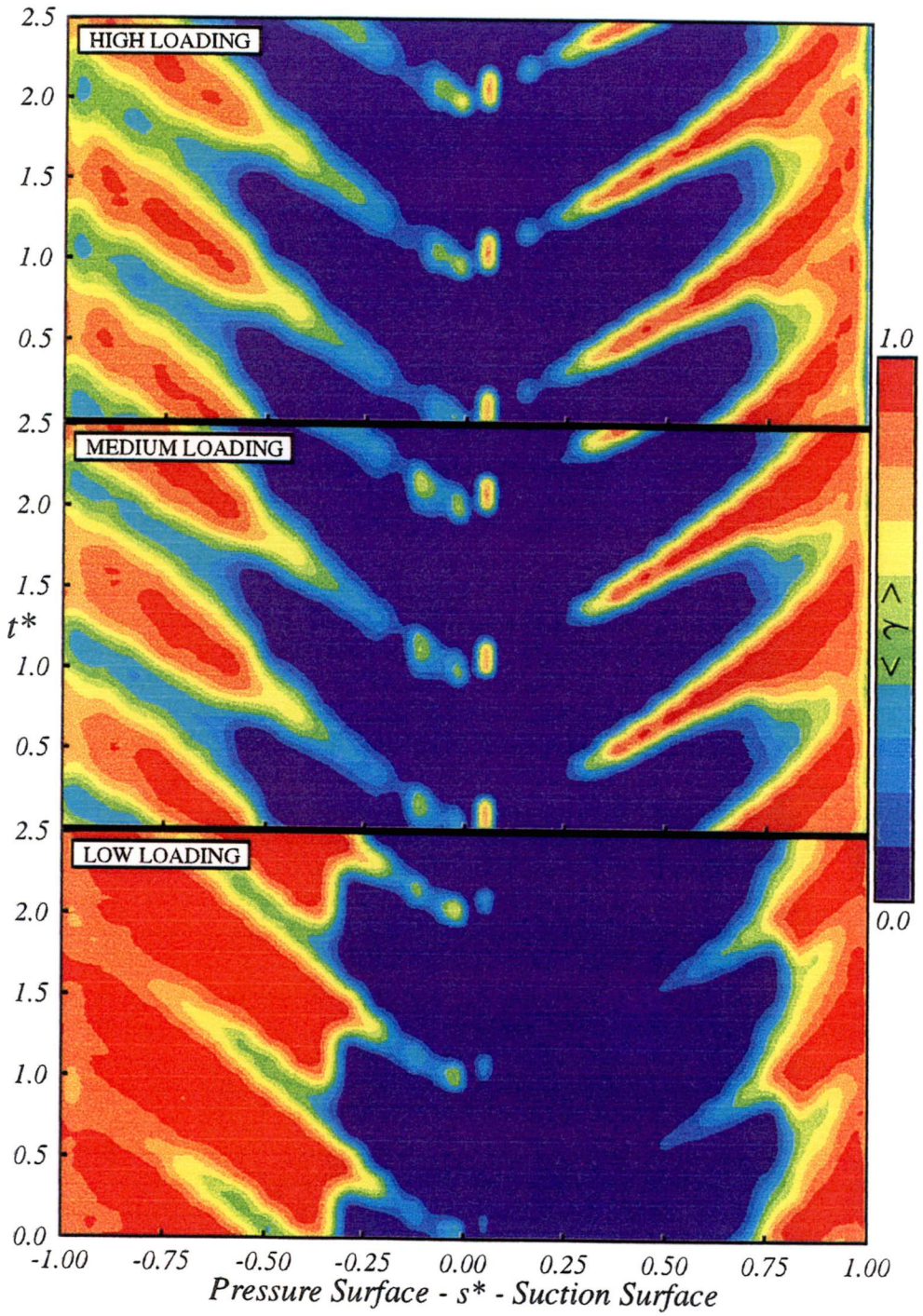

IGV wake street in passage ($a/S = 0.50$)

Figure 7.11: Ensemble average intermittency $<\gamma>$. SAG case, Re_{ref} = 120 000, a/S = 0.50.

layer turbulence. This situation should not occur on the suction surface, where the wake jet is convecting rotor wake fluid away from the stator.

Figs. 7.9 and 7.11 show the influence of the reduction in rotor-stator axial spacing (RAG case) on the space-time diagrams of intermittency for the corresponding blade loading and IGV clocking cases previously presented. With the IGV wake street on the stator blade (a/S= 0.00) the results are similar: compare Fig. 7.9 with Fig. 7.5. At the high and medium loading conditions there is a trend for the wake-induced transition to start later on the suction surface and earlier on the pressure surface, although this is only marginal, and is thought to be predominantly associated with the reduction in incidence associated with the rotor-stator axial spacing change outlined in Table 4.1. An increase in the amount of turbulent flow identified around the leading edge is noted, particularly at the medium loading condition. The fall in intermittency at the trailing edge associated with turbulent separation is still apparent and there is some evidence that the older turbulent fluid inside the wake-induced strip separates earlier. On the pressure surface there is little evidence of the streak of low level intermittency prior to sustained transition noted in the LAG case. It appears that both the suction and pressure surface transition behaviour is more periodic than previously noted and this is supported by the increased level of non-turbulent relaxing flow identified in Figs. 7.8 and 7.10.

The effect of reducing the axial blade row spacing on the unsteady bubble transition mechanisms is observed by comparing the bottom portion of all four intermittency figures (see Figs. 7.5, 7.7, 7.9 and 7.11) . The effects on the pressure surface are minor, although there is some change in the unsteady re-attachment location of the leading edge separation bubble in the path between wake-induced strips for the a/S= 0.50 case. The effects on the mid-chord separation bubble on the suction surface are more pronounced with the appearance of stronger wake-induced transitional strips. These occur at $s^* \simeq 0.60$ and 0.50 for the a/S= 0.00 and 0.50 cases, respectively. The stronger wake-induced strip is accompanied by an increase in the relaxing flow probability (see Figs. 7.8 and 7.10). This increase in calming lengthens the transitional flow region in the path between wake-induced events and there are still regions of transitional flow persisting to the trailing edge in the a/S= 0.50 case (see Fig. 7.11). The unsteady effects on the transition in the mid-chord bubble are attributed to the increased rotor wake turbulence combined with the increase in strength of the rotor wake-jet effect, although the relative magnitude of the two effects is not known. These unsteady changes are too far rearward to be influence by leading edge interactions.

7.4.3 Long term mean intermittency and relaxing flow probability

Plots of time-mean intermittency $\overline{\gamma}$ and relaxing flow probability $\overline{\kappa}$ give a simplified picture of the variation in transitional flow behaviour associated with the changes in freestream periodicity. The left-hand side of Fig. 7.12 shows the variation of $\overline{\gamma}$ with blade loading when the IGV wake street passes over the stator blade (a/S= 0.00): the right-hand portion indicates the alternative IGV clocking case (a/S= 0.50). The closed symbols are the LAG case, whilst the open symbols represent the RAG case. The $\overline{\gamma}$ curves exhibit local peaks in apparent intermittency at the leading edge for both the high and medium loading cases, regardless of IGV wake location, with the highest levels observed at the medium-loading a/S= 0.00 case. These decay rapidly until a

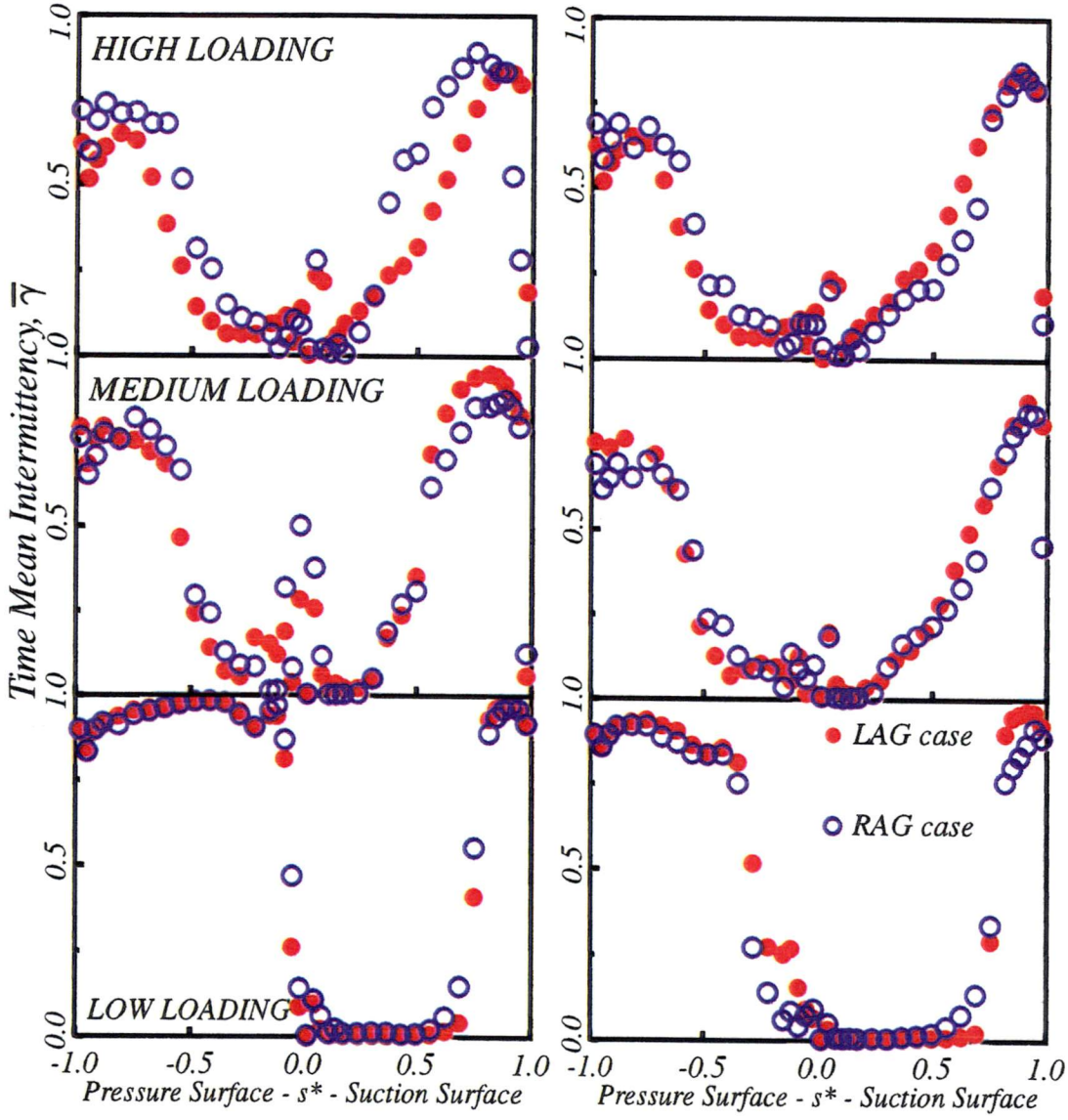

(a) a/S= 0.00 – IGV wake on stator. (b) a/S= 0.50 – IGV wake in passage.

Figure 7.12: Long term mean intermittency. Variation with stator loading and IGV clocking and axial row spacing.

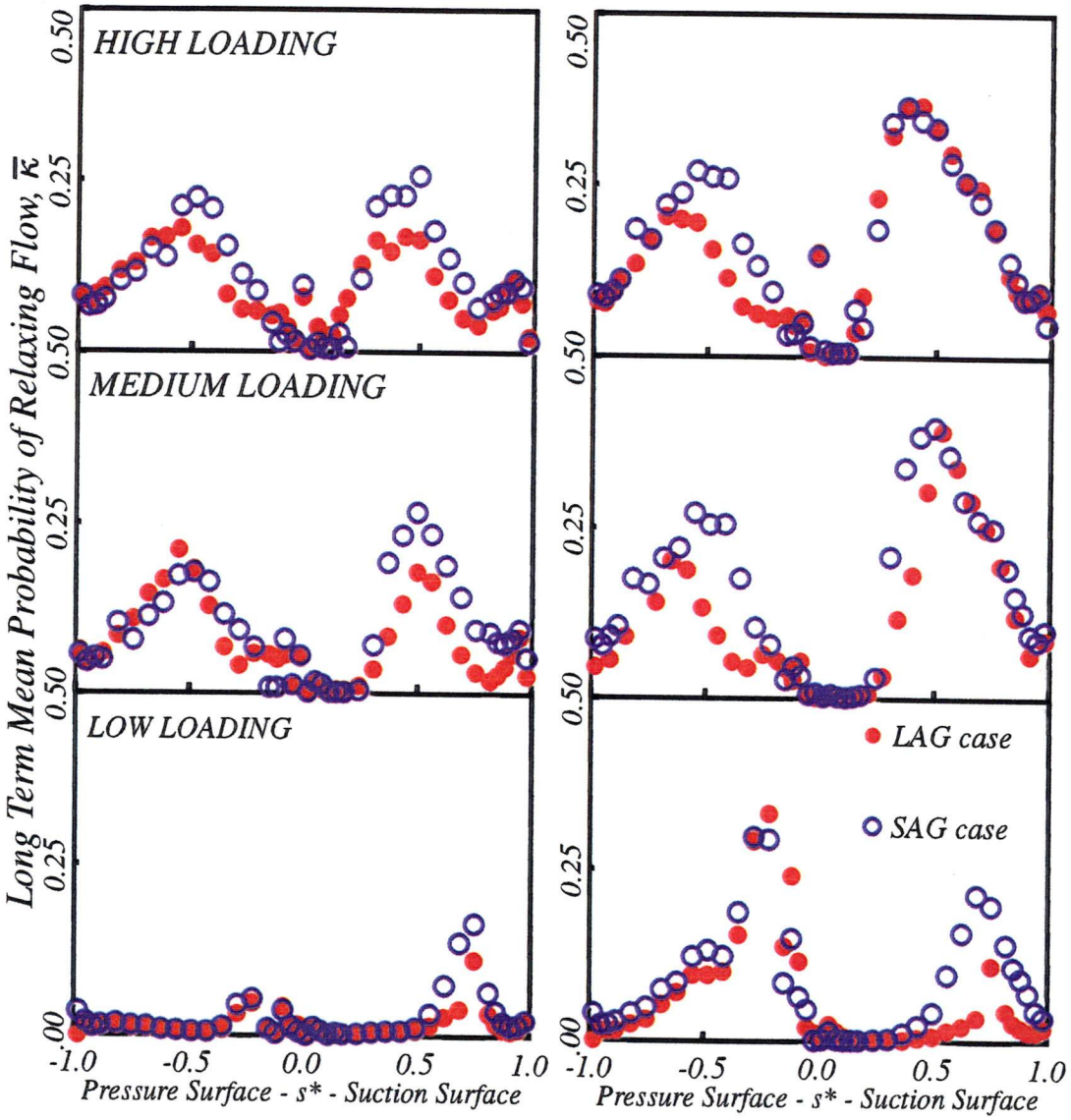

(a) a/S= 0.00 – IGV wake on stator. (b) a/S= 0.50 – IGV wake in passage.

Figure 7.13: Long term mean probability of relaxing flow. Variation with stator loading and IGV clocking and axial row spacing.

sustained increase in $\overline{\gamma}$ occurs further along the blade surface. The level of $\overline{\gamma}$ prior to this increase is significantly higher on the pressure surface, possibly due to boundary layer perturbation by rotor wake jet impingement. On this surface there is a trend for the level of $\overline{\gamma}$ to be higher for the a/S= 0.00 case. Transition is completed more rapidly on the suction surface at high and medium loading and the pressure surface at low loading. It is most abrupt when transition occurs on the pressure surface via the leading edge separation bubble, when the IGV wake is incident on the stator leading edge, and there is no observable calming effect delaying the onset and completion of transition. On the opposite surface of the stator in these respective cases, altering the freestream periodicity produces little change in the distribution of $\overline{\gamma}$.

Fig. 7.13 indicates that the significant variations in $\overline{\gamma}$ seen in the space-time diagrams of Figs. 7.5, 7.7, 7.9 and 7.11 are accompanied by marked changes of the relaxing flow probability $\overline{\kappa}$. The stronger freestream periodicity for a/S= 0.50 (right-hand side of Fig. 7.13) produces corresponding increases in the transitional flow length and the magnitude of calming (as indicated by higher peak values of $\overline{\kappa}$). At high and medium loading, relaxing flow events (or calming) are observed over 70-80% of the suction surface, and the distributions of $\overline{\kappa}$ indicate that transition is not quite complete at the trailing edge. For the cases in which IGV clocking produces a negligible change in the intermittency distribution there is a similarly small variation in the relaxing flow probability. The variation in $\overline{\kappa}$ for the RAG case are at least equal and generally greater in magnitude than the results for the LAG case, emphasising the increase in periodicity with reduction in axial blade row spacing.

7.4.4 Extent of transitional flow

The extent of transitional flow on the stator for the large axial spacing condition is presented on an ensemble average basis in Fig. 7.14. The periodic variations in transitional flow are indicated by shading on the $t^* \sim s^*$ diagram between limits of $<\gamma>$ = 0.10 for transition onset and $<\gamma>$ = 0.90 for transition completion. These limiting values were chosen to minimise spurious effects of turbulence mis-identification which occur at very low and very high intermittency. The full extent of transitional flow will be a little greater than that indicated. A slight difference in arrival times of the wake-induced transitional strips is evident for the two IGV clocking positions. This differential increases with loading, and may be due to circumferential variations in mean velocity altering the rotor wake convection speed.

Periodic fluctuations in the onset of transition are much weaker for the clocking case a/S= 0.00, where the IGV wake street impinges on the stator and the freestream periodicity is lowest. This is seen most clearly on the suction surface at high and medium loading. For a/S= 0.50, transition onset occurs much later in the regions between successive rotor wake passages. The theoretical predictions of Solomon et al. [127] show that the earlier onset for a/S= 0.00 is largely due to the higher level of freestream turbulence $<Tu>$ when the IGV wake impinges on the stator. The calming effects of preceding wake-induced transitional strips appear to have had only a slight influence on the inter-wake transition onset for a/S = 0.50. There are two main reasons for this behaviour. First, the wake-induced transitional strips do not occur on every rotor wake passage; hence there will always be some transition events where calming is non-existent. Second, the region in which calming is significant spreads only gradually

from the vertex of the wake-induced transitional strips, with a limiting convection speed of approximately $0.3U$ at its trailing edge.

Increased freestream periodicity, characterised by an increase in the amplitude of the phase-locked periodic turbulence (see overlaid graphs on Figs. 7.5 and 7.7), generally produces both a later transition onset and a lengthening of the transition region between successive rotor wake passages. The inter-wake transitional region extends to the rear of the suction surface at high and medium loading, and will apparently be terminated only by turbulent contamination from adjacent wake-induced turbulent strips. The lengthening of the transition region will be influenced by calming from the wake-induced transitional strips and also by the effects of fluctuating blade surface pressure distributions on boundary layer stability. It is conceivable that the latter effect may be most marked on the pressure surface where unsteadiness may cause the pressure gradient to fluctuate between positive and negative.

The most dramatic effect of increased periodicity is observed on the pressure surface for the low loading case. Here transition occurs through a leading edge separation bubble which is little affected by freestream unsteadiness for the case of IGV wake impingement on the stator, a/S= 0.00; but the impingement of stronger rotor wake disturbances for a/S= 0.50 produces a marked change in the transitional flow distribution. Transition onset occurs at the leading edge in a thin strip along the rotor wake path for a/S= 0.50. This is immediately followed (in time) by a region of strong calming ($<\kappa>_{max} \simeq 0.8$) along which the transition region is greatly extended. After this calming region there appears to be a marked leading edge separation, with reattachment around 25% chord characterised by a very short transition and associated region of very high wall shear stress fluctuations (shown in Figs. 7.7 and 7.11).

7.5 Conclusions

The periodicity of transition on the outlet stator was strongly influenced by blade loading, clocking of the upstream IGV row and axial row spacing. The magnitude of these effects tended to increase with incidence, and were strongest when transition occurred through a leading edge separation bubble. The leading edge and mid-chord bubbles respond in a characteristically different manner to the effects of altered inlet disturbance field and axial blade row spacing. The effects of changing the freestream disturbance field are most pronounced when transition occurs through a leading edge separation bubble; there is little change in mid-chord bubble behaviour. Transition via a mid-chord bubble was more sensitive to the effects of axial blade row spacing.

Marked variations in transitional flow periodicity were never observed on both suction and pressure surfaces at once. The surface hot-film observations showed significant fluctuations from leading edge potential flow interactions with rotor wake disturbances; they also indicated perturbed laminar boundary layer behaviour on the pressure surface in regions of rotor wake jet impingement. The existence of significant potential flow (pressure field) interaction at the stator leading edge is confirmed by hot-wire observations outside the boundary layer.

The measurements reported here relate to a single blade element at mid-span. Skewing of the IGV wake street relative to the radial direction as it convects downstream will cause stator blade elements at different radial positions to experience unsteady flow

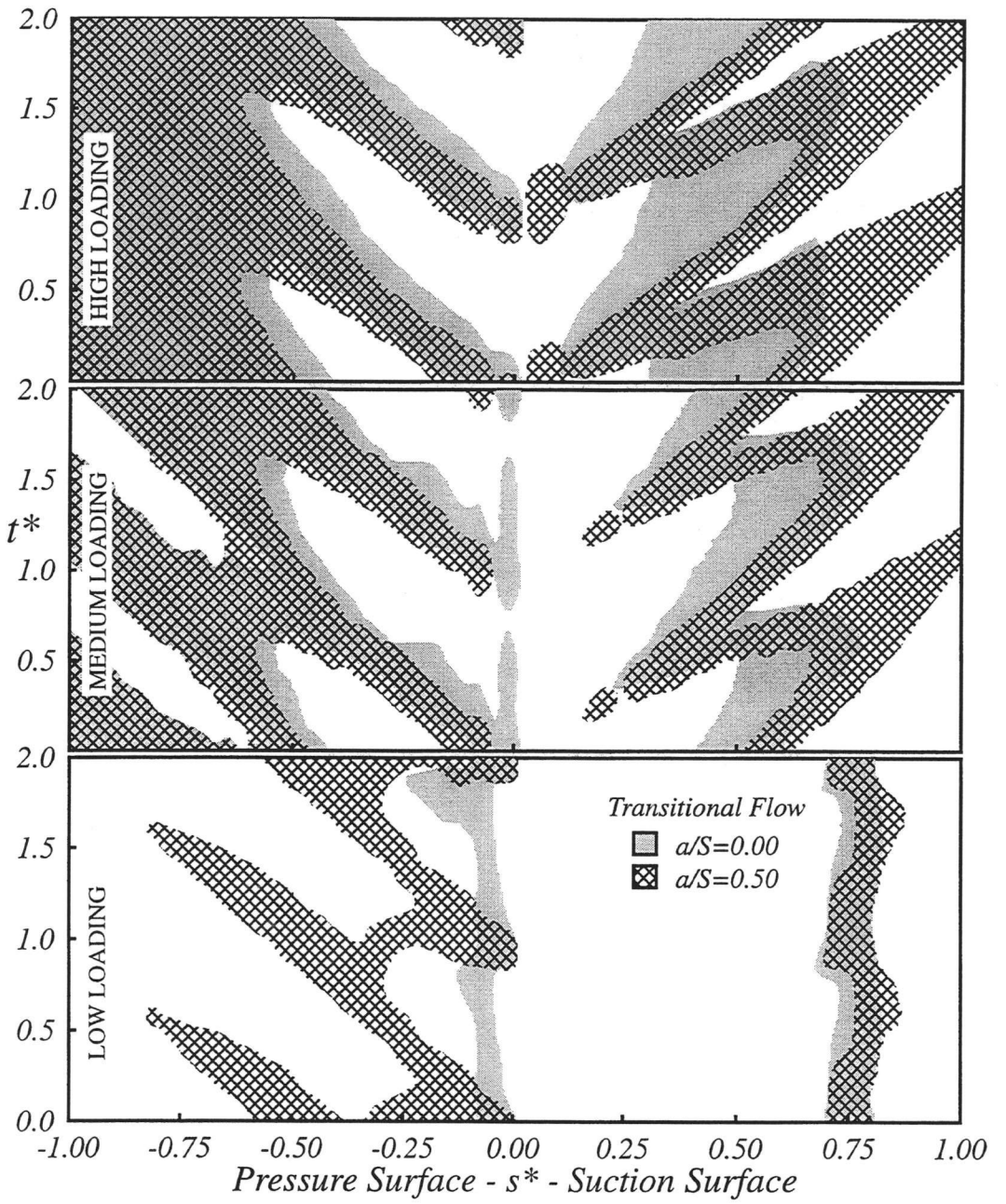

Figure 7.14: Extent of transitional flow on stator, showing influence of stator loading and IGV clocking. (Transition onset : $<\gamma> = 0.10$; transition end : $<\gamma> = 0.90$.)

behaviour ranging between the two limiting cases of maximum and minimum periodicity. The blades of an embedded rotor row in a multi-stage machine will experience similar flow variations.

It is important to appreciate the resulting range of unsteady conditions under which axial turbomachine blade elements have to operate. It appears from observations of the stator suction surface behaviour at low loading that flow acceleration at the leading edge will reduce transitional flow periodicity at design conditions. Thus more modern blade sections with peak suction further rear-ward could show a reduced transitional flow periodicity. On the other hand, the lower axial spacings in practical turbomachines would tend to increase the magnitude of periodic freestream disturbances and associated periodic transition phenomena.

Chapter 8

Onset of Transition

8.1 Introduction

Studies of transition under conditions representative of an embedded axial turbomachine blade row are rare. The definitive investigation of Halstead et al. [58, 59, 60, 61] provided extensive data from surface film arrays on a third stage compressor stator and second stage turbine stator. These workers claimed no evidence of Tollmien-Schlichting (T-S) waves prior to the appearance of turbulent breakdowns. Solomon and Walker [124], however, noted some evidence of T-S wave activity from raw surface film traces obtained under essentially similar conditions.

Solomon et al. [127] used the MISES code of Youngren and Drela [152] in a quasi-steady manner to predict the temporal variation of transition onset on an axial compressor stator blade over a rotor passing period. Parallel computations for natural transition and bypass transition indicated that the natural transition mode tended to dominate for the compressor blade. The success of the MISES transition onset predictions provided strong circumstantial evidence for the importance of natural transition mechanisms in strongly decelerating flow on the blades of the compressor used in the current study.

The work covered in this chapter gained its initial impetus from these predictions. It is therefore appropriate to review the computational methods that are implemented in the MISES code, and the following section is devoted to this. The chapter continues by reviewing processes important to transition onset for gas turbine blades and highlights experimental observations where T-S waves appear to play an important role prior to the inception of turbulent spots. Data from the surface hot-film array presented in Chapter 7 are re-analysed to look for direct evidence of natural transition phenomena. An algorithm is developed to identify instability waves within the T-S frequency range. The algorithm is combined with a turbulent intermittency detection routine to produce space~time diagrams showing the probability of instability wave occurrence prior to regions of turbulent flow. Extensive regions of amplifying instability waves are identified. This indicates that linear stability theory remains important for transition in an adverse pressure gradient, even under elevated free-stream turbulence levels. This work challenges the conventional view that transition at such elevated disturbance levels should occur entirely in a bypass mode. The related implications for transition prediction in decelerating flow regions on axial turbomachine blades are discussed in

conclusion.

8.2 MISES Background

MISES evolved from an external aerodynamics flow solver and inherited an e^n -type transition correlation. This method, based on the Orr-Somerfield equation, is used to predict the growth of T-S waves in the laminar boundary layer. Natural transition is predicted when the amplification ratio computed from linear stability theory has reached some critical level, $e^{n_{crit}}$. At low turbulence levels commonly found in external aerodynamics, n_{crit} =9.0 is typically used. The transition model in MISES uses a correlation due to Mack [89] to adjust n_{crit} for elevated turbulence levels. Further adjustment to n_{crit} is made to allow for larger turbulence levels than the original Mack correlation. The relationship between n_{crit} and turbulence Tu used in MISES is given by

$$n_{crit} = -8.43 - 2.4ln(0.027tanh(Tu/2.7)) \tag{8.1}$$

A bypass transition criterion based on the Abu-Ghannam and Shaw [1] correlation is also included in MISES. Drela [33] found that when this transition correlation is expressed in its original form, using the pressure gradient parameter λ_θ, the coupled viscous-inviscid problem becomes ill-posed. Drela re-expressed the correlation in terms of boundary layer shape factor H to avoid this problem. The MISES version of the Abu-Ghannam and Shaw correlation is given by

$$Re_\theta(H, n_{crit}) = 155 + 89.0\left(0.25tanh\left(\frac{10}{H-1} - 5.5\right) + 1\right)(n_{crit})^{1.25} \tag{8.2}$$

This expression closely matches the original Abu-Ghannam and Shaw correlation for $Tu>$ 0.5%. At lower turbulence levels, Eqn. (8.2) over-predicts $Re_{\theta crit}$ compared with the original formulation.

In the standard version of MISES, both the e^n and Abu-Ghannam and Shaw (natural and bypass) transition models are active simultaneously. Transition is initiated by whichever of the two alternative criteria is satisfied first. Fig. 8.1 (from Drela [33]) compares the behaviour of the two transition models for similar flows. In adverse pressure gradients, where the shape factor H is high, the e^n method predicts transition significantly earlier at all turbulence levels. The discrepancy in $Re_{\theta crit}$ predictions at similar conditions for the two alternative transition modes brings the accuracy of both correlations into question. Drela [33] notes that with most adverse pressure gradient flows found on airfoils $Re_{\theta crit}$ for the e^n method will be larger than indicated in Fig. 8.1, and therefore closer to the Abu-Ghannam and Shaw criterion. Drela also speculates that the adverse pressure gradient experiments of Abu-Ghannam and Shaw [1] involved significant T-S-wave growth and that transition was not the result of direct bypass transition: this implies that the Abu-Ghannam and Shaw criterion represents bypass transition in favourable pressure gradients, but mostly T-S-wave transition in adverse pressure gradients.

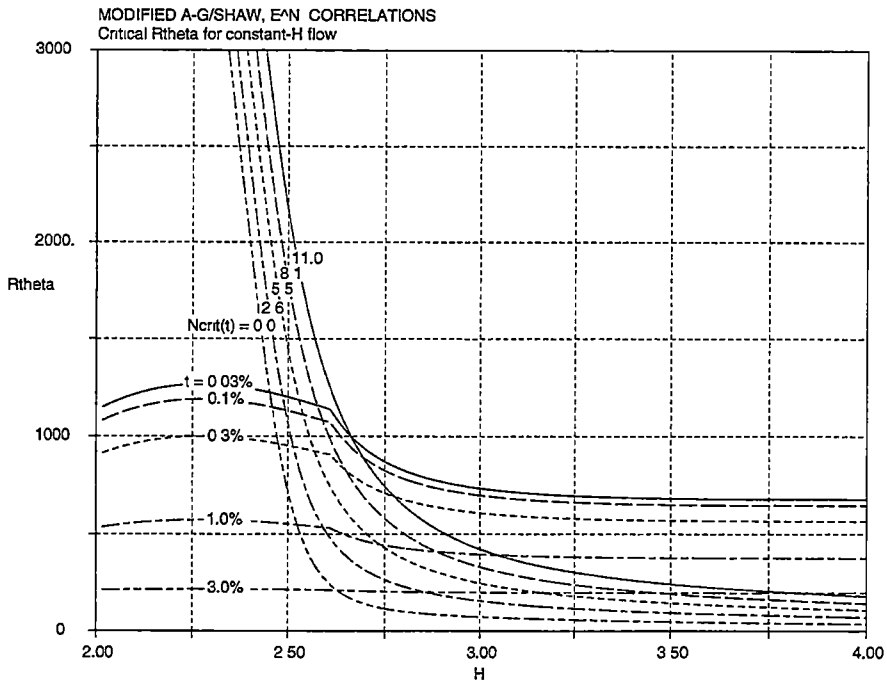

Figure 8.1: Critical R_θ versus shape parameter H for similar flows. Comparison of e^n method and Abu-Ghannam and Shaw method predictions. From Drela [33].

8.3 Natural vs Bypass Transition

As previously noted in Chapter 7 the boundary layers on blades of an embedded row in a multi-stage axial turbomachine are dominated by the effect of the adjacent upstream stage. The unsteady laminar-turbulent transition behaviour under these conditions is largely controlled by periodic transition induced by the relative motion of blade wakes from the row immediately upstream. The overall morphology of unsteady transition behaviour for compressors and turbines is well documented by the extensive set of observations reported by Halstead et al. [58, 59, 60, 61].

The three important processes identified by Mayle [93] in his review of laminar-turbulent transition in gas turbines are:

- Natural transition
- Bypass transition
- Separated flow transition

Both Halstead et al. [58] and Mayle [93] provide detailed discussions of these phenomena. They are more thoroughly reviewed in Chapter 2.

The natural transition process, which occurs under conditions of very low free-stream turbulence level, can be divided into four main regions:

(1) A region of instability to small two-dimensional disturbances (T-S waves). The onset of instability and the initial growth of T-S waves are well described by linearised theory.

(2) The appearance of three-dimensional instability which produces periodic spanwise flow distortions. This introduces streamwise vorticity and causes a rapid nonlinear amplification of the spanwise waves into vortex loops (hairpin eddies or lambda vortices).

(3) The initiation of turbulent spots (or "breakdowns") through the appearance of high frequency fluctuations in regions of high shear near the heads of the vortex loops.

(4) A transition zone in which adjacent turbulent spots merge to form a continuously turbulent flow.

Bypass transition, as described by Mayle [93], "... is caused by large disturbances in the external flow (such as free-stream turbulence) and completely bypasses the T-S mode of instability." Turbulent spots are then "... directly produced within the boundary layer under the influence of the free-stream disturbances." Mayle concluded that linear stability theory would be irrelevant in the case of bypass transition. However, Walker [142] took a contrary view, arguing that stability theory should at least be of relevance in relation to the length of transitional flow in the bypass mode.

Basic experiments on artificially generated turbulent spots such as those of Tso et al. [132], Breuer and Haritonidis [15], Breuer and Landahl [16] and Cohen et al. [21] show that stages 1–2 of natural transition (as defined above) are not necessarily absent from transitional flows generated by external disturbances. Perturbations of the boundary layer by a pulsed jet or surface membrane produce a combination of transient and three-dimensional wave packet disturbances. For weak initial disturbance amplitudes the transient component decays; turbulent breakdown occurs well downstream of the initial disturbance location after the wave packet has been sufficiently amplified; the initial wave packet growth is well described by linear stability theory. For strong initial disturbance amplitudes the transient component grows rapidly and turbulent breakdown occurs almost immediately.

The above-mentioned experiments were conducted in zero pressure gradient conditions, whereas Gostelow et al. [51] studied artificially generated turbulent spots under a pressure gradient representative of a controlled diffusion airfoil with low free-stream turbulence levels. The introduced wave packet showed strong amplification of instabilities in the T-S frequency range prior to the development of a turbulent spot. Wave packets attending the turbulent spot were also observed.

Grek et al. [55] made comparative studies of transition in varying pressure gradient on an isolated airfoil under conditions of high (1.75%) and low (0.04%) free-stream turbulence with artificial disturbances introduced by a vibrating ribbon. They observed T-S waves with a linear development at the high turbulence level. In this case the boundary layer eigenoscillations (T-S waves, wave packets and turbulent spots) were the same as those excited under low free-stream turbulence conditions. However, under the high free-stream turbulence the boundary layer structures were scattered in time and space with different intensity and phase.

By introducing controlled oscillations with a vibrating ribbon Boiko et al. [13] were able to demonstrate that T-S waves can exist and develop in a zero pressure gradient boundary layer subjected to a free-stream turbulence intensity of 1.5%. They concluded that T-S waves play a role in the transition process even at this increased level of

freestream turbulence, although they are difficult to distinguish among the externally-imposed "noise". They also argue that the term "bypass transition" is difficult to define, since both linear (T-S-wave) and non-linear mechanisms are always at work.

Various workers have identified natural transition mechanisms in flows representative of turbomachinery. Dong and Cumpsty [31] investigated unsteady flow transition in a large scale two-dimensional compressor cascade with moving blade wakes simulated by bar passing. They observed T-S wave activity in the regions between wake-induced turbulent events when the flow was returning to a separated laminar state. Similar results for the development of the unsteady suction surface boundary layer of a highly loaded LP turbine airfoil in a rectilinear cascade were presented by Schulte and Hodson [119]. Dring et al. [34] identified T-S waves in the decelerating flow region on the stator suction surface of a single stator/rotor turbine stage. Identification of T-S wave activity in the above experiments all occurred when the background turbulence level between passing wakes was less than 1.0%.

8.4 Identification Methods

8.4.1 Introduction

The following section outlines the success of a number of techniques for identifying instability mechanisms in pre-transitional laminar boundary layers. The most significant of these is the wavelet transform and a brief review is given to previous uses of this analysis method for turbomachinery type flows. The wavelet transform has been used to analyse transitional boundary layer flow in both steady and unsteady environments at varying levels of free-stream turbulence. In particular, Lewalle and Ashpis [84] and Lewalle et al. [85] used the continuous wavelet transform to study the transitional data of Sohn and Reshotko [122]. This data was obtained from x-type hot-wires in a boundary layer subjected to 1.1% free-stream turbulence intensity. They used conditional sampling to separate laminar and turbulent zones, and identified dominant scales for energy and momentum transport. They tentatively identified events characteristic of T-S wave frequencies in the neighbourhood of turbulent spots. Volino [137] used similar ideas to investigate boundary layer transition subjected to a free-stream turbulence intensity of 8%. Regions immediately preceding and following a turbulent spot were investigated to identify possible dominant frequencies. No evidence supporting the existence of particular frequencies in these regions was found, but the author noted a high degree of uncertainty in the data.

Schobeiri et al. [115] applied continuous wavelet techniques to extract information on the dominant frequency and time scales of their cascade experiments, in which airfoils were subjected to unsteady wake passing. It must be noted that much of the above work with wavelet techniques has been aimed at improving turbulence modelling in the transitional flow region. The focus there has been on flow behaviour subsequent to turbulent breakdown.

The following sections examine the use of signal processing techniques to identify instability phenomena in a compressor blade boundary layer. Here the emphasis is on the flow behaviour prior to breakdown. The adverse pressure gradients on the compressor blade make the identification of wave phenomena more challenging, due to the amplitude of the wall shear stress fluctuations being significantly lower than those

of velocity fluctuations in the critical layer.

8.4.2 Fourier Techniques

Fourier-based analyses have been the traditional methods for extracting the spectral components from experimental data. It has long been recognised that analysis of non-periodic signals would benefit from a compromise of sequential and spectral views. The Fourier work outlined here is not included to encourage this as a means of information gathering, but rather to highlight the inadequacy of this method in the current situation.

Fig. 8.2 shows a typical record from the film gauge at $s^* = 0.3108$ on the compressor stator suction surface over 6 rotor blade passing periods. There is strong periodicity at the blade passing frequency (around 300 Hz); however, the wake-induced transitional strips show some variability in both phase and amplitude due to the randomness associated with turbulence in the passing wake disturbances. There is even greater randomness in the occurrence of instability phenomena between the wake-induced strips; wave packets are clearly evident around t^*= 1.1 and 2.0, but are not seen for the remaining 4 rotor blade passages.

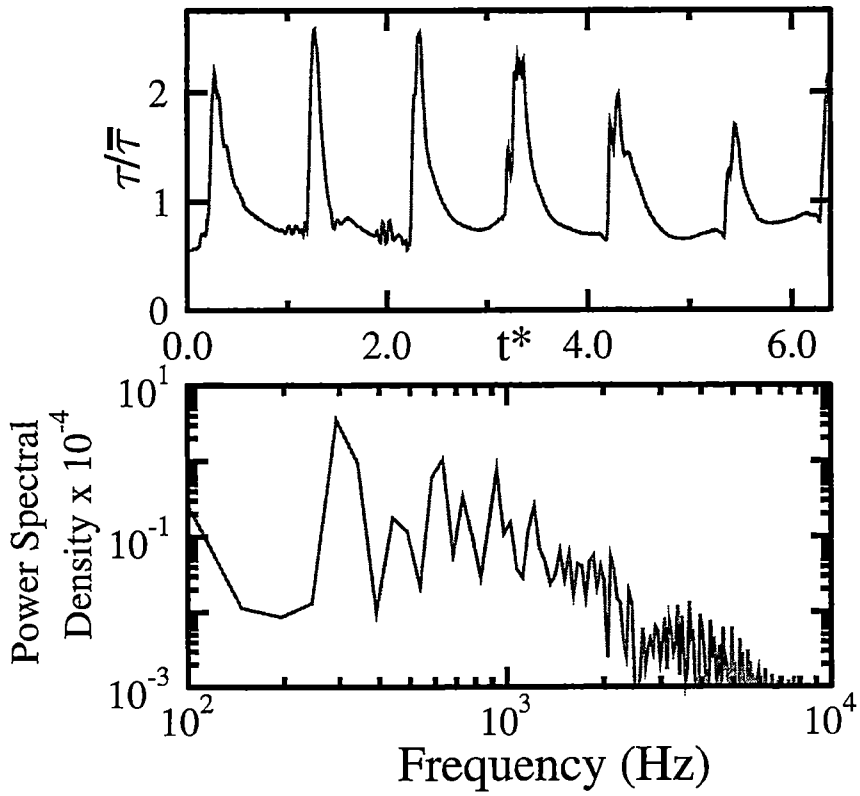

Figure 8.2: Record from gauge at $s^* = 0.3108$ and Fourier spectrum.

Fourier analysis of this signal produces the spectrum shown in the lower half of Fig. 8.2. There are prominent spectral peaks at the blade passing frequency and its harmonics, but there is little significant evidence of energy at the frequency of the wave packets (around 5 kHz) and their harmonics. The Fourier analysis does not detect the

instability phenomena because of the transient nature and random appearance of the wave packets.

8.4.3 Continuous Wavelet Analysis

Farge [40] gives a thorough review of the history of wavelet transforms, both discrete and continuous algorithms, and their applications to turbulent flow. Lewalle [83] provides an introduction to continuous wavelet transforms and illustrates applications to experimental data. The continuous wavelet transform essentially returns a correlation of the analysing function and the signal at different translations along the signal. Since the wavelet is localised in space, only the local information of the signal is extracted. This process is repeated for different scales (or durations) of the analysing wavelet and therefore decomposes the original signal into both location and duration scales. The localisation of the analysing function in the wavelet transform makes it ideal for studying transient phenomena.

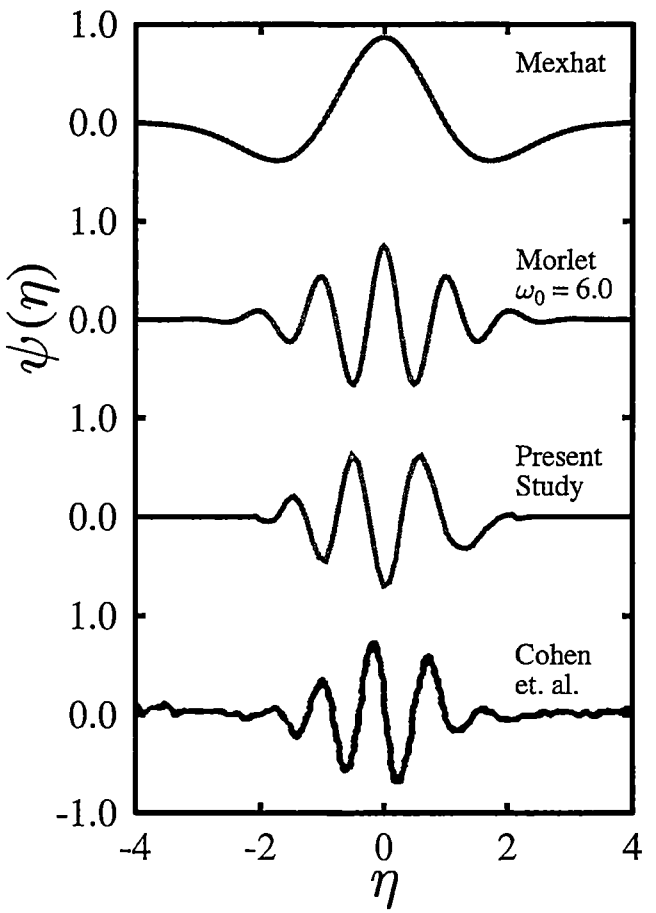

Figure 8.3: Comparison of Mexican hat and Morlet wavelets with typical data from the present study and Cohen et al. [21]. Note only the real part of the Morlet wavelet is plotted.

Much of the following basic theory is contained in Torrence and Compo [131] and is

presented here in discrete form with minor changes in nomenclature. The wavelet is a function (real or complex) which must satisfy the admissibility criterion. This requires, for an integrable function, that the mean be zero. The Morlet wavelet is defined by

$$\psi_0(\eta) = \pi^{-1/4} e^{i\omega_0 \eta} e^{-\frac{1}{2}\eta^2} \tag{8.3}$$

where ω_0 is the non-dimensional frequency. Because the Morlet wavelet is only admissible with the addition of some small correction terms, care must be taken with the choice of ω_0. All results presented here are with $\omega_0 = 6.0$, which means that the correction terms become unnecessary because they are of the same order as typical computer round-off errors (see Farge [40]). The Mexican hat wavelet is the second derivative of the Gaussian function (m=2) and is defined by

$$\psi_0(\eta) = \frac{(-1)^m}{\sqrt{\Gamma(m+\frac{1}{2})}} (\eta^2 - 1) e^{-\frac{1}{2}\eta^2} \tag{8.4}$$

Fig. 8.3 compares the Mexican hat and Morlet wavelets with instability wave packets observed in the present study and the flat plate experiments of Cohen et al. [21]. As the wavelet transform is the inner product of the analysing wavelet and the signal, the transform coefficients combine information about both the signal and the wavelet. Thus the choice of analysing wavelet should reflect the type of features present in the signal. As seen from Fig. 8.3 the Morlet is clearly preferable to the Mexican hat wavelet for the identification of wave packet phenomena in unstable laminar boundary layers. Farge [40] has also noted the suitability of the Morlet wavelet for analysing coherent structures in turbulent flow.

The continuous wavelet transform of a discrete sequence x_n is defined as the convolution of x_n with a scaled and translated version of $\psi_0(\eta)$,

$$W_n(s) = \sum_{n'=0}^{N-1} x_{n'} \psi^* \left[\frac{(n'-n)\delta t}{s} \right] \tag{8.5}$$

where $*$ indicates the complex conjugate. The convolution theorem allows all N convolutions to be performed simultaneously in Fourier space with a Discrete Fourier Transform (DFT). The DFT of x_n is

$$\hat{x}_k = \frac{1}{N} \sum_{n=0}^{N-1} x_n e^{-2\pi i k n / N} \tag{8.6}$$

where k=0,1,2...,N-1 is the frequency index. In the continuous limit the Fourier transform of a function $\psi(t/s)$ is $\hat{\psi}(s\omega)$. By the convolution theorem the wavelet transform is the inverse Fourier transform of the product

$$W_n(s) = \sum_{k=0}^{N-1} \hat{x}_k \hat{\psi}^*(s\omega_k) e^{i\omega_k n \delta t} \tag{8.7}$$

where the angular frequency is defined as

$$\omega_k = \begin{cases} \frac{2\pi k}{N\delta t} & k \leq \frac{N}{2} \\ -\frac{2\pi(N-k)}{N\delta t} & k > \frac{N}{2} \end{cases} \tag{8.8}$$

Normalisation of the wavelet transform, reconstruction of the signal from wavelet coefficients and determination of wavelet power spectrum are detailed by Torrence and Compo [131].

8.4.3.1 Wavelet Analysis of Continuous Signal

Fig. 8.4 shows an analysis of the signal from the film gauge at $s^* = 0.3108$ using both Mexican hat and Morlet wavelets. The results are presented in the form of energy maps: the wavelet transform modulus squared. The cross-hatched region at each end indicates where edge effects influence the results, and is called the "cone of influence".

The energy maps are dominated by the periodic wake-induced transition events (at intervals of t^* =1), which are characterised by the continuous cascade of frequencies up to 8 kHz. Both wavelet transforms clearly capture the wave packet around $t^* = 2.0$. There is also evidence for a developing packet around $t^* = 1.1$, but this is less distinct. Since the Morlet wavelet exhibits more oscillations than the Mexican hat, it is somewhat better at identifying specific frequencies in the flow. Conversely, the Mexican hat wavelet has advantages in better resolving locations of specific events in time. It should be noted that with all wavelets that there is a trade off between spectral and temporal resolution. This is clearly evident when comparing the information in the region of the identified wave packet for both transforms. The Mexican hat transform has clearly identified the location of the wave packet, but the information is more diffuse in the spectral domain.

By using the Parseval theorem (see Lewalle et al. [85]) the energy maps can be integrated to produce a mean wavelet spectrum, which parallels the Fourier power spectrum. Fig. 8.5 compares the Fourier power spectrum with the results obtained from both wavelet energy maps. As demonstrated earlier in Fig. 8.2 it is the blade passing frequency and its harmonics which dominate. The region between 2 kHz and 8 kHz is magnified and inset: again it is difficult to identify any particular peaks corresponding to the instability wave phenomena. It should be noted that the wavelet transform acts as a bandpass filter on the Fourier spectrum. Hence the averaged wavelet spectra actually reveal less detail than the Fourier spectrum.

One of the most powerful features of wavelet analysis is the ability to compare spectral properties of the signal at different locations in physical space, which is not possible with Fourier techniques. In order to successfully apply this technique the signal needs to be decomposed into specific regions.

8.4.3.2 Wavelet Analysis of Laminar Component

Whilst the wavelet analysis described above identifies the transient wave packet phenomena in the non-turbulent flow regions, it does not give a clear indication of the basic instability frequencies. There is an identifiable frequency around 5 kHz for the wave packet appearing in Fig. 8.4 at $t^* = 2.0$, but is this the basic instability frequency

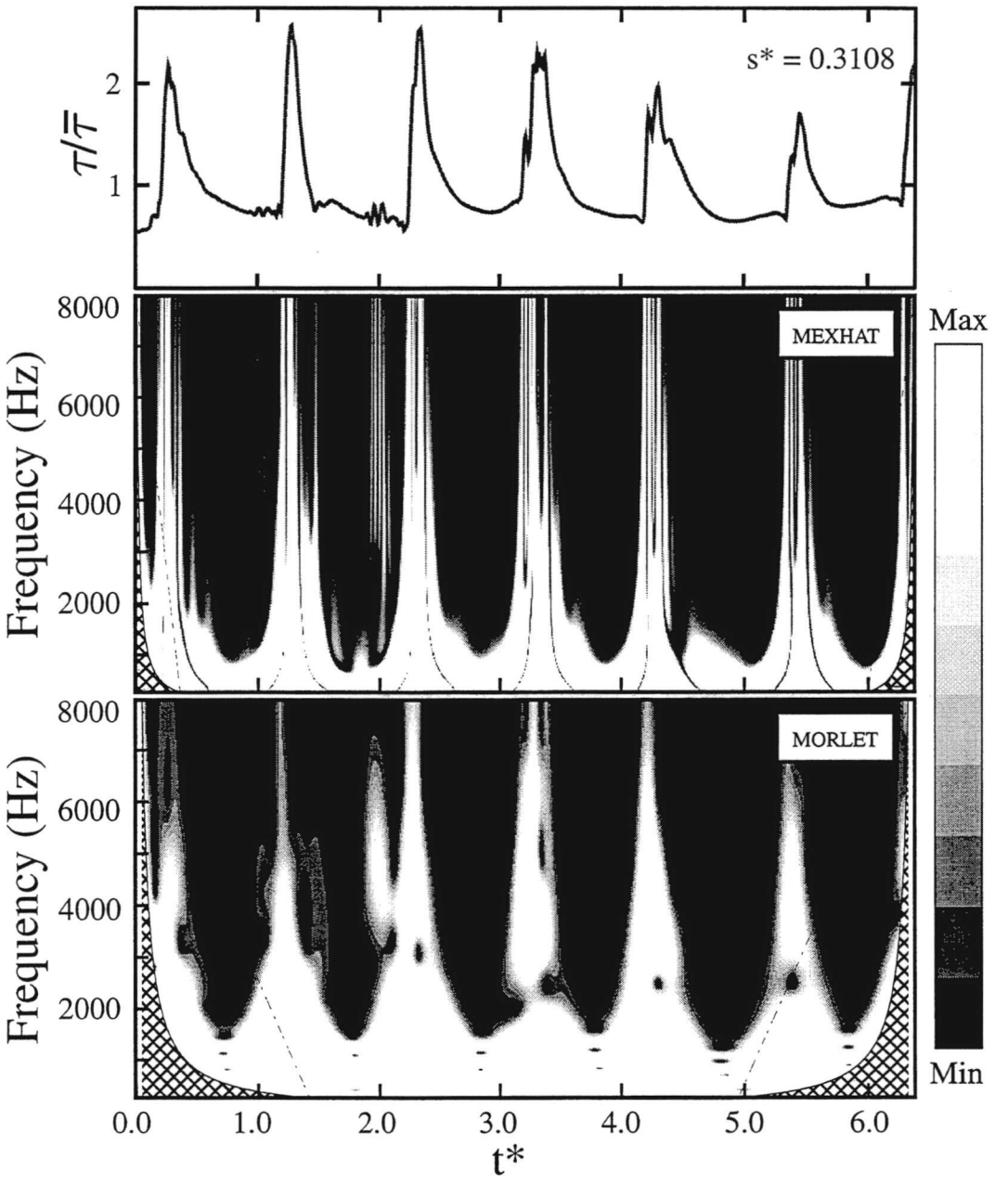

Figure 8.4: Comparison of energy maps for Mexican hat and Morlet ($\omega_0 = 6.0$) wavelet transforms. Top: Raw signal from $s^* = 0.3108$, Middle: Energy map for Mexican hat wavelet transform, Bottom: Energy map for Morlet wavelet transform. Cross-hatch region indicates cone of influence for both wavelets.

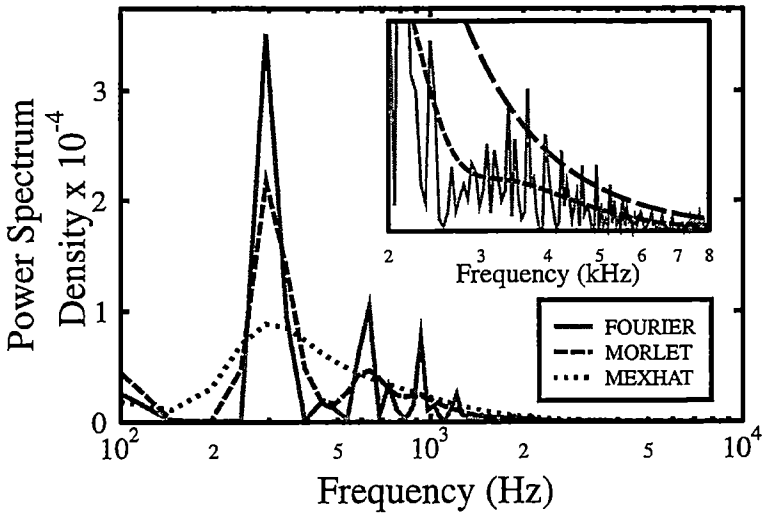

Figure 8.5: Comparison of mean wavelet spectra produced by Mexican hat and Morlet wavelet transforms, with Fourier power spectrum of gauge record at $s^* = 0.3108$.

or a harmonic? The difficulty arises because much of the frequency information below 2.5 kHz is masked by the blade passing frequency and its harmonics.

To examine this problem in more detail, the non-turbulent flow region between the wake-induced strips at $t^* = 1.4$ and 2.2 has been isolated using the intermittency detection algorithm of Section 7.3. A wavelet analysis for this isolated signal portion is presented on an expanded scale in Fig. 8.6. The results were obtained by performing an analysis on the whole signal and enlarging the laminar regions. This method is preferable to analysing each laminar region separately, as it reduces the influence of edge effects and therefore the contamination of the results due to numerics. However, neither analysing the laminar components separately or as regions of the continuous signal completely isolates the results from the influence of the surrounding signal.

The results presented are the real part and the modulus of the wavelet transform, using the Morlet wavelet. The real part of the transform returns results which are qualitatively similar to the transform using the Mexican hat wavelet. The wave packet is again clearly identifiable in both the real part and the modulus, with an obvious frequency component around 5 kHz. The plots also enhance a feature which is superimposed on the relaxing flow region (around $t^* = 1.4$). It appears that this feature is another developing wave packet with a slightly lower frequency, although it is difficult to determine its frequency content due to the blade passing effects.

8.4.4 High Pass Filtering

In an attempt to overcome the low frequency distortion effects associated with blade passing phenomena, the signal was digitally smoothed using a Savitzky-Golay filter. The filter uses a least squares method to fit a quartic polynomial to a window extending approximately one period of the basic instability wave on either side of the point of interest. Bromba and Ziegler [17] present transfer functions for filters with polynomials of increasing order. The signal was high-pass filtered by subtracting the smoothed sig-

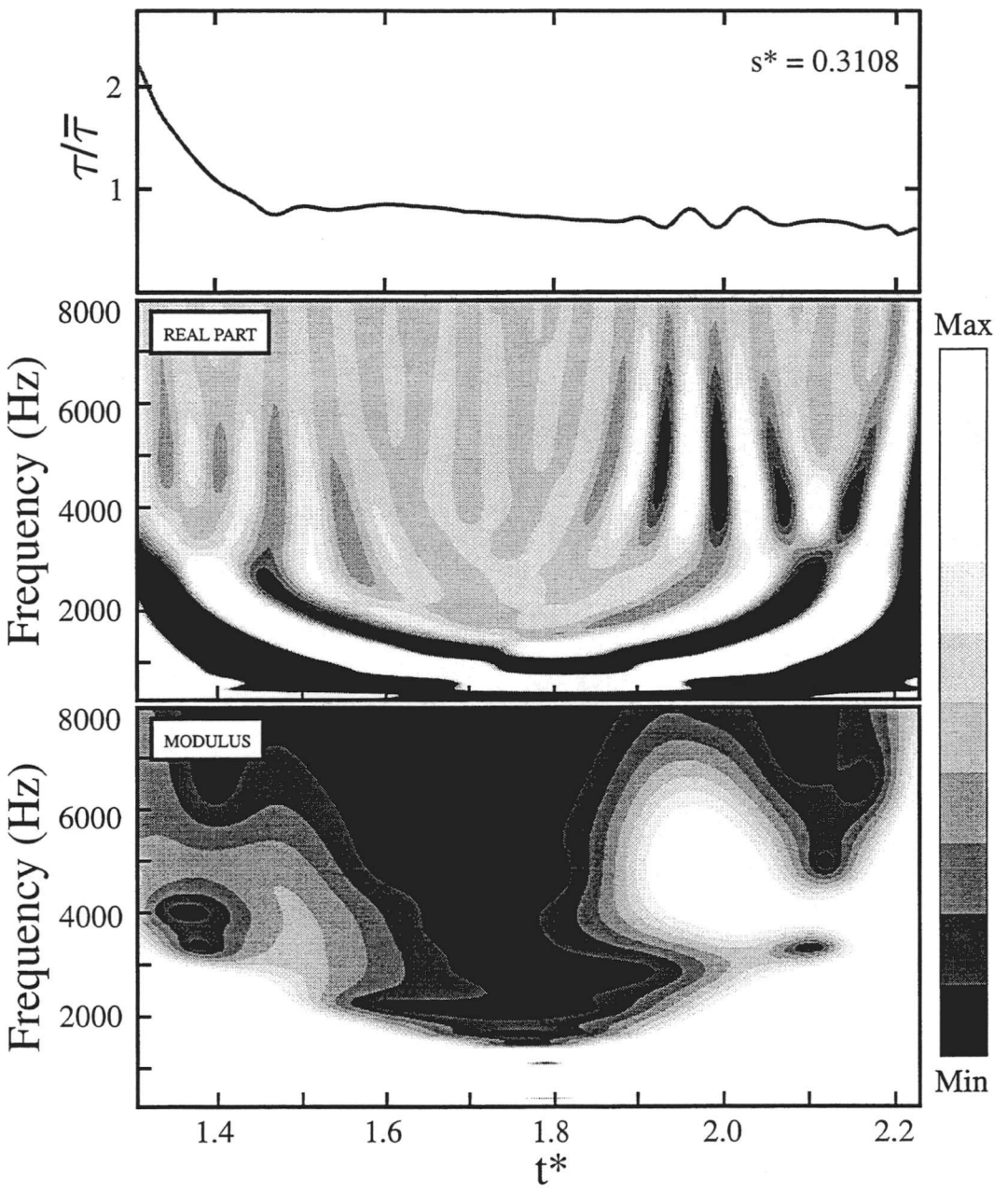

Figure 8.6: Morlet wavelet transform of the laminar portion of the signal between t^* = 1.4 and 2.2. Top: Raw signal from s^* = 0.3108, Middle: Real part of the wavelet transform, Bottom: Modulus of the wavelet transform.

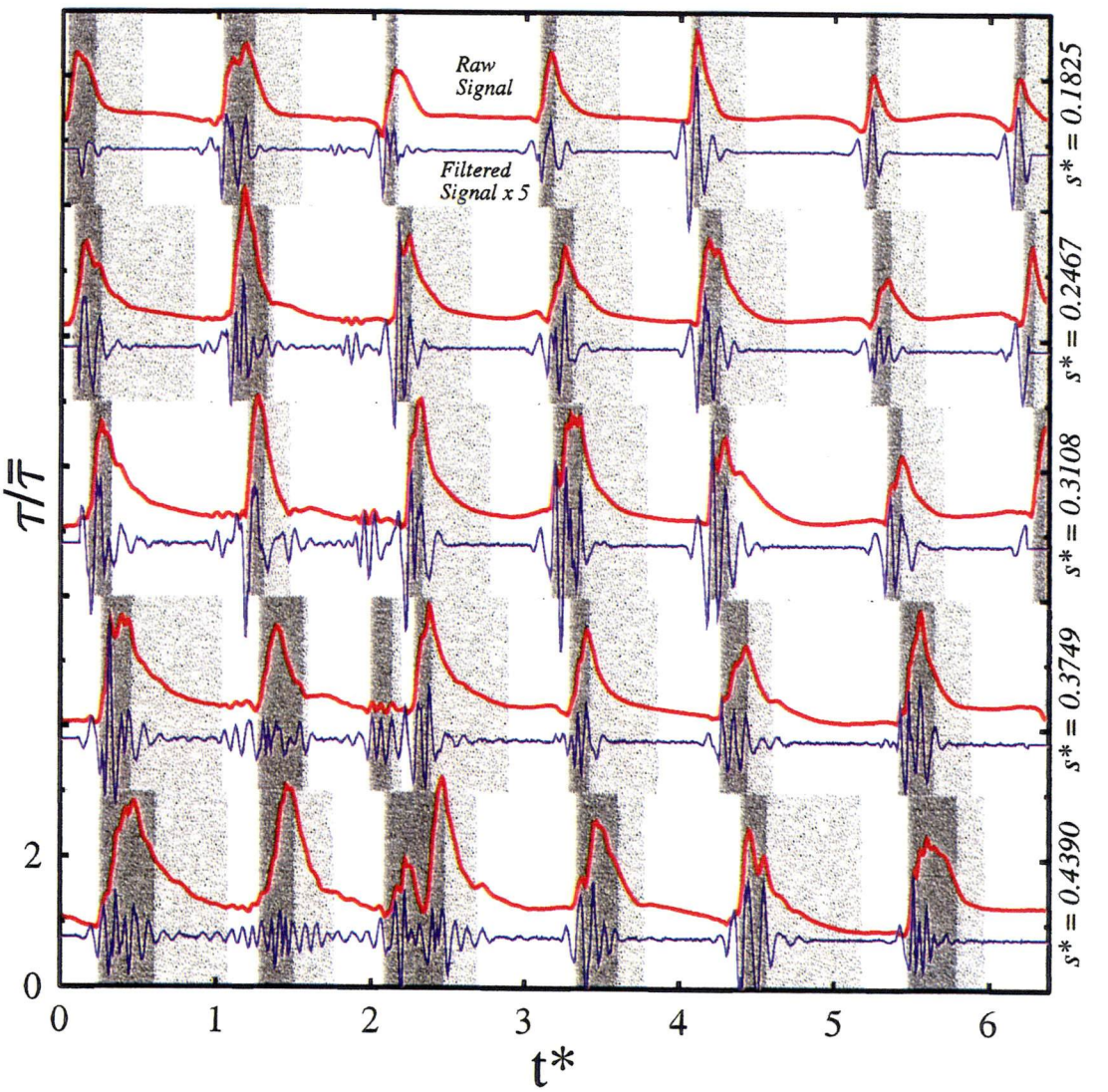

Figure 8.7: High-pass filtered traces (blue) amplified five times and overlaid on raw signals (red) for all five simultaneous gauge records. Darker shaded regions indicate turbulent flow: lighter shaded regions indicate relaxing non-turbulent flow.

nal from the original. The results from this high-pass filtering technique are presented in Fig. 8.7. All five simultaneous gauge records between 18.25% and 43.90% suction surface distance are presented. The darker shading regions indicate flow identified as turbulent; lighter shading indicates regions identified as relaxing non-turbulent flow. The simple identification criterion for relaxing flow that $d\tau/dt$ remains negative following the passage of a turbulent region has been employed. Superimposed below each original trace is the amplified (x5) high-pass filtered signal.

The growth of the previously identified wave packet around $t^* = 2.0$ can clearly be seen in both the original and filtered traces. The packet is amplified and finally identified as turbulent at $s^* = 0.3749$. The second packet identified in the wavelet transform of the laminar component at $t^* = 1.4$ in Fig. 8.6 is clearly visible at $t^* = 1.5$ in the last filtered trace. On closer inspection there appear to be wave packets on either side of the preceding wake-induced turbulent strip. This is reminiscent of attendant wave packets surrounding artificially generated turbulent spots as reported by Gostelow et al. [51].

The most striking feature of the filtered traces is the regular appearance of periodic phenomena associated with the turbulent strips. Much of this information is difficult to observe in the raw traces due to the fact that the relatively small amplitude of the wave packets is superimposed on the large amplitude variations created by the wake-induced transition. However, closer inspection of the raw traces definitely reveals these fluctuations, especially in the leading edge of the advancing turbulent strips.

The approach applied here is similar to that applied by Seifert and Wygnanski [120] for identifying attendant wave packets (and consequent breakdowns) for artificially generated turbulent spots in an adverse pressure gradient. Kachanov [78] presents a discussion of the problems involved with filtering of wave packets and the effect on the Fourier spectra produced: high-pass filtering of a signal with a decaying spectrum may introduce an artificial spectral peak. Individual events at frequencies close to the cut-off may experience significant phase distortion; but this does not invalidate the use of filtering to reveal the existence of periodic phenomena. The fact that such events are visible in the raw data indicates that the phenomena evident in the high-pass filtered signals of Fig. 8.7 are essentially genuine and not an artifact of the filtering process.

A Morlet modulus plot for the high-pass signal from the raw data trace of Fig. 8.4 is presented in Fig. 8.8. The aim is to examine whether pre-filtering reveals any additional evidence of fundamental wave periodicity or sub-harmonic behaviour which might have been masked by the strong low frequency components of blade passing events in the modulus plot of Fig. 8.4. The first two wake passing events around $t^* = 1$ and 2 (which are associated with well-developed turbulent spots) show nothing but the appearance of an artificial spectral peak as predicted by Kachanov [78]. The following three events around $t^* = 3$,4 and 5 (which are associated with less advanced turbulence development) do appear to show weak evidence of isolated spectral peaks above the cut-off frequency. In retrospect, however, it is concluded that there is little of significance in Fig. 8.8 that was not already evident from the modulus plot of Fig. 8.4. The technique of filtering before wavelet analysis is therefore not necessary to identify instability wave activity, although it does significantly aid in the visual interpretation.

There are strong similarities between the identified wave packets from the present investigation and those measured in the experiments of Cohen et al. [21]. Fig. 8.3 shows a comparison of wave packets from both studies. The wave packets in Cohen

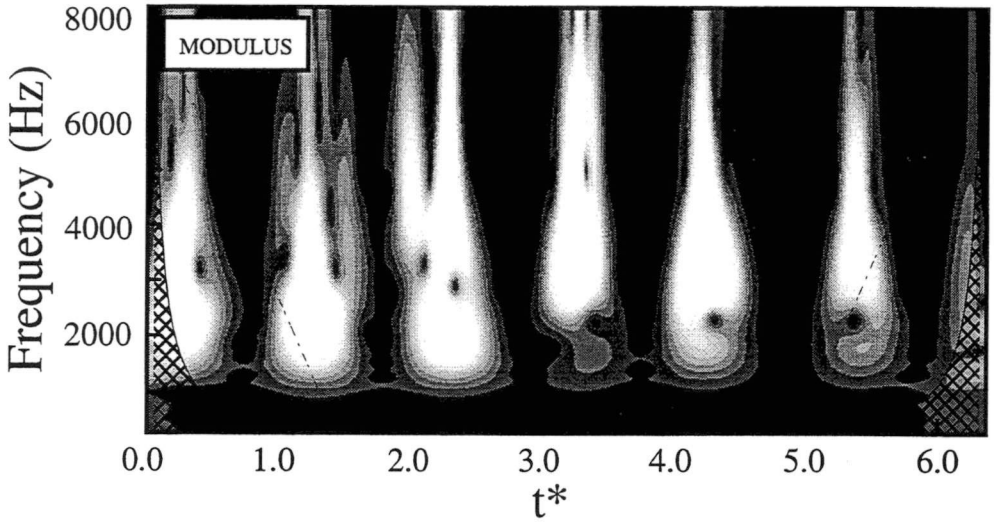

Figure 8.8: Morlet modulus plot for the high-pass filtered signal from the raw data trace at $s^* = 0.3108$. Scale is the same as for the lower portion of Fig. 8.6.

et al. [21] were generated with a "weak" three dimensional disturbance in a laminar flat plate boundary layer, and measured at various stations through the regions of amplification and eventual breakdown into turbulent spots. Three stages of transition were observed: the wave packet could initially be treated as a superposition of two and three dimensional waves governed by linear stability theory; this was followed by the appearance of a band of sub-harmonics overtaking the fundamental band; during the final stage a turbulent spot developed. Cohen et al. [21] found that linear stability theory performed well in the first stage, but was unable to predict the generation of oblique waves in the second stage of transition.

8.4.5 Flow Identification

In retrospect it is possible to make some comments about the identification of fine structure in turbulent or transitional shear layers by peak-valley counting, which is used in the intermittency algorithm of Solomon [123]. For surface film sensors the monotonic decrease in shear stress associated with the relaxation process following the passage of a turbulent spot largely eliminates sign reversals in temporal rate of change of shear stress. This will result in premature termination of turbulent flow identification and a slight underestimation of intermittency. Signal peaks and valleys will only be identified near the end of wave packet development if the wave amplitude is large or the relaxing flow gradient is weak. This problem could be alleviated by high-pass filtering of the film signals prior to peak-valley analysis. Similar comments apply to the analysis of hot-wire signals obtained in the inner region of transitional boundary layers.

The development of instability wave packets in a region of non-turbulent relaxing flow will result in the identification of such regions being prematurely terminated. Several cases are illustrated in Fig. 8.7, for example the event around $t^* = 4.5$ at $s^* = 0.3749$ which causes a brief sign reversal in $d\tau/dt$. This under-estimation of relaxing flow could be overcome by low-pass filtering the film signal prior to analysis.

The wavelet transform may offer a more universal approach to the identification of turbulent and non-turbulent relaxing flow regions. The wavelet transform resolves the basic signal into different frequency components and simultaneously effects both the high-pass and low-pass filtering operations described above. Turbulent flow is characterised by an energy cascade from larger to smaller wavelengths: this information is readily accessible in the high frequency output from the wavelet transform. It would be relatively simple to implement an algorithm to identify turbulent regions in a time based signal with a wavelet-based approach.

8.5 T-S Wave Detection Algorithm

8.5.1 Introduction

An algorithm will now be developed to identify instability waves, at the T-S wave frequency, utilising the signal processing techniques outlined in the previous sections. The detection algorithm is divided into the stages listed below, and each item is discussed (with supporting figures) with respect to a simultaneous set of data obtained from the stator blade hot-film array:

- Estimation of the local T-S wave frequency
- High-pass filtering of the hot-film signal
- Wavelet transform of the filtered signal
- Exclusion of turbulent flow regions
- Identification of instability waves in the laminar flow

8.5.2 Prediction of T-S wave frequency

In order to identify T-S waves it is first necessary to predict the range of frequencies receiving amplification for given local boundary layer conditions. The approximate method of Thwaites [130] is used to predict the streamwise variation in laminar boundary layer properties which would be obtained for the steady flow with the measured time mean surface velocity distributions. Periodic transition and its associated effects mean that it is possible to encounter regions of laminar flow well past the point of separation predicted by a time mean calculation, and it is therefore necessary to continue the calculation artificially past this point. The instability wave frequency in a separated shear layer should be related to the momentum thickness of the layer, which remains basically constant until transition and re-attachment commence. In order to achieve this expected consistency of wave frequency, the shape factor $H = \delta^*/\theta$ is assumed to remain constant after separation when calculating a displacement thickness value for application of Eqn. (8.9).

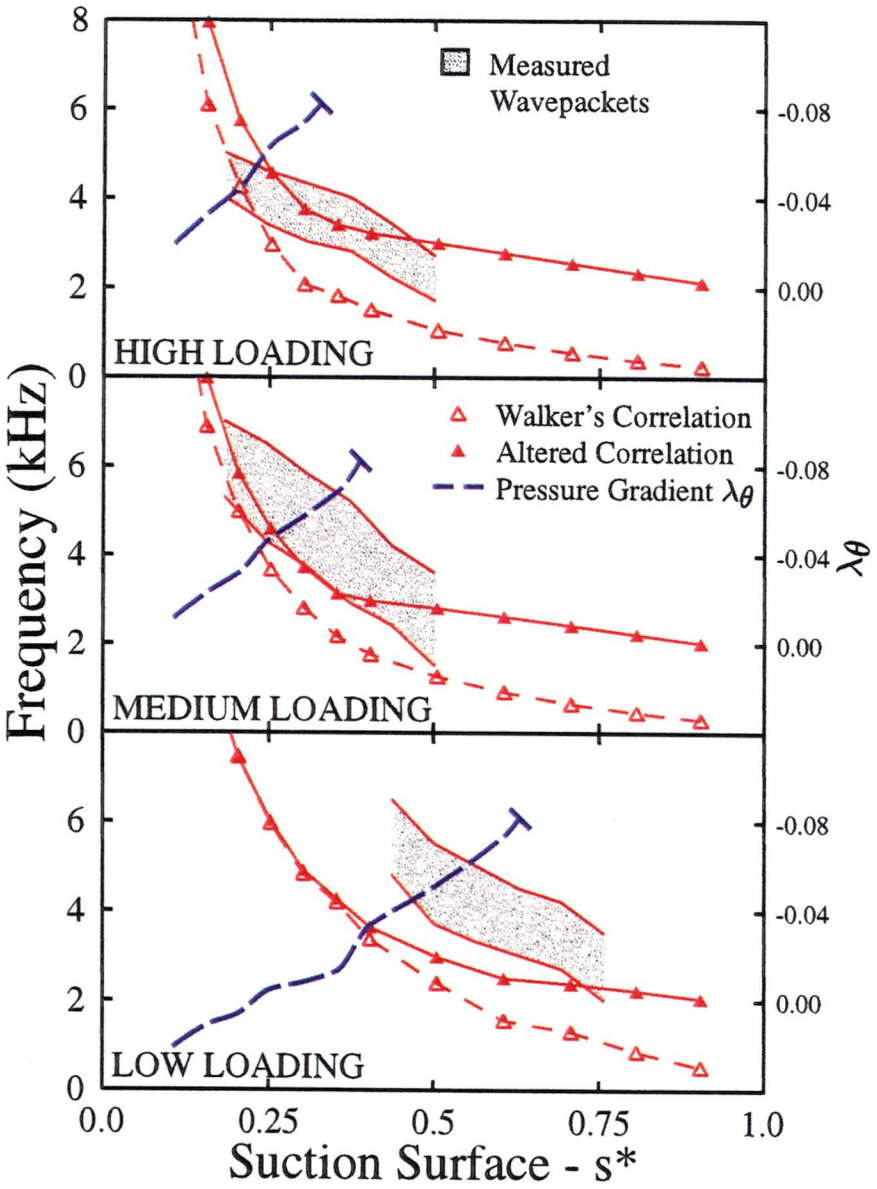

Figure 8.9: Comparison of predicted T-S wave frequency and measured instability wave packet frequency

Walker [141] correlated the dimensionless frequency of T-S waves receiving maximum amplification rate against boundary layer displacement thickness Reynolds number by

$$\frac{\omega\nu}{U^2} = 3.2Re_{\delta^*}^{-\frac{3}{2}} \tag{8.9}$$

In conjunction with the local boundary layer properties computed as described above Eqn. (8.9) is used to predict the chordwise variation of T-S frequency. The results for different blade loadings are plotted in Fig. 8.9. Also shown is the measured frequency range of instability wave packet phenomena, as identified by inspecting the wavelet transforms for a number of individual traces. The values predicted by the correlation are usually less than the measured values. This is to be expected because the correlation returns the frequency of waves with the maximum amplification rate, whose frequency lies close to the centre of the neutral stability curve. The observed wave packets are those with maximum amplitude, whose frequency will lie close to the upper branch of the neutral stability curve.

In adverse pressure gradients the frequency range of instability waves receiving amplification is much broader than for zero or favourable pressure gradients. It is therefore likely that as streamwise distance increases, the frequency of wave packets having the maximum amplitude will increasingly differ from that of waves experiencing maximum amplification rate. The maximum amplitude wave packets will be those that have already been amplified upstream, and these will tend to have higher frequencies.

To account for the differences between the maximum amplitude and maximum amplification rate cases the predicted frequency has been modified according to the value of the Pohlhausen pressure gradient parameter. For zero or favourable pressure gradients the predicted T-S wave frequency is not altered. As the pressure gradient becomes increasingly adverse, the change in predicted frequency with streamwise distance is simply biased towards the value upstream. There is a linear variation in biasing up to the separation value. Beyond separation the change in T-S wave frequency is limited such that there is almost no change with increasing streamwise distance. The effects on the predicted frequency are clearly illustrated in Fig. 8.9.

8.5.3 High-pass filtering

The upper portion of Fig. 8.10 shows the signal from a hot-film gauge located at $s^* = 0.3108$ on the stator suction surface. The signal shows evidence of both wake-induced turbulent strips (labelled "A" around $t^* = 3.6$ and 4.6) and regions where the passing wake has failed to induce transition. As the regularity of turbulent strips increases, the laminar turbulent switching of the boundary layer tends to dominate the signal output and generally mask the presence of small amplitude high frequency fluctuations. The high-pass signal is overlaid with the original signal in Fig. 8.10. It is possible to visually identify regions of instability activity which will be discussed further in the light of the wavelet transform. It is stressed that the high-pass filtering is extremely useful for revealing instability waves in the time series data, but it is not an essential adjunct for the wavelet analysis.

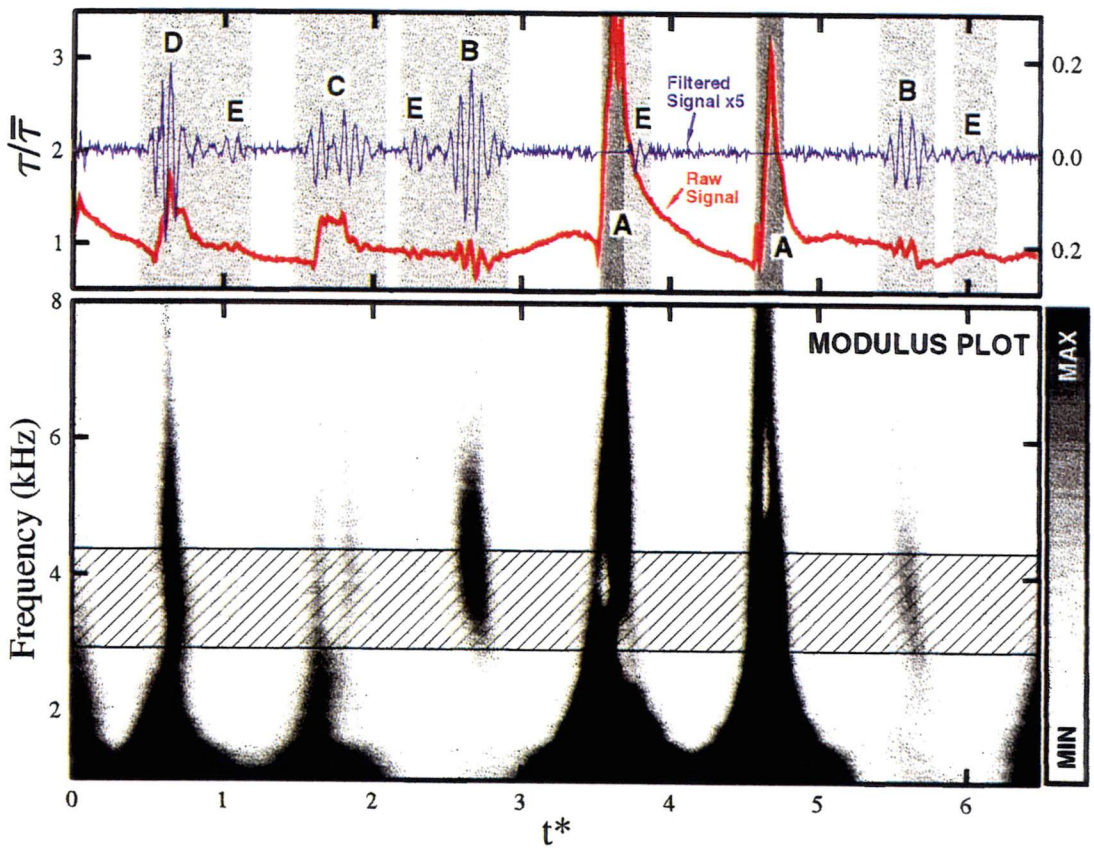

Figure 8.10: Top: Quasi-wall-shear stress record from a hot-film gauge located at s^* =0.3108 on the stator suction surface for the medium loading case. High-pass filtered signal amplified five times and superimposed. Darker shaded regions indicate turbulent flow: lighter shaded regions indicate instability wave occurrence. Bottom: Modulus of the Morlet wavelet transform for the above quasi-wall-shear stress record. Hatching indicates frequency range under consideration by the detection algorithm.

8.5.4 Wavelet Transform

As mentioned in Section 8.4.3, the continuous wavelet transform essentially returns a correlation of the analysing function and the signal at different translations along the signal. Since the wavelet is localised in time, only the local information of the signal is extracted. This process is repeated for different scales (or durations) of the analysing wavelet and therefore decomposes the original signal into both location and duration scales. The localisation of the analysing function in the wavelet transform makes it ideal for studying transient phenomena.

The bottom portion of Fig. 8.10 shows the modulus plot for the above raw film signal. The transform is obtained with a Morlet wavelet, which closely resembles the signature of typical wave packets on the compressor blade (see Fig. 8.3): the measured instability wave is not symmetric, but still exhibits the characteristic modulated sinusoidal form. In combination with the filtered signal it is possible to identify individual events and their associated frequency content. The turbulent nature of the wake-induced strips (A) is evident from the cascade of frequencies present. Events (B) at $t^* = 2.6$ and 5.6 are large amplitude instability waves in the regions where the wake passing has failed to induce earlier transition. There are three other events worthy of attention: event (C) which appears to be a developing turbulent spot with attendant wave packets; event (D) which is a young turbulent spot with evidence of instability wave frequencies persisting into the new turbulent flow; events (E) which are wave packets developing in the regions between wake-induced transition paths.

8.5.5 Turbulent flow detection

Regions of turbulent flow are detected using the intermittency routine outlined in Section 7.3 . Once identified, the turbulent flow regions are not subjected to scrutiny by the T-S wave detection algorithm; therefore instability waves can only be identified in regions of laminar flow. The results of the intermittency detection are shown as regions of dark shading overlaid on the film signal in Fig. 8.10. The events previously labelled A are both identified as turbulent, which agrees well with a visual inspection of the wavelet transform results. The overall uncertainty of the intermittency results is estimated to be of the order of 10%.

8.5.6 Identification of instability waves

The coefficients of the wavelet transform are weighted by the value of the input signal. Therefore the gauge outputs are normalised by the long term average value for that particular gauge before high-pass filtering and calculation of the wavelet transform. This procedure accounts for the large chordwise variations in shear stress observed over the blade surface. A simple threshold criterion is then used to identify instability waves from the modulus of the wavelet transform for each individual trace. The results presented are obtained with a constant threshold level. A range of frequencies spanning $\pm 10\%$ of the predicted frequency is searched: this area is highlighted by hatching on the modulus plot in Fig. 8.10. Light shading on the original signal is used to highlight events which have been identified in the T-S frequency range by the current method.

The threshold level was set to give reasonable agreement with a visual inspection of wave packet events in the high-pass filtered signal. This threshold value was then

applied for all data processing. Variations of ± 20% of threshold level were investigated, but these made no significant difference to the shape of the instability onset boundary or the general qualitative picture of instability wave occurrence in the $t^*{\sim}s^*$plane.

8.6 Results

8.6.1 Simultaneous Raw Surface Film Traces

Fig. 8.11 shows simultaneous traces from 5 gauges on the stator suction surface spanning from $s^* = 0.1825$ to 0.4390 for the medium loading case, with minimum inflow periodicity ($a/S = 0.00$). This corresponds to the intermittency results plotted in Fig. 7.5 of Chapter 7. Both the raw signal and the high-pass filtered signal are shown for each gauge. The middle gauge record, at $s^* = 0.3108$, is the same as for Fig. 8.10: the events A, B and E are again labelled, with their development in the streamwise direction highlighted by the dashed lines. Turbulent regions are identified by the darker shading, while the lighter shading indicates regions of instability wave activity.

Localised instability wave packets are clearly seen to amplify in the streamwise direction, both inside and outside the wake-induced transition paths. The most remarkable feature of Fig. 8.11 is that all turbulent flow is preceded by regions of wave packet amplification. At the last gauge ($s^* = 0.4390$) the laminar regions between the wake induced strips are almost entirely dominated by instability wave activity. This is characteristic of the behaviour in a wide range of similar traces. There is little evidence for the direct production of turbulent spots even in the wake-induced paths where the random free-stream turbulence levels are about ten times larger than the initial pulse amplitudes of the Cohen et al. [21] wave packet experiments.

The event labelled A is characteristic of the above-mentioned behaviour. There is instability wave activity at $s^* = 0.1825$, which breaks down by $s^* = 0.2467$ and is a well developed turbulent strip in the remaining gauge records. Event B, which also lies in the wake-induced path, shows a much longer region of amplification before breakdown. The wave packet is clearly identifiable at $s^* = 0.2467$ and continues to be amplified through the next gauge position; turbulent flow is not detected until $s^* = 0.3749$, 12% surface distance further downstream.

Event E illustrates that transition in the regions between wake-induced paths is also preceded by regions of instability wave activity. The event is first identified at $s^* = 0.3108$ and continues to be amplified at the last gauge. The above-mentioned events clearly indicate that transition to turbulence in the current situation, either in the wake-induced path (as in events A or B) or in between the wake induced paths (as in event E) is always preceded by instability phenomena. There is no evidence for direct spot production.

It is useful to re-examine the results of Halstead et al. [59] in the light of the present work. Their Fig. 17(a), which presents raw shear stress traces for the complete suction surface of a third stage compressor stator blade, is reproduced in Fig. 8.12 and shows strong similarities to Fig. 8.11. An event similar to that labelled A in Fig. 8.11 is evident along trajectory W_4 in Fig. 8.12. Activity very similar in nature to event B can be seen along trajectory W_2. There is also evidence for a number of events of type E (between trajectories W_1 and W_2 and area 6). Halstead et al. [59] concluded that T-S waves were not present in their raw data. This is understandable given the difficulties

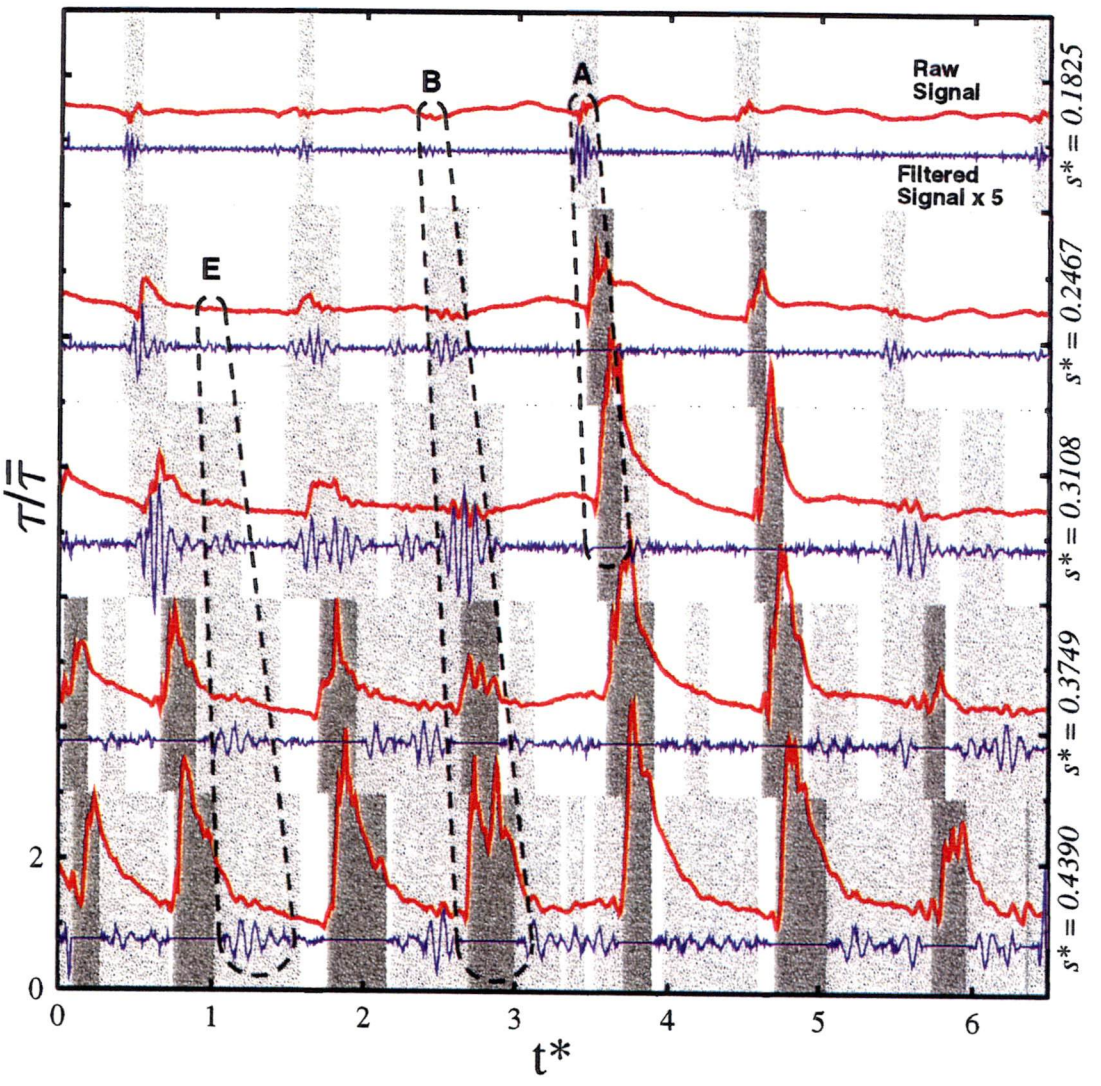

Figure 8.11: Simultaneous quasi-wall-shear stress records from five gauges spanning from $s^* = 0.1825$ to 0.4390 on the stator suction surface. High-pass filtered traces amplified five times and overlaid on each raw signal. Darker shaded regions indicate turbulent flow: lighter shaded regions indicate instability wave occurrence. Individual events from Fig. 8.10 are highlighted by dashed lines.

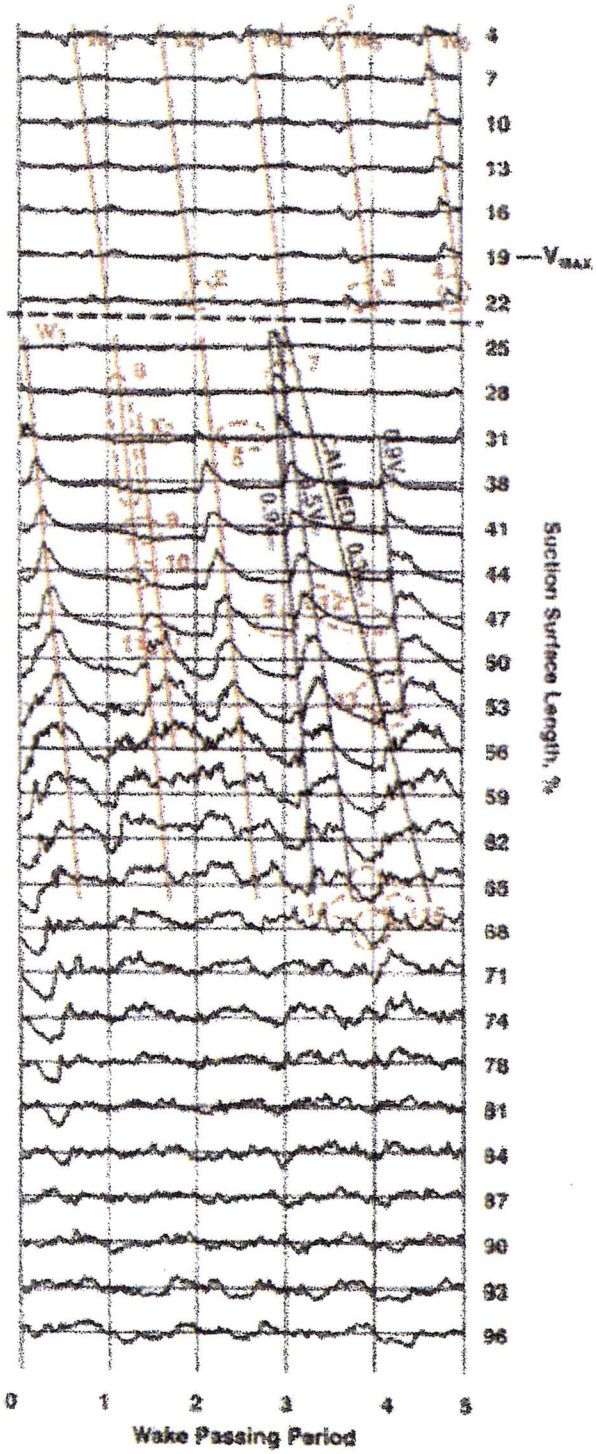

Figure 8.12: Figure 17(a) reproduced from Halstead et al. [59]. Raw time traces from surface hot-film gauges operated simultaneously on the suction surface of third-stage stator S3, Compressor Test Point 2B.

of identifying small amplitude instability waves in comparison with the large amplitude fluctuations from laminar turbulent switching caused by wake-induced transition. The filtering techniques of the present investigation suggest a different conclusion.

8.6.2 Ensemble Average Results

Figs. 8.13 and 8.15 show line contours of constant ensemble average probability of instability wave occurrence for the two IGV clocking cases presented in Section 7.4.2. These space~time diagrams have been determined by the method outlined in the previous section. The contours are spaced at intervals of 0.2, with a contour at 0.1 to indicate the onset of instability wave activity. These may be used to overlay the ensemble average values of turbulent intermittency $<\gamma>$ previously presented in Section 7.4.2, and have been reproduced here in Figs. 8.14 and 8.16. The additional dashed contour indicates the 10% probability boundary for the subsequent relaxing non-turbulent flow region.

The most notable feature of Figs. 8.13 and 8.15 is that regions of instability wave amplification exist prior to the appearance of turbulent flow for nearly all cases. Only when transition occurs through a leading edge bubble (low-loading, pressure-surface) or when the wake induced transition starts very close to the leading edge (high-loading, suction-surface) is there an absence of detectable instability wave activity. The length of unstable flow is as much as 20% of chord in the path between wake-induced transitional strips. Regions of wake-induced transition also exhibit lengths of unstable laminar flow, but they are much shorter.

Instability waves are regularly observed in the regions where non-turbulent relaxing flow has been identified. Only when relaxing flow is identified close to the leading edge on the pressure surface is there an absence of instability wave occurrence. In this case the wake jet effect will impress turbulent fluid into the boundary layer, similar to the suction surface behaviour on turbine blading; This may cause either spurious turbulence identification or genuine turbulent flow and associated calming which can not be sustained and undergoes reverse transition. At s^* = -0.4 the predicted momentum thickness Reynolds number of $Re_\theta = 140$ from a steady laminar boundary layer calculation is well below the value for self-sustaining turbulence in a steady zero pressure gradient flow; this makes reverse transition a distinct possibility.

With the stator blade inside the IGV wake street ($a/S = 0.00$), the suction surface exhibits a high probability of instability wave occurrence in the regions between wake-induced transition events for high and medium loading. In this clocking case the turbulence level between rotor wake passages is generally higher than when the stator blade lies outside the IGV wake street (a/S=0.50). This triggers instability events before the calming effect has a chance to delay their development.

With the stator blade outside the IGV wake street ($a/S = 0.50$), the suction surface shows reduced probability of instability wave occurrence in the regions between wake-induced transition events for high and medium loading. There is a general trend for the onset of instability waves to occur further rearward than in the $a/S = 0.00$ case. The high levels of instability wave occurrence leading and following wake-induced turbulent strips provide evidence for attendant wake packets similar to those reported by Seifert and Wygnanski [120] for artificially generated turbulent spots in adverse pressure gradients. The wave packets attending the front of the strip are "overtaken" by

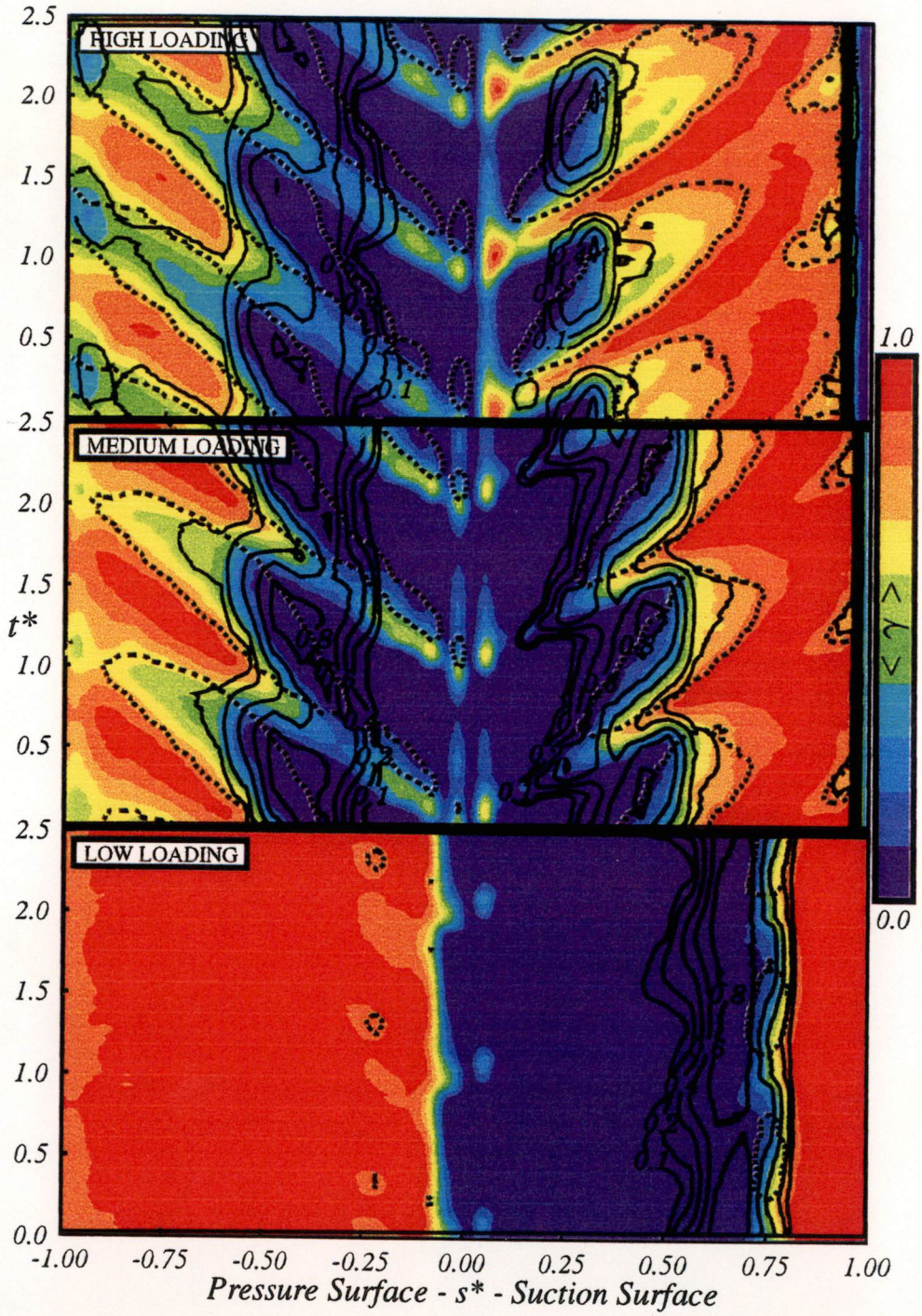

IGV wake street on stator ($a/S = 0.00$)

Figure 8.13: Ensemble average probability of instability wave occurrence. LAG case, Re_{ref} = 120 000, $a/S = 0.00$.

Figure 8.14: Ensemble average intermittency <γ> indicated by colour shading. Dashed line indicates 10% probability contour for relaxing non-turbulent flow. LAG case, Re_{ref} = 120 000. $a/S = 0.00$

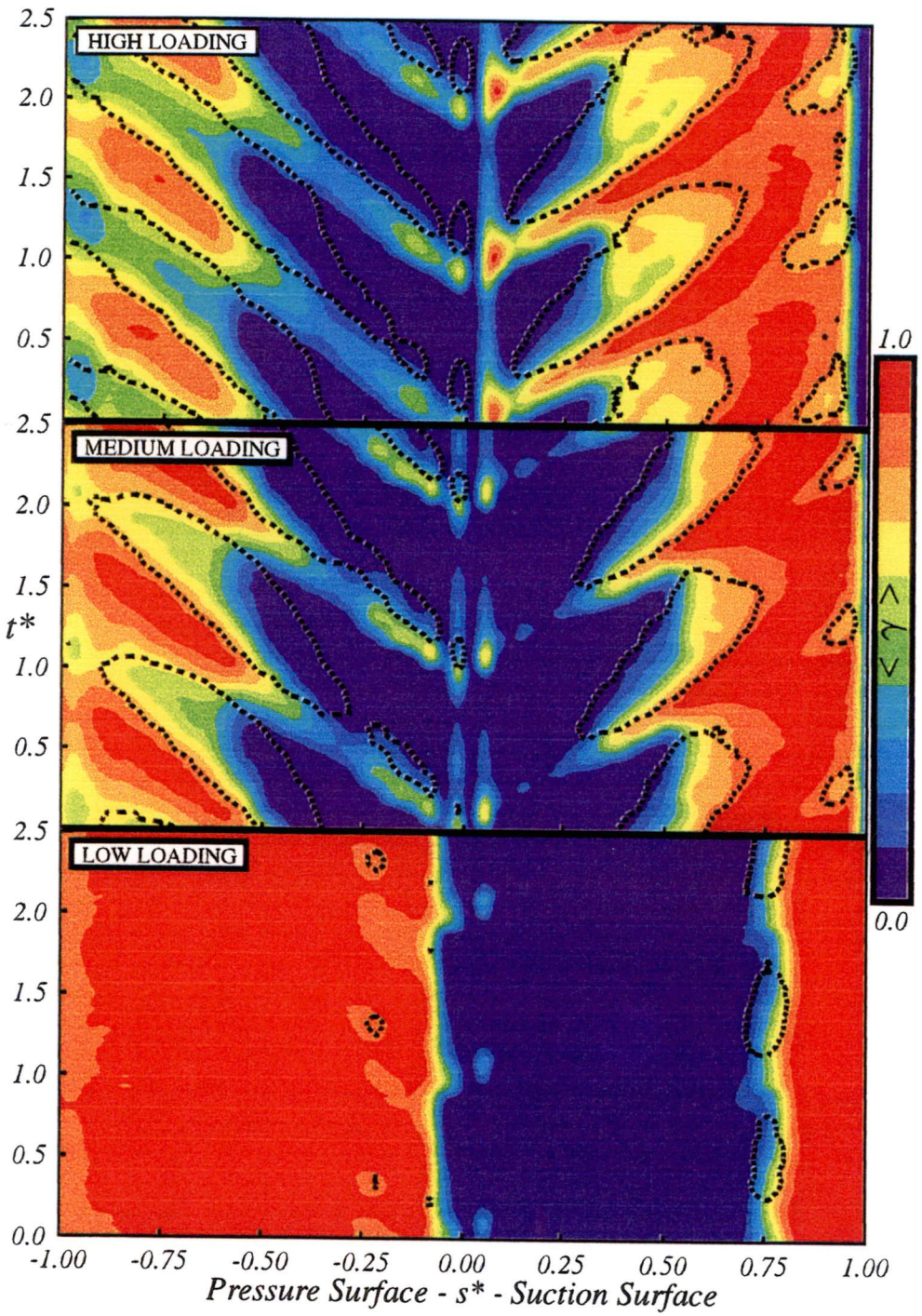

IGV wake street on stator ($a/S = 0.00$)

Figure 8.14: Ensemble average intermittency <γ> indicated by colour shading. Dashed line indicates 10% probability contour for relaxing non-turbulent flow. LAG case, Re_{ref} = 120 000. $a/S = 0.00$

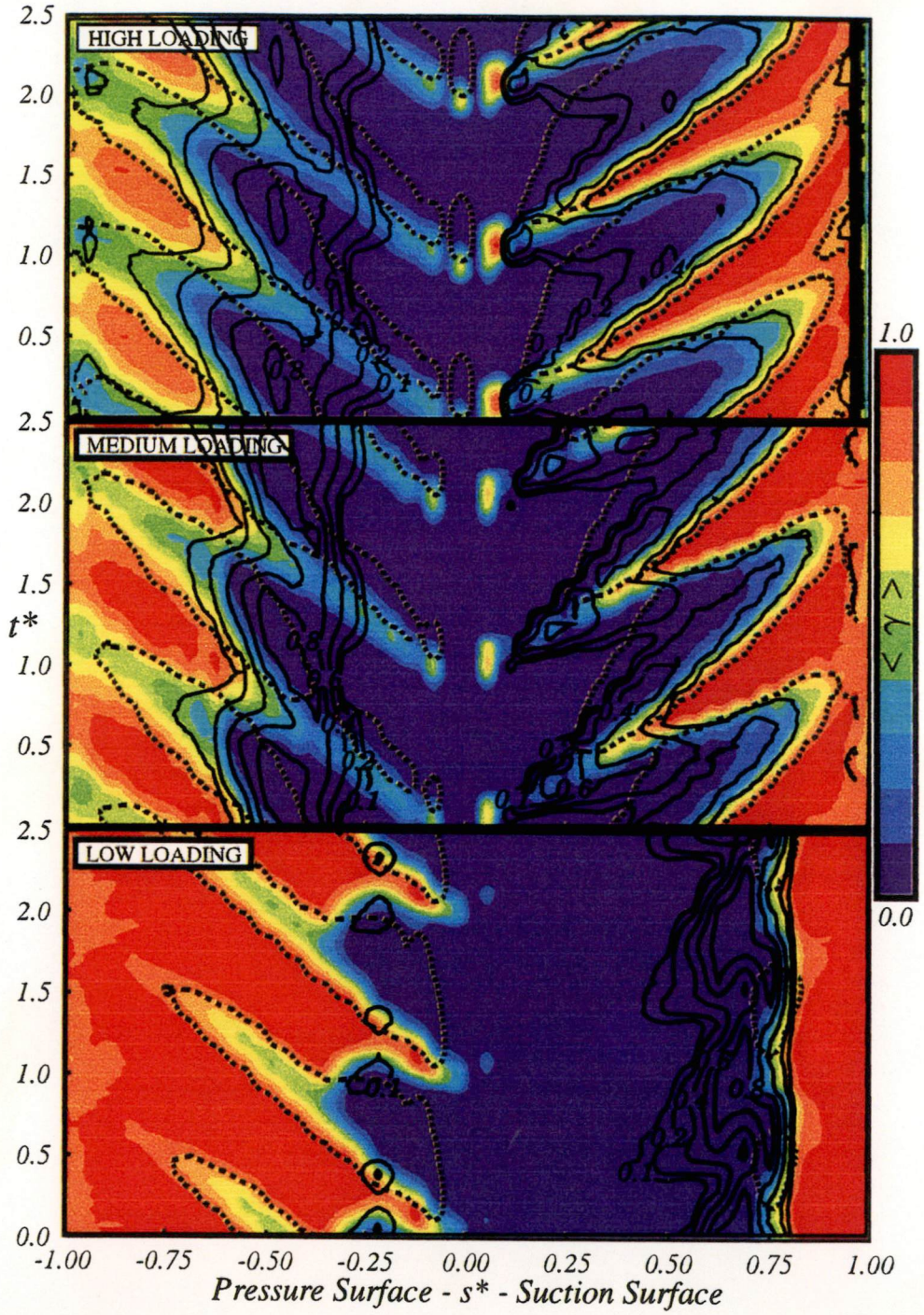

IGV wake street in passage ($a/S = 0.50$)

Figure 8.15: Ensemble average probability of instability wave occurrence. LAG case, $Re_{ref} = 120\ 000$, $a/S = 0.50$.

Figure 8.16: Ensemble average intermittency $<\gamma>$ indicated by colour shading. Dashed line indicates 10% probability contour for relaxing non-turbulent flow. LAG case, $Re_{ref} = 120\ 000$. $a/S = 0.50$

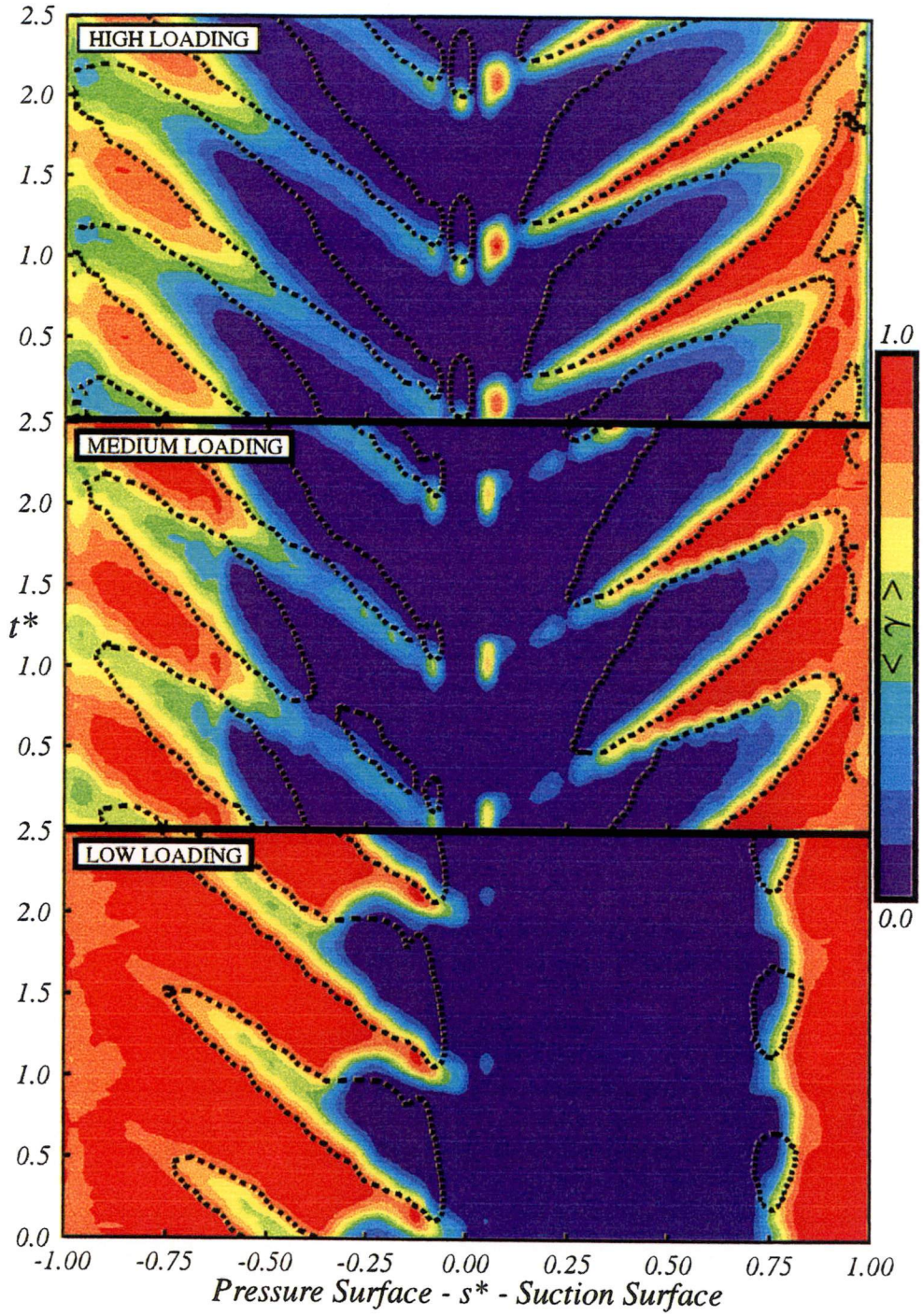

Figure 8.16: Ensemble average intermittency $<\gamma>$ indicated by colour shading. Dashed line indicates 10% probability contour for relaxing non-turbulent flow. LAG case, Re_{ref} = 120 000. $a/S = 0.50$

the turbulent strip leading edge due to its greater convection speed. Individual traces also show instability phenomena first identifiable in the regions of strong relaxing flow following the strip. The instability wave packet lags the turbulent strip trailing edge and appears to slide down the relaxing flow tail, thus moving into regions of reduced calming effect. This allows amplification and eventual breakdown to occur. Whether the wave packets are generated by the local perturbation effects of turbulence within the strip or they are packets attending the strip trailing edge remains unclear, but there is strong circumstantial evidence for the wake-induced strip acting as a source of disturbances for the surrounding laminar boundary layer.

There is little change in the pressure surface results with clocking for the high and medium loading cases. Although instability waves are identifiable in the raw traces on the pressure surface, inspecting the results of the T-S wave detection algorithm show that there is a general tendency for the occurrence to be overestimated in this region. The results could possibly be improved by applying a more sophisticated thresholding technique than the one currently employed.

Another striking feature of Figs. 8.13 and 8.15 is the similarity in shapes of the instability occurrence onset and transition onset contours over a rotor passing period. It should be noted that the method for detecting instability wave occurrence is not related to that of turbulent identification. The two methods are inherently different in nature and the onset detections for both methods are entirely independent. The agreement in shape of the respective onset contours therefore strengthens confidence in both identification techniques.

Differences in instability wave occurrence onset and transition onset are greatest when transition occurs through a mid-chord separation bubble on the suction surface at low loading. Here the suction peak is much further rearward (around $s^* = 0.3$) than for the other loading cases and there are no detectable instability waves in the accelerating flow region. It is not until $s^* = 0.4$, in the adverse pressure gradient region, that the onset of instability waves is identified. In the separated shear layer the output from the surface-mounted gauges will be influenced by the rapid attenuation of small scale disturbances, and low-frequency high-amplitude shear layer flapping type behaviour. These factors make positive identification of turbulent events by the intermittency detection routine difficult. The wavelet transform of these "missed" turbulent events almost certainly contains energy at the predicted T-S frequency and events that are wrongly identified as T-S waves. The general effect is that the turbulent intermittency is underestimated and the probability of instability wave occurrence is overestimated in the mid-chord separation bubble.

Results for variations in mid-chord separation bubble behaviour with reduced axial rotor/stator row spacing were presented in Chapter 7. They show an increased periodicity of the free-stream disturbance and increased evidence of wake-induced transition. The transition onset contours therefore agree more closely with the onset of instability waves shown in Figs. 8.13 and 8.15.

There is no evidence of instability wave occurrence on the pressure surface for the low loading case. Here transition occurs through a leading edge bubble. The dramatic changes in behaviour with blade row clocking (a/S) were shown by Solomon et al. [127] to be the result of changes in random free-stream turbulence level. In the leading edge bubble the separated shear layer will be thin and therefore the T-S wave frequency will be very high. The predicted T-S wave frequency is well above 10kHz for the first

10% of surface distance from the leading edge. The flow behaviour in this region and the greater gauge spacing relative to the length of the transition zone make detection difficult and therefore confidence in the results is greatly reduced.

There are general differences in the onset of instability occurrence depending on the location of transition. When transition occurs close to the leading edge, potential flow interactions associated with varying incidence during rotor wake chopping cause large temporal fluctuations of the onset location. As the onset of transition moves rearward these leading edge effects become less pronounced and the instability wave probability contours in the $t^* \sim s^*$ tend to straighten. This effect is most pronounced on the pressure surface for the high and medium loading cases.

8.7 Discussion

The current investigation has produced no evidence for bypass transition resulting in the direct production of turbulent spots within the boundary layer. Under adverse pressure gradient conditions on the compressor there are identifiable regions of instability wave amplification in practically all cases before the appearance of turbulent spots. This evidence supports the view of Walker [142] that linear stability theory is still relevant to bypass transition in the turbomachinery environment. The passage of free-stream disturbances will excite eigenmodes of the relevant stability equations within the laminar boundary layer, and the scale of these perturbations will ultimately govern the production rate of turbulent spots as described by Walker [141]. Thus stability theory will also be of significance in relation to the length of transitional flow (see for example Boyle and Simon [14]).

The current results are for a blade design based on the British C4 section which has a fairly linear deceleration on the suction surface at design conditions. More modern controlled diffusion airfoils exhibit a suction peak further rearward than the C4 section, followed by a region of rapid diffusion which is relaxed as the trailing edge is approached. This profile shape will generally delay transition onset when compared to C4 blades of similar loading. The increased region of favourable pressure gradient at the front of the blade will reduce the potential interactions associated with rotor wake chopping. The length of unstable laminar flow will be influenced by two counter-acting effects:

(1) the greater adverse pressure gradient following the suction peak will tend to reduce the length of unstable laminar flow;

(2) the more rearward location of the suction peak will increase the boundary layer Reynolds number and tend to increase the length of both unstable laminar flow and transitional flow.

The instability frequency will scale with the boundary layer thickness and will therefore tend to decrease with a more rearward neutral stability point; this will lower the spot production rate and therefore lengthen the region of transitional flow on the controlled diffusion airfoil. The calming effect following a wake-induced turbulent strip will be weaker on the controlled diffusion airfoil due to the region of favourable pressure gradient delaying transition onset.

8.8 Conclusions

8.8.1 Identification Techniques

The continuous wavelet transform has been shown to provide a powerful tool for identifying instability wave phenomena in the relaxing non-turbulent flow regions between periodic wake-induced turbulent strips on axial turbomachine blades. The main advantage of wavelet analysis is its ability to locate transient events in time and determine their associated frequency content. However, there is a trade off between spectral and temporal resolution depending on the wavelet form used. The Mexican hat wavelet is superior for temporal resolution whilst the Morlet gives better spectral resolution. The Morlet is further preferred for the analysis of transitional flow because of its close similarity to the signature of typical instability wave packets. The time-averaged power spectra produced by wavelet analysis are actually inferior to those of Fourier analysis, which has no temporal resolution capability at all. High-pass filtering of the film-gauge output focuses attention on the wave phenomena and gives useful detail on their structure. The filtering process does not generally reveal further information than is contained in the output of the wavelet transform, although it does help to elucidate the details.

8.8.2 Concluding Remarks

Previous investigations have found little evidence of instability wave activity from visual inspection of the raw data from surface film sensors on turbomachinery blades. Undoubtedly this is due to the small amplitude of instability wave activity being masked by the large amplitude shear stress fluctuations associated with laminar-turbulent switching of wake-induced transition. The application of wavelet analysis and filtering techniques greatly assist the identification of wave packets that appear randomly in time under the influence of free-stream turbulence.

The present investigation has indicated an almost universal appearance of instability wave amplification prior to turbulent breakdown in decelerating flow regions on an axial compressor blade. There was no evidence for direct production of turbulent spots in the boundary layer despite free-stream turbulence levels up to 8%. These observations closely resemble the wave packets and their ultimate breakdown in basic experiments on artificially generated spots arising from weak initial disturbances. It is therefore clear that high free-stream turbulence conditions do not imply the universal occurrence of transition via a bypass mode characterised by direct turbulent spot production.

Unstable laminar flow regions up to 20% chord in length were observed on the compressor blade in the present investigation, both in the path of the wake-induced transition and in regions between wake-induced paths. The length of transitional flow, which is governed by turbulent spot inception rate, may also reach 20% of chord. Thus the total length of blade surface over which the flow is governed by linear stability theory (either directly through wave packet amplification or indirectly though determining the T-S wave frequency which governs the turbulent spot inception rate) may be as much as 40% of chord.

Wave activity may both occur in, and originate from, the calmed region following a wake-induced turbulent strip. This may be either from the attendant wave packets which occur in adverse pressure gradients (as with artificially generated turbulent spots)

or from the turbulent perturbations within the wake-induced turbulent strip itself. The more stable flow in the ensuing "calmed region" does not guarantee the total absence of instability wave activity.

The present observations of instability wave activity relate entirely to regions of decelerating flow. It is likely that a bypass mode of transition, i.e. a more immediate breakdown, will predominate in accelerating flow regions at high free-stream turbulence levels. However it is speculated that the turbulent spot inception rate and length of transitional flow should still be governed by stability theory even under these conditions.

Chapter 9

Conclusions

The unsteady boundary layer development on a compressor blade, under conditions representative of an embedded stage in a multistage axial turbomachine, has been investigated. The measurements performed in a 1.5-stage axial flow compressor extend the observations of Reynolds number and blade loading influence reported by Solomon [123]. Time-resolved hot-wire and hot-film measurements of the flow in the neighbourhood of the outlet stator under the influence of wake passing combined with variations in blade loading, IGV clocking and axial row spacing have been presented. The viscous and inviscid flow mechanisms important in modifying the transition process have been identified and this section both reinforces and amplifies some of the previously stated findings.

Ensemble averaged hot-wire measurements downstream of the rotor trailing edge reported in Chapter 5 indicated significant dispersion of inlet guide vane wakes by the rotor, and subsequent interactions between the IGV and rotor blade wakes. The measurements support the observations of Lockhart and Walker [88] that the dominant mechanism for the local accumulation of low energy fluid is the interaction of the rotor and IGV wake flows. This occurred rapidly in the region downstream of the rotor trailing edge, and produced regular circumferential variations in both the time-mean and unsteady flow. These low-energy accumulations were still observable downstream of the stator trailing edge and their position relative to the stator blade surfaces was strongly influenced by the position of the upstream IGV blade row. For the current machine, this mechanism of circumferential flow redistribution was determined to be more important than the interception of wake fluid by the downstream blade rows as reported by Kerrebrock and Mikolajczak [79]. Downstream of the rotor trailing edge the (time-averaged) total disturbance level Tu_D reached values of 6% in regions outside the IGV wake street. However, the unsteady flow field was largely dominated by the periodic disturbance component $\widetilde{Tu}$ and the random disturbance level Tu was much lower, peaking at 3% within the IGV wake street. The ensemble average turbulence level $<Tu>$ reached peak values of 9% within the regions of low energy rotor wake fluid at circumferential locations where the time-average turbulence level Tu was a minimum. Evaluation and comparison (see Camp and Shin [19]) of the turbulent integral length scale in the neighbourhood of the outlet stator blade row further confirmed that the current research machine possesses a disturbance field characteristic of a multistage compressor.

Chapter 6 examined the influence of rotor-stator axial spacing and IGV clocking on stator losses through ensemble average measurements of the stator wake. Separate evaluation of the suction and pressure side momentum thickness components for the stator wake was attempted. The individual components showed a lower harmonic content than the composite wake thickness, which was influenced by phase lags between periodic wake-induced phenomena on the stator blade suction and pressure surfaces. Significantly lower amplitudes of periodic fluctuations in the stator wake were observed when the stator blades were immersed in the avenue of dispersed IGV wake segments. It was difficult to draw firm conclusions about the time-mean stator loss values, as the observed variation in losses was comparable in magnitude with the uncertainty in the data. However, there did appear to be a reduction when the wake street from the IGV passed down the middle of the stator passage for the reduced axial spacing configuration.

Chapter 7 reported observations of the periodic transition behaviour of the outlet stator mid-span element as determined by an array of surface mounted hot-film gauges. The influence of blade loading, axial row spacing and clocking of the upstream IGV row were assessed. Presentation of space~time diagrams of intermittency revealed that the periodicity of the boundary layer transition behaviour tended to increase with incidence, and was strongest when transition occurred through a leading edge separation bubble. The periodic behaviour was also increased by a reduction in rotor-stator axial spacing; at off-design conditions there was evidence of suppression of a mid-chord separation bubble by unsteady transition phenomena. It also appears from observations of the stator suction surface behaviour at off-design conditions that flow acceleration at the leading edge will reduce transitional flow periodicity. Thus more modern blade sections with peak suction further rearward could show a reduced transitional flow periodicity. However, this effect may be nullified by the lower axial spacings of modern turbomachines as this would tend to increase the magnitude of periodic freestream disturbances and associated periodic transition phenomena. The surface hot-film observations showed significant fluctuations from leading edge potential flow interactions with rotor wake disturbances; they also indicated perturbed laminar boundary layer behaviour on the pressure surface in regions of rotor wake jet impingement.

All the measurements reported throughout this work only relate to the flow at mid-span. Skewing of the IGV wake street relative to the radial direction as it convects downstream will cause stator blade elements at different radial positions to experience unsteady flow behaviour ranging between the two limiting IGV clocking cases presented. The blades of an embedded rotor row in a multi-stage machine will experience similar flow variations.

Chapter 8 has shown that the continuous wavelet transform is a powerful tool for identifying instability wave phenomena in the periodically disturbed boundary layer on axial turbomachine blades. The main advantage of wavelet analysis is its ability to locate transient events in time and determine their associated frequency content. The Morlet wavelet was preferred for the analysis of transitional flow because of its close similarity to the signature of typical instability wave packets. Instability phenomena identified by wavelet analysis were shown to be well masked in the raw data from surface film gauges on the compressor blade because of large amplitude variations in wall shear stress produced by the passage of wake-induced turbulent strips. The application of wavelet analysis also assisted in identification of wave packets as they appear randomly

in time under the influence of free-stream turbulence. High-pass filtering of the film-gauge output helped focus attention on the wave phenomena.

The work reported in Chapter 8 has indicated an almost universal appearance of instability wave amplification prior to turbulent breakdown in decelerating flow regions on the compressor blade investigated. Evidence for direct production of turbulent spots in the boundary layer despite free-stream turbulence levels up to 8% was not observed. These observations closely resemble the wave packets and their ultimate breakdown in basic experiments on artificially generated spots arising from weak initial disturbances. It is therefore clear that high free-stream turbulence conditions do not imply the universal occurrence of transition via a bypass mode.

Further significant findings reported in Chapter 8 are,

(1) For the compressor blade investigated, the total length of blade surface over which the flow is governed by linear stability theory (either directly through wave packet amplification or indirectly though determining the T-S wave frequency which governs the turbulent spot inception rate) may be as much as 40% of chord.

(2) Wave activity may both occur in and originate from the calmed region following a wake-induced turbulent strip.

(3) The more stable flow in the ensuing *calmed region* does not guarantee the total absence of instability wave activity.

9.1 Future Work

The boundary layer on a downstream blade has been shown to respond in different ways to the various inflow disturbance components found in a multistage environment. The random disturbance component has been shown to directly influence the laminar-turbulent transition. Although it has not been directly measured, it is assumed that the periodic component operates indirectly through modifying the blade surface pressure distribution and/or boundary layer velocity profiles. The use of total disturbance level as a predictor of bypass transition has been questioned. Further study is required to resolve these issues and develop reliable unsteady boundary layer computations for axial turbomachine blades.

The experimental observations presented here will facilitate the development of these computational methods. It is therefore opportune to ask whether, armed with these predictive tools, it is possible to design compressor blades that exhibit an increase in performance similar to the recent improvements seen in LP Turbine blade design. Generally, the blade rows which are not dominated by three dimensional flows are associated with high aspect ratio and are located in the early stages of the compression system. For these early blade rows it is also likely that the turbulence levels between passing wakes will be lower than further rearward in the machine: in particular the fan outlet guide vane. Unfortunately, the design of these blades suffers from the complications of high Mach number flows and the possibility of shock/boundary layer interaction. This would add another degree of complexity to the modelling process and need further investigation in order to produce reliable designs. The observations on

the current blades have indicated that more forwardly loaded profiles exhibit increased periodicity of transitional flow and it could be argued that this is the path to increased compressor blade loadings. In the design of multistage axial compressors, forwardly loaded profiles are generally associated with a decrease in stable operating range, although the exact mechanisms for this reduction are not known. There can be little benefit in dramatically increasing the mid-span loading at the expense of the stability of blade endwall regions. On the other hand, more rearwardly loaded profile designs could benefit from a greater extent of low loss flow, but this may be counter acted by a reduction in the periodicity of the transitional flow. These hypotheses will need further investigation.

There is definite scope for extending the use of wavelet analysis techniques to aid the interpretation of unsteady flow phenomena. It has already been established that wavelet techniques can be used to improve intermittency detection and identification of relaxing flow following the passage of wake-induced turbulent strips on axial turbomachine blades. The analysis of periodic structures within recently developed turbulent spots is another topic of worthy of further investigation with wavelet techniques.

Appendix A

Periodic Unsteady Data Processing

This section outlines the use of averaging techniques to study the periodically varying flows downstream of a moving blade row commonly encountered in the turbomachinery environment. Typical flows are composed of random (freestream turbulence or vortex shedding [1]) and periodic (blade row interactions) disturbances, and are therefore categorised as a non-stationary random process (see Bendat and Piersol [8] for definitions). The random non-stationary nature of the signals mean that ensemble averaging techniques must be used to determine the relevant properties. The definitions presented here closely follow Solomon [123] and are based on the work of Evans [38], with some minor changes in nomenclature.

A.1 Long Term Averaging

If $Q(t)$ is a property measured at a fixed location in space at time t, sampled at n evenly spaced time periods (Δt) to give an array of data $Q(i)$ (each at time $t_i = t_0 + i\Delta t$) then the *long term mean* value of $Q(t)$ is

$$\overline{Q} = \frac{1}{n}\sum_{i=1}^{n} Q(i) \tag{A.1}$$

The instantaneous variation from the long term mean is

$$Q'(i) = Q(i) - \overline{Q} \tag{A.2}$$

and so the *long term RMS* value of $Q(t)$ is

$$Q'_{RMS} = \left[\frac{1}{n}\sum_{i=1}^{n} Q'(i)^2\right]^{1/2} \tag{A.3}$$

For measurements in a machine environment, accurate determination of long term values requires averaging over many periods to include variations of the order of once per rotor scale and possibly larger.

[1] Vortex shedding is a quasi-periodic phenomena. It may contribute to the periodic unsteadiness if phase-locked with the rotor passing period. Alternatively it will appear as random disturbances superimposed on the ensemble average if not phase-locked.

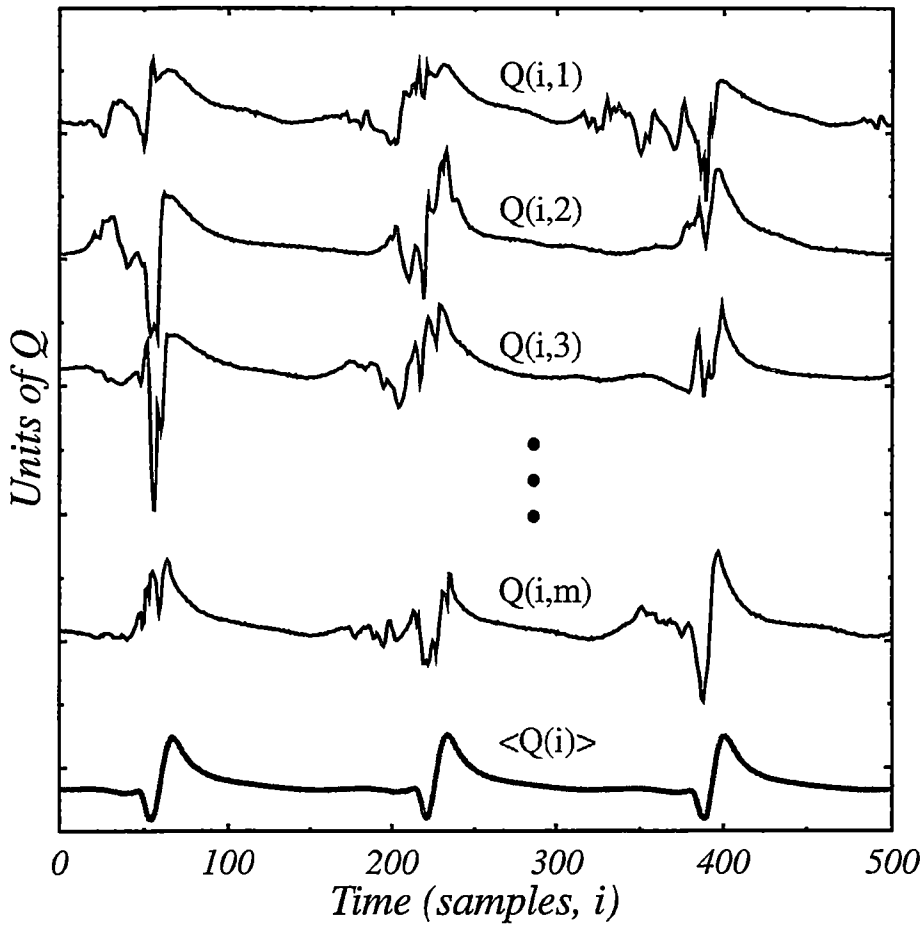

Figure A.1: Typical instantaneous realisations $Q(i,k)$ over three rotor blade passing periods with the resulting ensemble average $<Q(i)>$ shown at bottom.

A.2 Ensemble Averaging Techniques

Ensemble averaging is used to resolve phase-locked periodic components from non-stationary signals. Sampling is synchronised relative to a periodic event, commonly triggered by rotor passing for turbomachines, and as such is also referred to as phase-locked averaging. Data is acquired in a two-dimensional array $Q(i,k)$ of size $(n \times m)$ where the index k identifies the individual realisation from the ensemble of m realisations. The k realisations all start at the same relative reference time $t_{0,k}$ defined by the trigger point, and therefore each data point $Q(i,k)$ is acquired at time $t_{i,k} = t_{0,k} + i\Delta t$. The *ensemble average* of $Q(t)$ at a particular time $t_i = t_0 + i\Delta t$ can then be calculated by taking the average over all m realisations (see Fig. A.1). Thus

$$<Q(i)> = \frac{1}{m}\sum_{k=1}^{m} Q(i,k) \tag{A.4}$$

True random fluctuations in the signal are given by the excursion from the ensemble

mean level:

$$Q''(i,k) = Q(i,k) - <Q(i)> \tag{A.5}$$

The *ensemble variance* or *ensemble RMS* at time t_i is then

$$<Q(i)>_{RMS} = \left[\frac{1}{m}\sum_{k=1}^{m} Q''(i,k)^2\right]^{1/2} \tag{A.6}$$

Appropriate normalisation of the ensemble RMS signal may alter depending on the relative value of the mean or ensemble mean.

A.3 Disturbance and Turbulence Level Analysis

If $Q(i)$ is the velocity $U(i)$, then the instantaneous velocity may be expressed as

$$U(i) = \overline{U} + U'(i) = <U(i)> + U''(i) \tag{A.7}$$

The *unsteadiness* of $U(i)$ is defined as the excursion of the ensemble average value from the long term mean value at the given point t_i in the period and is given by

$$\widetilde{U}(i) = <U(i)> - \overline{U} \tag{A.8}$$

Therefore, the *periodic unsteadiness level* $\widetilde{Tu}$ is

$$\widetilde{Tu} = \frac{\sqrt{\frac{1}{n}\sum_{i=1}^{n}\widetilde{U}(i)^2}}{\overline{U}} \tag{A.9}$$

It is important to note that either many periods or an integral number of periods are used to calculate $\widetilde{Tu}$ with minimum bias. This generally applies to the other properties, but to a lesser extent. In a machine, variations in flow between different blade passages will increase the measured unsteadiness unless sampling is over the same blade passage(s) for each realisation.

Following Evans [38] the *ensemble local randomness* or *freestream turbulence* $<Tu(i)>$ is defined as

$$<Tu(i)> = \frac{<U(i)>_{RMS}}{\overline{U}} \tag{A.10}$$

The *long term freestream turbulence* can be found by averaging the local values over an integral number of periods (or a large number of periods).

$$Tu = \frac{1}{\overline{U}}\left[\frac{1}{mn}\sum_{k=1}^{m}\sum_{i=1}^{n} U''(i,k)^2\right]^{1/2} \tag{A.11}$$

$$= \left[\frac{1}{n}\sum_{i=1}^{n} <Tu(i)>^2\right]^{1/2} \tag{A.12}$$

Over the ensemble the *total disturbance level* is

$$Tu_D = \frac{1}{\overline{\overline{U}}} \left[\frac{1}{mn} \sum_{k=1}^{m} \sum_{i=1}^{n} U'(i,k) \right]^{1/2} \tag{A.13}$$

Evans [38] shows that, with some minor approximations, the periodic unsteadiness and freestream turbulence are related to the total disturbance level by

$$Tu_D{}^2 = \widetilde{Tu}^2 + Tu^2 \tag{A.14}$$

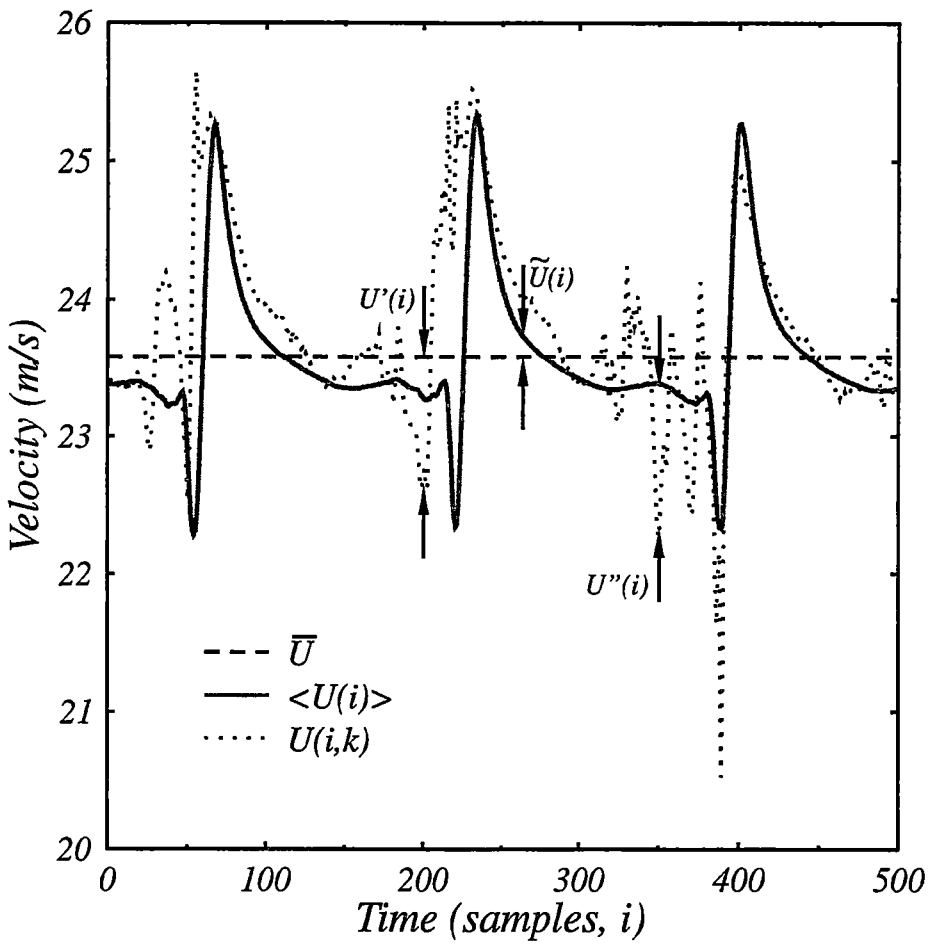

Figure A.2: Typical instantaneous velocity trace, long term and ensemble average values showing three rotor blade passing events. Definitions of random and periodic disturbances also shown.

Appendix B

Sensor Locations

This section gives the locations of the pressure tappings and the hot-film sensors for the instrumented stator blades. Solomon [123] used the original C4 polynomial definitions to reconstruct the blade shapes and calculate the sensor locations relative to the leading edge. The leading edge was defined as the end of the camber line. Results are presented in both graphical and tabular form.

B.1 Pressure Tapping Locations

Table B.1 gives the locations of the pressure tappings for the suction and pressure surface tapped blades. The surface distances s^* and the x, y coordinates are referenced to 0,0 at the leading edge. The x/c positions are accurate to the diameter of the tappings (0.5 mm). Fig. B.1 shows both suction and pressure tapping locations on the same blade, whereas the instrumented surfaces are actually on separate stator blades in the same flow passage.

B.2 Hot-film Sensor Locations

The Senflex array of 61 hot-film sensors were manufactured with a pitch of 2.54 mm and then wrapped around the stator blade at mid-span. The nominal chord of the stator blades was $c = 76.2$mm, but measurements of the instrumented blade indicated it had a chord $c = 75.7$ mm giving a maximum surface distance $s_{c,max} = 76.6$ mm. Solomon [123] determined the individual sensor locations by measuring the distance of the first sensor from the trailing edge: calculating the positions for the remaining sensors using the blade profile information and comparing the calculated and measured position of the last sensor with respect to the trailing edge. The results agreed to within the measurement accuracy of 0.3% chord. The sensors are numbered in a clockwise direction, with sensor #1 close to the trailing edge on the suction surface, and sensor #61 close to the trailing edge on the pressure surface. The sensor locations are illustrated in Fig. B.2.

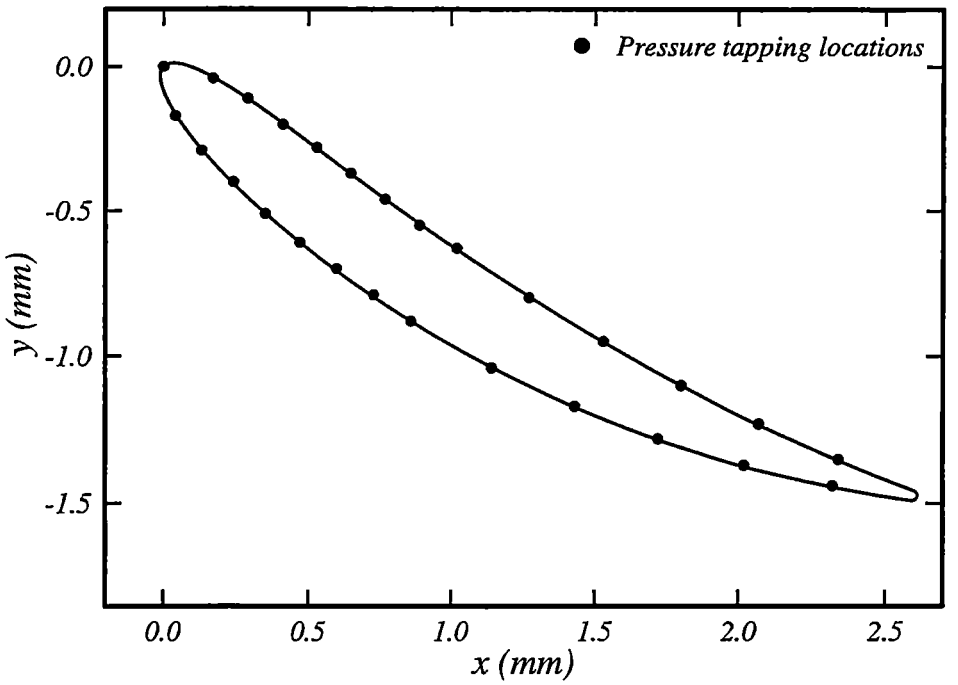

Figure B.1: Pressure tapping locations around stator blade profile at mid-blade height, from Solomon [123]

Table B.1: Pressure tapping positions , $C = 75.7mm$, $\theta = 31.1°$ and $\xi = 29.5°$. $S_1 = S_c/S_{c,max}$ and $S_2 = S_u/S_{u,max}$ on the suction surface and $S_3 = S_l/S_{l,max}$ on the pressure surface where $S_{u,max} = 79.23$ mm, and $S_{l,max} = 76.27$ mm and $S_{c,max} = 76.64$ mm.

Pressure tappings								
#	x/c	S_1	S_2	$x[mm]$	$y[mm]$	S_3	$x[mm]$	$y[mm]$
1	0.00	0.0000	0.0000	0.00	0.00	0.0000	0.00	0.00
2	0.05	0.0479	0.0580	1.05	4.22	0.0592	4.20	0.91
3	0.10	0.0965	0.1067	3.35	7.33	0.1080	7.37	2.86
4	0.15	0.1456	0.1556	5.97	10.17	0.1565	10.40	4.98
5	0.20	0.1952	0.2048	8.82	12.84	0.2052	13.40	7.18
6	0.25	0.2453	0.2546	11.85	15.36	0.2542	16.41	9.40
7	0.30	0.2958	0.3047	15.02	17.76	0.3036	19.45	11.62
8	0.35	0.3466	0.3552	18.30	20.04	0.3533	22.54	13.82
9	0.40	0.3976	0.4058	21.68	22.20	0.4032	25.68	15.97
10	0.50	0.5000	0.5074	28.70	26.14	0.5035	32.10	20.13
11	0.60	0.6024	0.6089	35.98	29.55	0.6042	38.69	24.07
12	0.70	0.7042	0.7095	43.42	32.40	0.7047	45.41	27.75
13	0.80	0.8048	0.8087	50.94	34.68	0.8045	52.23	31.13
14	0.90	0.9035	0.9056	58.42	36.43	0.9030	59.10	34.19

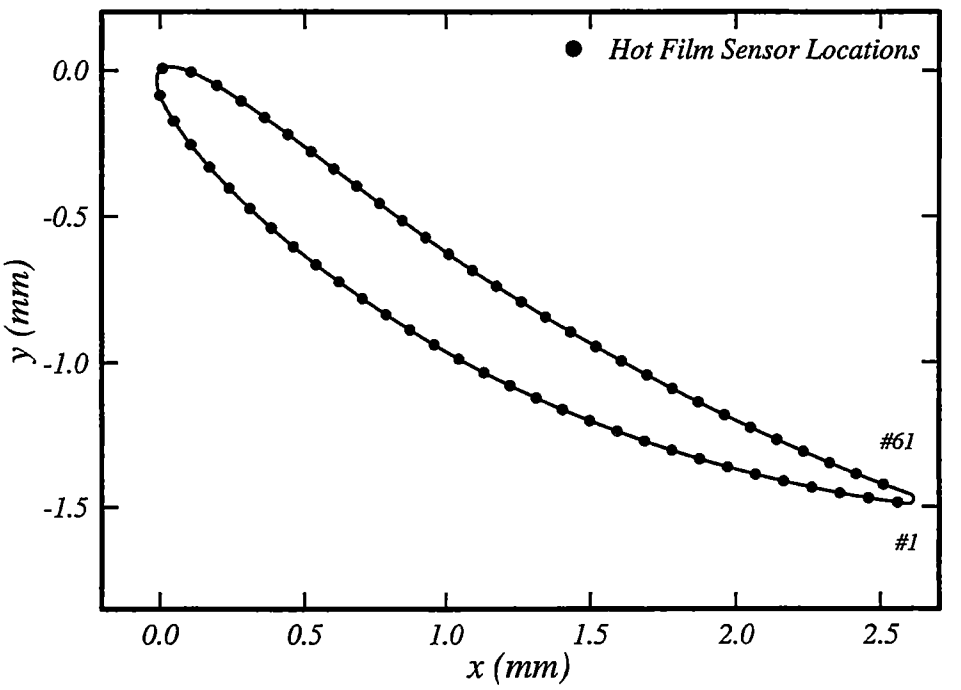

Figure B.2: Hot-film sensor locations around stator blade profile at mid-blade height, from Solomon [123]

Table B.2: Hot-film sensor positions for instrumented blade, $C = 75.7mm$, $\theta = 31.1°$ and $\xi = 29.5°$. $S_1 = S_c/S_{c,max}$ and $S_2 = S_u/S_{u,max}$ on the suction surface and $S_2 = S_l/S_{l,max}$ on the pressure surface where $S_{u,max} = 79.23$ mm, and $S_{l,max} = 76.27$ mm and $S_{c,max} = 76.64$ mm.

Suction Surface				
#	S_1	S_2	$x[mm]$	$y[mm]$
1	0.9836	0.9840	64.53	37.48
2	0.9508	0.9519	62.02	37.09
3	0.9180	0.9199	59.52	36.64
4	0.8853	0.8878	57.03	36.14
5	0.8527	0.8557	54.55	35.59
6	0.8200	0.8237	52.09	34.99
7	0.7875	0.7916	49.63	34.33
8	0.7549	0.7596	47.20	33.61
9	0.7224	0.7275	44.77	32.85
10	0.6899	0.6955	42.37	32.03
11	0.6575	0.6634	39.99	31.16
12	0.6251	0.6313	37.62	30.23
13	0.5927	0.5993	35.28	29.25
14	0.5603	0.5672	32.96	28.22
15	0.5280	0.5352	30.66	27.13
16	0.4957	0.5031	28.39	25.99
17	0.4633	0.4711	26.15	24.79
18	0.4310	0.4390	23.94	23.55
19	0.3987	0.4069	21.76	22.25
20	0.3665	0.3749	19.60	20.90
21	0.3342	0.3428	17.49	19.49
22	0.3019	0.3108	15.40	18.04
23	0.2696	0.2787	13.36	16.53
24	0.2373	0.2467	11.36	14.97
25	0.2051	0.2146	9.40	13.35
26	0.1728	0.1825	7.51	11.66
27	0.1405	0.1505	5.69	9.89
28	0.1083	0.1184	3.95	8.03
29	0.0762	0.0864	2.34	6.07
30	0.0444	0.0543	0.90	3.98
31	0.0139	0.0223	-0.17	1.68

Pressure Surface				
#	S_1	S_2	$x[mm]$	$y[mm]$
32	0.0039	0.0102	0.71	-0.29
33	0.0328	0.0435	3.14	0.37
34	0.0653	0.0768	5.37	1.58
35	0.0986	0.1101	7.51	2.95
36	0.1323	0.1434	9.59	4.40
37	0.1662	0.1767	11.65	5.89
38	0.2001	0.2100	13.70	7.40
39	0.2341	0.2433	15.74	8.91
40	0.2682	0.2766	17.78	10.41
41	0.3022	0.3099	19.84	11.90
42	0.3363	0.3432	21.91	13.37
43	0.3703	0.3765	24.00	14.82
44	0.4044	0.4098	26.10	16.25
45	0.4384	0.4431	28.22	17.65
46	0.4724	0.4764	30.35	19.03
47	0.5063	0.5097	32.50	20.38
48	0.5402	0.5430	34.67	21.70
49	0.5741	0.5763	36.85	23.00
50	0.6079	0.6096	39.05	24.28
51	0.6417	0.6429	41.26	25.52
52	0.6755	0.6762	43.49	26.73
53	0.7091	0.7095	45.74	27.92
54	0.7427	0.7428	48.00	29.08
55	0.7763	0.7761	50.28	30.20
56	0.8097	0.8094	52.57	31.29
57	0.8432	0.8427	54.88	32.35
58	0.8765	0.8760	57.20	33.38
59	0.9098	0.9093	59.54	34.37
60	0.9430	0.9426	61.89	35.33
61	0.9761	0.9759	64.26	36.25

Appendix C

Measurements Downstream of Rotor Trailing Edge

C.1 Large Axial Spacing Results

The following section contains the results obtained from hot-wire measurements downstream of the rotor trailing edge for the Large Axial Gap (LAG) configuration (119% chord IGV-rotor and 106%chord rotor-stator axial blade row spacings) at the medium loading condition.

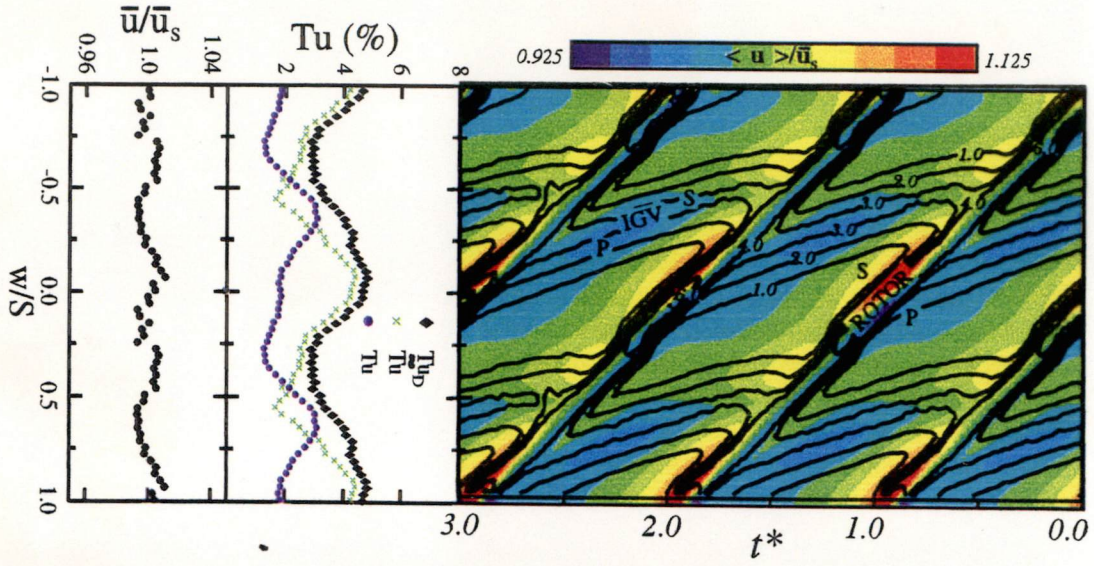

Figure C.1: Contours of ensemble average turbulence level $<Tu>$. S = Suction Side; P = Pressure Side. LAG case, $\phi = 0.675$, $Re_{ref} = 120\ 000$.

Figure C.3: Unsteady flow field 4.6%c axial distance downstream of rotor trailing edge. Left: Time-averaged velocity. Middle: Random, periodic and total turbulence. Right: Ensemble average velocity. LAG case, $\phi = 0.675$, $Re_{ref} = 120\ 000$.

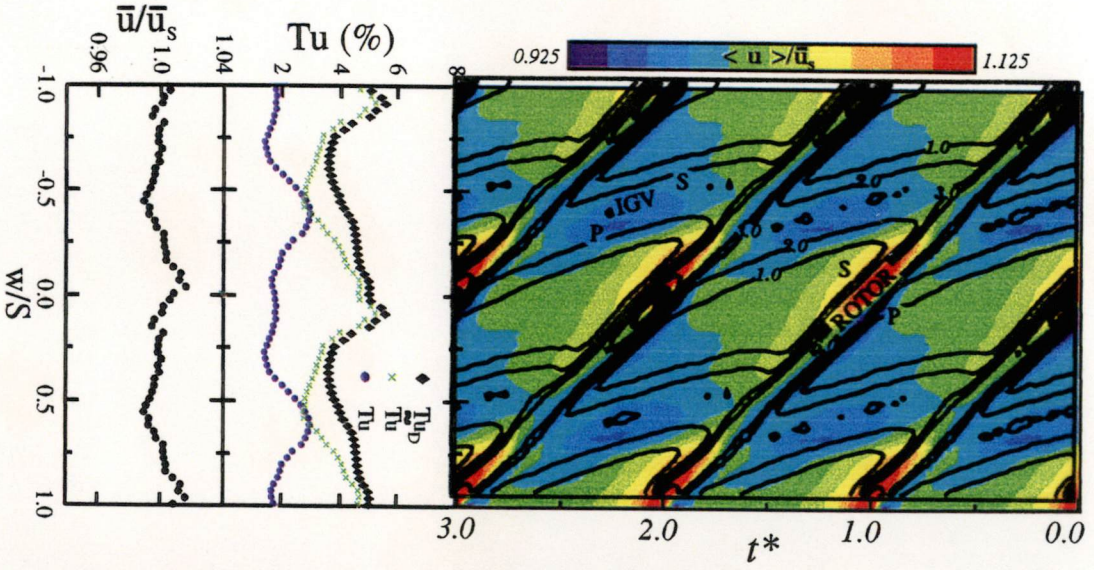

Figure C.2: Contours of ensemble average turbulence level $<Tu>$. S = Suction Side; P = Pressure Side. LAG case, $\phi = 0.675$, $Re_{ref} = 120\ 000$.

Figure C.4: Unsteady flow field 7.5%c axial distance downstream of rotor trailing edge. Left: Time-averaged velocity. Middle: Random, periodic and total turbulence. Right: Ensemble average velocity. LAG case, $\phi = 0.675$, $Re_{ref} = 120\ 000$.

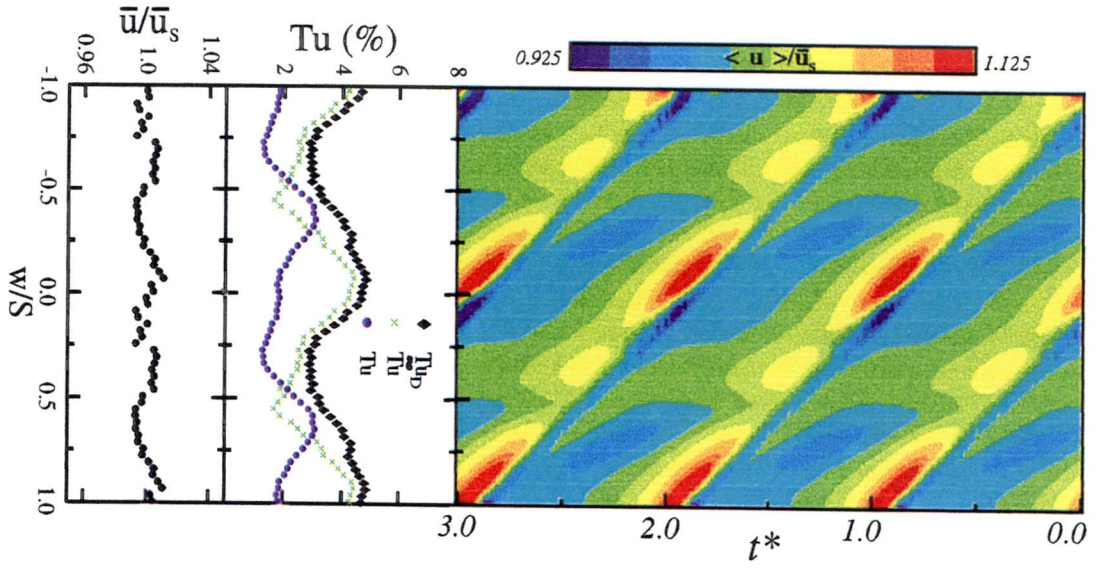

Figure C.3: Unsteady flow field 4.6%c axial distance downstream of rotor trailing edge. Left: Time-averaged velocity. Middle: Random, periodic and total turbulence. Right: Ensemble average velocity. LAG case, $\phi = 0.675$, $Re_{ref} = 120\ 000$.

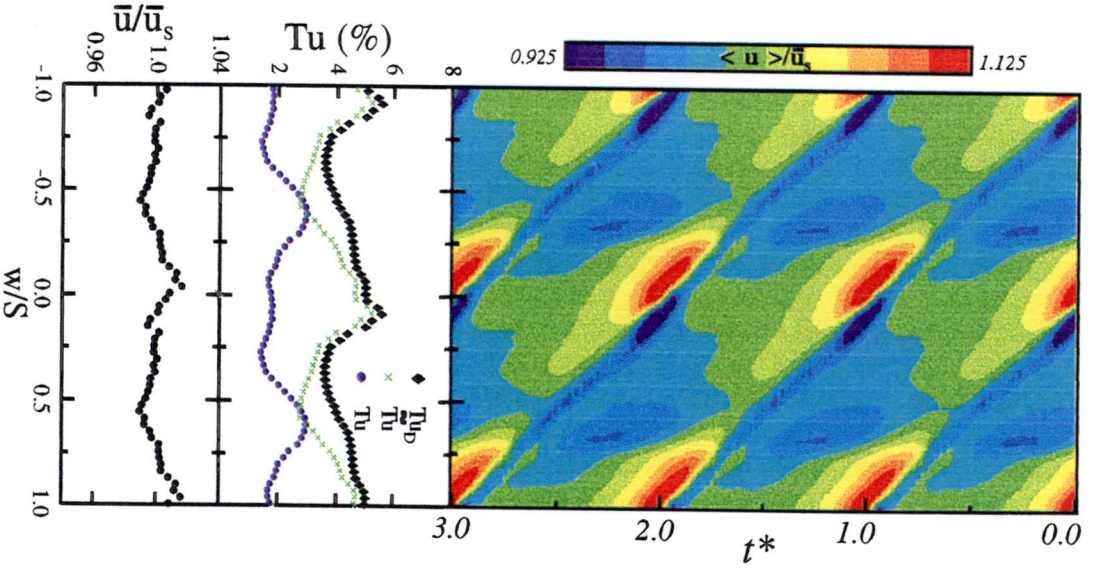

Figure C.4: Unsteady flow field 7.5%c axial distance downstream of rotor trailing edge. Left: Time-averaged velocity. Middle: Random, periodic and total turbulence. Right: Ensemble average velocity. LAG case, $\phi = 0.675$, $Re_{ref} = 120\ 000$.

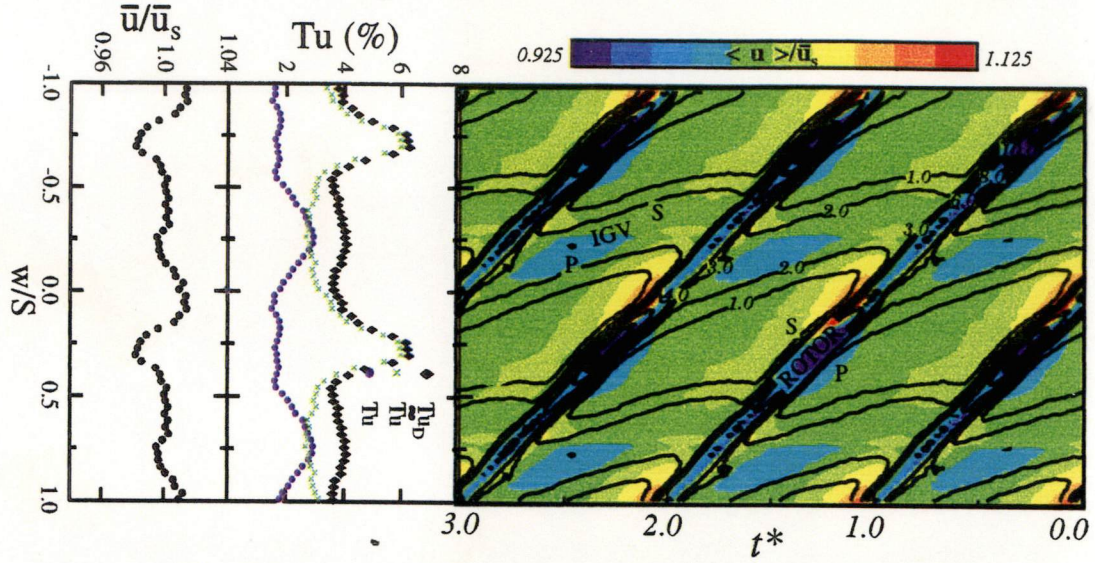

Figure C.5: Contours of ensemble average turbulence level $<Tu>$. S = Suction Side; P = Pressure Side. LAG case, $\phi = 0.675$, $Re_{ref} = 120\ 000$.

Figure C.7: Unsteady flow field 16.6%c axial distance downstream of rotor trailing edge. Left: Time-averaged velocity. Middle: Random, periodic and total turbulence. Right: Ensemble average velocity. LAG case, $\phi = 0.675$, $Re_{ref} = 120\ 000$.

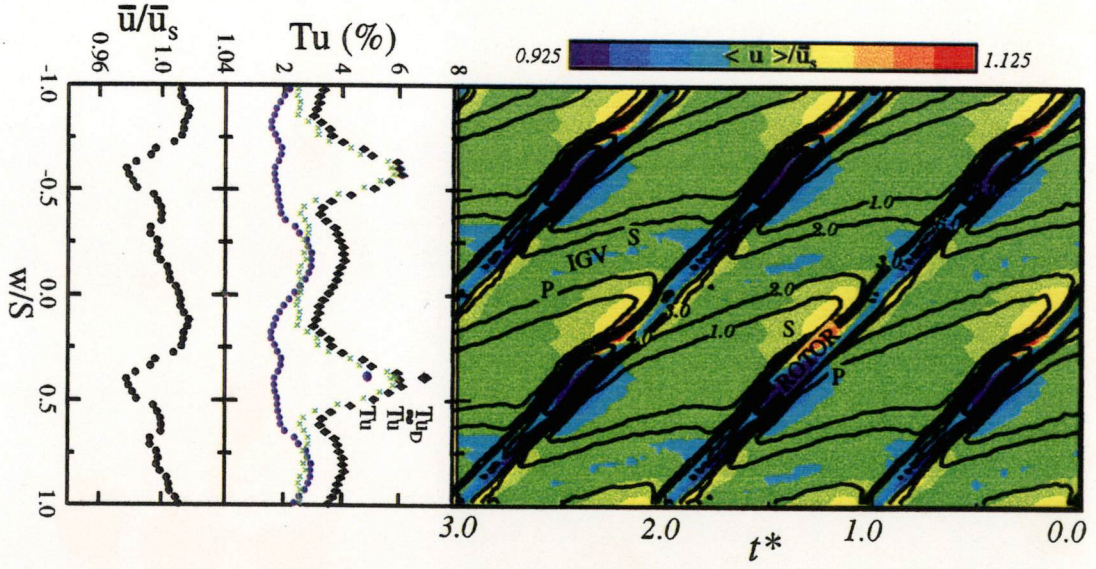

Figure C.6: Contours of ensemble average turbulence level $<Tu>$. S = Suction Side; P = Pressure Side. LAG case, $\phi = 0.675$, $Re_{ref} = 120\ 000$.

Figure C.8: Unsteady flow field 26.8%c axial distance downstream of rotor trailing edge. Left: Time-averaged velocity. Middle: Random, periodic and total turbulence. Right: Ensemble average velocity. LAG case, $\phi = 0.675$, $Re_{ref} = 120\ 000$.

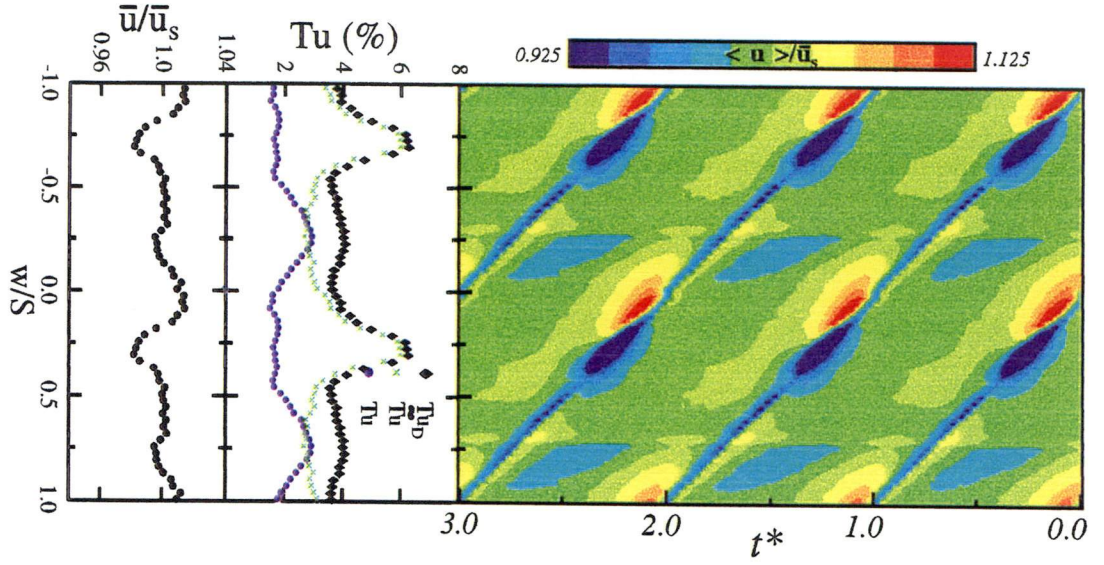

Figure C.7: Unsteady flow field 16.6%c axial distance downstream of rotor trailing edge. Left: Time-averaged velocity. Middle: Random, periodic and total turbulence. Right: Ensemble average velocity. LAG case, $\phi = 0.675$, $Re_{ref} = 120\ 000$.

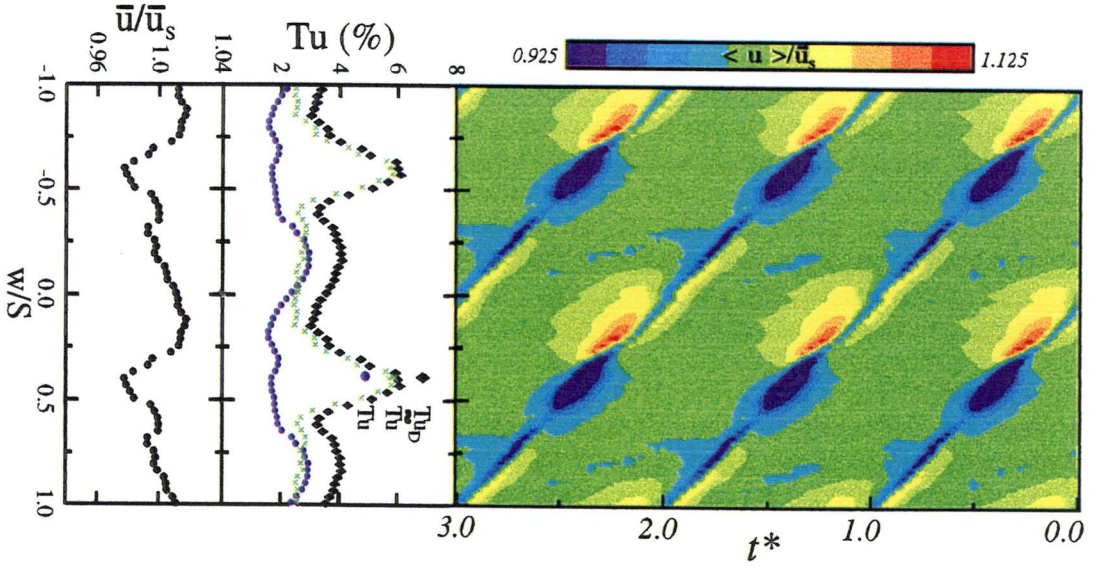

Figure C.8: Unsteady flow field 26.8%c axial distance downstream of rotor trailing edge. Left: Time-averaged velocity. Middle: Random, periodic and total turbulence. Right: Ensemble average velocity. LAG case, $\phi = 0.675$, $Re_{ref} = 120\ 000$.

Appendix D

Measurements Downstream of Stator Trailing Edge

D.1 Large Axial Spacing Results

The following section contains the results obtained from hot-wire measurements 14.4%chord downstream of the stator trailing edge for the Large Axial Gap (LAG) configuration (119% chord IGV-rotor and 106%chord rotor-stator axial blade row spacings) at the medium loading condition.

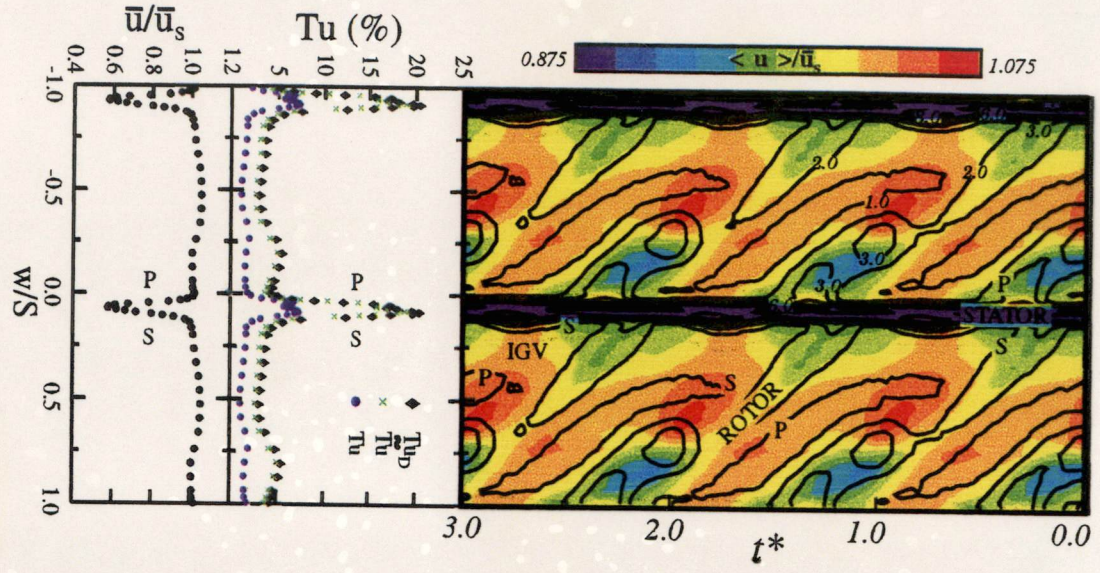

Figure D.1: Dashed lines indicate periodic variation of stator wake edge and centre line. LAG case, $\phi = 0.675$, $Re_{ref} = 120\ 000$, $a/S = 0.00$.
Figure D.3: Contours of ensemble average turbulence level $<Tu>$. S = Suction Side; P = Pressure Side. LAG case, $\phi = 0.675$, $Re_{ref} = 120\ 000$, $a/S = 0.00$.
Figure D.5: Unsteady flow field 14.4%c axial distance downstream of stator trailing edge. Left: Time-averaged velocity. Middle: Random, periodic and total turbulence. Right: Ensemble average velocity. LAG case, $\phi = 0.675$, $Re_{ref} = 120\ 000$, $a/S = 0.00$.

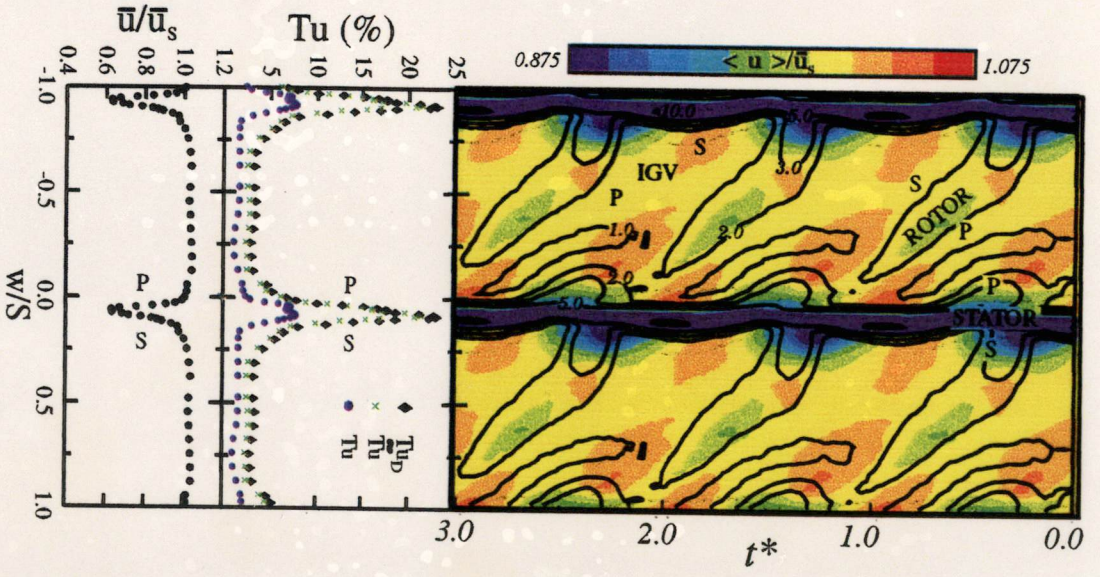

Figure D.2: Dashed lines indicate periodic variation of stator wake edge and centre line. LAG case, $\phi = 0.675$, $Re_{ref} = 120\ 000$, $a/S = 0.25$.
Figure D.4: Contours of ensemble average turbulence level $<Tu>$. S = Suction Side; P = Pressure Side. LAG case, $\phi = 0.675$, $Re_{ref} = 120\ 000$, $a/S = 0.25$.
Figure D.6: Unsteady flow field 14.4%c axial distance downstream of stator trailing edge. Left: Time-averaged velocity. Middle: Random, periodic and total turbulence. Right: Ensemble average velocity. LAG case, $\phi = 0.675$, $Re_{ref} = 120\ 000$, $a/S = 0.25$.

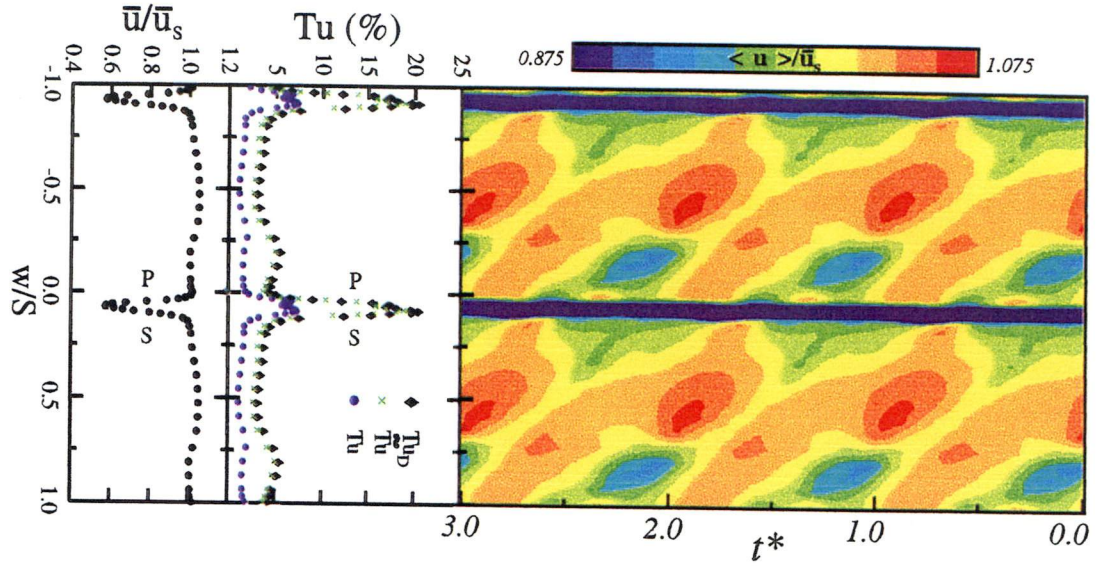

Figure D.5: Unsteady flow field 14.4%c axial distance downstream of stator trailing edge. Left: Time-averaged velocity. Middle: Random, periodic and total turbulence. Right: Ensemble average velocity. LAG case, $\phi = 0.675$, $Re_{ref} = 120\ 000$, $a/S = 0.00$.

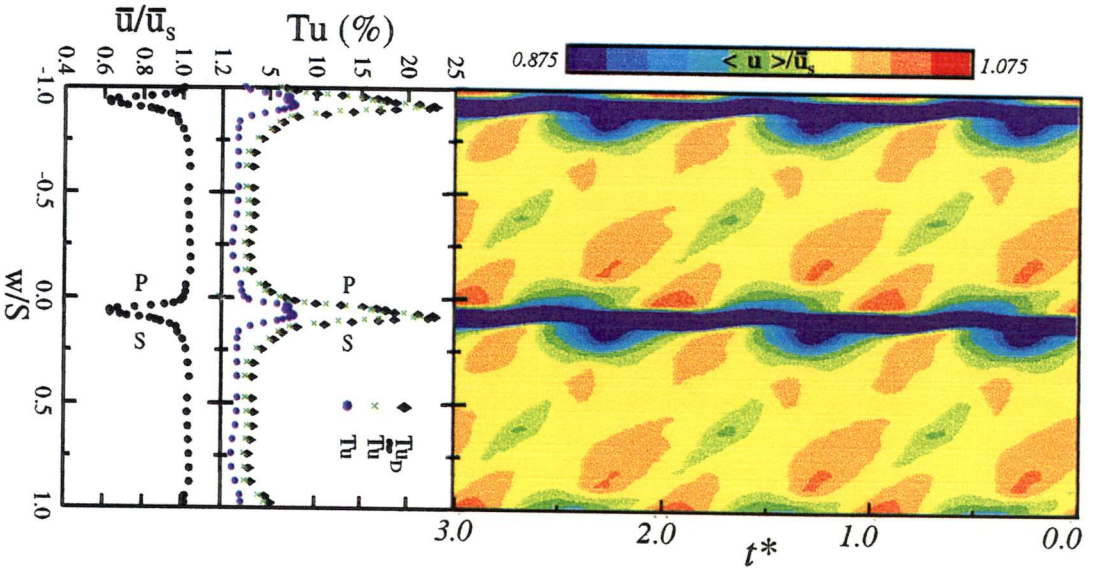

Figure D.6: Unsteady flow field 14.4%c axial distance downstream of stator trailing edge. Left: Time-averaged velocity. Middle: Random, periodic and total turbulence. Right: Ensemble average velocity. LAG case, $\phi = 0.675$, $Re_{ref} = 120\ 000$, $a/S = 0.25$.

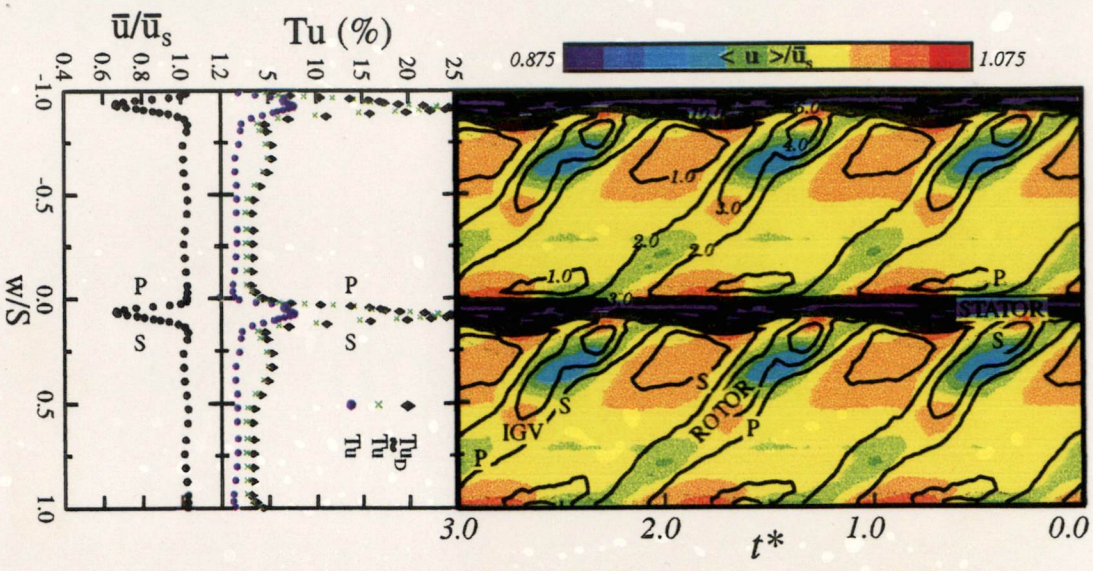

Figure D.7: Dashed lines indicate periodic variation of stator wake edge and centre line. LAG case, $\phi = 0.675$, $Re_{ref} = 120\ 000$, $a/S = 0.50$.
Figure D.9: Contours of ensemble average turbulence level $<Tu>$. S = Suction Side; P = Pressure Side. LAG case, $\phi = 0.675$, $Re_{ref} = 120\ 000$, $a/S = 0.50$.
Figure D.11: Unsteady flow field 14.4%c axial distance downstream of stator trailing edge. Left: Time-averaged velocity. Middle: Random, periodic and total turbulence. Right: Ensemble average velocity. LAG case, $\phi = 0.675$, $Re_{ref} = 120\ 000$, $a/S = 0.50$.

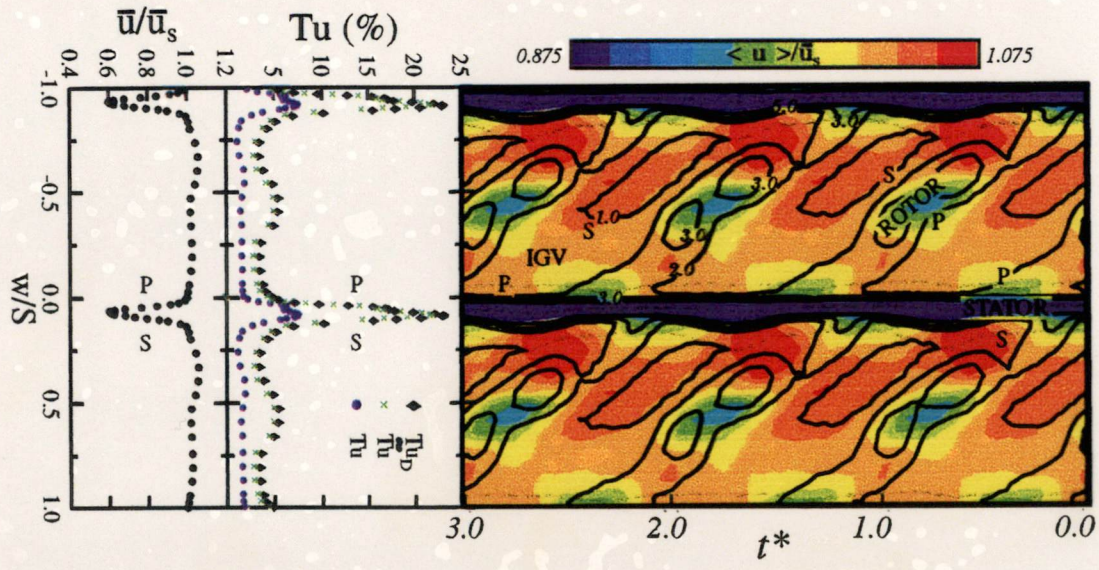

Figure D.8: Dashed lines indicate periodic variation of stator wake edge and centre line. LAG case, $\phi = 0.675$, $Re_{ref} = 120\ 000$, $a/S = 0.75$.
Figure D.10: Contours of ensemble average turbulence level $<Tu>$. S = Suction Side; P = Pressure Side. LAG case, $\phi = 0.675$, $Re_{ref} = 120\ 000$, $a/S = 0.75$.
Figure D.12: Unsteady flow field 14.4%c axial distance downstream of stator trailing edge. Left: Time-averaged velocity. Middle: Random, periodic and total turbulence. Right: Ensemble average velocity. LAG case, $\phi = 0.675$, $Re_{ref} = 120\ 000$, $a/S = 0.75$.

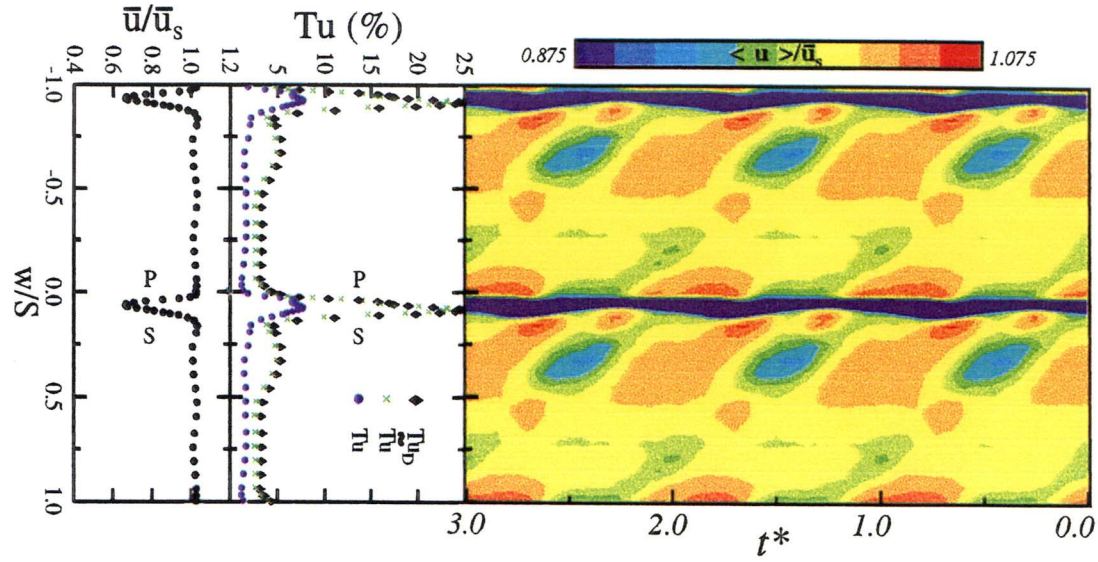

Figure D.11: Unsteady flow field 14.4%c axial distance downstream of stator trailing edge. Left: Time-averaged velocity. Middle: Random, periodic and total turbulence. Right: Ensemble average velocity. LAG case, $\phi = 0.675$, $Re_{ref} = 120\ 000$, $a/S = 0.50$.

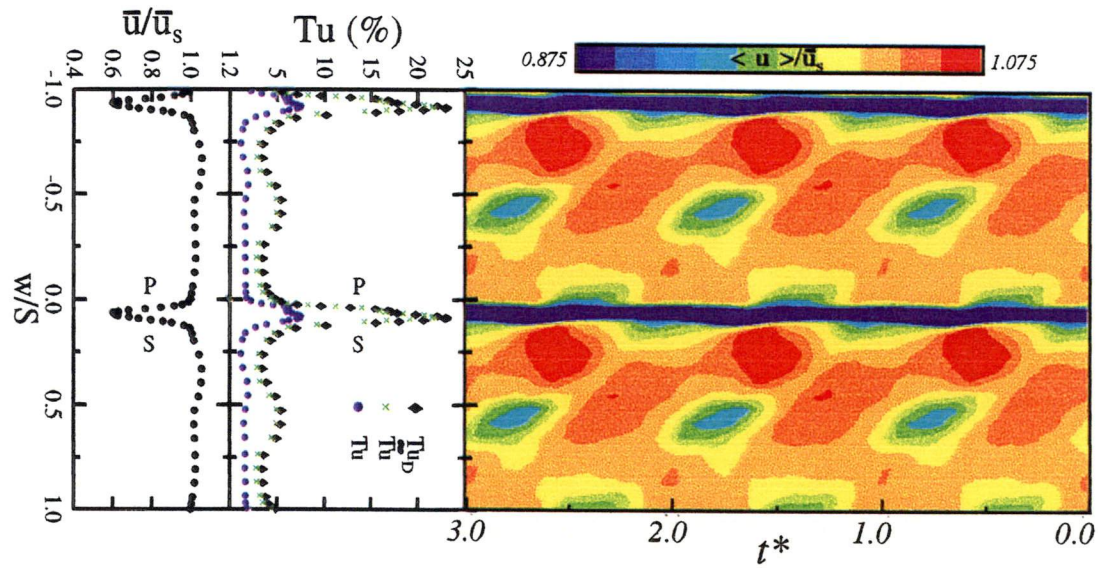

Figure D.12: Unsteady flow field 14.4%c axial distance downstream of stator trailing edge. Left: Time-averaged velocity. Middle: Random, periodic and total turbulence. Right: Ensemble average velocity. LAG case, $\phi = 0.675$, $Re_{ref} = 120\ 000$, $a/S = 0.75$.

D.2 Reduced Axial Spacing Results

The following section contains the results obtained from hot-wire measurements 14.4%chord downstream of the stator trailing edge for the Reduced Axial Gap (RAG) configuration (117% chord IGV-rotor and 41.6%chord rotor-stator axial blade row spacings) at the medium loading condition.

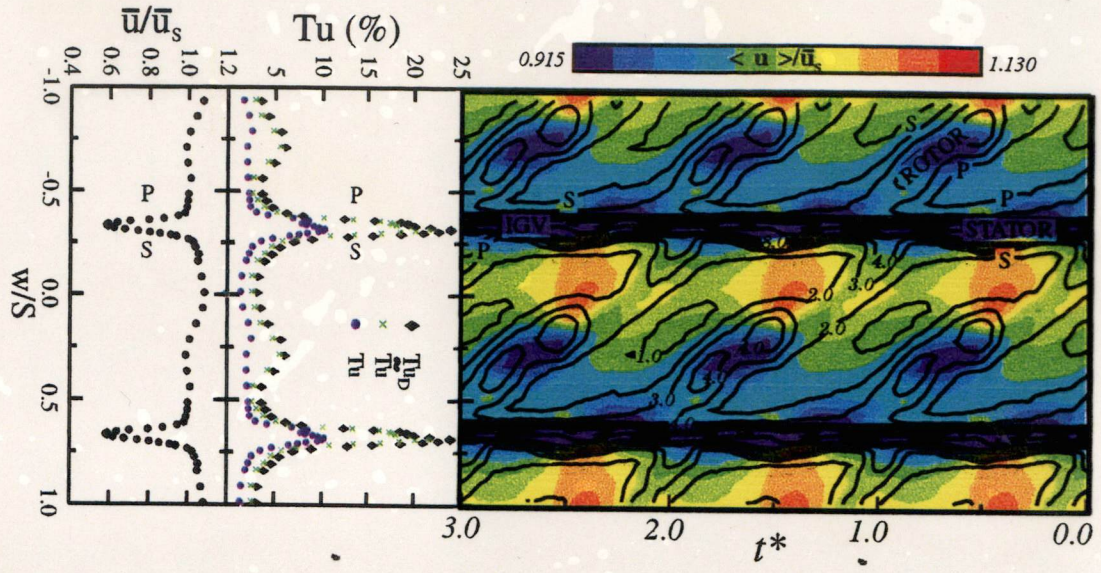

Figure D.13: Dashed lines indicate periodic variation of stator wake edge and centre line. RAG case, $\phi = 0.675$, $Re_{ref} = 120\ 000$, $a/S = 0.00$.
Figure D.15: Contours of ensemble average turbulence level $<Tu>$. S = Suction Side; P = Pressure Side. RAG case, $\phi = 0.675$, $Re_{ref} = 120\ 000$, $a/S = 0.00$.
Figure D.17: Unsteady flow field 14.4%c axial distance downstream of stator trailing edge. Left: Time-averaged velocity. Middle: Random, periodic and total turbulence. Right: Ensemble average velocity. RAG case, $\phi = 0.675$, $Re_{ref} = 120\ 000$, $a/S = 0.00$.

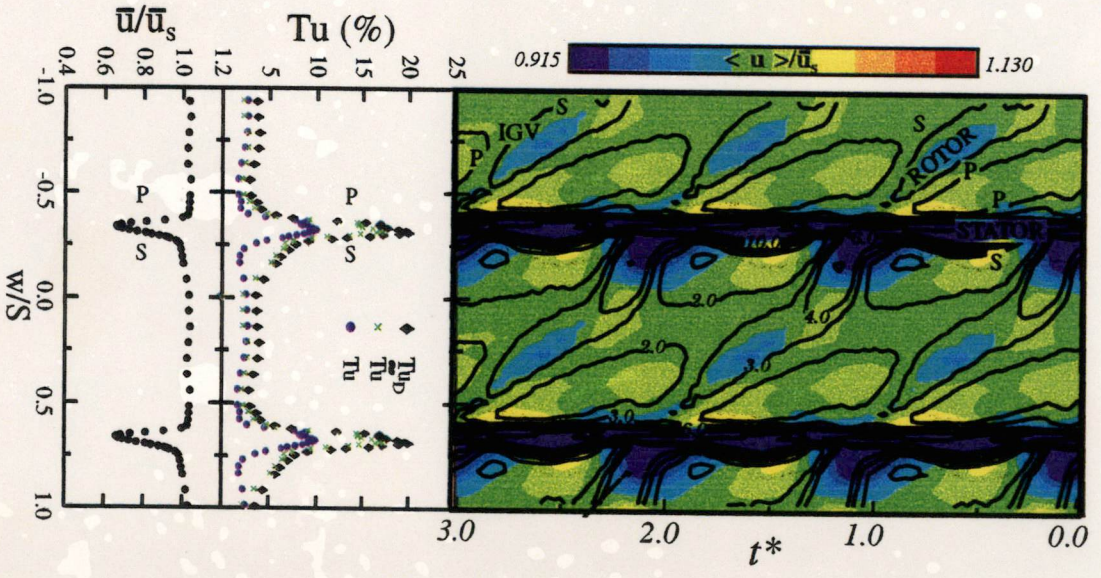

Figure D.14: Dashed lines indicate periodic variation of stator wake edge and centre line. RAG case, $\phi = 0.675$, $Re_{ref} = 120\ 000$, $a/S = 0.50$.
Figure D.16: Contours of ensemble average turbulence level $<Tu>$. S = Suction Side; P = Pressure Side. RAG case, $\phi = 0.675$, $Re_{ref} = 120\ 000$, $a/S = 0.50$.
Figure D.18: Unsteady flow field 14.4%c axial distance downstream of stator trailing edge. Left: Time-averaged velocity. Middle: Random, periodic and total turbulence. Right: Ensemble average velocity. RAG case, $\phi = 0.675$, $Re_{ref} = 120\ 000$, $a/S = 0.50$.

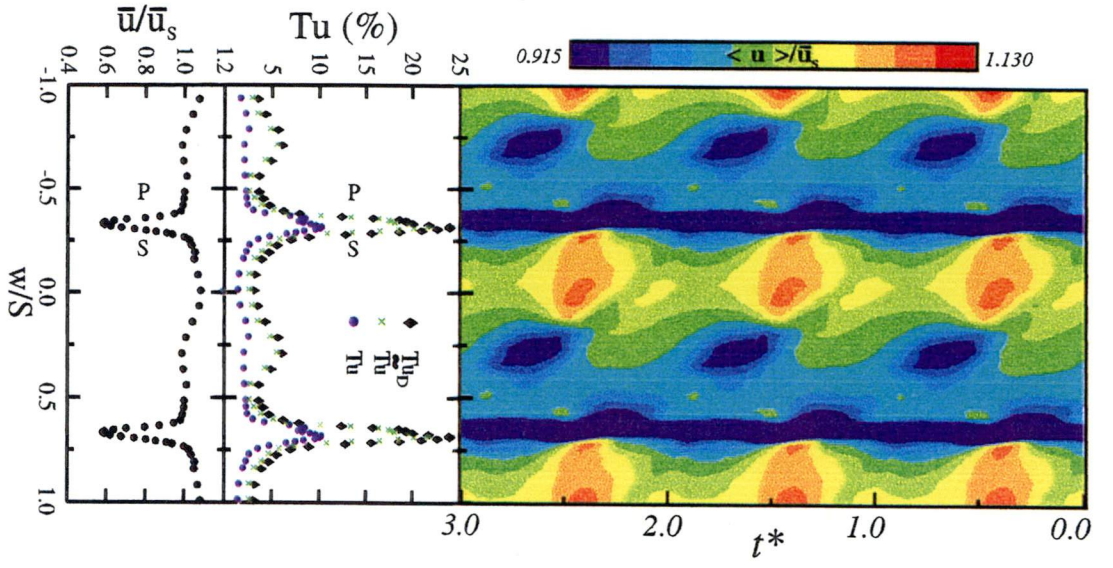

Figure D.17: Unsteady flow field 14.4%c axial distance downstream of stator trailing edge. Left: Time-averaged velocity. Middle: Random, periodic and total turbulence. Right: Ensemble average velocity. RAG case, $\phi = 0.675$, $Re_{ref} = 120\,000$, $a/S = 0.00$.

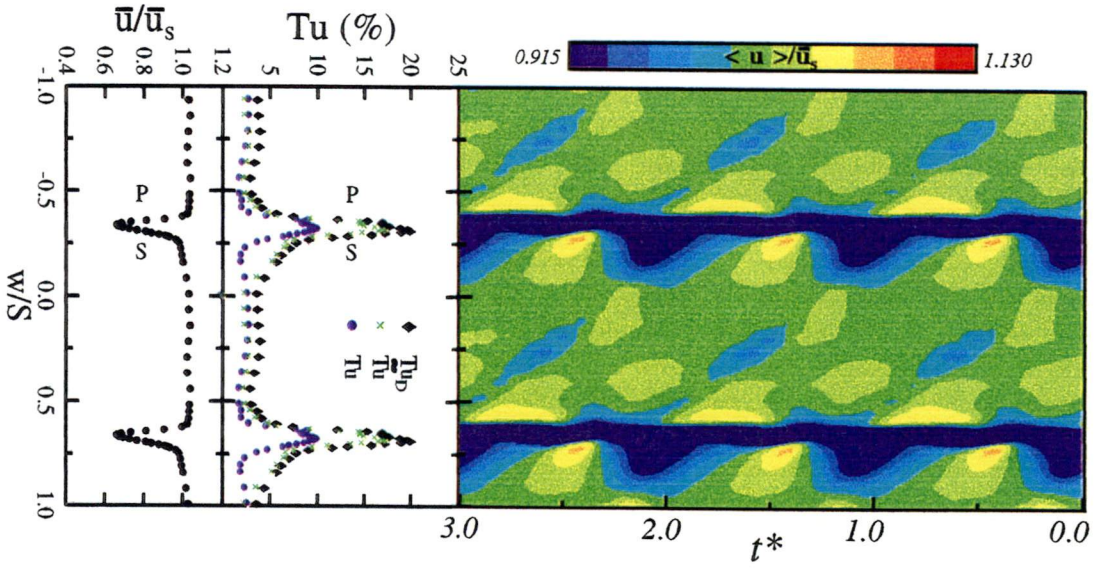

Figure D.18: Unsteady flow field 14.4%c axial distance downstream of stator trailing edge. Left: Time-averaged velocity. Middle: Random, periodic and total turbulence. Right: Ensemble average velocity. RAG case, $\phi = 0.675$, $Re_{ref} = 120\,000$, $a/S = 0.50$.

Bibliography

[1] Abu-Ghannam, B. J. and Shaw, R. Natural transition of boundary layers - the effects of pressure gradient and flow history. *Journal of Mechanical Engineering Science*, 22(5):213–228, 1980.

[2] Adamczyk, J. J. Wake mixing in axial flow compressors. ASME Paper 96-GT-29, Birmingham, 1996.

[3] Adamczyk, J. J. Aerodynamic analysis of multistage turbomachinery flows in support of aerodynamic design. ASME Paper 99-GT-80, Indianapolis, 1999.

[4] Addison, J. S. and Hodson, H. P. Unsteady transition in an axial flow turbine, Part 1: Measurements on the turbine rotor. *ASME Journal of Turbomachinery*, 112:206–214, 1990.

[5] Addison, J. S. and Hodson, H. P. Unsteady transition in an axial flow turbine, Part 2: Cascade measurements and modeling. *ASME Journal of Turbomachinery*, 112:215–221, 1990.

[6] Barankiewicz, W. S. and Hathaway, M. D. Effects of stator indexing on performance in a low speed multistage axial compressor. ASME Paper 97-GT-496, Orlando, 1997.

[7] Bellhouse, B. J. and Schultz, D. L. Determination of mean and dynamic skin friction, separation and transition in low-speed flow with a thin film heated element. *Journal of Fluid Mechanics*, 24(2):379–400, 1966.

[8] Bendat, J. S. and Piersol, A. G. *Random Data: Analysis and Measurement Procedures*. Wiley Interscience, First edition, 1971.

[9] Blair, M. F. Influence of free-stream turbulence on boundary layer transition in favorable pressure gradients. *ASME Journal of Engineering for Power*, 104: 743–750, 1982.

[10] Blair, M. F. Boundary layer transition in accelerating flows with intense freestream turbulence. Tech. Report UTRC91-1, UTRC, East Hartford, Connecticut, 1991.

[11] Blight, F. G. and Howard, W. Tests on four aerofoil cascades Part I: Deflection, drag and velocity distribution. Report E 74, Aeronautical Research Laboratories, Melbourne, Australia, 1952.

[12] Blight, F. G. and Howard, W. Tests on four aerofoil cascades part II: Boundary layer characteristics. Report E 75, Aeronautical Research Laboratories, Melbourne, Australia, 1952.

[13] Boiko, A. V., Westin, K. J. A., Klingmann, B. G. B., Kozlov, V. V., and Alfredsson, P. H. Experiments in a boundary layer subjected to free stream turbulence. Part 2. The role of TS-waves in the transition process. *Journal of Fluid Mechanics*, 281:219–245, 1994.

[14] Boyle, R. J. and Simon, F. F. Mach number effects on turbine blade transition length prediction. ASME Paper 98-GT-367, Stockholm, 1998.

[15] Breuer, K. S. and Haritonidis, J. H. The evolution of a localized disturbance in a laminar boundary layer. Part 1. Weak disturbances. *Journal of Fluid Mechanics*, 220:569–594, 1990.

[16] Breuer, K. S. and Landahl, M. T. The evolution of a localized disturbance in a laminar boundary layer. Part 2. Strong disturbances. *Journal of Fluid Mechanics*, 220:595–621, 1990.

[17] Bromba, M. U. A. and Ziegler, H. Application hints for Savitzky-Golay digital filters. *Analytical Chemistry*, 53:1583–1586, 1981.

[18] Brown, G. L. Theory and application of heated films for skin friction measurement. In *Proceedings of the 1967 Heat Transfer and Fluid Mechanics Institute*, pages 361–381, 1967. Paper 18.

[19] Camp, T. R. and Shin, H.-W. Turbulence intensity and length scale measurements in multistage compressors. *ASME Journal of Turbomachinery*, 117:38–46, 1995.

[20] Chen, K. K. and Thyson, N. A. Extension of Emmons' spot theory to flows on blunt bodies. *AIAA Journal*, 9(5):821–825, 1971.

[21] Cohen, J., Breuer, K. S., and Haritonidis, J. H. On the evolution of a wave packet in a laminar boundary layer. *Journal of Fluid Mechanics*, 225:575–606, 1991.

[22] Collis, D. C. and Williams, M. J. Two-dimensional convection from heated wires at low reynolds numbers. *Journal of Fluid Mechanics*, 6:357–384, 1959.

[23] Cumpsty, N. A. *Compressor Aerodynamics*. Longman Scientific & Technical, first edition, 1989.

[24] Cumpsty, N. A., Dong, Y., and Li, Y. S. Compressor blade boundary layers in the presence of wakes. ASME Paper 95-GT-443, International Gas Turbine and Aeroengine Congress and Exposition, Houston, Texas, 1995.

[25] Curtis, E. M., Hodson, H. P., Banieghbal, M. R., Denton, J. D., and Howell, R. J. Development of blade profiles for low pressure turbine applications. ASME Paper 96-GT-356, Birmingham, 1996.

[26] Davies, M. R. D., Fitzgerald, J. E., Duffy, J. T., and O'Donnell, F. K. Measurements of aerodynamic wall shear stress with heated thin film gauges. ASME Paper 97-GT-211, Orlando, 1997.

[27] Denton, J. D. Loss mechanisms in turbomachines. *ASME Journal of Turbomachinery*, 120:28–35, 1994.

[28] Deregel, P. and Tan, C. S. Impact of rotor wakes on steady-state axial compressor performance. ASME Paper 96-GT-253, Birmingham, 1996.

[29] Dhawan, S. and Narasimha, R. Some properties of boundary layer flow during the transition from laminar to turbulent motion. *Journal of Fluid Mechanics*, 3: 418–436, 1958.

[30] Dong, Y. and Cumpsty, N. A. Compressor blade boundary layers: Part 1 — Test facility and measurements with no incident wakes. *ASME Journal of Turbomachinery*, 112:222–230, 1990.

[31] Dong, Y. and Cumpsty, N. A. Compressor blade boundary layers: Part 2 — Measurements with incident wakes. *ASME Journal of Turbomachinery*, 112:231–240, 1990.

[32] Doorly, D. J. and Oldfield, M. L. G. Simulation of wake passing in a stationary turbine rotor cascade. *AIAA Journal of Propulsion and Power*, 1:316–318, 1985.

[33] Drela, M. MISES implementation of modified abu-ghannam/shaw transition criterion. in MISES Code Documentation, MIT, 1995.

[34] Dring, R. P., Joslyn, H. D., Hardin, L. W., and Wagner, J. H. Turbine rotor-stator interaction. *ASME Journal of Engineering for Power*, 104:729–742, 1982.

[35] Dunham, J. Prediction of boundary-layer transition on turbomachinery blades. AGARD AG 164, No. 3, 1972.

[36] Emmons, H. W. The laminar-turbulent transition in a boundary layer - Part I. *Journal of Aerospace Sciences*, 18(7):490–498, 1951.

[37] Eulitz, F., Engel, K., and Gebing, H. Numerical investigation of clocking effects in a multistage turbine. ASME Paper 96-GT-26, Birmingham, 1996.

[38] Evans, R. L. Turbulence and unsteadiness measurements downstream of a moving blade row. *ASME Journal of Engineering for Power*, 97:131–139, 1975.

[39] Falco, R. E. and Gendrich, C. P. The turbulence burst detection algorithm of Z. Zarić. In Kline, S. J. and Afgan, N. H., editors, *Near-Wall Turbulence 1988 Zoran Zarić Memorial Conference*, pages 911–931. Hemisphere, 1990.

[40] Farge, M. Wavelet transforms and their applications to turbulence. *Annual Review of Fluid Mechanics*, 24:395–457, 1992.

[41] Freymuth, P. and Fingerson, L. M. Electronic testing of frequency response for thermal anemometers. *TSI Quarterly*, 3:5–12, 1977. (Appendix A of TSI IFA-100 manual.).

[42] Funazaki, K. Unsteady boundary layers on a flat plate disturbed by periodic wakes : Part I - Measurement of wake-affected heat transfer and wake-induced transition model. *ASME Journal of Turbomachinery*, 118:327–336, 1996.

[43] Funazaki, K. Unsteady boundary layers on a flat plate disturbed by periodic wakes : Part II - Measurements of unsteady boundary layers and discussion. *ASME Journal of Turbomachinery*, 118:337–346, 1996.

[44] Funazaki, K., Kitazawa, T., Koizumi, K., and Tanuma, T. Studies on wake-disturbed boundary layers under the influences of favourable pressure gradient and free-stream turbulence, Part I: Experimental setup and discussions on transition model. ASME Paper 97-GT-451, Orlando, 1997.

[45] Gaster, M. A theoretical model of a wave packet in the boundary layer on a flat plate. *Proc.Roy.Soc.Lond.*, A347:271–289, 1975.

[46] Gaster, M. and Grant, I. An experimental investigation of the formation and development of a wave packet in a laminar boundary layer. *Proc.Roy.Soc.Lond.*, A347:253–269, 1975.

[47] Giles, M. and Haimes, R. Validation of a numerical method for unsteady flow calculations. *ASME Journal of Turbomachinery*, 115:110–117, 1993.

[48] Giles, M. B. Calculation of unsteady wake/rotor interactions. *AIAA Journal of Propulsion and Power*, 4:356–362, 1988.

[49] Gorrell, S. E., Copenhaver, W. W., and Chriss, R. M. Effects of upstream wakes on the performance of a transonic compressor stage. Proc. 13th International Symposium on Air Breathing Engines, Chattanooga, 1997.

[50] Gostelow, J. P., Blunden, A. R., and Walker, G. J. Effects of free-stream turbulence and adverse pressure gradients on boundary layer transition. *ASME Journal of Turbomachinery*, 116:392–404, 1994.

[51] Gostelow, J. P., Hong, G., Melwani, N., and Walker, G. J. Turbulent spot development under a moderate adverse pressure gradient. *ASME Journal of Turbomachinery*, 118:737–743, 1996.

[52] Gostelow, J. P., Melwani, N., and Walker, G. J. Effects of a streamwise pressure gradient on turbulent spot development. *ASME Journal of Turbomachinery*, 118 (4):737–743, 1996.

[53] Gostelow, J. P., Walker, G. J., Solomon, W. J., Hong, G., and Melwani, N. Investigation of the calmed region behind a turbulent spot. ASME Paper 96-GT-489, International Gas Turbine and Aeroengine Congress and Exposition, Birmingham, UK, 1996.

[54] Graf, M. B., Greitzer, E. M., Marble, F. E., and Sharma, O. P. Effects of stator pressure field on upstream rotor performance. ASME Paper 99-GT-99, International Gas Turbine Congress, Indianapolis, Indiana, 1999.

[55] Grek, H. R., Kozlov, V. V., and Ramazanov, M. P. Receptivity and stability of the boundary layer at a high turbulence level. In Arnal, D. and Michel, R., editors, *Laminar-Turbulent Transition, IUTAM Symposium Toulouse/France*, pages 511–521. Springer-Verlag, 1989.

[56] Griffin, L. W., Huber, F. W., and Sharma, O. P. Performance improvement through indexing of turbine airfoils: Part 2 - numerical simulation. *ASME Journal of Turbomachinery*, 118:636–642, 1996.

[57] Hall, D. J. and Gibbings, J. C. Influence of stream turbulence and pressure gradient on boundary layer transition. *Journal of Mechanical Engineering Science*, 14:134–146, 1972.

[58] Halstead, D. E., Wisler, D. C., Okiishi, T. H., Walker, G. J., Hodson, H. P., and Shin, H-W. Boundary layer development in axial compressors and turbines: Part 1 of 4 – Composite picture. *ASME Journal of Turbomachinery*, 119(1):114–127, 1997a.

[59] Halstead, D. E., Wisler, D. C., Okiishi, T. H., Walker, G. J., Hodson, H. P., and Shin, H-W. Boundary layer development in axial compressors and turbines: Part 2 of 4 – Compressors. *ASME Journal of Turbomachinery*, 119(3):426–444, 1997b.

[60] Halstead, D. E., Wisler, D. C., Okiishi, T. H., Walker, G. J., Hodson, H. P., and Shin, H-W. Boundary layer development in axial compressors and turbines: Part 3 of 4 – LP Turbines. *ASME Journal of Turbomachinery*, 119(2):234–246, 1997c.

[61] Halstead, D. E., Wisler, D. C., Okiishi, T. H., Walker, G. J., Hodson, H. P., and Shin, H-W. Boundary layer development in axial compressors and turbines: Part 4 of 4 – Computations and Analyses. *ASME Journal of Turbomachinery*, 119(1): 128–139, 1997d.

[62] Hazarika, B. K. and Hirsch, Ch. Transition over C4 leading edge and measurement of intermittency factor using PDF of hot-wire signal. ASME Paper 95-GT-294, 1995.

[63] Hobson, G. V., Wakefield, B. E., and Roberts, W. B. Turbulence amplification with incidence at the leading edge of a compressor cascade. ASME Paper 96-GT-409, Birmingham, UK, 1996.

[64] Hodson, H. P. Boundary layer and loss measurements on the rotor of an axial-flow turbine. *ASME Journal of Engineering for Gas Turbines and Power*, 106: 391–399, 1984.

[65] Hodson, H. P. Boundary layer transition and separation near the leading edge of a high speed turbine blade. *ASME Journal of Engineering for Gas Turbines and Power*, 107:127–134, 1985.

[66] Hodson, H. P. and Dawes, W. N. On the interpretation of measured profile losses in unsteady wake-turbine blade interaction studies. ASME Paper 95-GT-494, International Gas Turbine and Aeroengine Congress and Exposition, Birmingham, UK, 1996.

[67] Hodson, H. P., Huntsman, I., and Steele, A. B. An investigation of boundary layer development in a multistage LP turbine. *ASME Journal of Turbomachinery*, 116: 375–383, 1994.

[68] Horton, H. P. A semi-empirical theory for the growth and bursting of laminar separation bubbles. Current Paper 1073, Aeronautical Research Council, 1969.

[69] Hourmouziadis, J. Aerodynamic design of low pressure turbines. In Fottner, L., editor, *AGARD Lecture Series No. 167, Blading Design for Axial Turbomachines*, pages 8.1–8.40. AGARD, 1989.

[70] Howell, A. R. Fluid dynamics of axial compressors. *Proc. Inst. Mech. Eng. E*, 153:441–452, 1945.

[71] Howell, A. R. Private Communication - to A. R. Oliver, University of Tasmania. 1973.

[72] Huber, F. W., Johnson, P. D., Sharma, O. P., Staubach, J. B, and Gaddis, S. W. Performance improvement through indexing of turbine airfoils: Part 1 - experimental investigation. *ASME Journal of Turbomachinery*, 118:630–635, 1996.

[73] Hughes, J. D. and Walker, G. J. Natural transition phenomena on a axial compressor blade. ASME Paper 2000-GT-0269, International Gas Turbine Congress, Munich, Germany, 2000.

[74] Hughes, J. D., Walker, G. J., and Gostelow, J. P. Identification of instability phenomena in periodic transitional flows on turbomachine blades. Proc. 14th International Symposium on Air Breathing Engines, Florence, 1999.

[75] Johnson, Mark W. A bypass transition model for boundary layers. *ASME Journal of Turbomachinery*, 116:759–764, 1994.

[76] Johnson, Mark W. and Ercan, Ali H. A boundary layer transition model. ASME Paper 96-GT-444, International Gas Turbine and Aeroengine Congress and Exposition, Birmingham, UK, 1996.

[77] Johnson, Mark W. and Ercan, Ali H. Predicting bypass transition: A physical model versus empirical correlations. ASME Paper 97-GT-475, 1997.

[78] Kachanov, Y. S. On the resonant nature of the breakdown of a laminar boundary layer. *Journal of Fluid Mechanics*, 184:43–74, 1987.

[79] Kerrebrock, J. L. and Mikolajczak, A. A. Intra-stator transport of rotor wakes and its effect on compressor performance. *ASME Journal of Engineering for Power*, 92:359–368, 1970.

[80] Kittichaikarn, C., Ireland, P. T., Zhong, S., and Hodson, H. P. An investigation on the onset of wake-induced transition and turbulent spot production rate using thermochromatic liquid crystals. ASME Paper 99-GT-126, International Gas Turbine and Aeroengine Congress and Exposition, Indianapolis, Indiana, 1999.

[81] Klebanoff, P. S., Tidstrom, K. D., and Sargent, L. M. The three-dimensional nature of boundary layer instability. *Journal of Fluid Mechanics*, 12:1–34, 1962.

[82] Knapp, C. F. and Roache, P. J. A combined visual and hot-wire anemometer investigation of boundary layer transition. *AIAA Journal*, 6:29–36, 1968.

[83] Lewalle, J. Tutorial on continuous wavelet analysis of experimental data. Mechanical Aerospace and Manufacturing Engineering Dept., Syracuse University. World Wide Web: http://www.mame.syr.edu/faculty/lewalle/ tutor/tutor.html, 1995.

[84] Lewalle, J. and Ashpis, D. E. Transport in bypass transition: Mapping active time scales using wavelet tehniques. *Tenth Symposium on Turbulent Shear Flows*, 2:2–37–2–42, 1995.

[85] Lewalle, J., Ashpis, D. E., and Sohn, K-H. Demonstration of wavelet techniques in the spectral analysis of bypass transition data. NASA TP 3555, USA, 1997.

[86] Lieblein, S. and Roudebush, W. Theoretical loss relations for low-speed two-dimensional cascade flow. NACA TN 3662, 1956.

[87] Lighthill, M. J. A mathematical method of cascade deisgn. ARC Reports and Memoranda 2104, 1945.

[88] Lockhart, R. C. and Walker, G. J. The influence of viscous interactions on the flow downstream of an axial compressor stage. Paper presented at the 2nd International Symposium on Air Breathing Engines, Sheffield UK, 1974.

[89] Mack, L. M. Transition and laminar instability. Jet Propulsion Laboratory Publication 77–15, Pasadena, California, 1977.

[90] Mack, L. M. Boundary-layer linear stability theory. In Michel, R., editor, *Special Course on Stability and Transition of Laminar Flow*, pages 3.1–3.81. AGARD, 1984. Report No. 709.

[91] Malkiel, E. and Mayle, R. E. Transition in a separation bubble. *ASME Journal of Turbomachinery*, 118:752–759, 1996.

[92] Manwaring, S. R. and Wisler, D. C. Unsteady aerodynamics and gust response in compressors and turbines. *ASME Journal of Turbomachinery*, 115(4):724–740, 1993.

[93] Mayle, R. E. The role of laminar-turbulent transition in gas turbine engines. *ASME Journal of Turbomachinery*, 113:509–537, 1991. The 1991 IGTI Scholar Lecture.

[94] Mayle, R. E. Unsteady multimode transition in gas turbine engines. AGARD PEP 80, 1992.

[95] Mayle, R. E. A theory for predicting the turbulent-spot production rate. *ASME Journal of Turbomachinery*, 121:588–593, 1999.

[96] Mayle, R. E., Dullenkopf, K., and Schulz, A. The turbulence that matters. *ASME Journal of Turbomachinery*, 120:402–409, 1998.

[97] Mayle, R. E. and Schulz, A. The path to predicting bypass transition. *ASME Journal of Turbomachinery*, 119:405–411, 1997.

[98] McDonald, H. and Fish, R. W. Practical calculations of transitional boundary layers. Advisory Group for Aerospace Research and Development AGARDograph 164, North Atlantic Treaty Organisation, 1972.

[99] Morkovin, M. V. On the many faces of transition. In Wells, C. Sinclair, editor, *Viscous Drag Reduction*, pages 1–31. Plenum Press, New York, 1969.

[100] Narasimha, R. On the distribution of intermittency in the transition region of a boundary layer. *Journal of Aerospace Sciences*, 24(9):711–712, 1957.

[101] Narasimha, R. The laminar-turbulent transition zone in the boundary layer. *Progress in Aerospace Science*, 22:29–80, 1985.

[102] Obremski, H. J. and Fejer, A. A. Transition in oscillating boundary layer flows. *Journal of Fluid Mechanics*, 29:93–111, 1967.

[103] Obremski, H. J., Morkovin, M. V., and Landahl, M. A portfolio of stability characteristics of incompressible boundary layers. Advisory Group for Aerospace Research and Development AGARDograph 134, North Atlantic Treaty Organisation, 1969.

[104] Oliver, A. R. Comparison between sand cast and machined blades in the vortex wind tunnel. Report ME 103, Aeronautical Research Laboratories, Melbourne, Australia, 1961.

[105] Orth, U. Unsteady boundary-layer transition in flow periodically disturbed by wakes. *ASME Journal of Turbomachinery*, 115:707–713, 1993.

[106] Pfeil, H., Herbst, R., and Schröder, T. Investigation of the laminar-turbulent transition of boundary layers disturbed by wakes. *ASME Journal of Engineering for Power*, 105:130–137, 1983.

[107] Ravindranath, A. and Lakshminarayana, B. Structure and decay characteristics of turbulence in the near and far-wake of a moderately loaded compressor rotor blade. *ASME Journal of Engineering for Power*, 103:131–140, 1981.

[108] Riley, J. J. and Gad-el-Hak, M. The dynamics of turbulent spots. In Davis and Lumley, editors, *Frontiers of Fluid Mechanics*, pages 123–155. Springer, 1985.

[109] Roberts, W. B. The effect of Reynolds number and laminar separation on axial compressor performance. *ASME Journal of Engineering for Power*, pages 261–274, 1975.

[110] Roberts, W. B. Calculation of laminar separation bubbles and their effect on airfoil performance. *AIAA Journal*, 18:25–31, 1980.

[111] Roudebush, W. H. and Lieblein, S. Viscous flow in two-dimensional cascades. In Johnsen, I. A. and Bullock, R. O., editors, *Aerodynamic Design of Axial-Flow Compressors*, pages 151–182. NASA SP-36, 1965.

[112] Samoilovich, G. S. and Yablokov, L.D. Measurements of periodically fluctuating flows in turbomachinery by ordinary pitot tubes. *ASME Journal of Turbomachinery*, 17(9):105–110, 1970.

[113] Saric, W. S. Boundary-layer stability and transition. In hiro Mori, Kazu, editor, *Proceedings of the Fifth International Conference on Numerical Ship Hydrodynamics*, pages 23–33. National Academy Press, 1990. Paper 18.

[114] Schlichting, H. *Boundary Layer Theory.* McGraw-Hill, fourth edition, 1962.

[115] Schobeiri, M. T., Read, K., and Lewalle, J. Effect of unsteady wake passing frequency on boundary layer transition: Experimental investigation and wavelet analysis. ASME Paper 95-GT-437, International Gas Turbine Congress, Houston, Texas, 1995.

[116] Schubauer, G. B. and Klebanoff, P. S. Contributions on the mechanics of boundary layer transition. NACA TN 3489, 1955.

[117] Schubauer, G. B. and Skramstad, H. K. Laminar boundary layer oscillations and transition on a flat plate. NACA Tech. Rept. 909, 1948.

[118] Schulte, V. and Hodson, H. P. Prediction of the becalmed region for LP turbine profile design. ASME Paper 97-GT-398, Orlando, 1997.

[119] Schulte, V. and Hodson, H. P. Unsteady wake-induced boundary layer transition in high lift LP turbines. *ASME Journal of Turbomachinery*, 120:28–35, 1998.

[120] Seifert, A. and Wygnanski, I. J. On turbulent spots in a laminar boundary layer subjected to a self-similar adverse pressure gradient. *Journal of Fluid Mechanics*, 296:185–209, 1995.

[121] Smith, L. H. Wake dispersion in turbomachines. *ASME Journal of Basic Engineering*, 88:688–690, 1966.

[122] Sohn, K-H. and Reshotko, E. Experimental study of boundary layer transition with elevated freestream turbulence on a heat flat plate. Technical Report NASA CR 187068, USA, 1991.

[123] Solomon, W. J. *Unsteady Boundary Layer Transition on Axial Compressor Blades.* PhD thesis, University of Tasmania, Hobart, Australia, 1996.

[124] Solomon, W. J. and Walker, G. J. Incidence effects on wake-induced transition on an axial compressor blade. In *Proc. 12th International Symposium on Air Breathing Engines*, pages 954–964. Melbourne, Australia, 1995.

[125] Solomon, W. J. and Walker, G. J. Observations of wake-induced transition on an axial compressor blade. ASME Paper 95-GT-381, 1995.

[126] Solomon, W. J., Walker, G. J., and Gostelow, J. P. Transition length prediction for flows with rapidly changing pressure gradients. *ASME Journal of Turbomachinery*, 118(4):744–751, 1996.

[127] Solomon, W. J., Walker, G. J., and Hughes, J. D. Periodic transition on an axial compressor stator - Incidence and clocking effects. Part II - Transition onset predictions. *ASME Journal of Turbomachinery*, 121:408–415, 1999.

[128] Squire, H. B. and Winter, K. G. The secondary flow in a cascade of aerofoils. *Journal of Aeronautical Science*, 18:271, 1951.

[129] Tain, L. *Compressor Leading Edges in Incompressible and Compressible Flows.* PhD thesis, Cambridge University Engineering Department, 1998.

[130] Thwaites, B. Approximate calculation of the laminar boundary layer. *The Aeronautical Quarterly*, 1:245–280, 1949.

[131] Torrence, C. and Compo, G. P. A practical guide to wavelet analysis. *Bulletin of the American Meteorogical Society*, 79(1):61–78, 1998.

[132] Tso, J., Chang, S. I., and Blackwelder, R. F. On the breakdown of a localised disturbance in a laminar boundary layer. In Arnal, D. and Michel, R., editors, *Laminar-Turbulent Transition, IUTAM Symposium Toulouse/France*, pages 199–214. Springer-Verlag, 1989.

[133] Valkov, T. V. and Tan, C. S. Effect of upstream rotor vortical disturbance on the time average performance of axial compressor stators: Part 1 – Framework of technical approach and wake-stator blade interactions. ASME Paper 98-GT-312, Stockholm, 1998.

[134] Valkov, T. V. and Tan, C. S. Effect of upstream rotor vortical disturbance on the time average performance of axial compressor stators: Part 2 – Rotor tip vortex/streamwise vortex-stator blade interactions. ASME Paper 98-GT-313, Stockholm, 1998.

[135] van Hest, B. F. A. *Laminar-Turbulent Transition in Boundary Layers with Adverse Pressure Gradient.* PhD thesis, Delft University of Technology, 1996.

[136] Van Zante, D. E., Adamczyk, J. J., Strazisar, A. J., and Okiishi, T. H. Wake recovery performance benefit in a high-speed axial compressor. ASME Paper 97-GT-535, Orlando, 1997.

[137] Volino, R. J. Wavelet analysis of transitional flow data under high free-stream turbulence conditions. ASME Paper 98-GT-289, International Gas Turbine Congress, Stockholm, Sweden, 1998.

[138] Walker, G. J. *An Investigation of the Boundary Layer Behaviour on the Blading of a Single-Stage Axial-Flow Compressor.* PhD thesis, University of Tasmania, 1972.

[139] Walker, G. J. The unsteady nature of boundary layer transition on an axial compressor blade. ASME Paper 74-GT-135, Zurich, 1974.

[140] Walker, G. J. Observations of separated laminar flow on axial compressor blading. ASME Paper 75-GT-63, Houston, 1975.

[141] Walker, G. J. Transitional flow on axial turbomachine blading. *AIAA Journal*, 27(5):595–602, 1989.

[142] Walker, G. J. The role of laminar-turbulent transition in gas turbine engines — A discussion. *ASME Journal of Turbomachinery*, 117:207–217, 1993.

[143] Walker, G. J. and Gostelow, J. P. Effects of adverse pressure gradients on the nature and length of boundary layer transition. *ASME Journal of Turbomachinery*, 112:196–205, 1990.

[144] Walker, G. J. and Hughes, J. D. The occurrence of natural transition phenomena in periodic transition on axial compressor blades. IUTAM Symposium on Laminar-Turbulent Transition, Sedona, Arizona, 1999.

[145] Walker, G. J., Hughes, J. D., Köhler, I., and Solomon, W. J. The influence of wake-wake interactions on loss fluctuations of a downstream axial compressor blade row. *ASME Journal of Turbomachinery*, 120:695–704, 1998.

[146] Walker, G. J., Hughes, J. D., and Solomon, W. J. Periodic transition on an axial compressor stator - Incidence and clocking effects. Part I - Experimental data. *ASME Journal of Turbomachinery*, 121:398–407, 1999.

[147] Walker, G. J., Hughes, J. D., Solomon, W. J., and Köhler, I. Wake mixing and blade clocking effects in an axial compressor. Proc. 13th International Symposium on Air Breathing Engines, Chattanooga, 1997.

[148] Walker, G. J., Subroto, P. H., and Platzer, M. F. Inviscid interaction analysis of low Reynolds number airfoil flows involving laminar separation bubbles. ASME Paper 88-GT-32, International Gas Turbine Congress, Amsterdam, 1988.

[149] Walreavens, R. E. and Cumpsty, N. A. Leading edge separation bubbles on turbomachine blades. ASME Paper 93-GT-91, Cincinnati, 1993.

[150] Wisler, D. C. Loss reduction in axial-flow compressors through low-speed model testing. *ASME Journal of Engineering for Gas Turbines and Power*, 107:354–363, 1985.

[151] Wisler, D. C., Halstead, D. E., and Beacher, B. F. Improving compressor and turbine performance through cost-effective low-speed testing. Proc. 14th International Symposium on Air Breathing Engines, Florence, 1999.

[152] Youngren, H. and Drela, M. Viscous-inviscid method for preliminary design of transonic cascades. AIAA Paper 91-2364, AIAA Joint Propulsion Conference, 1991.

[153] Zierke, W. C. and Okiishi, T. H. Measurement and analysis of total-pressure unsteadiness data from an axial compressor stage. *ASME Journal of Engineering for Power*, 104:479–488, 1982.

[154] Zohar, Y. *Fine Scale Mixing in a Free Shear Layer.* PhD thesis, University of Southern California, 1990. See also Y. Zohar and C-M. Ho. Dissipation scale and control of fine-scale turbulence in a plane mixing layer. *Journal of Fluid Mechanics.* 320, pp 139–161, 1996.